Mechanisms of Fixed Contamination of Commonly Engineered Surfaces

By

Rebecca Claire Williamson

Being a thesis submitted to Lancaster University in partial fulfilment for the requirements for the degree of

DOCTOR OF PHILIOSOPHY

August 2018

Lancaster University

DECLARATION

The work described in this thesis was conducted at the Department of Engineering, Lancaster University between October 2009 and September 2013. Unless stated otherwise it is the work of the author and has not been submitted in support of any other degree.

Signature: _____

Rebecca Williamson

August 2018

ABSTRACT

An abstract of the thesis of Rebecca Claire Williamson for the award of Doctor of Philosophy submitted August 2018.

Title: Mechanisms of Fixed Contamination of Commonly Engineered Surfaces.

This project is concerned with developing a greater understanding of the deposition of radioactive solids, colloids, or ions suspended in aqueous liquid onto the surface of stainless steel. Fixed contamination on contaminated metallic surfaces is commonly removed using (electro) chemical methods. The most common methods employed are the use of mineral acids or MEDOC (Metal Decontamination by Oxidation with Cerium). However, these result in dissolution of the passive oxide layer formed at the metal surface. This increases the level of secondary waste which, in turn, increases the burden of effluent treatment plants. The passivation of steels in HNO_3 is complicated by the autocatalytic reduction of HNO_3 to aqueous HNO_2 which attacks the steel surface. We describe the effect of this behaviour on process steels in stagnant and/or flowing conditions. Rotating Disk Electrode (RDE) studies indicate that at HNO_3 concentrations $\leq$20% wt. the reaction is surface based. At HNO_3 concentration $\geq$20% wt. the reaction occurs in the bulk solution. We established a series of corrosion potentials for varying concentrations of nitric acid. These corrosion potentials allowed us to age steel in a controlled fashion. Thus, we describe work carried out on electrochemically accelerated oxide growth on 316L SS and SS2343 in HNO_3 media and HNO_3 media with radionuclide surrogates (depleted U, Ce and Eu). Characterisation was performed using combined Linear Sweep Voltammetry (LSV), Electrochemical Impedance Spectroscopy (EIS) and Electrochemical Quartz Crystal Microgravimetry (EQCM) measurements. Areas of active, passive, high voltage passive, transpassive and secondary passivation regimes in the associated current voltage were identified. Further, we have directly measured the growth of that layer by using in situ microgravimetry. X-Ray Photoelectron Spectroscopy (XPS) was used to determine film composition and presence of contaminant uptake. The passive film on 316L SS is formed of a passive film consisting of Cr(III) hydroxide rich layer and Cr(III) oxide layers at lower potentials. With increasing HNO_3 and potential the layer becomes more Cr(III) oxide rich before oxidising to Cr(VI). No radionuclide surrogate contaminants were detected within passive films formed in this study.

Contents

List of Figures

Chapter 1

Chapter 2

Chapter 3

Chapter 4

Chapter 5

Chapter 6

Chapter 8

List of Tables

Chapter 1

Chapter 3

Chapter 8

Acknowledgements

Special thanks to my Director of Studies Colin Boxall for his help and enthusiasm during my PhD tenure and for the opportunity to work within the Nuclear Engineering department at Lancaster University.

I would like to thank the Nuclear Decommissioning Authority for funding of this project and the Universities of Ulster (non-active studies) and Bristol (active studies) for use of their XPS. Thanks to Dr Richard (Barney) Wilbraham for his patience and assistance in training, experiment design, proof reading and discussion of every aspect of my work.

Thanks to staff/students: Kath Ruscastle (for answering all of my questions) Barney, Phil, Mik, James, Pat, Andrew, Nadya, Ioannis, Miriam and Sukhraj for providing an entertaining working environment over the years.

Huge thanks to Sue Brown, without your patience and understanding I would never have got this done.

Most of all, thanks to my amazing husband Michael, who has put up with the late nights, train cancellations, proof reading and general ranting about experiment failures and thanks to my parents and brother for all their support and much needed encouragement.

Glossary of Terms

Major Symbols

Symbol	Meaning
δ	Diffusion layer thickness
λ	Wavelength
v	Kinematic viscosity
ω	frequency
ω	Angular velocity
w	Radial frequency
ϕ/θ	Phase angle
ΔE	Potential step
Δf	Frequency change
Δm	Mass change
μ_q	Sheer modulus of quartz for an AT cut crystal
ρ_q	Density of quartz
c	concentration
c_0	Concentration at electrode surface
c_∞	Concentration in bulk (near infinite from the electrode)

Symbol	Meaning
C_{dl}	Double layer capacitance
D	Diffusion coefficient
E	Potential
e^-	Electron
E^0	Standard electrode potential
E_0	Potential response amplitude
E_{corr}	Corrosion potential
F	Faraday constant
f_0	Resonant frequency
I/i	Current
I_0	Current response amplitude
i_{corr}	Corrosion current
j_e	Electrochemical flux
j_{mt}	Species flux to electrode surface
k_e	Electrochemical reaction rate constant
k_{mt}	Mass transfer rate constant
M	Mass
Ox	Oxidising Agent
P	Product

Symbol	Meaning
Q	Total charge passed
R	Reactant
R*ed*	Reducing Agent
R_p	Polarisation resistance
R_s	Solution resistance
T	Temperature
t	Time
v^{-1}	Scan rate
V	Potential
W	Warburg impedance
Z	Impedance
Z’	Real component of impedance
Z”	Imaginary component of impedance
Z_0	Magnitude of impedance

Standard Abbreviations

Symbol	Meaning
A	Electron Acceptor
CB	Conduction Band
CORD	Chemical Oxidising Reduction Decontamination
CV	Cyclic Voltammetry
D	Electron Donor
DF	Decontamination factor
EDAX	Energy Dispersive X-ray Analysis
EQCM	Electrochemical Quartz Crystal Microbalance
I.E.P	Isoelectric Point
ICP-MS	Inductively Coupled Plasma Mass Spectrometry
LOMI	Low Oxidation State Metal Ions
M	Metal
MEDOC	Metal Decontamination by Oxidation with Cerium
MSE	Mercurous Sulphate Electrode
NHE	Normal Hydrogen Electrode
OK	Odourless Kerosene

Ox	Oxidant (any species capable of gaining electrons)
PUREX	Plutonium Uranium Extraction
QCM	Quartz Crystal Microbalance
RDE	Rotating Disk Electrode
Red	Reductant (any species capable of losing electrons)
SCE	Standard Calomel Reference Electrode
SEM	Scanning Electron Microscope
SODP	Strong Ozone Decontamination Process
SSS	Superactive Surface States
TBP	Tributyl Phosphate
UV/Vis	Ultraviolet/Visible Light
VB	Valence Band
XPS	X-ray Photoelectron Spectroscopy
XRD	X-ray Diffraction

Project Objectives

Decontamination of nuclear facilities for decommissioning allows for the reduction of waste classification levels with concomitant decreases in waste consignment costs, remote handling, hazard and personnel risk. Development of cost effective decontamination strategies - including selection of a suitable technique, identification of their R&D needs, confidence in efficacy and minimisation of secondary wastes - requires a fundamental understanding of the interfacial science of radionuclide contaminants and the way in which they are associated with surfaces to be decontaminated. Due to their high corrosion resistance, steels are ubiquitous on nuclear sites as process plant and construction materials. However, current understanding of the mechanisms of adherence and penetration of contamination into steels is inadequate to support informed choice of decontamination methods.

Surface contamination, generally derived from the "plating out" of solids, colloids or metal ions from a liquid/solution phase, is broadly classified as being of two main types: non-fixed and fixed contamination. Here, 'Plate-out' is a general term associated with the contamination and clean-up of contaminated surfaces and is defined as: 'The deposition of radioactive solids, colloids, or ions suspended in aqueous liquid onto the surface of stainless steel holding the liquid.' [1]. In general the two types of contamination may be mechanistically defined as follows:

1. Non-fixed contamination - Here contaminants are held weakly on the surface by electrostatic attractions or may be held on the surface through chemical bonds to the upper oxide surface. Alternatively, if the surface is exposed to a highly concentrated solution then a pure precipitate of radioactive metal-oxide may form on the steel surface.

2. Fixed contamination - The contaminant is precipitated or co-precipitated with iron or chromium to form a specific mineral phase e.g. substituting iron within one of the many oxide phases which form on corroding steel. Alternatively, contaminants may channel down grain boundaries (especially in chromium deficient areas of a steel) [1].

Whilst Rouppert *et al.* [2] have suggested that fixed contamination is chemisorbed and non-fixed is physisorbed, the distinction between the two types is in reality more subtle. Studies indicate that inter-

conversion between a fixed and a non-fixed state is possible, depending upon the environmental conditions [3].

A high percentage of 'plated-out' contamination will be loosely bound to the surface through the afore mentioned non-fixed contamination mechanisms. This material is easily removed by most physical clean-up techniques. Technical difficulties start to arise following the removal of the weakly bound, non-fixed material. The steel may only be slightly contaminated but such contamination is held within difficult to remove oxide layers.

Such fixed contamination on conducting metallic surfaces is commonly removed using (electro) chemical methods. The most common methods employed are the use of simple mineral acids or multi-step oxidative chemical processes such as MEDOC (Metal Decontamination by Oxidation with Cerium). However, such treatments frequently result in dissolution of the chromium passive oxide layer formed at the metal surface resulting in excessive dissolution of the underlying bulk iron. This increases the level of secondary waste which, in turn, increases the burden on effluent treatment plants.

Thus, improving the understanding of contaminant radionuclides interaction with and attachment to process engineering materials in plant environments is essential to enable the development of targeted decontamination techniques. Importantly, from the limited literature relating to radionuclide sorption mechanisms on engineering metals, key studies [2], [4] have found that sorbed contamination is almost entirely located in the outermost 0.5-1μm of the passive oxide layer formed at the steel surface. This suggests such heavily oxidising techniques could be replaced by more targeted/milder chemical treatment processes. Alternative techniques, such as mechanical process (jet blasting etc.), are unsuitable due to the large volumes of secondary wastes produced and also the lack of accessibility to the contaminated surface e.g. contamination of the inner surface of metal pipework.

The thickness and character of the aforementioned passive oxide layer formed on stainless steel surfaces is influenced by the type of stainless steel as well as by environmental factors including the pH of the local environment [1]. This project is concerned with developing a greater understanding of contamination under reprocessing plant conditions (e.g. PUREX), in particular aqueous acidic conditions, where steel corrosion/re-precipitation is most likely to be prevalent and fixed contamination most likely. HNO_3 concentration varies throughout the reprocessing flow sheet. Thus, the behaviour of stainless steel

in a range of HNO_3 concentrations will be studied to investigate the possibility of contaminant sorption/co-deposition on passive oxide films formed in HNO_3. Study of the passive layer is in contrast to previous studies which have looked at the *corrosion products* formed on those metals.

The proposed research can therefore be divided into two sections:

1. First, we investigate the electrochemical behaviour and surface composition of oxides formed on the surface of 316L SS in HNO_3 and the affect that the redox behaviour in HNO_3 has on these. Corrosion results from the coupling of two processes, one oxidative and one reductive. HNO_3 can sustain a reduction process at high HNO_3 concentrations, understanding how this couples with stainless steel oxidation may provide insights into HNO_3 promoted corrosion of stainless steels. Previous studies on HNO_3 by Balbaud [5] and Fauvet [6] indicate that at low concentrations the autocatalytic electrochemical reduction of HNO_3 is a slow surface based reaction. At higher concentrations, studies by Lange [7] and Carta and Pigford [8] suggest that the autocatalytic electrochemical reduction of HNO_3 shifts to a rapid solution based mechanism. The effect of the difference between these two types of HNO_3 reduction on passive oxide formation is explored.

2. Finally, In order to determine whether radionuclide surrogate contaminants become entrained in oxides formed under HNO_3 conditions similar to reprocessing, the electrochemical behaviour and surface composition of oxides formed on the surface of 316L SS in the presence of radionuclide surrogates will be assessed.

   Chapter 1 provides an introduction to the nuclear fuel cycle, electrochemistry and corrosion concepts and the corrosion of austenitic stainless steels. Also, a review of actinide chemistry and research into surface contamination is presented, followed by an overview of available decontamination techniques.

   Chapter 2 of this work describes the experimental details pertaining to work undertaken towards the characterisation of 316L SS in HNO_3 and in the presences of radionuclide surrogates.

   The third and fourth chapters describe the electrochemical and surface characterisation of 316L SS in low and high concentrations of HNO_3, through the use of Linear Sweep Voltammetry

(LSV), Electrochemical Impredance Spectroscopy (EIS), Electrochemical Quartz Crystal Microgravimetry (EQCM) and X-Ray Photoelectron Spectroscopy (XPS).

Chapter 5 deals with the electrochemical and surface characterisation of 316L SS in high and low concentrations of HNO_3in the presence of radionuclide surrogates.

The final chapter summarises the main conclusions that can be drawn from the work and outlines possible future work.

Chapter 1

Introduction

1 INTRODUCTION

1.1 The Nuclear Fuel Cycle

There are more than 400 operating nuclear reactors throughout the world. These reactors supply about 11% of the world's electricity production capacity [9]. In the UK, there are currently fourteen Advanced Gas-cooled Reactors (AGR) and one Pressurised Water Reactor (PWR) (Sizewell B). These fifteen reactors generate approximately 21% of the UK's electricity [10].

In order to provide fuel for the UK's nuclear reactor fleet, the UK imports mined uranium which is then milled, enriched (Urenco, Capenhurst) and fabricated into fuel (Springfields, Preston) for both AGR and PWR reactors [10], [11]. When used fuel is reprocessed (recycled) this is referred to as a "closed fuel cycle", a diagram of which is shown in Figure 1-1:

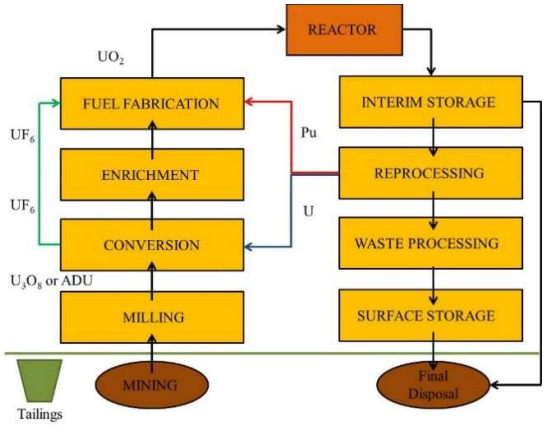

Figure 1-1 –A simplified schematic of a closed nuclear fuel cycle [12].

An "open fuel cycle" refers to used nuclear fuel that is sent to interim storage after being removed from the reactor before being sent for disposal at a Geological Disposal Facility (GDF) without undergoing reprocessing.

While the UK may in the future move towards an open fuel cycle, currently a closed fuel cycle is operated through the use of the THermal Oxide Reprocessing Plant (THORP) and MAGNOX (MAGnesium Non-

Oxidising) Reprocessing Plant, both located at Sellafield. Thus, reprocessing is an important component of the UK's nuclear fuel cycle and power generation strategy.

1.2 Nuclear Fuel Reprocessing

Nuclear reprocessing involves chemical treatment of spent nuclear fuel in order to separate the remaining U and Pu from the highly active waste component (composed of fission products and higher actinides). The reprocessing of spent nuclear fuel is undertaken for several reasons: i) Recovery of valuable fissile materials, ii) recovery of special isotopes and iii) reduction in the volume of high level waste.

Once reprocessed the U, Pu and TRU (TRansUranic waste) from UK AGR fuel can re-enter the fuel cycle for use in fuel fabrication, nuclear research applications or may be manufactured into MOX (Mixed OXide) fuel for use in other nuclear reactor designs. All current industrial reprocessing in the UK is centred on a liquid-liquid solvent extraction process known as PUREX (Plutonium URanium Extraction).

In the UK, nuclear fuel reprocessing has been carried out at Sellafield, Cumbria since the 1950s. There are two nuclear fuel reprocessing plants on site: (1) THORP, which deals with fuel from British Advanced Gas-cool Reactors (AGR) and global Light Water Reactors (LWR) and (2) B205, which deals with MAGNOX fuel from Britain's early nuclear reactors (e.g. Calder Hall) [13]. Here we focus on the more prolific THORP plant and the PUREX chemical extraction process used therein for nuclear fuel reprocessing.

1.2.1 Reprocessing at THORP

THORP at Sellafield commenced operation in 1994. THORP combines all the facilities needed to reprocess both UK and foreign spent oxide fuel. A flow diagram of reprocessing at THORP is shown in Figure 1-2:

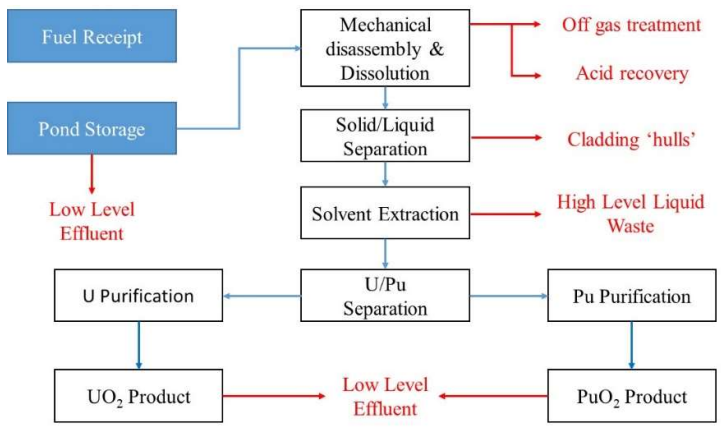

Figure 1-2 –Flow Diagram of Aqueous Reprocessing at THORP [12].

Transport flasks containing spent fuel from power stations are delivered to Sellafield by rail. On arrival the fuel is removed from the transport flasks underwater and stored in storage ponds to allow the fuel to cool further before reprocessing. Once the fuel has cooled sufficiently it is transferred from the storage pond to the Head End Plant shear cave where the fuel is chopped into sections. The fuel is then dropped into a dissolver vessel where the fuel is dissolved in nitric acid. The dissolved fuel liquor is then forwarded to the chemical separation plant [14], [15]. Each of these processes is described in more detail in the following sections.

1.2.1.1 Receipt and storage

Nuclear fuel is usually removed from a reactor after 1-3 years (depending on design and reactor burnup/operation cycle). Due to the high level of radiation produced by fission fragments, fuel is immediately unloaded into an adjacent interim storage pond for a period of several months (or years, again depending on burnup/operation cycle) to allow the short lived fission products to decay to safe levels for transportation [15]. The spent fuel is then sent to Sellafield and either immersed in long term

storage ponds on site or transferred directly to THORP for reprocessing (if held in interim storage for a long period) [15], [16]. The length of time required in long term pond storage before reprocessing depends on the fuel type and different rates of fuel burnup [12], [17]. For AGR it is usually around 3 years and for LWR around 5 years [12].

1.2.1.2 Head End: Disassembly and dissolution

In order to dissolve the uranium fuel pellets in preparation for reprocessing, first the steel cladding needs to be either partially or fully removed.

In THORPs Head End, AGR (stainless steel clad)/LWR (zircaloy clad) fuel element assemblies are sheared into small (~5cm) pieces which are allowed to fall into a basket partly immersed in ~7 mol dm^{-3} 90ºC nitric acid (HNO_3). The stainless steel or zircaloy clad solids, often referred to as 'hulls', are removed from the dissolver first and treated as Intermediate Level Waste (ILW) [18]. As the AGR/LWR fuel is dissolved in HNO_3, both the uranium and plutonium components are oxidised to the 6+ valence state and nitric oxide/nitrogen dioxide gases may be released as seen in equations (1.1) and (1.2) below.

$$3UO_2 + 8HNO_3 \rightarrow 3UO_2(NO_3)_2 + 2NO + 4H_2O \tag{1.1}$$

$$UO_2 + 4HNO_3 \rightarrow UO_2(NO_3)_2 + 2NO_2 + 2H_2O \tag{1.2}$$

Some fission products may also be released during fuel dissolution as gases or steam. For example, iodine is removed with the off-gases during shearing and is removed using a caustic wash. The standard PUREX process cannot be used to separate other long-lived fission products, such as Cs and Sr, and they follow the high level waste raffinate [19], [20].

After fuel dissolution, the HNO_3 concentration is adjusted to a lower concentration of 2-3 mol dm^{-3}. Additions of hydrogen peroxide (H_2O_2), nitrous acid (HNO_2) or nitrogen tetroxide (N_2O_4) are then made in order to adjust the plutonium component to its most extractable oxidation state of +4, ready for the next chemical separation step [16], [21].

1.2.1.3 Chemical Separation

Liquid-liquid extraction is the process of extracting a desired solute from a feed (inlet stream containing the substance to be extracted) by use of a solvent (second immiscible liquid into which the solute is transferred) to produce an extract (outlet stream containing solute) and a raffinate (feed material minus solute) [22].

During the PUREX process, an aqueous phase, initially containing all of the dissolved fuel (feed), is exposed to an organic solvent phase (solvent) in a series of contactors. In these devices, the two immiscible phases are thoroughly agitated and then allowed to separate as shown in Figure 1-3. At each stage the desired product (U and Pu) is extracted from the aqueous phase by the organic solvent. Eventually, the solvent phase contains U and Pu (extract) and fission products remain in the aqueous phase (raffinate). In each contactor, the separation process may not be complete, and several stages are often necessary to achieve the desired separation [16], [23].

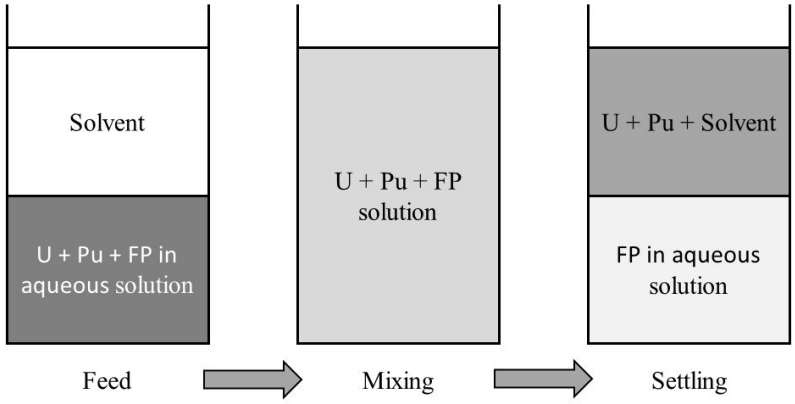

Figure 1-3 - Mixer-settler principle of organic solvent extraction for nuclear fuel reprocessing [20].

The first stage separates the uranium and the plutonium in the aqueous nitric acid stream from fission products and minor actinides by a solvent extraction process, using TriButyl Phosphate (TBP) dissolved in Odourless Kerosene (OK). Uranium and plutonium enter the organic phase as the TBP/nitrate mixed complexes $Pu(NO_3)\cdot TBP$ and $UO_2(NO_3)\cdot TBP$, while the fission products and other elements remain in the aqueous phase [14]. In the second stage, plutonium is stripped from the solvent phase by reducing the plutonium to its trivalent state using ferrous sulfamate, allowing back extraction of plutonium to the aqueous phase. Once the uranium and plutonium are separated the uranium is evaporated to

$UO_2(NO_3)_2 \cdot 6H_2O$ and thermally denitrated to UO_3, while the plutonium is precipitated as PuF_3 and PuO_2 and then converted to Pu metal via reduction with Ca. These high level strategic materials are then either solidified and disposed of or re-used in fuel manufacture [14], [16], [21], [24], [25].

Having discussed the processes and chemicals involved in a PUREX separation we now discuss the key properties of the main material from which reprocessing pipework and associated plant are compromised (e.g. contactors, evaporators and mixer settlers), stainless steel.

1.2.2 Stainless Steels in Nuclear Reprocessing

The integrity and availability of nuclear fuel reprocessing plants for uninterrupted operation depends on the quality and performance of critical engineering components. Any failure of a component could lead to leakage of radioactive material.

Stainless steels are used worldwide in chemical process plants because of their high corrosion resistance (compared to iron or carbon steels), ease of fabrication and availability. Stainless steels are an iron based alloy in which chromium is the main alloying additive, with a concentration of at least 12% wt. The high corrosion resistance inferred by the chromium addition has allowed stainless steels to be used in a wide range of chemical process applications [26], [27]. Further, both nuclear and conventional power plants have many key components formed from stainless steels, including, but not limited to: pressure vessels, pumps, turbines, power condensers and feed-water heaters [17].

As such stainless steels are also used at THORP (Sellafield) as the main constituent material for reprocessing plant vessels and pipework, in particular where the concentration of HNO_3 is ≤ 8 mol dm^{-3}. Stainless steels provide two main benefits over iron or carbon steels for process work:

(1) The formation of a chromium oxide or chromium containing oxide film gives stainless steels excellent corrosion resistance in oxidising media such as nitric acid (see below).

(2) Stainless steels are believed to be relatively easy to decontaminate compared to iron or carbon steels where heavy multi oxide state iron deposits can form, making them essentially maintenance free [28], [29].

These benefits are essential characteristics, as access for maintenance is difficult or sometimes impossible, therefore complete reliability is required [30].

1.2.2.1 Steel Crystal Structures

Solid metals and alloys consist of randomly oriented grains that have a well-defined crystalline structure, or lattice, within the grains. Many of the properties of stainless steels depend upon which crystalline lattice occurs. Common crystalline structures that occur within the grains have been given names such as ferrite, austenite and martensite [31].

1.2.2.1.1 Ferrite

The main alloying element of ferritic stainless steels is Cr at 11-30% wt. with low C content which results in ferritic steels having limited strength. They have low temperature strength and weldability but exhibit good formability and excellent resistance to chloride stress corrosion cracking [31], [32]. Ferritic steels usually cost less than austenitic steels, due to the absence of Ni. Ferric stainless steels have a 'body-centred cubic' crystal structure at ambient temperatures, as shown in Figure 1-4.

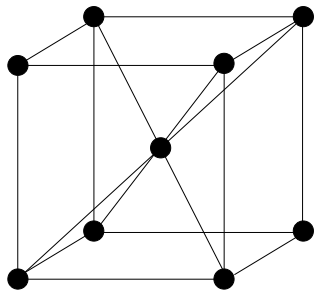

Figure 1-4 – Example of a body-centred cubic crystal structure. Where the black dots represent atoms and the black lines are present to aid structure visibility [31].

1.2.2.1.2 Austenite

Austenitic stainless steels form the largest group of stainless steel, in terms of usage and contain 18-25% wt. Cr, 8-20% wt. Ni and low C. The addition of nickel changes the crystal structure into a 'face-centred cubic' form. In general austenitic steels are easier to shape and bend, more weldable and less brittle than ferritic alloys [31], [32].

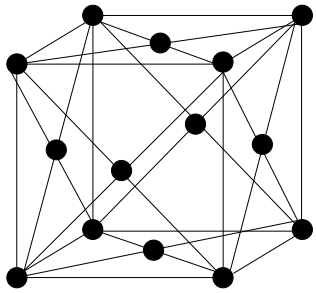

Figure 1-5 – Example of a face-centred cubic crystal structure. Where the black dots represent atoms and the black lines are present to aid structure visibility [31].

Austenitic grades tend to be employed to resist corrosion. Increasing the levels of Cr, Mo and N result in increased resistance to pitting and crevice corrosion in chloride environments [32].

Low carbon content (typically <0.03% wt.) reduces the possibility sensitisation due to chromium carbide formation either during welding or when exposed to a high temperature thermal cycle. When a sensitised steel is exposed to a corrosive environment, intergranular corrosion can occur. Reducing C content does not affect resistance to pitting, crevice and stress corrosion cracking [32].

Further effects of alloying will be discussed in section 1.2.2.2.

1.2.2.1.3 Martensite

Martensite is a stable structure at room temperature and is more similar to ferrite than austenite. Martensite is alloyed with Cr and has a relatively high C content.

Martensite has a 'body-centred' tetragonal structure, as shown in Figure 1-6.

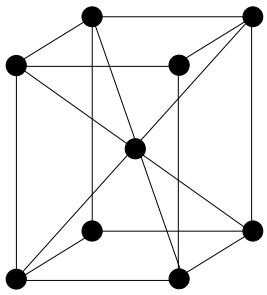

Figure 1-6 - Example of an elongated body-centred crystal structure. Where the black dots represent atoms and the black lines are present to aid structure visibility [31].

Martensite is produced by heat treatment or by cold working cubic crystals of ferrite and austenite. Martensite is the strongest of the three crystalline forms but that makes it the least workable. It exhibits excellent wear or abrasion resistance but limited corrosion resistance [31], [32].

1.2.2.2 Effect of Alloying Elements on Austenitic Stainless Steel

Apart from the major alloying element of chromium, other alloying elements also influence the chemical, physical and mechanical properties of austenitic stainless steel. The addition of other alloying elements therefore allows stainless steel properties such as ductility and weldability to be tailored specifically to the required construction application. Examples of the mechanical/chemical properties and steel grade produced by alloying element addition are shown in Figure 1-7.

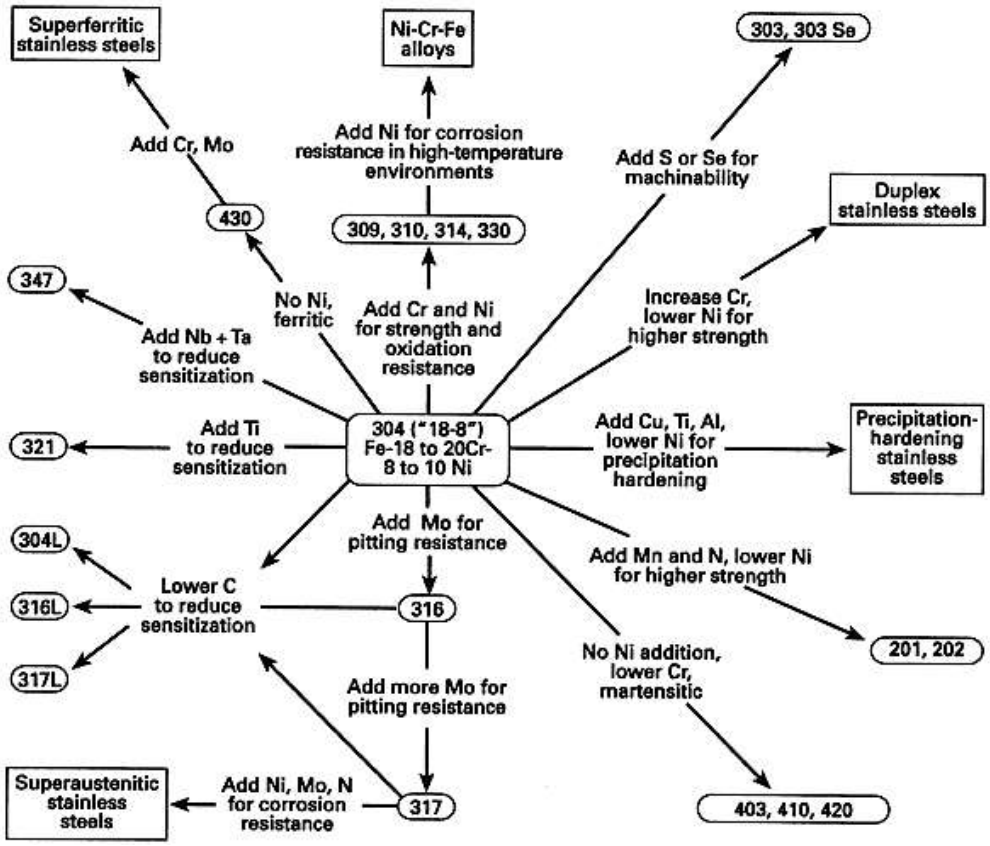

Figure 1-7 –Different types of stainless steel after compositional modifications starting at 18-8/AISI 304 stainless steel [33].

Considering the chemical environments encountered by nuclear process steels, the specific effects on corrosion resistance of some of the alloying elements shown in Figure 1-7 are discussed in more detail below. [26], [33]–[37].

1.2.2.2.1 Chromium

Chromium (Cr) is added to increase steel resistance to oxidation and pitting. The resistance of metal alloys to chemical effects of a corrosive agent is determined by their ability to protect themselves through formation of an adherent, insoluble film. Cr produces a very fine chromium oxide (Cr_2O_3) passive film on the order of ~1-2 nm thick. Increasing the chromium content within the steel results in increased corrosion resistance, through enhancement of the stability of the passive film. In practise stainless steels must have ~14-18% wt. chromium for passivity to occur, less than this and the film is inconsistent and greater than this and the film becomes unstable. Thus, chromium is an essential alloying element for corrosion resistance in nitric acid environments because it readily forms this passive film in response to oxidising conditions.

1.2.2.2.2 Nickel

Austenitic stainless steels generally have a high nickel (Ni) content, between 8 and 20% wt. The addition of nickel leads to the formation of the austenitic crystal phase. This improves the metals formability, weldability, toughness and the high and low temperature behaviour of the steel. Nickel is also responsible for an increase in corrosion resistance for chromium-nickel alloys, particularly in reducing environments. Nickel has no effect on pit/crevice initiation, however, pit/crevice propagation is greatly reduced with increased nickel content [36], [38], [39].

1.2.2.2.3 Molybdenum

When added to Cr-Ni austenitic stainless steel, molybdenum (Mo) improves resistance to pitting corrosion, especially in chloride environments. Because Mo is a ferrite former, the nickel content of the steel is usually also increased (e.g. ~3% wt. extra Ni in Mo containing 316L SS over 304L SS) in order to maintain the austenitic structure. However, Mo is rapidly attacked by oxidising agents and therefore nitric acid is one of the few environments in which additions of Mo does not improve corrosion resistance. Such differences can be seen in Figure 1-8, which shows a comparison between the domains of stability

of a Mo containing steel (316L SS) and two low Mo containing steels is (304L SS and 310L SS) in nitric acid.

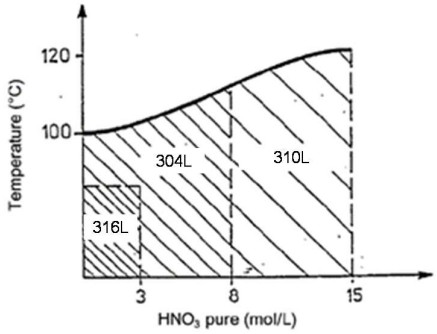

Figure 1-8 - Comparison between the domains of stability of a Mo containing steel (316L SS) and two low Mo steels is (304L SS and 310L SS) in nitric acid as a function of concentration and temperature [6].

Thus, Mo containing steels are often inferior to other stainless steels in terms of resistance to nitric acid. However, in some of the potentially chloride-containing environments/streams encountered at THORP due to the coastal location, Mo containing stainless steels may still be employed in certain areas of high pitting corrosion risk.

1.2.2.2.4 Niobium

Niobium, which is alloyed into 18Cr/13Ni/1Nb for corrosion resistance (see below), is completely resistant to nitric acid and other oxidising media at temperatures below 100ºC. Thus, introduction of niobium into process steels can greatly improve corrosion resistance. Furthermore, the presence of niobium retards the precipitation of Cr-rich carbides in stabilised stainless steel grades, reducing risk of intergranular corrosion.

1.2.2.2.5 Titanium

Titanium is added to stainless steels for carbide stabilisation. Titanium combines with carbon to form stable titanium carbides, in preference to chromium carbides, which are hard to dissolve in steel. This is particularly useful when the material is to be welded and tends to minimise the occurrence of intergranular corrosion.

1.2.2.3 Grades and Materials Selection

18Cr-13Ni-1Nb and 18Cr-8Ni-Ti were the primary grades of stainless steel used in Magnox reprocessing at Sellafield until the 1980s. 18Cr-13Ni-1Nb was developed in the 1950s specifically for HNO_3 duty in nuclear reprocessing in the U.K. It was used for plant handling of corrosive liquids, high temperatures and areas of high radioactivity. These steels were shown to have deficiencies in operation such as end grain corrosion and attacks at welds which are susceptible to corrosion in HNO_3 vapours and iodine vapours. For the THORP reprocessing plant, nitric acid grade (NAG) 18-10L and 304L stainless steel have replaced 18Cr-13Ni-1Nb and 18Cr-8Ni-Ti respectively [40], [41]. NAG 18-10L is essentially 304L stainless steel that is developed with controlled chemical composition e.g. reduced carbon, and modified microstructures that lead to the elimination of weaker sites that may allow passive film breakdown and dissolution. Furthermore, closer control on residual elements gives improved strength against transpassive dissolution [29], [42], [43]. Table 1-1 shows the composition of the various steels/alloys used at THORP.

Table 1-1 - Composition of various Stainless Steels (% wt.) [44]–[47].

Metals	Cr	Ni	C	Mn	Si	P	S	Mo	Nb
NAG18-10L	18.77	9.64	0.015	1.54	0.32	0.015	0.008	-	<0.01
304L	18	11	0.03	2.0	1.0	0.045	0.03	-	-
316L	16.6	10.03	0.016	1.49	0.48	0.03	0.002	2.06	0.004
18Cr-13Ni-1Nb	16.6	12.6	0.09	0.99	0.51	0.07	0.006	0.08	0.92
310L	25	20	0.015	<2	<0.03	-	<0.3	<0.3	<0.25

Type 304L is predominantly used for the fabrication of vessels, tank piping and equipment in THORP where the concentration of HNO_3 is ≤8 mol dm^{-3} [43]. AISI (American Steel and Iron Institute) Type 316L stainless steel (316L SS) is used in the construction of some process vessels and pipe work that contain concentrations of HNO_3 < 3 mol dm^{-3}. It is also used in liquor storage cans and some outdoor plant areas at THORP that may be effected by saline spray from the Cumbrian coastline as the added Mo improves resistance to pitting corrosion from the chloride environment (see above) [45]. 18Cr-13Ni-1Nb (a fully austenitic variant of type 347 [48]) is used for high HNO_3 concentration areas in THORP. An example of this is Evaporator C. This evaporator concentrates Highly Active Aqueous Raffinate (HAAR), from a concentration of ~3 mol dm^{-3} HNO_3 to ~8 mol dm^{-3} HNO_3.

1.2.2.4 Potential Corrosion Problems in Reprocessing Plants

As discussed above, nuclear fuel reprocessing flow sheets use nitric acid at varying high concentrations and temperatures. Therefore, constituent materials used for reprocessing plant equipment must be chosen and used carefully. As alluded to in the previous section, consideration must be given to:

- The nature of the medium encountered
- Concentration of HNO_3
- Temperature
- Plant operating conditions
- Level of radioactivity

As discussed above, austenitic stainless steels owe their good corrosion resistance properties in nitric acid solution to the formation of a chromium rich passive oxide layer. However, under certain conditions passivity may no longer be possible. For example, active dissolution of Cr^{3+}, Fe^{2+} and Ni^{2+} may occur if reprocessing stream conditions become sufficiently reducing. Alternatively, if the reprocessing stream becomes excessively oxidising, chromium (III) oxide (Cr_2O_3) could dissolve into hexavalent chromium (chromate). This would result in passive film dissolution, known as 'transpassive corrosion', typically causing intergranular corrosion at grain boundaries [49].

Having described the materials and possible vulnerabilities of reprocessing pipework/vessels it is now important to discuss the process of metallic corrosion itself and the types of corrosive action that could be encountered in a reprocessing waste stream scenario.

1.3 Electrochemistry and Corrosion Concepts

The International Standards Organisation defines corrosion as:

"Physiochemical interaction between a metal and its environment that results in changes in the properties of the metal, and which may lead to significant impairment of the function of the metal, the environment, or the technical system, of which these form a part" (ISO 8044-1999).

Note: This interaction is often electrochemical in nature. [50]

Due to the corrosion of metal being electrochemical in nature it is important to understand the electrochemical behaviour of metals in aqueous solutions and corrosion related processes.

1.3.1 Electrochemistry Concepts

An electrochemical reaction is characterised by the exchange of electrons.

$$Ox + e^- \underset{\text{Oxidation}}{\overset{\text{Reduction}}{\leftrightarrow}} Red \tag{1.3}$$

Ox = Oxidising agent or electron acceptor

Red = Reducing agent or electron donor

When a reaction takes place with the transfer of electrons into the external circuit, it is referred to as an oxidation. The electrode at which oxidation takes place is called the anode. If a reaction takes place with the transfer of electrons from the external circuit, it is referred to a reduction, the electrode this occurs at is called the cathode [27], [51].

Many corrosion processes are electrochemical in nature because they involve redox reactions [52]. For example, the corrosion of metal atoms to form an ionic species and the liberation of electrons is shown in the generic metal oxidation reaction below:

$$M \rightarrow M^{n+} + ne^- \tag{1.4}$$

Equation 1.4 represents the generalised corrosion reaction that removes the metal atom by oxidising it to its ion (at an anodic site). An example of a real metal would be the oxidisation of iron (Fe), as shown in Equation 1.5:

$$Fe \rightarrow Fe^{2+} + 2e^- \tag{1.5}$$

This is called a half-cell reaction. However, to make a balanced chemical process the electrons liberated by the oxidation reaction must be consumed by a reduction reaction (at a cathode site). One reduction

reaction that is common in corrosion processes in acids is evolution of hydrogen, which is shown in Equation (1.6) [52], [53]:

$$2H^+ + 2e^- \rightarrow H_2 \tag{1.6}$$

The complete reaction would be:

$$Fe + 2H^+ \rightarrow Fe^{2+} + H_2 \tag{1.7}$$

This is demonstrated in Figure 1-9, in this case the surface of the metal serves as both anode and cathode.

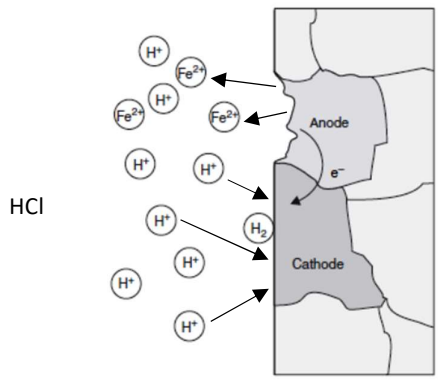

Figure 1-9 – Formation of ions at an anodic area and release of hydrogen at a cathodic area in a local cell on an iron surface in hydrochloric acid [54].

1.3.1.1 Electrode Potential

Two types of processes occur at electrodes:

1. Faradaic – Faradaic processes are sometimes referred to as charge transfer processes where charge is transferred across the metal-solution interface. Electron transfer causes oxidation and reduction to occur [55].

2. Non-Faradaic – no charge transfer reactions occur but processes such as adsorption and desorption can occur. The structure of the electrode-solution interface can change with changing potential or solution composition.

If a piece of metal, M, is surrounded by an aqueous solution containing ions of the metal, M^{n+}, then electrode reactions of the type shown in equation (1.4) take place at the surface of the metal until charge separation and equilibrium is reached. These reactions ultimately lead to an 'electrical double layer', a zone of charge separation at the electrode/electrolyte interface being established, as shown in Figure 1-10. The existence of this electrical double layer means that the piece of metal exhibits a different electrical potential (Φ_m) to that of the electrolyte ($\Phi_{\sigma,b}$). Electronically, when a faradaic current is flowing, this region behaves like a capacitor in parallel with a resistor (double layer capacitance and charge transfer resistance respectively). However, importantly for the corrosion chemist, a relative value of Φ_m can be measured via comparison with a reference electrode, many of which are based on a simple metal/metal chloride couple e.g. the saturated calomel electrode (Hg/Hg_2Cl_2) and the saturated silver chloride electrode (Ag/AgCl). The so-called measured quantity is commonly referred to as the electrode potential, E [27], [53]. The electrode potential of a metal is very useful in corrosion studies, as it enables determination of oxidative or reductive stresses derived from the solution environment that may induce corrosion or passivation [56]. This is explored in more detail in the following two sections.

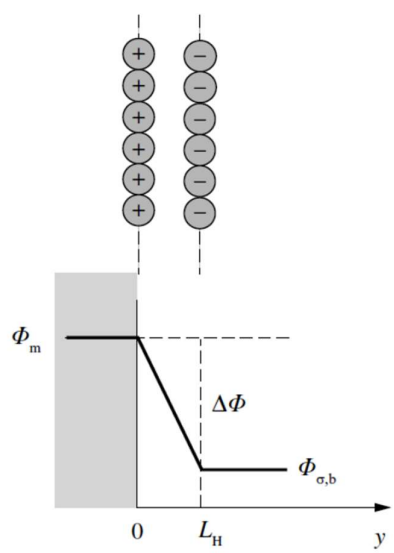

Figure 1-10 – Helmholtz model of the formation of the electrical double layer. L_H is layer thickness in nm and Φ is potential [53].

1.3.2 Pourbaix Diagrams

A potential-pH diagram, commonly referred to as a Pourbaix diagram after Marcel Pourbaix who first assembled such diagrams for all elements into a comprehensive atlas [57], is a summary of thermodynamic data (speciation) in the form of electrode potential vs. pH diagrams. The simplest pH-potential diagram is for water, Figure 1-11.

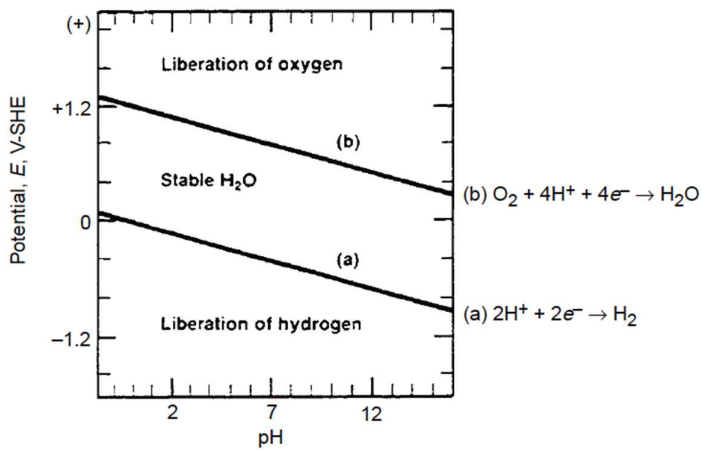

Figure 1-11 - Potential/pH diagram for water [58].

The diagonal lines labelled as (a) and (b), mark the region of stability of water as a function of potential and pH. At any value of pH and potential below line (a), water is thermodynamically unstable and results in the generation of hydrogen gas. Alternatively, for any value of potential and pH above line (b), water is thermodynamically unstable and results in the evolution of oxygen. For potential and pH conditions between lines (a) and (b), water is thermodynamically stable.

Such thermodynamic considerations become more important when considering metal/water systems. As an example the potential-pH diagram for iron is shown in Figure 1-12.

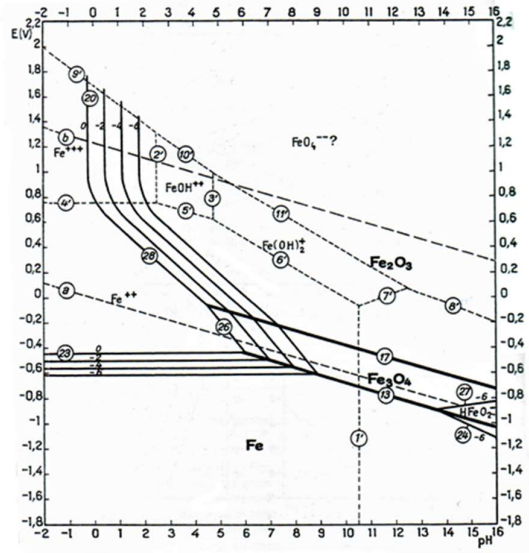

Figure 1-12 - Potential pH diagram of the Iron/Water system at 25°C [57].

From Figure 1-12 it can be seen that different regions of corrosion (soluble species of Fe^{2+} and Fe^{3+}), passivation (solid oxides of Fe_2O_3) and immunity (Fe is the stable species) can be identified. This allows construction of simplified corrosion diagrams that allow rapid identification of regions of corrosion, immunity and passivation, Figure 1-13.

Two key considerations should be made when using potential-pH diagrams. Firstly, any dissolved species can participate in complex formation which could cause alterations to the stability boundaries of water potential-pH diagram [27]. Secondly, the diagrams are based purely on thermodynamic data, thus they do not reveal any information as to rates of reaction or other kinetic parameters [59].

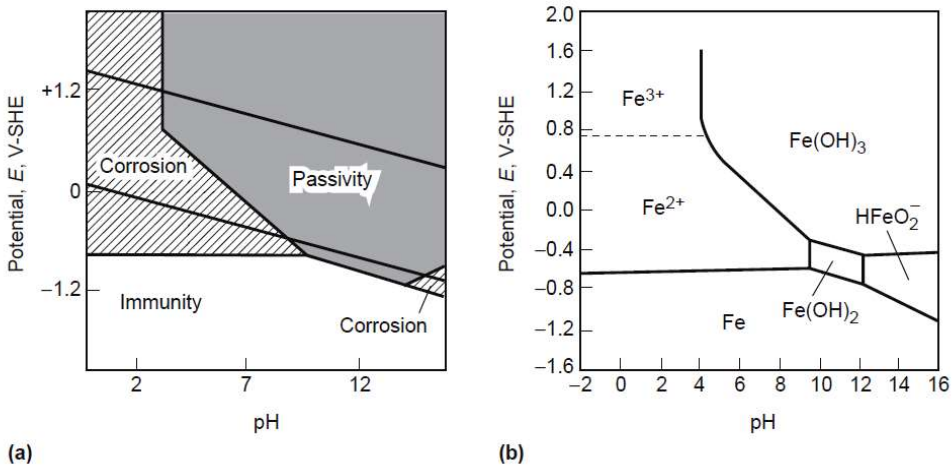

Figure 1-13 – Simplified potential pH diagram of the Iron/Water system at 25°C. a) Simplified corrosion diagram, b) primary species involved in immunity, corrosion and passivity [57], [58].

As described in section 1.2.2.2, the corrosion resistance of stainless steels is often improved by introduction of other oxide layer forming metals such as nickel, chromium or elements such as molybdenum that expand the region of passivity. The potential-pH diagrams for Chromium, Nickel and Molydenum are shown in Figure 1-14, Figure 1-15 and Figure 1-16 repectively.

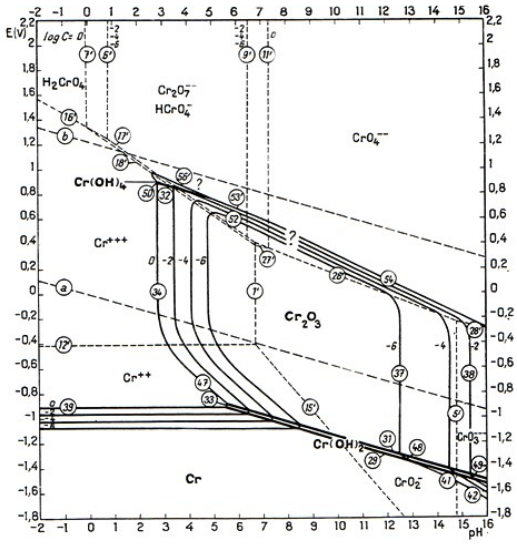

Figure 1-14 - Potential pH diagram of the Chromium/Water system at 25°C [57].

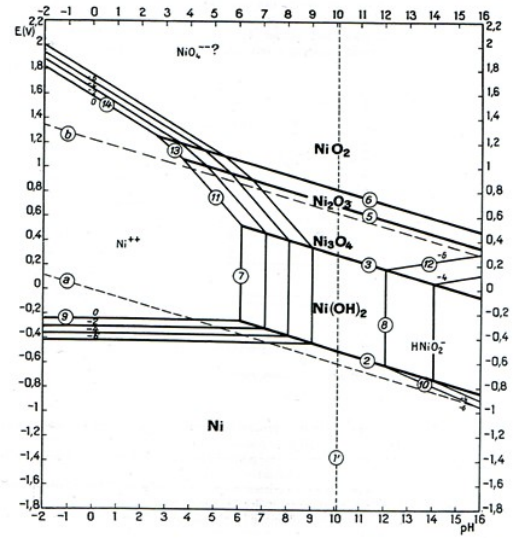

Figure 1-15 - Potential pH diagram of the Nickel/Water system at 25°C [57].

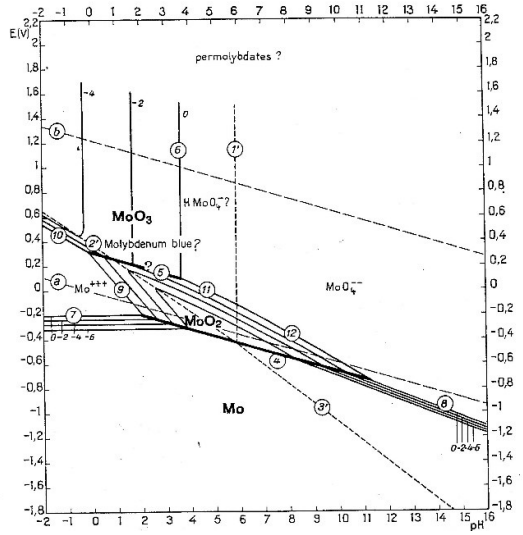

Figure 1-16 - Potential pH diagram of the Molybdenum/Water system at 25°C [57].

The introduction of such metals may also improve the stability and mechanical properties of the steel by creating a tougher austenitic crystal phase. Using potential-pH diagrams the thermodynamically predicted corrosion resistance properties of each alloying element may be more easily understood by overlaying the regions of passivation, in the case of 316L, 304L and 18Cr/13Ni/1Nb, for iron, chromium, nickel and molybdenum. This is shown in Figure 1-17 where the passive regions for Fe, Cr, Ni and Mo are shaded in red, green, blue and pink respectively.

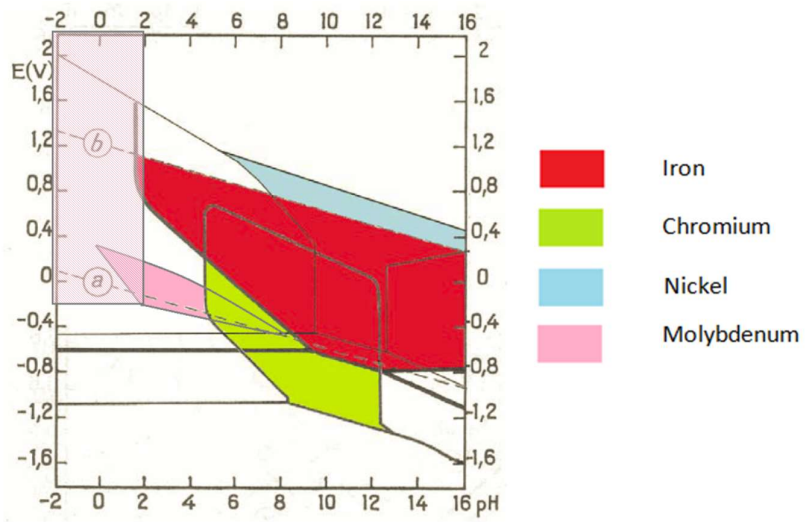

Figure 1-17 – Pourbaix diagram for the Fe-H_2O system showing conditions for corrosion (E = V/SHE). Overlaid are conditions of passivation for Iron (red), Chromium (green), Nickel (blue) and Molybdenum (pink). The shaded pink area indicates an area of possible passivation by Molybdenum oxide [57].

Figure 1-17 shows that iron and chromium are the primary passivators in steel, the latter being particularly resistive to reductive dissolution. Nickel provides improved resistance in neutral to alkaline, oxidative solutions while the addition of molybdenum improves passivation in the low pH, mid-high potential region.

1.3.3 Voltammetric Determination of the Corrosion Behaviour of Stainless Steels

The previous section described how knowledge of the electrode potential and solution pH can allow thermodynamic determination of whether active corrosion or passivation of a metal will take place. However, an alternative to measuring the open circuit potential or O.C.P. (the potential between a metal electrode and a reference electrode under conditions where no current is allowed to pass between these electrodes) is to actively drive the potential positive or negative of O.C.P. and record the current that obtains. This technique is known as voltammetry. As the change in potential can result in the occurrence of oxidation or reduction reactions at the working electrode (due to either oxidation/reduction of the

working electrode or due to oxidation/reduction of electroactive solution species), the charge passed during such reactions may be directly related to the kinetics of oxidation/reduction via Faraday's 1st law of electrolysis [55], [60]. In the case of linear current-voltage curves (linear sweep voltammetry or LSV) such measurements are often expressed as log current density vs. potential plots, often known as polarisation curves, in order to emphasise changes in current during the potential sweep.

Figure 1-18 shows a typical polarisation curve for a metal that exibits a region of passivation. Such a curve is also observed for similarly behaving alloys such as stainless steel.

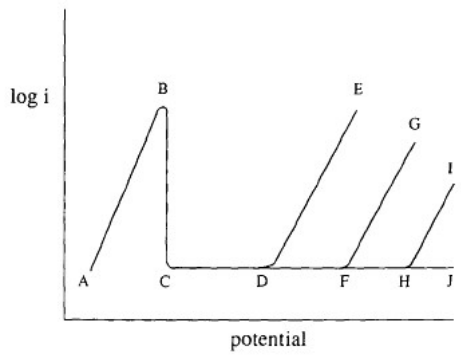

Figure 1-18 – Schematic of an anodic polarisation curve of a metal, labelled regions are described in the text.

Considering first the low potential region of Figure 1-18. Region AB indicates the region of active corrosion. Here the current is high due to oxidative metal dissolution. As the potential increases further the so-called passivation potential or Flade potential is reached, and the current density is reduced as the formation of a thin, protective coating occurs (passivity). In stainless steels this largely consists of mixed iron-chromium oxides and hydroxides [61]. The metal is passive at potentials more positive than C. If the solution contains aggressive anions, i.e. ions that promote corrosion reactions or increase the solubility of passive films, such as chloride (Cl^-), passivity may break down at D (the pitting potential) and the current rises with further increase in potential (D to E) as pits in the passive film nucleate and propagate (see section 1.4.2 for more details). If pitting agents such as Cl^- are absent, the passive film can transpassively dissolve (F to G) as the protective chrome oxide/iron oxide layer is oxidised. This is discussed in more detail in the following section and is not returned to here. For sufficiently stable passive films with good electronic conductivity which are chemically and electrochemically stable, then oxygen

evolution rather than transpassive dissolution may occur. This accounts for the observed current at the high anodic potentials. Oxygen evolution commences at H and increases in rate to I whilst the metal remains passive. If the film is stable and insulating to electrons, oxide film growth continues with a further increase in potential (HJ) and the metal remains passive [38], [53].

With regards to corrosion in oxidative nitric acid environments, it is the higher potential regions of passivity and transpassivity that are of most interest in this study. Thus, each of these regions is described in more detail below.

1.3.3.1 Passive Behaviour of Stainless Steels

As described briefly in section 1.2.2.2.1, the corrosion resistance of stainless steels in the passive region arises from a chromium enriched (Iron-Chromium spinel) oxide film that forms on the surface. These oxides are extremely thin <5 nm however, they are strongly adherent and chemically stable [38], [62], [63]. The ease with which stainless steels can passivate increases with the level of Cr. Materials with higher Cr content are more readily passive (lower current density and the active/passive transition is at a lower potential). This is demonstrated in Figure 1-19, which shows the electrochemical differences between Fe, stainless steel and pure Cr.

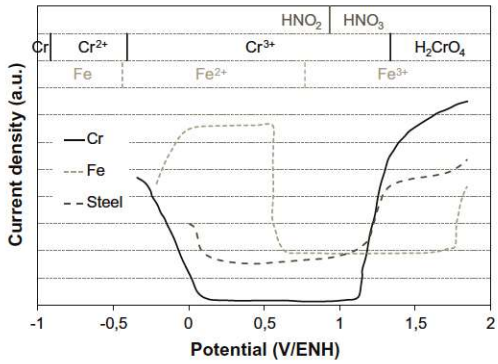

Figure 1-19 – Standard potentials vs ENH (Normal Hydrogen Electrode (NHE)) at 25°C for different electrochemical couples and steady anodic curves for iron chromium and stainless steel (in H_2SO_4 0.5 mol dm^{-3}) [64]

From Figure 1-19 it can be seen that the addition of Cr to Fe to form steel dramatically increases the passive region in the negative potential direction compared to that of pure Fe (or carbon steels). While not shown in Figure 1-19, materials with higher Cr content are also passive (higher pitting potential) in more aggressive anion environments than iron or carbon steels, due to the reduced ease of formation of soluble chlorides [38]. The primary species of chromium passivation is its trivalent state, Cr_2O_3, other species include the mixed iron-chromium spinels; such as $FeCr_2O_4$. The thickness of the passive film increases linearly with applied potential due to oxide growth, rather than hydroxide to oxide formation, which is independent of potential [63]. However, when the potential increases above ~1.1-1.2 V vs. NHE, the oxidation state increases to its hexavalent state to form $HCrO_4^-$ or $HCr_2O_7^-$. The oxides formed in this environment are generally more soluble in nitric acid (see section 1.3.4), leading to Cr dissolution from the oxide layer, causing the passive film to disintegrate [57], [63], [65]. Such behaviour is described in more detail in section 1.3.3.3.

It is important to note that the passivating oxide coating formed on steel surfaces is influenced by the composition of the steel as well as by environmental factors, including oxygen, moisture, the presence of other ions, the electrostatic potential of the surface and pH of the local environment [1]. However, while film thickness/composition can change within a couple of seconds in response to a potential change, time is required to stabilise film properties in response to an environmental change. For example, increasing the pH from acidic to neutral leads to a lower Cr_2O_3 dissolution rate which, in turn, increases the thickness of the passive film. Increasing the pH into basicity leads to an increased iron content in the passive film due to increased stability of the iron oxides Fe_2O_3 and Fe_3O_4 [63].

1.3.3.2 Theories of Passive Film Growth

Growth of passive films has been extensively researched [66]–[72]. There are two model types for predicting film growth in response to a potential change.

1. If the electric field in the passive layer is assumed to increase upon a change in potential, the film growth is limited by high field ion conductivity through the oxide, the High Field Model (HFM). In this, the growth rate is controlled by ion conduction through the film. The HFM equation for film growth is shown in Equation (1.8).

$$\frac{d\xi}{dt} = k_{film} i_0^{hf} R_g(t) e^{\frac{B[\xi_0 E_0 + \Delta U(t)]}{\xi_0 \Delta\xi(t)}} \tag{1.8}$$

Where dξ/dt represents film growth, k_{film} is the film growth constant, i_0^{hf} is a constant, proportional to the number of charge carriers in the film, R_g is the growth fraction (i_{growth}/i_{tot}), ξ_0 and E_0 represent the start values of the film thickness and electric field, respectively, ΔU is the applied potential.

2. The Interface Model (IFM), shown in Figure 1-20, where the film growth rate is limited by the kinetics of charge transfer processes occurring at either;

    a. The metal-oxide interface (Point Defect Model)

    b. The oxide-electrolyte interface

For the two IFMs, the parameter controlling growth is the extra potential at the metal/film or film/solution interface and is shown in Equation (1.9). *Note*: This equation is independent of initial film thickness, ξ_0, and there is no direct influence of the growth fraction.

$$\frac{d\xi}{dt} = \left(k_{film} i_0^{hf}\right) e^{g^{if} \ [\Delta U_{(t)} - E_0 \Delta\xi_{(t)}]} \tag{1.9}$$

Where i_0^{if} and g^{if} are the fit parameters. A full description of the HFM and IFM numerical simulations can be found in Reference [68]

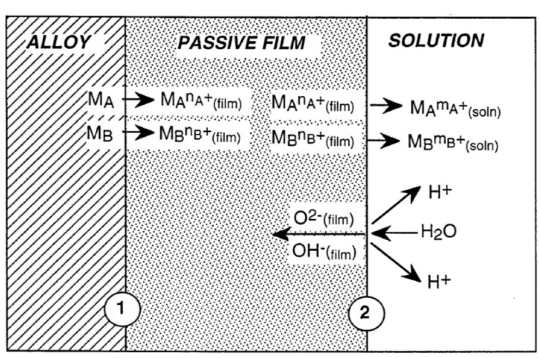

Figure 1-20 – Schematic showing the charge transfer reactions at the metal-oxide (1) and the oxide-electrolyte interfaces (2) of a binary alloy AB [73]

Recent work with the electrochemical quartz crystal microbalance (EQCM) has been used to investigate passive film growth [68], [73]. The EQCM provides in situ information that allows for the production of

real time growth curves of the passive film. Both the IFM and HFM were assessed, using type 304L material, and the IFM was found to provide a more satisfactory fit to the growth curves produced.

1.3.3.3 Transpassive Behaviour of Stainless Steels

Cr and Mo are employed in industry to minimise the localised corrosion risk in highly aggressive electrolyte environments. However, in highly oxidising environments the use of highly alloyed materials increases the risk of corrosion via the transpassive dissolution of Cr, Mo and to a lesser extent Ni from the alloy [74].

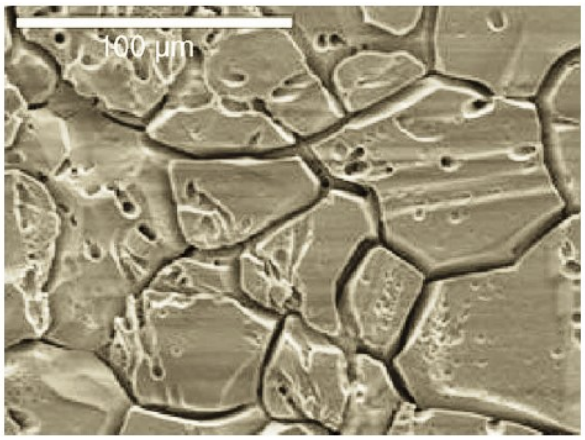

Figure 1-21 –Transpassive dissolution of 304L austenitic stainless steel in nitric acid [75].

The transpassive oxidation of a metal can be defined as the formation of a chemical species in a valence state higher than that in the primary passive film formed on the material [74], [76]. In most cases, these species have higher solubility and are thus transferred to solution, resulting in uniform dissolution of the material or alternatively localised stable pit formation on the metal surface where the film has been weakened (discussed further in section 1.4). It is this process that is observed in the higher potential regions of Figure 1-19 and shown schematically in Figure 1-18 (trace F to G).

As described in the previous section, when the metal passivates, Cr forms a passive film of chromium (III) oxide, Cr_2O_3, which is insoluble and provides and effective barrier against corrosion. At the transpassive potential the trivalent Cr_2O_3 is oxidised to hexavalent CrO_3 which has a high solubility in aqueous media. Mixed iron-chromium oxides can also form in the passive region, most commonly exhibiting an AB_2O_4 stoichiometry with a spinel-type structure. In the transpassive region, the Cr(III) is

again oxidised to a soluble Cr(VI) compound, leaving an iron rich phase at the surface which may provide secondary passivation, as described below.

Depending on the pH, CrO_3 will form chromate ions CrO_4^{2-} (under basic conditions) or bichromate ions $Cr_2O_7^{2-}$ (under acidic conditions). The transpassive dissolution of Cr, therefore, corresponds to the following stoichiometric equations under basic and acidic conditions respectively:

$$CrO_4^{2-} + 4H_2O + 6e^- \rightleftarrows Cr + 8OH^- \qquad E^0 = 0.37 \text{ V/SHE} \tag{1.10}$$

$$Cr_2O_7^{2-} + 14H^+ + 12e^- \rightleftarrows Cr + 7H_2O \qquad E^0 = 0.29 \text{ V/SHE} \tag{1.11}$$

Note, E^0 is much less than that of O_2 formation in either pH range therefore transpassive dissolution of Cr can occur before O_2 evolution [53].

The point at which metal dissolution takes place from local sites where the passive film has broken down is called the transpassivation potential or breakdown potential. In the presence of corrosively aggressive anions, in particular chloride ions (that may complex with Fe, Cr or Ni ions, so disrupting their solubility and this disrupting the formation of passive oxide layers containing those ions), such a potential may be accessed at much lower potentials than in the absence of such anions. However, in the absence of aggressive anions and under solution conditions where the Fe oxides (in particular Fe_2O_3) or Ni oxides are stable at high potentials, the resulting Fe oxide or Ni oxide can provide some passivity (secondary passivation) in the absence of a Cr oxide layer. Such stable high oxidation state oxides have a transpassive potential that is higher than the reversible potential of oxygen evolution. As such Fe and Ni oxides are electron conducting in nature and when the metal is anodically polarised to a sufficiently high potential, anodic oxygen evolution is observed. Eventually, as the film breakdown potential is reached oxygen evolution gives way to rapid anodic dissolution.

1.3.4 Nitric Acid Reduction Mechanism – Theory

Having discussed the general electrochemical mechanisms of corrosion of steel, we now briefly discuss the effect of the reprocessing media, principally nitric acid, on steel corrosion.

Nitric acid undergoes partial thermal decomposition at room temperature [77]:

$$4HNO_3 \rightleftarrows 4NO_2 + 2H_2O + O_2 \tag{1.12}$$

The nitrogen dioxide then disproportionates into nitric acid and nitrous acid [78]:

$$2NO_2 + H_2O \rightleftarrows HNO_2 + HNO_3 \tag{1.13}$$

Nitric acid complicates the passive behaviour of stainless steels. Stainless steels may autocatalytically interact with HNO_3 (see below) resulting in a variety of nitrogen-oxygen based reduction products, in particular strongly oxidising conditions, nitrous acid (HNO_2). With increasing nitric acid concentration the reduction rate of the nitrate derived HNO_2 (shown in Equations (1.12) and (1.13)), and thus the oxidising power of the electrolyte also increases. This behaviour accelerates the corrosion rate due to the nitrous acid-driven oxidation of alloying elements, such as Fe and Cr. Consequently Cr, which, as discussed, is important to passive film stability, depletes from the surface [6], [79].

This HNO_3 reduction process has been previously studied on Platinum and on 304L stainless steels in nitric acid condensates [80]. For concentrations of 1 to 10 mol dm^{-3} HNO_3 two different mechanisms of nitric acid reduction have been proposed by Vetter and Schmid [81]–[87].

Vetter [81]–[83] describes the autocatalytic reduction of HNO_3 as a heterogeneous process, where the chemical regeneration of NO_2 (electroactive species) occurs at the electrode surface. In this case, stirring has no influence on the current density due to the adsorbed nature of the reactions.

$$HNO_{2(ads)} + H^+ \rightleftarrows NO^+_{ads} + H_2O \tag{1.14}$$

$$NO^-_{3(ads)} + NO^+_{(ads)} \rightleftarrows N_2O_{4(ads)} \tag{1.15}$$

$$N_2O_{4(ads)} \rightleftarrows 2NO_{2(ads)} \tag{1.16}$$

$$NO_{2(ads)} + e^- \rightleftarrows NO^-_{2(ads)} \tag{1.17}$$

$$NO^-_{2(ads)} + H^+ \rightleftarrows HNO_{2(ads)} \tag{1.18}$$

Schmid [84]–[87] describes the reduction of HNO_3 as a homogenous process, where the chemical regeneration of NO^+ (electroactive species), occurs in the bulk in a layer near the electrode.

$$\mathrm{HNO_2} + \mathrm{H^+} \rightleftarrows NO^+ + \mathrm{H_2O} \tag{1.19}$$

$$NO^+ + e^- \rightleftarrows NO \tag{1.20}$$

$$2NO + HNO_3 + H_2O \rightarrow 3HNO_2 \tag{1.21}$$

If Schmid obtains, then stirring of the solution should provoke a decrease in the current density as the accelerating NO^+ species is swept away from the electrode surface.

More recently, Balbaud *et al.* suggested a mechanism that is dependent on the concentration of acid [5]. Balbaud *et al.* employed parallel thermodynamic studies (to determine reaction potential) and electrochemical experiments (to determine the key reduction step), resulting in a mechanism that has much in common with Schmid and can be described overall as follows:

$$HNO_{2(el)} + H^+ + e^- \rightleftarrows NO_{ads} + H_2O \tag{1.22}$$

$$HNO_3 + NO_{(ads)} \rightleftarrows HNO_{2(el)} + NO_{2(ads)} \tag{1.23}$$

$$2NO_{2(ads)} + H_2O \rightleftarrows HNO_3 + HNO_{2(el)} \tag{1.24}$$

Where *el* indicates solution based species in the near electrode solution volume and *ads* indicates a species adsorbed at the electrode surface.

Side reactions were also identified:

$$NO_{(ads)} \rightleftarrows NO \tag{1.25}$$

$$NO_{2(ads)} \rightleftarrows NO_2 \tag{1.26}$$

$$HNO_{2(el)} \rightleftarrows HNO_2 \tag{1.27}$$

Balbaud *et al.* indicate that reactions (1.22) to (1.24) are the elementary steps in the reduction process that occur across the HNO_3 concentration range. However, they identify two limiting cases depending on HNO_3 concentration.

At low HNO_3 concentrations < 6 mol dm^3, reaction (1.23) will be slow, leading to an accumulation of NO at the electrode surface which may eventually evolve via reaction (1.25). However, the accumulated NO may also react with HNO_3 in accordance with reaction (1.29) below, leading to the following overall mechanism for HNO_3 concentrations < 6 mol dm^3,

$$HNO_{2(el)} + H^+ + e^- \rightleftarrows NO_{ads} + H_2O \tag{1.28}$$

$$HNO_3 + 2NO_{ads} + H_2O \rightleftarrows 3HNO_{2(el)} \tag{1.29}$$

which is essentially a heterogeneous version of Schmid above with the NO being adsorbed at the electrode surface instead of present in solution near the electrode surface.

At HNO_3 concentrations > 6 mol dm^{-3}, as a result of increased HNO_3 concentration and increased thermodynamic stability of the intermediates such as NO_2 [6] (see below), reaction (1.23) proceeds fast enough to produce, in concert with reaction (1.24), an autocatalytic cycle for HNO_2 reduction and regeneration. This ultimately leads to enhanced rates of HNO_3 reduction on the electrode surface, at HNO_3 concentrations > 6 mol dm^{-3} via:

$$HNO_{2(el)} + H^+ + e^- \leftrightarrow NO_{ads} + H_2O \tag{1.22}$$

$$HNO_3 + NO_{(ads)} \rightleftarrows HNO_{2(el)} + NO_{2(ads)} \tag{1.23}$$

$$2NO_{2(ads)} + H_2O \rightleftarrows HNO_3 + HNO_{2(el)} \tag{1.24}$$

Whilst this mechanism can be considered heterogeneous with regard to the main product of the electrochemical reduction, NO, the following reactions are heavily dependent upon the supply of HNO_3 from homogenous bulk solution.

Thus, the mechanisms proposed by Balbaud *et al.* can be considered a hybrid, or surface and solution based reactions, as the regeneration step takes place at the electrode surface. The gaseous species NO and NO_2 are adsorbed at the surface and HNO_2 is a soluble compound that is formed at the electrode that diffuses into solution [5], [6], [88].

A third mechanism, most recently described by Lange [7] and essentially revisiting some early studies by Carta and Pigford [8] and Abel and Schmid [89]–[91], suggests the following hybrid mechanism (in 8 mol dm^3 HNO_3) based on the Schmid mechanism:

$$HNO_{2(aq)} + H^+ \rightleftarrows NO^+_{ads} + H_2O \tag{1.30}$$

$$NO^+_{(ads)} + e^- \rightleftarrows vNO_{(ads)} \tag{1.31}$$

$$NO_{(ads)} \rightleftarrows NO \tag{1.32}$$

$$HNO_2 + H^+ + NO_3^- \rightleftarrows 2N_2O_4 + H_2O \tag{1.33}$$

$$N_2O_4 \rightarrow 2NO_2 \tag{1.34}$$

$$NO_2 + NO + H_2O \rightleftarrows 2HNO_2 \tag{1.35}$$

Again, the Lange *et al*. mechanism reactions (1.30) to (1.35) are a hybrid of surface and solution based reactions.

However, a common view amongst Balbaud *et al*, Schmid and Lange *et al* is that the common electrochemical reduction steps, be they homogeneous or heterogeneous, can be summarised as follows:

$$HNO_2 + H^+ \rightleftarrows H_2O + NO^+ \tag{1.36}$$

$$NO^+ + e^- \rightleftarrows NO \tag{1.37}$$

With the reactions for NO, and thus the degree of autocatalysis in operation, being determined by HNO_3 concentration. This will be discussed further in Chapters 3 and 4.

Whilst the electrochemical reduction of HNO_3 on inert metals, such as Pt, is otherwise well understood, the effect of HNO_3 concentrations > 5% wt. (>1.13 mol dm^{-3}), typical of those found in aqueous

reprocessing streams, on nuclear process steel, such as 316L SS, has not been extensively explored, and that will be the subject of work presented later in this thesis.

1.4 Corrosion of Austenitic Stainless Steels

Having discussed corrosion from an electrochemical standpoint, it is now necessary to describe the physical processes of corrosion. Different steel types, geometries and weld points will produce different physical corrosion characteristics that may lead to materials failure in a reprocessing stream. Common areas for materials failure occurs at grain boundaries. A grain boundary is the interface between two regions of the same crystal structure but of a different orientation. Grain boundaries are defects within the crystal structure and tend to be the preferred sites of the onset corrosion [92]. Another common area for material failure is where inclusions are present within the steel itself. Inclusions are local heterogeneities present in alloys. They are produced in the chemical reactions and physical processes that occur during the melting, pouring and rolling etc. of alloy metals [93].

The common types of corrosion processes that may be encountered with stainless steel are described below.

1.4.1 Uniform Corrosion

In uniform corrosion, dissolution of the steel occurs at approximately the same rate across the entire exposed surface area. Electrochemically, this means the steel becomes a combined anodic and cathodic surface, with equal electrochemical activities [27], [38], [58]. The result is a relatively uniform penetration or thinning of the entire surface. Due to their excellent passivity stainless steels are normally subject to more localised forms of corrosion. However, in lower chromium content steels or under transpassive conditions uniform corrosion produces a somewhat roughened surface by removing a substantial amount of exposed metallic iron once the passive layer is penetrated. The iron will then either dissolve in the environment or produce a loosely adherent, porous coating of corrosion products (rust). Uniform corrosion in such materials can be prevented or reduced by appropriate material selection, such as the use of coatings or inhibitors or cathodic or anodic protection [27], [38].

1.4.2 Pitting Corrosion

Pitting corrosion is a highly localised corrosive attack, resulting in the production of sharply defined holes ('pits') or defects, Figure 1-22.

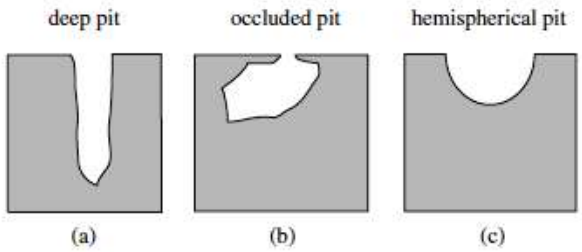

Figure 1-22 –Shape of corrosion pits (a) deep pit; (b) occluded pit; and (c) hemispherical pit [53]

These holes may be small (1-2 µm) or large (10-20 µm) in diameter [94], but in most cases they are relatively small. Pits may be isolated from each other or close together where they may resemble a roughened surface. Pitting is a dangerous form of corrosion for the nuclear engineer as it can lead to the contamination of pipework and, in more severe cases, could cause the perforation of vessels or pipework. Due to the small scale of these perforations, such defects are difficult to detect [36], [38], [95]. Therefore, measurements of the level of pitting corrosion of a material are usually based on the number of pits per unit area, mean pit diameter and mean depth measurement, rather than individual pit characteristics [96].

The likelihood of steel pitting occurring in a reprocessing environment depends on a number of physical and chemical factors:

- Chemical composition and microstructure of the metal
- Surface states and presence of inclusions
- Chemical composition of the electrolyte, especially the concentration of aggressive and non-aggressive anions
- Temperature
- Convection conditions

Chemically, initiation of pitting requires the presence of aggressive anions, most often Cl^-, and an oxidising agent such as oxygen. Cl^- ions compete with OH^- and O_2 for adsorption on site surfaces. If Cl^-

ions are adsorbed on the oxide surface then Me-Cl^- complexes are formed instead of oxyhydroxides and oxides. The Me-Cl^- complexes are less strongly bound to the oxide matrix and their activation energy of transfer to the electrolyte is decreased. As a consequence localised film dissolution occurs and further film growth is restricted. After localised depassivation, Cl^- ions will also compete with OH^- ions for adsorption on the metal surface. Repassivation at the metal surface is then hindered/prevented and this can lead to pit nucleation at less restrictive sites (e.g. weaker areas such as grain boundaries) [36], [97].

After pit initiation, the pit is metastable and may become inactive after a period of a few seconds or less, with minimal penetration of the metal surface. If the pit stabilises, then an autocatalytic corrosion process is setup, shown in Figure 1-23 [38], [58], [98].

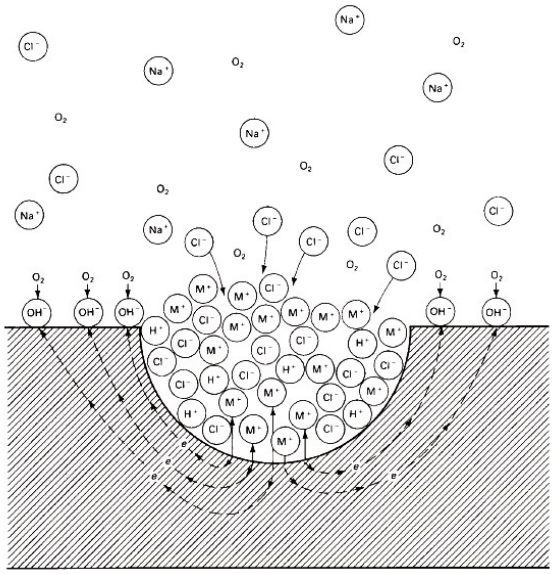

Figure 1-23 – Autocatalytic processes occurring in a corrosion pit .The metal, M, is being pitted by an aerated sodium chloride (NaCl) solution. Rapid dissolution occurs within the pit, while oxygen reduction takes place on the adjacent surfaces [58].

Figure 1-23 shows that rapid dissolution of the metal bulk occurs within the pit interior (anodic), with the reduction of oxygen taking place on the larger adjacent passivated surface (cathodic). The rapid dissolution of the metal within the pit produces an excess of positive charge in this area, causing the electromigration of negatively charged chloride ions into the pit. Therefore, in the pit there is a high concentration of metal chlorides (M^+Cl^-). M^+Cl^- is hydrolysed by water to the hydroxide and free acid as:

$$M^{+}Cl^{-} + H_2O \rightarrow MOH + H^{+}Cl^{-} \quad (1.38)$$

The acid produced by reaction (1.38) keeps the pH value within the pit below pH 2. Cl^- stimulates the dissolution of most metals and alloys and the whole process accelerates with time [58].

1.4.3 Crevice Corrosion

Crevice corrosion is also a form of localised corrosion that occurs in narrow openings or at shielded surfaces where a stagnant solution is present [33]. Crevice corrosion usually occurs in two different engineering situations: Pooling of a corrosive solution in one area while the surrounding areas remain dry or, if the metal is in solution, the corrosive liquid within the crevice is stagnant.

Crevice corrosion follows a similar mechanism to pitting corrosion and is initiated by changes in local chemistry within the crevice [99], for example: depletion of an inhibitor, depletion of oxygen, a shift to acidic conditions or a build-up of aggressive ions e.g. Cl^-.

An example of crevice corrosion at a steel joint in an oxygenated chloride solution is shown in Figure 1-24.

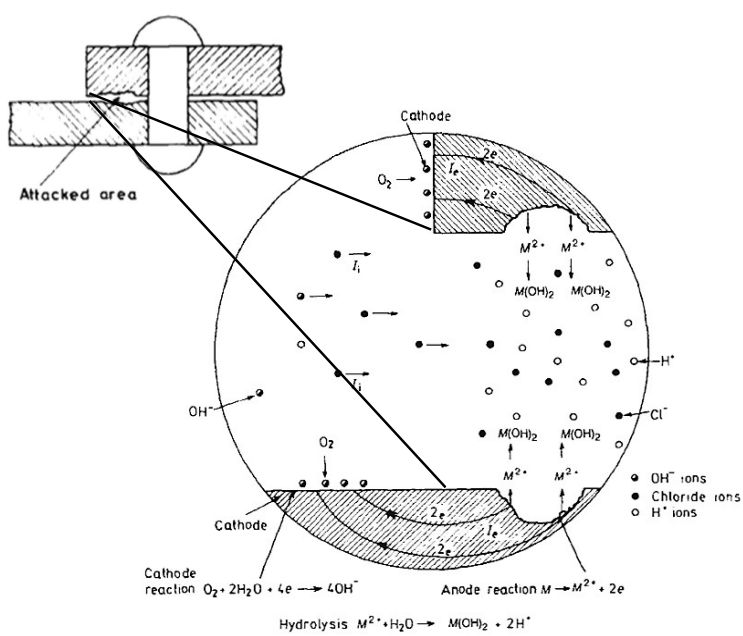

Figure 1-24 – Mechanism of crevice corrosion at a the steel joint shown immersed in an oxygenated chloride solution [38].

Initially, the whole surface will be in contact with the oxygenated solution, with the reduction of oxygen providing the cathodic process for surface attack. However, while the freely exposed surface will have access to dissolved oxygen via convection and diffusion, the crevice will only have access to oxygen via diffusion. Furthermore, oxygen reduction will result in the rapid removal of oxygen from areas outside the crevice. Under these conditions the oxygen concentration within the crevice will become negligible and oxygen reduction inside the crevice will cease.

The large cathodic reduction of oxygen on the external surface results in the anodic dissolution of the metal within the crevice. The generation of metal cations (M+) within the crevice results in the migration of Cl^- and OH^- from the bulk solution into the crevice to maintain neutrality, leading to the formation of a metal chloride (M^+Cl^-). As discussed in the previous section, the so-formed metal chloride is hydrolysed by water, resulting in the formation of a metal hydroxide (non-passivating) and free acid. This leads to a fall in pH which, in combination with the high chloride content, prevents the passivation and facilitates further dissolution of the metal, supporting crevice growth [38].

1.4.4 Intergranular Corrosion

Intergranular corrosion is defined as the selective dissolution of grain boundaries, or closely adjacent regions, without appreciable attack on the grains themselves [58].

Metals are polycrystalline by nature, with boundaries between individual crystallite grains. When a metal solidifies or is heat treated, the grain boundaries can take on chemical characteristics different to that of the bulk of the grain, resulting in areas between grains that are susceptible to corrosive attack. In stainless steels, the most common form of intergranular corrosion occurs through chromium carbide formation at grain boundaries. This can occur during manufacturing if the carbon concentration is too high, or if unfavourable heat treatment of the steel has occurred, e.g. the heat affected zone along a weld [27]. In either case a depletion of chromium in the steel occurs as chromium carbide is formed at grain boundaries from added carbon, as shown in Figure 1-25.

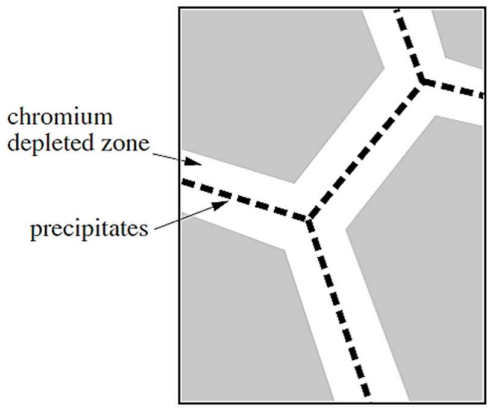

Figure 1-25 – Schematic of chromium depletion at grain boundaries due to the precipitation of chromium carbides [53].

Under corrosive conditions (e.g. mild acids), the grain bulk where chromium is not bound to carbon forms a protective oxide film. However, at the grain boundary where chromium carbide has formed there is not enough free chromium available to form a cohesive chromium oxide film, creating zones of local corrosion around the grain. [43], [100].

1.4.5 Stress Corrosion Cracking

Stress corrosion cracking results from the combined action of a tensile or shear stress (applied or residual) and corrosion. Typically the stress initiates attack, with corrosion proceeding via an anodic process, as demonstrated in pitting or crevice corrosion [53].

A tensile stress can be a residual stress remaining from earlier deformation or an applied stress from a direct load. The corrosive medium is specific to the metal concerned, e.g. chloride ions for austenitic stainless steels [27]. There are two main stages of stress corrosion cracking, *initiation*, which occurs before any crack is visible and *propagation,* where crack growth occurs and can results in a fracture, as shown in Figure 1-26.

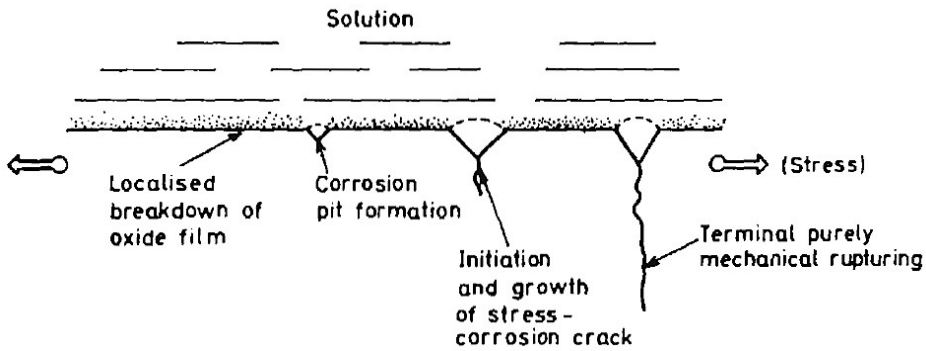

Figure 1-26 - Breakdown of oxide film leading to a pit and crack when a high-strength steel is subjected to a tensile stress in a chloride solution [38].

Different phenomena may be at the origin of a crack nucleus; mechanisms for crack initiation include:

- Pitting
- Intergranular corrosion
- Hydrogen accumulation in the metal due to corrosion
- Mechanical rupture of the passive film
- Microstructural defects such as inclusions, voids or microcracks

Pits can act as crack initiation sites if they lead to a higher local stress intensity (as shown in Figure 1-26). Precipitation reactions at grain boundaries can make an alloy more sensitive to intergranular corrosion, with the corroding grain boundary then serving as the crack initiation site [27], [38], [53]. Tensile stress at the crack tip could break the passive oxide film or selective dissolution of alloy components could also lead to activation of the crack by exposing the base metal to the electrolyte.

The widely accepted model explaining the role of stress for crack growth is the *slip dissolution model*. The slip dissolution model assumes that introducing stress to the material under corrosion can lead to plastic deformation at the crack tip. This deformation can cause dislocations in the slip planes which can lead to fractures of the passive film. Fractures in the passive film leads to exposure of the bare metal to solution. Propagation of the crack can then occur via active dissolution at the crack tip, while a passive film protects the walls of the crack [53], as shown in Figure 1-27.

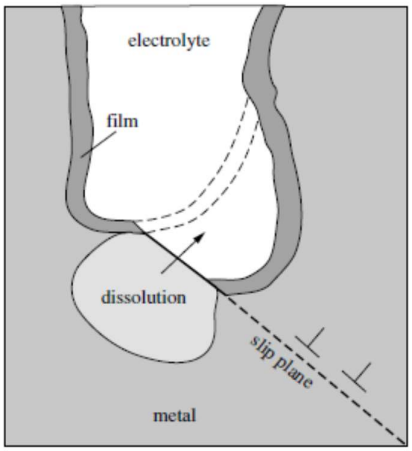

Figure 1-27 – Slip-dissolution model of stress corrosion cracking. Due to a slip the metal is unprotected by the passive film and comes into contact with the electrolyte allowing active dissolution at the crack tip for a period of time [53].

1.4.6 Erosion Corrosion

The simultaneous action of erosive wear and corrosion is called erosion corrosion. Erosion corrosion is often encountered in pumps and pipes, or in the case of nuclear reprocessing, centrifugal contactors, exposed to turbulent flow in the presence of suspended particles. In practice, the term erosion corrosion is often used broadly to designate accelerated corrosion in turbulent flow systems, independently of whether solid particles are present or not [53].

A schematic of erosion corrosion of a stainless steel surface is shown in Figure 1-28.

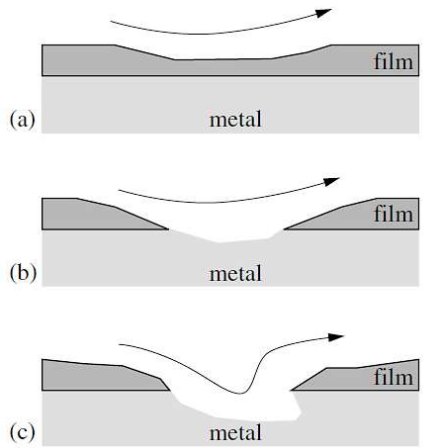

Figure 1-28 –A schematic showing the sequence of events in erosion corrosion: (a) corrosion of the film;(b) corrosion of the metallic surface exposed to the flow; and (c) formation of pits with characteristic elongated shape [53].

First erosion of the protective chromium oxide layer occurs through action of the turbulent flow on the metal, Figure 1-28(a). Alternatively if the metal has been newly exposed to corrosive media the formation of the protective oxide layer is disturbed, leaving areas with a weakened oxide film. The intensity of erosive action is affected by the presence of abrasive particles, air bubbles, metal composition and degree of flow turbulence. Once the film is breached a pit is formed *via* the mechanism described in section 1.4.2, Figure 1-28(b). However, due to the flow dynamics of the erosive stream, pits formed in this fashion are usually significantly larger and elongated in the direction of flow compared to those formed under stagnant pitting conditions, Figure 1-28(c). [101].

Having described the principal mechanisms of corrosion, many of which may lead to the entrainment of adventitious radioactive contaminants, we now move to discuss the chemistry of the actinides that are relevant to such sorption/entrainment.

1.5 Radionuclide Chemistry and Surface Contamination

The development of cost effective decontamination strategies requires a fundamental understanding of the interfacial science of radionuclide contaminants and the way in which they are associated with surfaces to be decontaminated. Recent work in Hungary, the US and the UK [4], [102]–[107] has demonstrated the ease with which uranium (U) may be incorporated into, or adsorbed onto, corrosion product oxide layers on steels. The possibility of uranium incorporation into passive oxide layers on process steels has yet to be addressed and, given the radiotoxicity of U, has potentially profound implications for the disposal strategies of such steels. There is therefore a need to better understand the interaction of U with steels, both to quantify the problem and to develop more informed strategies for its remediation/decontamination. Thus, the following sections first briefly describe the general chemistry of the α-emitting actinides. This is followed by a review of recent work in the scientific literature on determining the behaviour of the extensively studied β/γ emitting fission products with oxide layers on steels.

1.5.1 General Chemistry of the Actinides

The actinide elements are characterised by the filling of the seven 5f orbitals (except Actinium and Thorium which are 6d filled only). There are 15 chemical elements with atomic numbers, 89 (actinium) through 103 (lawrencium) as shown in Figure 1-29.

89	90	91	92	93	94	95	96	97	98	99	100	101	102	103
Ac	Th	Pa	U	Np	Pu	Am	Cm	Bk	Cf	Es	Fm	Md	No	Lr

Figure 1-29 – Period 7, The Actinide Series, taken from the periodic table [108]

The actinides are all radioactive elements. Actinium, thorium, protactinium and uranium are the only four actinides that have been found naturally in the environment, the others are artificial, being produced by particle accelerators or in nuclear reactors [11], [109]. The elements within the actinide series have several common properties [109]:

- Most elements (heavier that U) were discovered by synthetic means
- All actinide isotopes are radioactive

- Many have a large number of oxidation states. For example Pu can exist in aqueous solution simultaneously in four oxidation states (+3 to +6, with +7 exhibiting very different redox potentials)
- Actinium and the elements americium through lawrencium are similar in many respects to the lanthanides (elements that fill the 4f subshell). Elements thorium through to neptunium have some properties similar to those of the d-block transition elements.

Pu exhibits properties similar to both the lanthanides and d-block transition metals, presenting some unique challenges in the study of its chemical behaviour, as will be illustrated below.

1.5.1.1 Oxidation States and Aqueous Electrochemistry

Actinides in aqueous solution have several different oxidation states, as shown in Table 1-2:

Table 1-2 – Known oxidation states of the actinides and species in solution. The bold number represents the most stable oxidation state in solution of each element [110], [111].

Ac	Th	Pa	U	Np	Pu	Am	Cm	Bk	Cf	Es	Fm	Md	No
						2			2	2	2	2	**2**
3	3	3	3	3	3	**3**	**3**	**3**	**3**	**3**	**3**	**3**	3
	4	4	4	4	**4**	4	4	4	4				
		5	5	**5**	5	5							
			6	6	6	6							
				7	7								

Oxidation states up to +7 have been identified for some elements (Neptunium (Np), Plutonium (Pu) and Americium (Am)). This multivalent behaviour leads to very complex redox behaviour. For example, Pu has a wide variety of oxidation states ranging from +3 to +6 such as Pu^{3+}, Pu^{4+}, PuO_2^{+} or PuO_2^{2+} all of which can be present at the same time as a consequence of their very similar redox potentials [107], [111].

The aqueous speciation of the actinides in aqueous solution is shown in Table 1-3.

Table 1-3 – Actinide speciation in aqueous solution [110], [111].

Oxid$^{\underline{n}}$ State	**89**	**90**	**91**	**92**	**93**	**94**	**95**	**96**	**97**	**98**
+3	**Ac^{3+}**	Th^{3+}	Pa^{3+}	U^{3+}	Np^{3+}	Pu^{3+}	**Am^{3+}**	**Cm^{3+}**	**Bk^{3+}**	**Cf^{3+}**
+4		**Th^{4+}**	Pa^{4+}	U^{4+}	Np^{4+}	**Pu^{4+}**	Am^{4+}	Cm^{4+}	Bk^{4+}	Cm^{4+}
+5			**PaO_2**	UO_2^{+}	**NpO_2^{+}**	PuO_2^{+}	AmO_2^{+}			
+6				**UO_2^{2+}**	NpO_2^{2+}	PuO_2^{2+}	AmO_2^{2+}			
7					NpO_2^{5-}	PuO_2^{5-}				

The oxidation state of an actinide may alter due to a change in redox potential. The redox potential can be influenced by chemical composition of the solution, concentration of dissolved O_2 or pH [107].

Having discussed the general chemistry of the actinides, we now describe in more detail the solution chemistry of the three most likely to be encountered actinides in nuclear reprocessing streams: Uranium, plutonium and neptunium.

1.5.1.2 Uranium Solution Electrochemistry

Natural uranium occurs in three main isotopes, ^{234}U (0.0055% wt.), ^{235}U (0.72% wt.) and ^{238}U (99.27% wt.). Globally, the fissile isotope ^{235}U provides the most commonly used energy source of nuclear reactors and atomic weapons [112].

Uranium exists in aqueous solutions in the +3, +4, +5 and +6 oxidation states. U^{3+} is a powerful reducing agent which is slowly oxidised to U^{4+} in anoxic conditions and rapidly in the presence of oxygen. U^{4+} is regarded as a 'stable' species of U solution, but is slowly oxidised to UO_2^{2+} by air. UO_2^{+} has a short-lived existence in solution, it is most stable in the pH range 2-4. UO_2^{+} is prone to disproportionation at any pH to U^{4+} and UO_2^{2+} via the following reaction [110], [111]:

$$2UO_2^{+} + 4H^{+} \rightarrow U^{4+} + UO_2^{2+} + 2H_2O \tag{1.39}$$

The general electrochemical behaviour of uranium in aqueous solutions is dominated by the reduction of the hexavalent 'uranyl' ion, UO_2^{2+}. The uranyl ion is the most stable oxidation state and therefore difficult to reduce.

Figure 1-30 gives the oxidation potentials for uranium in pH 0 aqueous solution (akin to what would be expected in high nitric acid concentrations).

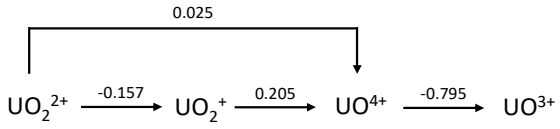

Figure 1-30 –Redox potentials (vs. SCE) of uranium in aqueous solutions at pH 0 [111], [113].

1.5.1.3 Plutonium Solution Electrochemistry

Plutonium exists in five oxidation states in aqueous solution: Pu(III), Pu(IV), Pu(V), Pu(VI) and Pu(VII) which occur as the hydrated ions Pu^{3+}, Pu^{4+}, PuO_2^{+}, PuO_2^{2+} and PuO_5^{3-} respectively. Tetravalent plutonium is the most stable oxidation state [114], [115].

Figure 1-31 gives the oxidation potentials for plutonium in pH 0 nitric acid solution.

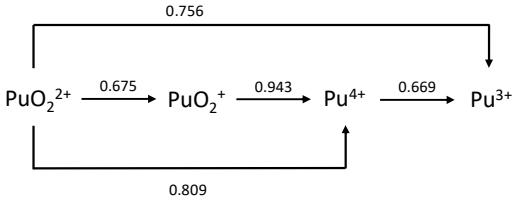

Figure 1-31 –Redox potentials (vs. SCE) of plutonium in a HNO_3 solution of pH 0 [113].

Pu(III) is unstable at pH 0 and can be oxidised by a variety of oxidants to Pu^{4+}. It can also be oxidised to Pu(IV) by the α radiation produced by plutonium isotopes. Pu(IV) is stable in concentrated acids, but in mild acids (free of complexing agents) Pu(IV) disproportionates to Pu(III) and (PuVI). Oxidation of Pu^{4+} in aqueous solutions produces hexavalent plutonium, PuO_2^{2+}.

Pentavalent plutonium, PuO_2^+, is only stable between pHs of 2 and 6, a pH value unlikely in strong nitric acid environments; thus its disproportionation, stoichiometrically analagous to that of uranium, is not considered here further. However, Hexavalent plutonium, PuO_2^{2+}, while stable in strong acidic solutions (see above) is slowly reduced by the products of the radiolysis of water by the α-radiation produced by plutonium isotopes. In an acid solution, in the absence of complexing agents, the disproportionation of Pu(IV) follows the reaction [114]:

$$3Pu^{4+} + 2H_2O \rightleftarrows 2Pu^{3+} + PuO_2^{2+} + 4H^+ \tag{1.40}$$

The disproportionation is temperature dependent and the rate at which it occurs is proportional to the concentration of H^+ [115].

The overall reaction of Equation (1.40) may be further split into two stages. The first stage involves two Pu(IV) combining to generate Pu(III) and Pu(V). The formation of Pu(V) is slow because it involves the formation of a Pu=O bond. In the second stage, the Pu(V) produced in the first stage reacts with Pu(IV) to produce Pu(III) and Pu(VI). This requires only an electron transfer which occurs rapidly.

$$2Pu^{4+} + 2H_2O \rightleftarrows Pu^{3+} + PuO_2^{+} + 4H^+ \tag{1.41}$$

$$PuO_2^{+} + Pu^{4+} \rightleftarrows Pu^{3+} + PuO_2^{2+} \tag{1.42}$$

Disproportionation is complete when reactions (1.41) and (1.42) have reached equilibrium [114], [115].

1.5.1.4 Neptunium Solution Electrochemistry

In aqueous solution, neptunium exists as ions in all oxidation states from 3+ to 7+. The stability of these ions is strongly affected by pH, oxidants and reductants, complexing agents and the concentration of Np itself.

In the absence of complexing agents, Np^{3+}, Np^{4+}, NpO_2^+ and NpO_2^{2+} exist as hydrated ions. Np^{3+} is quickly oxidised to Np^{4+} by air. In aqueous solutions of low acidity Np^{3+} and Np^{4+} form insoluble hydroxides where, once again, Np(III) is oxidised to the more stable Np(IV) by oxygen. In acidic solutions the pentavalent and hexavalent Np ions act as Lewis acids and form dioxo species, NpO_2^+ and NpO_2^{2+}. NpO_2^+ is stable in acidic solutions but is easily oxidised to NpO_2^{2+} [115], [116].

NpO_2^+ disproportionates to Np^{4+} and NpO_2^{2+} through the following reaction:

$$2NpO_2^+ + 4H^+ \rightleftarrows Np^{4+} + NpO_2^{2+} + 2H_2O \tag{1.43}$$

The extent of the disproportionation is dependent on high solution acidity and high NpO_2^+ concentration [116].

Figure 1-32 gives the oxidation potentials for neptunium in pH 0 aqueous solution.

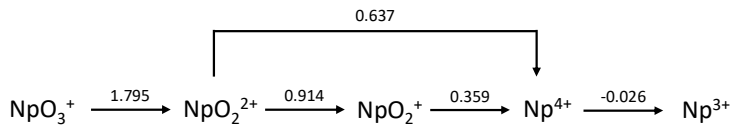

Figure 1-32 –Redox potentials (vs. SCE) of neptunium in aqueous solutions at pH 0 [116].

1.5.2 Surface Contamination

Surface contamination, which is generally derived from the 'plating out' of solids, colloids or metal ions from a liquid/solution phase, is broadly classified as being of 2 main types: Fixed and non-fixed.

Non-fixed contamination is loosely bound to the surface through weak electrostatic interactions and is easily removed by most clean-up techniques and, therefore, will not be considered further here [3]. However, fixed contamination is chemically or physically adhered to a surface, making decontamination more difficult. This form of contamination can be most readily detected by a radiological survey [117]. Studies of non-redox active Cesium (Cs) contamination of corroded and non-corroded stainless steel surfaces have also indicated that inter-conversion between fixed and non-fixed states is possible, depending on environmental conditions [3].

Fixed contamination of a steel surface may occur through a number of mechanisms [1]:

- Strongly held on the surface through chemical bonds between surface metal oxides and the contaminant
- Precipitation of a pure contaminant metal-oxide
- Co-precipitation with Fe or Cr to form a new mineral phase

- Channelling down grain boundaries

The solution chemistry of the aqueous media has a predominant effect on the surface chemistry and the corrosion state of the contaminated surface as well as the chemical forms of the contaminant species.

1.5.2.1 Uranyl $(UO_2^2)^{2+}$ and Fission Product Accumulation on Steel Surfaces

While there is limited accessible information available on the adsorption of uranyl on steels under reprocessing conditions, several studies have been published that deal with uranyl and fission product adsorption on nuclear plant materials in boric acid coolant and in geological repositories.

A detailed overview of uranium accumulation into various 'aged' steels has been produced by Steele [1]. Using a combination of chemical modelling techniques (Forcite Molecular Mechanics (MM) and Castep Quantum Mechanics (QM)), Steele studied the uptake of contaminants (U(IV), Co(II), La(III) and Sr(II)) into various iron oxides known to form on corroding steel structures. The main focus was on whether contaminant uptake or incorporation affects the stability of these iron oxides. Iron oxides were specifically investigated over chromium oxides due to their ability to trap contaminants by adsorption or incorporation within the bulk metal during formation of the oxide, and also their ability to re-release said contaminants. Thus, the following stages of contamination ingress and egress were modelled:

1. Fe oxide formation by precipitation or co-precipitation
2. Transformation of the Fe oxide to a more stable phase
3. Susceptibility of the Fe oxide to dissolve again or release incorporated trace components

The iron oxides assessed in the study were: magnetite (Fe_3O_4), wüstite (FeO), hematite (α-Fe_2O_3), lepidocrocite (α-FeOOH) and goethite (γ-FeOOH). Magnetite and wüstite are formed in oxygen deficient environments and are relatively dense Fe oxides found closest to the pure steel surface. Hematite is formed in oxygen rich environments and is usually an intermediate oxide layer. Goethite and lepidocrocite are found on the upper surface of the oxide layer in oxygen and moisture rich environments and are generally less dense than the other oxides, with goethite forming at a lower pH than lepidocrocite. This hierarchy of iron oxides on a steel surface is shown in Figure 1-33.

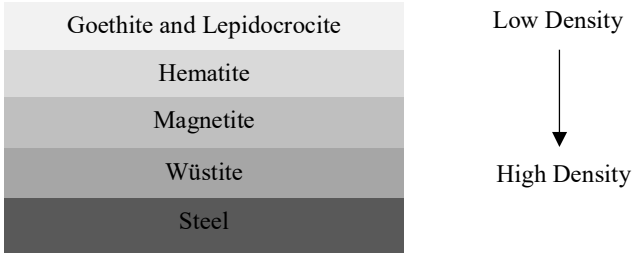

Figure 1-33 –A 4-layer model of oxide formation on steel surfaces. As you descend towards the steel surface, the ease with which these high Fe-oxides take up contaminants is reduced and the difficulties in removing the dense layers is increased, (recreated from [1]*).*

Steele [1] concluded that the high density base layer oxides of wüstite and magnetite preferentially take up U(IV) from solution, potentially due to the similarity of the iron (II) and iron (II/III) sites to the U(IV) site in uranite. However, due to instabilities within the oxide structure, unfavourable reaction energies and a predicted high cell volume change for wüstite in particular (leading to oxide structure failure), actual uptake is predicted to be low. Uptake of U by hematite is very favourable at low concentrations, but at high concentrations of contaminant, uptake is unfavourable. Thus, uptake of U at high concentrations is greatest into the surface layers of lepidocrocite and goethite than the more dense iron oxides at the pure steel surface. Steele [1] also highlights that changes in environmental conditions could lead to a transformation from one iron oxide to another, either increasing the probability of contaminant uptake or decreasing it. This is important when considering changes in parameters such as pH along the reprocessing route and how this could affect oxide formation.

Dombovari *et al.* [106] have studied uranyl adsorption chemistry in boric acid coolant solutions onto austenitic stainless steel type 08X18H10T (GOSZT 5632-61) and Zr(1%Nb) alloy) in PWR type nuclear reactors. Uranyl accumulation exhibits a time and pH dependence. After ~10 hours, adsorption of U species reaches a quasi-equilibrium condition. Accumulation of U species was also found to be greatest at pH 4.5 and 6. This is suggested by Dombovari *et al.* [106] to be due to the corrosion behaviour of the steel studied (AISI321) and the hydrolysis of uranyl cations in boric acid in this pH range. An increase in the accumulation of U species is attributed to the coadsorption of uranyl hydroxide and corrosion products containing Fe and Cr (likely Fe and Cr hydroxides) on the steel surface. The quantity and chemical forms of the Fe and Cr containing species dissolved from the steel surface plays a determinative role in the extent and kinetics of U accumulation. Modelling results in the same study support this,

suggesting that specific adsorption and deposition of (mainly colloidal and disperse) uranyl hydroxide occurs over the accumulation of other hydroxo complexes at pHs between 4.5 and 6. XPS measurements confirmed the presence of U(VI), supporting observations that U accumulation on steel tubes occurs via some specific adsorption and deposition processes to yield a passive oxide layer contaminated with U(VI) species.

Kádár *et al.* [107], [118] and Répánszki *et al.* [119], [120] have also studied the accumulation of U, transuranic elements and fission products on stainless steel surfaces in boric acid. Kádár *et al.* [107], [118] examined the behaviour of Pu, Cs, Cm, Ce and U isotopes in mildly acidic (pH 4.5) boric acid on two different steel types; stainless steel canister material, similar to AISI 321 and steam generator (SG) steel tube, similar to AISI 321H. AISI 321 is the basic austenitic 18/8 steel (304) stabilised with titanium, a choice material for applications with a temperature range up to ~900°C. AISI 321H is the same material but modified with a higher carbon content to improve high temperature strength. Considering first Pu and Cs, accumulation of cationic Pu and Cs on the canister was negligible and any interactions were non-specific (electrostatic) in nature and could be easily removed from the steel surface. On the SG sample, Pu and Cs cation accumulation was detected on the surface, giving a strong indication that specific adsorption (chemisoption) occurs between Pu and/or Cs species and some constituents of the steel oxide layer. Considering next Cm and Ce, both isotopes accumulate significantly on both steel samples at such high values that the accumulation can be considered completely independent of sample morphology. Finally uranium accumulation again differs between the two steel samples. After a fast sorption period on the canister material (~1h), slow desorption takes place and solution concentration of U approaches initial, prior to rapid sorption, concentrations. In the SG tube samples the concentration of uranium in solution decreases continuously, suggesting constant accumulation of uranium. XPS analysis of U on the SG tube surface determined that the uranium oxidation state is +4 in the deeper region of the steel passive layer, in agreement with the work by Dombovari *et al.* [106].

Geological repository based studies have also been conducted by Moyes *et al.* [102], Dodge *et al.* [104] and Eng *et al.* [105] to investigate U uptake onto synthesised iron oxides and corroded steel surfaces representative of corroding steel storage canisters containing U waste. U species have been found to behave differently in the presence of individual Fe oxide phases, with removal of U depending on its association with these oxides. Primarily, uranyl uptake on iron hydroxides, goethite and lepidocrocite

was found to occur in oxidised areas where the uranyl ion could form complexes; this ceased once these sites were saturated. As described above, such behaviour has also been seen by Dombovari *et al* [106], Kádár *et al.* [107], [118], Répánszki *et al.* [119], [120] and reported in the modelling studies of Steele [1], who observed that uranyl adsorption on oxide films reaches quasi-equilibrium after several hours. Also, steels that have been more heavily corroded retain more U species than steels that only possess a thin native oxide layer [121]. However, in the studies of Moyes, Dodge and Eng [102], [104], [105] U uptake on other mineral phases, such as, muscovite and mackinawite increases linearly with exposure time, suggesting the precipitation of a U phase on the surface [102]. Further, Dodge *et al.* [104] and Eng *et al.* [105] have shown that U is present in similarly exposed goethite, maghemite and magnetite, as its hexavalent form, uranyl oxyhydroxide. However, further studies with ferrihydrite and lepidocrocite, reveal U is present as a bidentate inner sphere complex, which resists dissolution in HCl, unlike the oxyhydroxide [104], [121].

Having described how surfaces are contaminated we now describe the process of decontamination and the techniques that are currently available to the nuclear engineer.

1.6 Decontamination Techniques

Decontamination is defined as the removal of contamination from surfaces of facilities or equipment by washing, heating, chemical or electrochemical action, mechanical cleaning, or other methods [122]. The primary objectives of decontamination are [123], [124]:

- Reduce the contamination from components to reduce dose level in the installation and reduce dose during dismantling
- To remove loose radioactive contaminants to minimise the potential for spreading contamination during further dismantling
- Reduce the volume of equipment and materials requiring storage and disposal in licensed disposal facilities
- Reduce the contamination of components to such levels that they can be recycled or reused

- Reduce the magnitude of the residual radioactive source in protective storage for public health and safety reasons, to reduce storage period or to minimise long-term monitoring and surveillance requirements

There is no single technique suitable for decontaminating surfaces, the selection of a technique depends on [123]–[125]:

- Facility history (power plant, fuel fabrication, fuel reprocessing type);
- Size, configuration and location of the contaminated surface (internal or external) and its relationship to other surfaces;
- Type of isotopes involved;
- Activity levels;
- Nature of the contamination (oxide, sludge etc.);
- Exposure level reduction requirements (recycling vs. disposal);
- Secondary waste types and quantities;
- Time to effect decontamination,
- Cost

Decontamination can be performed before dismantling to reduce dose rate and reduce the risk of contamination spread, after dismantling to change the waste category of the waste (reduce disposal cost) or to allow the material to be reused or recycled [123].

Different techniques are also suitable depending on whether the objective is to decontaminate an open or closed system, as shown in Figure 1-34.

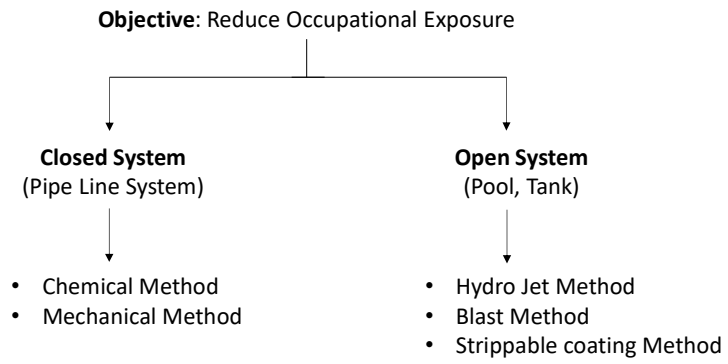

Figure 1-34 – Options for decontaminating open or closed systems. Adapted from Boing [123].

Techniques for decontamination can be split into 3 categories; Chemical, Electrochemical and Physical (Mechanical). The following sections will provide a high level description of these different decontamination categories and key techniques therein, their advantages and disadvantages and their applicability to the decontamination of steels and especially process pipework made from steel.

1.6.1 Chemical Decontamination

Chemical decontamination techniques use chemical reagents to dissolve the contamination layer covering the base material. Chemical solutions are generally most effective on non-porous surfaces, such as non-corroded stainless steel. The choice of chemical agent/s is crucial and must take into account the chemistry of the contaminant, the chemistry of the substrate and the ability to manage the waste generated during the process [122].

Chemical techniques are divided into two groups. *Mild techniques* involve non-corrosive reagents and are used for items where the objective is to remove contamination without attacking the base metal. *Aggressive methods* use chemicals including strong acids or alkalis and other corrosive agents. These techniques may involve one or more stages using different chemical solutions [122], [124].

The main advantages of chemical decontamination techniques is that they are relatively simple to apply and similar to conventional cleaning techniques used in industry for which there is a lot of experience. Chemical techniques have also proven very effective in reducing the radioactivity of large surface areas and are suitable for use on complex geometries as well as the treatment of inner and outer surfaces of equipment [122], [126].

Examples of single step chemical processes include [124];

- Processing using Ce^{4+}
    - REDOX (developed in Japan) – The REDuction-Oxidation process uses the oxidation power of Ce^{4+} and then electrochemically regenerates the reduced Ce^{3+}.
    - SC - Sulphuric Acid Cerium process, similar to the REDOX process, uses the oxidation power of Ce^{4+} and then electrochemically regenerates the reduced Ce^{3+}. SC uses a sulfuric acid environment, whereas REDOX uses a nitric acid environment.
    - SODP process (developed in Sweden) – The one-step Strong Ozone Decontamination Process which utilises Ce^{4+} as the oxidant, the reduced Ce^{3+} is then re-oxidised using ozone.
    - MEDOC (Developed in Belgium) – MEtal Decontamination by Oxidation with Cerium uses Cerium to rapidly attack the metal surface, the cerium is then regenerated using ozone. This process distinguishes itself from REDOX, SODP and SC by the continuous regeneration of the solution at the same temperature as the decontamination temperature, through the use of ozone in a gas-fluid contactor.
- HNO_3/HF washout – A sulfonitric mixture is applied either in a bath or pressure jet. Surface oxides are reduced and the metal beneath is attacked.
- DECOHA process – Based on the use of fluoroboric acid in a bath at ~90ºC or applied by pulverisation of a solution at a low temperature.

Examples of multi-step processes include:

- CORD – Chemical Oxidising Reduction Decontamination, a 3 step chemical process. Each cycle consists of: an oxidation step, using permanganic acid; a decontamination step using oxalic acid and a purification step by the addition of permanganic acid or hydrogen peroxide.
- LOMI – Low Oxidation state Metal Ion. The process incorporates vanadium (II) as a reducing agent and picolonic acid as the complexing agent.

The main disadvantage of chemical decontamination is the generation of high volumes of acidic/aggressive secondary waste. Other disadvantages of chemical decontamination include; the need

to handle corrosive and toxic chemicals, solutions usually have to be heated up to 70-90°C to improve the decontamination kinetics and relative inefficiency of porous surface decontamination [122].

1.6.2 Electrochemical Decontamination

Electrolytic polishing is an anodic dissolution technique. The material, usually a metal, to be decontaminated is the anode and the cathode is a separate steel electrode or the tank itself. Electrochemical techniques may only be applied as a means to remove radionuclide contamination from conductive surfaces, such as iron based alloys (including stainless steel), aluminium, copper, lead and molybdenum [122].

Examples of different electrochemical processes are [124], [125]:

- *The Phosphoric acid process* – this process can be applied to carbon and stainless steel. H_3PO_4 concentration is 40-80% wt. vol. as an electrolyte, with a working temperature of 40-80°C. The potential difference is 8-12 V_{dc} and a current density of 60-500 mA/cm^2.

- *The Nitric acid process* – this process was developed for the decontamination of stainless steel. HNO_3 is used at 1 mol dm^{-3} at ambient temperature with a current density from 2-3 mA/cm^2.

- *The Sulphuric acid process* – this process was developed in Japan for the decontamination of stainless steel pieces. H_2SO_4 is used at a concentration of 5% wt. at a temperature of 60°C with a current density of 300-1000 mA/cm^2.

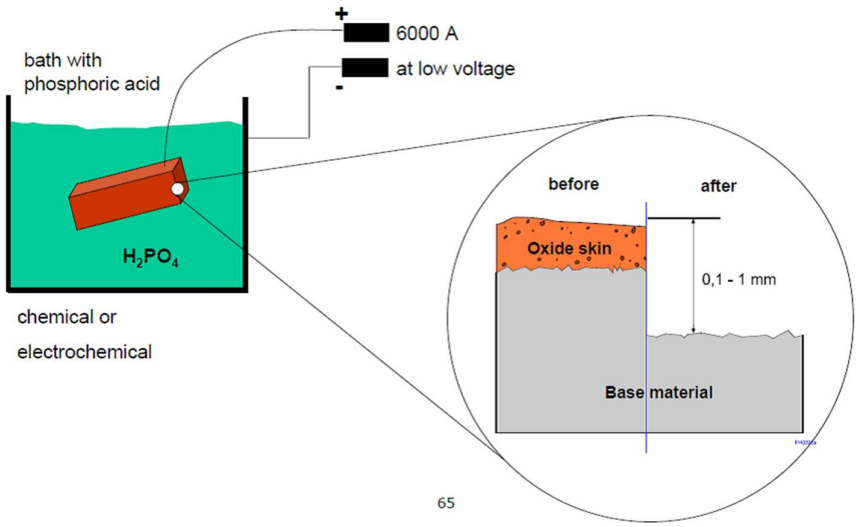

Figure 1-35 - Principle of Electropolishing using phosphoric acid [125].

Electropolishing techniques, such as those described above, are relatively inexpensive and can be used for the treatment of stainless steel, aluminium and carbon steel. However, as noted above, they require conducting surfaces; therefore any insulating coating, such as paint, must be removed from the workpiece before deployment. Removal of paint from a contaminated item may decontaminate a surface to a sufficient level. However, some paints are applied to contaminated surfaces to 'fix' contamination in place while a plant/area is still in use, effectively trapping any contamination underneath paint layers which would need removing prior to decontamination. While this technique is not suitable for small or complex geometry material with hidden parts and it does not remove any fuels, sludge or insulating material, it does have a relatively quick processing time with small amounts of secondary waste generated due to recycling of the tank electrolyte [125].

1.6.3 Mechanical Decontamination

Mechanical decontamination techniques can be classified as either surface cleaning (wiping and scrubbing) or surface removal (drilling, grit blasting and scarifying). Mechanical decontamination methods are less aggressive than chemical techniques but when used together they give good results [122]–[124].

Mechanical decontamination methods include, but are not limited to [125]:

- Cleaning in an ultrasonic bath
- Projection of CO_2 ice pellets or water ice pellets
- Pressurised water jetting
- Wet or dry abrasive blasting
- Mechanical action (grinding, polishing, brushing)

Generally abrasive/blasting techniques are highly effective and give good results in a relatively short time. Several methods remove tightly adherent material, including corrosion layers. There are two main general disadvantages to mechanical techniques: 1) the production of air-born dust and 2) the need for the treated surface to be easily accessible [125]. As such, these techniques produce a large amount of secondary waste, particularly if recycling or abrasives and/or water is not available.

As described above each decontamination technique, whether chemical or mechanical, has its advantages and disadvantages. In particular the most common problem is the generation of large volumes of secondary waste due to the indiscriminate attack of both chemical and mechanical techniques with regards to removing, in the specific case of the steels considered here, a contaminated oxide layer or base metal. Thus, by understanding the nature and size of the contamination layer formed at oxide films on stainless steel it is possible that either existing techniques can be improved with regards to application time (mechanical) or composition (chemical), or alternatively new techniques can be developed that allow more targeted surface decontamination, without damaging uncontaminated underlying substrate material and thus decreasing downstream, secondary waste loadings.

This chapter has reviewed the nuclear fuel cycle, nuclear fuel reprocessing, introduced basic electrochemical, corrosion and radionuclide chemistry concepts and provided an overview of current decontamination techniques. The next chapter reviews experimental techniques used within this work. The rest of the thesis will then describe the experimental data obtained using these techniques.

Chapter 2

Experimental Details

2 EXPERIMENTAL DETAILS

2.1 Reagents & Material

Nitric acid (ACS reagent 70% wt.), Europium (III) Nitrate Pentahydrate and Cerium (III) Nitrate Hexahydrate were all purchased from Sigma-Aldrich Ltd. (Gillingham, Dorset, UK). Uranyl Nitrate stock solution was prepared using a 10 g/L uranyl nitrate ICP standard in 2% wt. HNO_3 from Fisher Scientific (Loughborough, Leicestershire, UK).

All solutions were prepared using doubly deionised water. All water used was Ultrapure from a Direct-Q 3 UV Millipore water purification system (Millipore, Watford, UK) deionised to a resistivity of 18.2 MΩ.cm.

Type 316L SS, 2.54 cm diameter, polished planchets were purchased from Fisher Scientific. The 316L SS bars for rotating disk electrode experiments were purchased from Advent Research Materials Ltd. (Oxford, England). Stainless steel (SS2343) QCM crystals were purchased from Q-Sense (Biolin Scientific, Coventry, UK). The QCM crystals were quartz, AT cut, with a resonant frequency of 5 MHz and a 25 ^{o}C temperature profile.

2.2 Electrochemical Characterisation of Stainless Steel Behaviour in Nitric Acid

In order to investigate the electrochemical corrosion behaviour of 316L SS in nitric acid, two different electrochemical characterisation techniques have been employed: Linear sweep voltammetry and Electrochemical Impedance Spectroscopy.

2.2.1 Linear Sweep Voltammetry

In linear sweep voltammetry (LSV) the voltage is swept from a starting potential (Estart) to an end potential (Eend) at a set scan rate (V/s), as shown in Figure 2-1a. As with other voltammetric measurements, the LSV current response is plotted as a function of potential as seen in Figure 2-1b.

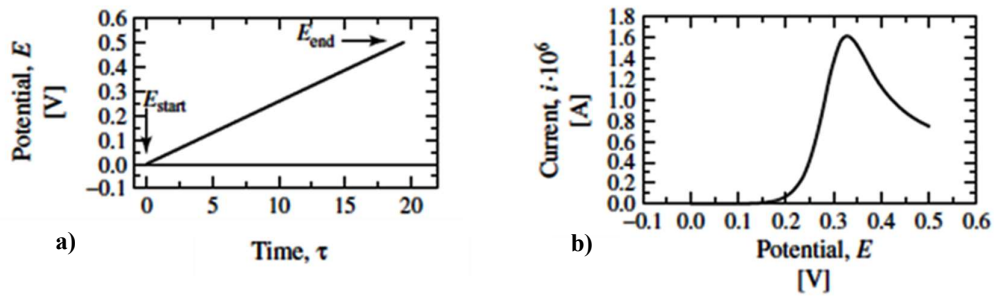

Figure 2-1 – a) Voltage as a function of time and b) current as a function of voltage for LSV [127].

However, more commonly log current density vs. potential plots, often referred to as polarisation curves, are produced in corrosion studies. These allow active, passive and transpassive potential regions to be defined based on the working electrode type and aqueous media (see Chapter 1). An example polarisation curve is shown in Figure 2-2.

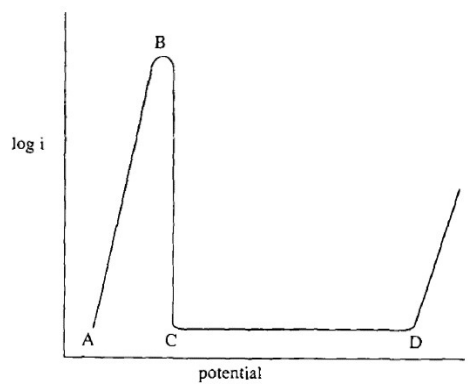

Figure 2-2 – Example anodic polarisation curve for a metal. Region A-B describes active dissolution of the metal. B-C is the active/passive transition with passivity commencing at B. Passivation is complete only at potentials higher than C (Flade Potential). The metal is passive between C and D [38].

2.2.1.1 LSV Experimental Setup

Unless indicated otherwise, LSV experiments were conducted using an Autolab PGSTAT100 potentiostat (Windsor Scientific Ltd.). Measurements were carried out at room temperature at a scan rate of 10 mV s^{-1}, in a three electrode cell, with a platinum mesh counter electrode (Advent Research Materials Ltd., Oxford, England) and a saturated calomel reference electrode (SCE, Russell-pH, Auchtermuchty, Fife, Scotland). For use as a working electrode, a polished 316L stainless steel electrode was placed in solution so that only the electrode face was exposed to solution. The electrode was prepared by polishing using a series of abrasives with decreasing size/grade of grit. Specifically, sandpaper grades 240-1200 and diamond abrasive compounds (Marcon, Codicote, Hitchin, Herts, UK) of 6 and 1 micron. Polishing was followed by rinsing the steel with acetone to remove any organic contaminants. After electrode immersion, but before any linear sweep voltammetric scan, the open circuit potential of the steel was monitored until it reached steady state (approximately 1 hour). All LSV scans reported here were started at -0.5 V and were scanned up to 1.5 V. A diagram of this experimental setup is shown in Figure 2-3.

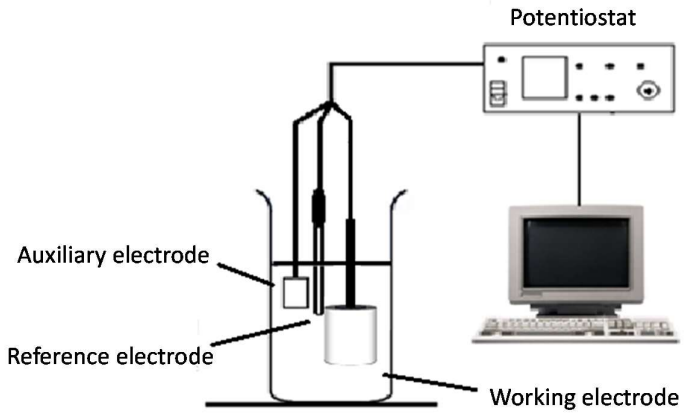

Figure 2-3 –Diagrammatic representation of the CV experimental setup.

10mV s^{-1} is considered to be a high scan rate for potentiodynamic polarisation experiments. Results from LSV experiments described here will be compared to Electrochemical Quartz Crystal Microgravimetry (EQCM) experimental results. The SS2342 layer on the QCM electrodes is very thin (50nm) and LSVs recorded over the potential range described would result in the complete stripping of the crystal before the scan is completed. By using the faster scan rate the complete stripping of the electrode material is avoided and/or reduced, making the results obtained using the two electrode systems compatible.

2.2.1.2 *Tafel Analysis*

Classic Tafel analysis is performed by extrapolating the linear portions of a Log I vs. E plot (aka. a Tafel plot) back to their intersection, as shown in Figure 2-4. The corrosion potential (E_{corr}) and corrosion current density (i_{corr}) can be found at the point of intersection [128].

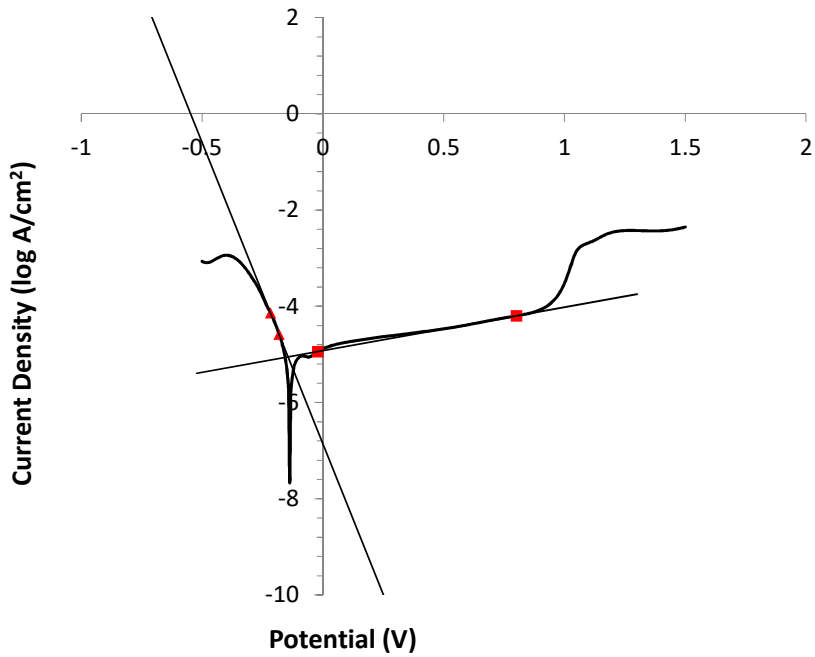

Figure 2-4 – An example of Tafel analysis performed on a Log I vs. E plot (316L SS in 10% HNO_3).

2.2.2 *Electrochemical Impedance Spectroscopy*

Impedance, Z is a circuit's tendency to resist the flow of an alternating current. Analogous to resistance, impedance is defined as the ratio between potential and current:

$$Z = \frac{E(t)}{I(t)} \tag{2.1}$$

Where Z is the impedance (ohms), E is the potential (volts) and I is the current (amperes).

In electrochemical impedance spectroscopy (EIS) a small sinusoidal potential is applied to the working electrode. The resulting sinusoidal current response signal from the electrochemical cell is then measured and analysed [129].

Through Ohm's law, the impedance response of the electrochemical cell to alternating potential signals of varying frequency can be calculated and interpreted on the basis of circuit models of the electrode/electrolyte interface. In turn these can be used to obtain insights into corrosion mechanisms such as passivation, pitting corrosion and active dissolution [130]. Typically, several cell elements and cell characteristics contribute to the system's EIS spectrum including, electrode double layer capacitance, electrode kinetics, diffusion layer size and the solution resistance.

2.2.2.1 Origin of the impedance signal

As described above, initially a sinusoidal potential change is applied to the working electrode at a range of frequencies, ω. The sinusoidal potential, expressed as a function of time, has the form:

$$E_t = E_0 \sin(\omega t) \tag{2.2}$$

Where E_t is the potential at time t, E_0 is the amplitude, and ω is the radial frequency of the applied signal [55], [131], [132].

Due to the inductance/resistance of the electrode, the resulting current response signal, I_t, is delayed leading to a shift in phase (θ) and has a different amplitude, I_0.

$$I_t = I_0 \sin(\omega t + \theta) \tag{2.3}$$

At each frequency the resulting sinusoidal current is out of phase with the applied potential by a certain amount known as, the phase angle, θ, shown in Figure 2-5.

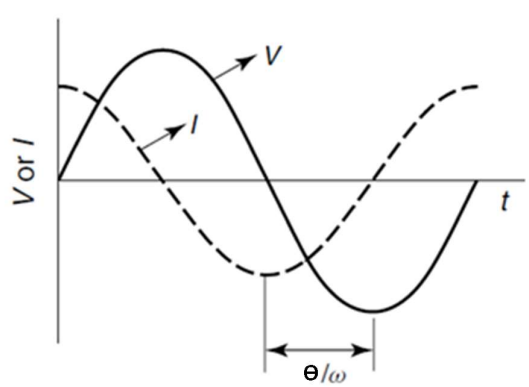

Figure 2-5 – Sinusoidal potential (V) perturbation, current (I) response and phase difference (θ) [132].

Combining equations (2.2) and (2.3) together with equation (2.1) allows us to calculate the impedance as [129], [132]:

$$Z = \frac{E(t)}{i(t)} = \frac{E_0 \sin(\omega t)}{I_0 \sin(\omega t + \theta)} = Z_0 \frac{\sin(\omega t)}{\sin(\omega t + \theta)} \tag{2.4}$$

Impedance is therefore expressed in terms of a phase shift, θ, and a magnitude, Z_0.

Using Eulers relationship it is possible to express impedance as a complex function.

$$exp(j\theta) = cos\theta + jsin\theta \tag{2.5}$$

Potential is described as:

$$E_t = E_0 exp(j\omega t) \tag{2.6}$$

The corresponding current response is then described as:

$$I_t = I_0 exp(j\omega t - \theta) \tag{2.7}$$

Impedance is then represented as a complex number via the following equation:

$$Z(\omega) = \frac{E}{i} = Z_0 \exp(j\theta) = Z_0(cos\theta + jsin\theta) \tag{2.8}$$

From equation (2.8) it can be seen that the complex number impedance is described by a real component, $Z_0\cos\theta$ or Z', and the imaginary component, $Z_0 j\sin\theta$ or -Z''. In electrochemical impedance analysis, two types of plots are commonly used: Nyquist plots and Bode plots. Nyquist plots, or complex plane plots, are plots of Z' (real) versus –Z'' (imaginary). An example nyquist plot is shown in Figure 2-6.

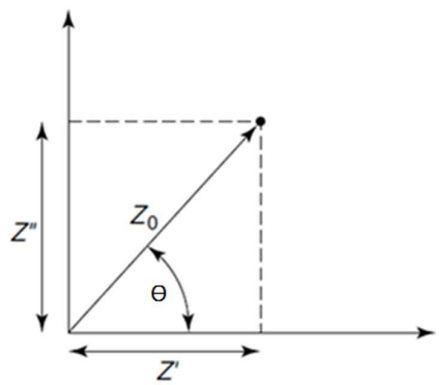

Figure 2-6 – Presentation of impedance in the complex plane (Nyquist plot). Z'' and Z' are the imaginary and real components of impedance, Z_0 is the magnitude of the impedance and θ is the phase angle [132].

However, as shown in Figure 2-6, the issue with Nyquist plots is that they give no frequency information. Thus, a second type of plot of impedance that uses frequency information is often used in conjunction with Nyquist plots, the Bode plot. There are two different common types of Bode plots. One shows impedance magnitude versus log frequency and one shows phase angle versus log frequency. Both types are shown schematically in Figure 2-7.

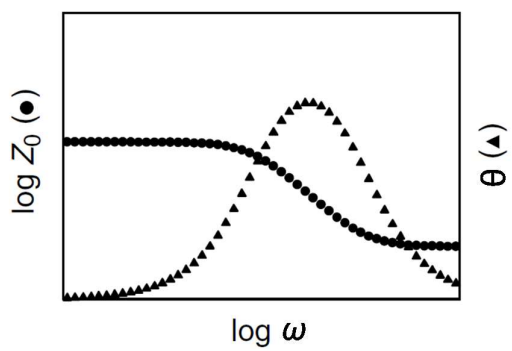

Figure 2-7 –An example of a Bode plot; where log ω is the logarithim of the frequency, θ is the phase angle and log Z_0 is the logarithm of the magnitude of the impedance [132].

2.2.2.2 Data analysis – Equivalent Circuit Modelling

The most common method used to analyse EIS spectra is equivalent circuit modelling. The model should have a basis in the physical electrochemistry of the system. For example, a resistor that models the cell's solution resistance. The behaviour of each element is then described in terms of 'classical' electrical components (resistors, capacitors, inductors) plus a few specialized electrochemical elements.

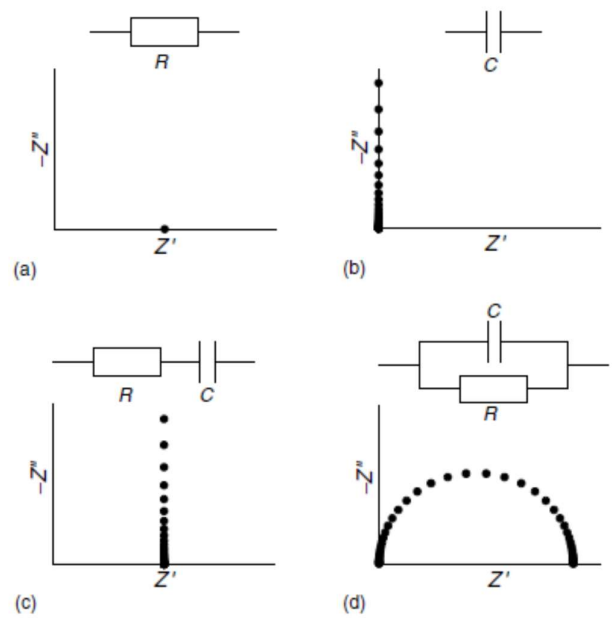

Figure 2-8 – Nyquist plots for different equivalent circuits [132]

If a sinusoidal voltage is applied to a pure resistor, *R*, then $Z_0 = R$ and $\theta = 0$ for all frequencies as shown in the nyquist plot shown in Figure 2-8a. When a sinusoidal voltage is applied across a pure capacitor (Figure 2-8b) the impedance can be calculated as:

$$Z = \frac{1}{j\omega C} = -\frac{j}{\omega C} \tag{2.9}$$

Where C is the capacitance and the magnitude of the impedance is calculated as:

$$Z_0 = -\frac{1}{\omega C} \tag{2.10}$$

The phase angle is $\theta = -\pi/2$, i.e. the impedance depends on the frequency and is entirely imaginary [132], [133].

When considering a resistor and capacitor in series, impedance can be calculated as:

$$Z = R + \frac{1}{j\omega C} \tag{2.11}$$

Where the real part of Z, Z', is simply R and the imaginary part, Z", is 1/ωC. Plotting Z = Z' + Z" leads to the plot shown in Figure 2-8c [132], [134].

An example of the use of two components in series would be a non-faradaic process (previously discussed in section 1.3.1.1) Due to the lack of charge transfer, non-faradaic processes can contain as few as two components [132], [135] as shown in Figure 2-9.

1. The resistance of the electrolyte solution between the working and reference electrodes, R_s.
2. The electrochemical double layer, expressed as a double layer capacitance, C_{dl}

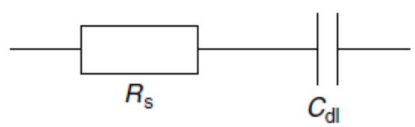

Figure 2-9 – Equivalent circuit for non-Faradaic impedance spectroscopy measurements in the absence of a redox probe [135].

A resistor and capacitor in parallel produces a semi-circle, as shown in Figure 2-8d. At high frequencies total impedance is zero. At low frequencies the impedance is purely resistive [132], [134]. Impedance can be calculated as:

$$\frac{1}{Z} = \frac{1}{R} - \frac{\omega C}{j} \qquad Z = \left(\frac{1}{R} - \frac{\omega C}{j}\right)^{-1} \tag{2.12}$$

The magnitude of the impedance is calculated as:

$$Z_0 = \left(\frac{1}{R^2} + \omega^2 C^2\right)^{-\frac{1}{2}} \tag{2.13}$$

The phase angle is:

$$\theta = \arctan(-R\omega C) \tag{2.14}$$

For a faradaic process, in this case an electrode process such as oxide film formation or the deposition and corrosion of metals, an electrochemical equivalent circuit should contain at least three components [60], [132].

1. The electrochemical double layer, expressed as a double layer capacitance, C_{dl}
2. The resistance of the charge transfer process, R_p
3. The resistance of the electrolyte solution between the working and reference electrodes, R_s

The simple model for characterising the metal-solution interface during a faradaic process, known as a 'Randle cell' and its equivalent Nyquist plot, is shown in Figure 2-10. Elements at the electrode-electrolyte interface are modelled in parallel because the total current is the sum of the individual contributions of the components, C_{dl} and R_p. All current must pass through the solution resistance, therefore, R_s is inserted into the equivalent circuit as a series to represent this effect [130], [132].

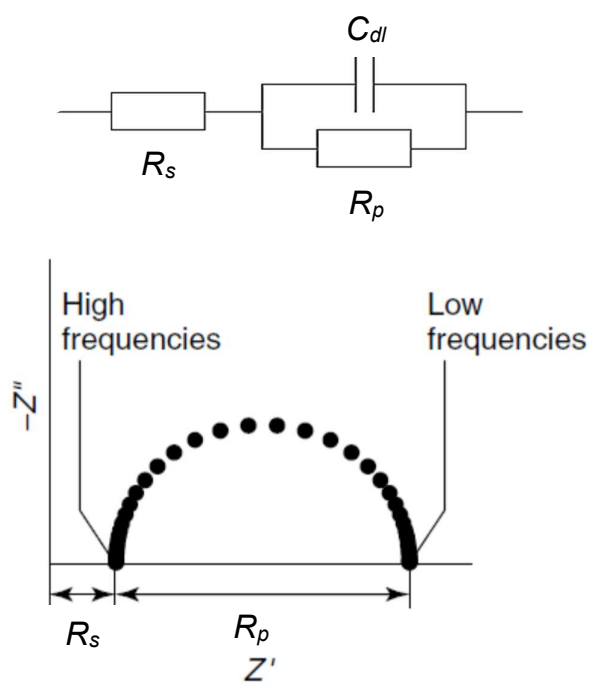

Figure 2-10 – Electrical equivalent circuit model and an example nyquist plot used to represent an electrochemical interface undergoing corrosion in the absence of diffusion control (Randle cell) [132].

Realistically, many equivalent circuit models possess more components and are more sophisticated than this, containing more than one Randle cell or many parallel branches.

Different electrode behaviours contain similar stages and processes, such as formation of the electrical double layer, charge transfer resistance of the electrochemical reaction, the presence of ohmic resistance, diffusion in solutions etc. The same equivalent circuit elements, but with different physical meaning, can simulate different processes occurring on the electrode.

Once an appropriate equivalent circuit model has been established, computer modelling software can be used to fit the equivalent circuit model to impedance data obtained in EIS experiments. Analysis using equivalent circuit models provides values for the electrical properties (R_s, C_{dl} and R_p) needed to characterise the metal-solution interface. The computer modelling software also calculates a 'goodness of fit', often this is the chi-squared (χ^2) statistical test, the sum of squares of differences between measured and modelled impedances. An ideal fit of the model to a dataset would result in a χ^2 statistic equal to 0. High χ^2 values suggest that the assumed equivalent circuit is not a good fit to the data [136].

2.2.2.3 EIS – Experimental Setup

EIS experiments were set up using the same 3 electrode cell, as previously described in section 2.2.1.1. However, the EIS experiments were performed using an Autolab PGSTAT20 potentiostat equipped with frequency response analyser modules, driven by GPES 4.9 and FRA 4.9 software (Eco Chemie, The Netherlands). All EIS measurements reported here were started at -0.5 V and were scanned up to 1.5 V. The potential was held every 0.1 V and the frequency scanned between 10,000-0.1Hz.

2.3 Electrochemical Quartz Crystal Microbalance (EQCM) Studies of the Passive Behaviour on SS2343 (316L Analogue) in Nitric Acid

2.3.1 Electrochemical Quartz Crystal Microgravimetry

In many electrochemical experiments, mass change occurs as material is deposited or stripped from the cell working electrode. Quartz Crystal Microgravimetry (QCM) is a well-established method for the measurement of small changes in mass at the electrode surface. QCM can also be used in combination with potentiostat controlled electrochemical measurements (EQCM) to measure mass changes associated with electrochemical processes such as, adsorption, electro-deposition and corrosion [55], [137].

Importantly, the EQCM has also been used to investigate passive film growth *in situ* on metallic surfaces [66], [67], [73], [138]–[140]. It provides information relating to the mass changes associated with film growth at the electrode surface with a time resolution sufficient to provide real time growth curves of the passive film, as established by Olsson *et al.* [68]. This makes microgravimetry useful in the study of the dynamic responses of passive metals and alloys to redox changes in the aqueous environment, particularly changed in response to solution oxidative stress or applied potential. For example, for a Fe-Cr alloy in an acidic electrolyte, shown in Figure 2-11, an increase in potential, either potentiostatically or via introduction of oxidising agents, leads to Cr enrichment within the passive film.

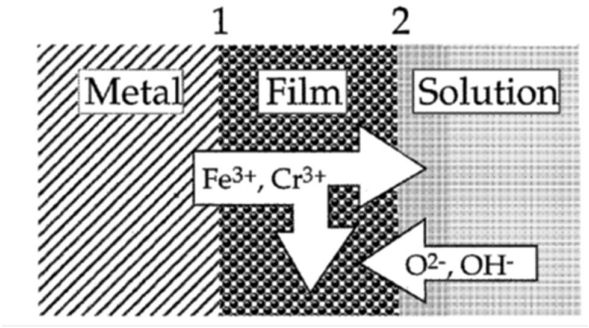

Figure 2-11 - Mass transfer during anodic film growth (example of binary Fe-Cr alloy) [66].

This implies either selective oxidation of chromium shown at interface 1 in Figure 2-11, or selective dissolution of Fe from the film into solution as shown in interface 2. Both processes would produce a similar increase in current in a standard LSV, making identification of which process was responsible for the current increase difficult. However, using the EQCM either a positive or negative mass change is observed depending on whether incorporation of anions into the anodic film or dissolution of the metal ions is dominating. It is important to note that while the EQCM provides additional data over LSV or CV techniques with regards to metal corrosion, the EQCM is not able to differentiate between the dissolution of the individual elements of an alloy, only the overall change in mass of the metal [73].

2.3.1.1 Principles

Microgravimetry is based on the inherent piezoelectric properties of quartz crystal. In 1880, Jacques and Pierre Curie discovered that a mechanical stress applied to the surfaces of various crystals, including quartz, afforded a corresponding electrical potential difference across the crystal. The magnitude of this potential difference is proportional to the applied stress, this is referred to as the 'piezoelectric effect'. The Curies also experimentally verified the 'converse piezoelectric effect' where an applied voltage across the crystal surface produces a corresponding crystal strain [98].

This forms the basis of the QCM technique [55], [141]–[143]. In QCM a piezoelectrode comprised of a thin quartz crystal sandwiched between two metal electrodes (as shown in Figure 2-12) is used. This deforms when an electric field is applied to it.

A) B)

Figure 2-12 - The two faces of a quartz piezoelectrode used in QCM experiments A) front face, consisting of the working electrode B) rear face, consisting of both electrode contacts, connects to the frequency counter [144].

Thus, by applying a small alternating voltage to the piezoelectrodes, highly stable oscillations are induced. The resonant frequency, f_o, of these oscillations can be shown to be linearly proportional to the total rigidly coupled mass of the crystal piezoelectode. Key to the QCMs function is that interfacial mass changes at the electrode surface can be related to changes in the quartz crystal oscillation frequency, (f_o). This relationship is typically expressed through the Sauerbrey equation [55], [145]:

$$\Delta f = \frac{-2f_o^2}{A\sqrt{\mu_q \rho_q}} \Delta m \tag{2.15}$$

Where Δf is the measured frequency shift (Hz), f_o is the frequency of the quartz crystal prior to the mass change (Hz), Δm is the mass change (g), A is the piezoelectrically active area (cm^2), $\Delta\rho_q$ is the density of the quartz (2.648 g/cm^2) and μ_q is the shear modulus (2.947×10^{11} g/cm^2).

The term $-2f_o^2/A(\mu_q\rho_q)^{1/2}$ in the equation above is usually abbreviated to a sensitivity constant, C_f.

$$\Delta f = C_f \Delta m \tag{2.16}$$

The value of C_f is usually determined experimentally by the electrochemical deposition and dissolution of a simple M/M^{n+} couple via cyclic voltammetry. Theoretically for a 5 MHz crystal this value should be 0.056 ng Hz^{-1} cm^{-2}. However, in practise this value may vary slightly due to small manufacturing defects between crystal batches. Thus, before doing any measurements with the QCM, the calibration factor was experimentally determined using the electrodeposition and stripping of a single couple such as Cu/Cu^{2+} or Ag/Ag^+. Here we have elected to use the Cu/Cu^{2+} system.

2.3.1.2 EQCM Calibration Using the Cu/Cu^{2+} Couple

The reduction of Cu^{2+} ions, leading to the deposition of a layer of Cu at the electrode surface, is commonly used for EQCM calibration [146], [147]. This is accomplished by obtaining the number of moles of electrons passed through the electrode surface from the CV current trace (charge passed) and comparing this to the simultaneously recorded frequency response (mass change). From these two results the mass sensitivity of the crystal can be determined [148]. These measurements were taken using the following procedure.

A solution of 10 mmol dm^{-3} copper (II) sulphate in 100 mmol dm^{-3} sulphuric acid was prepared in distilled deionised water. The solution was then degassed using nitrogen for 15 minutes so as to ovoid oxygen reduction interferences with the Cu^{2+} reduction current. A three electrode cell was employed featuring a platinum mesh counter with a Silver Chloride Electrode (Ag/AgCl). All potentials are referred to vs. SCE (-0.241 V vs. SHE). Using the QCM and combined potentiostat, a cyclic voltammogram (CV) and simultaneous voltamassogram (VM) were recorded. Figure 2-13 shows a typical CV and VM obtained under the conditions described above.

The data set presented in Figure 2-13 shows an anomalous peak on the reduction going sweep at ~0.22 V. This is believed to originate from a leaking Ag/AgCl electrode. The reaction $AgCl(s) + e^- \rightarrow Ag(s) + Cl^-(aq)$ has a standard electrode potential of 0.22V vs. SHE (0.02V vs Ag/AgCl) [57], this aligns with the onset of mass increase in Figure 2-13. The leak is not believed to have affected the EQCM calibration experiment.

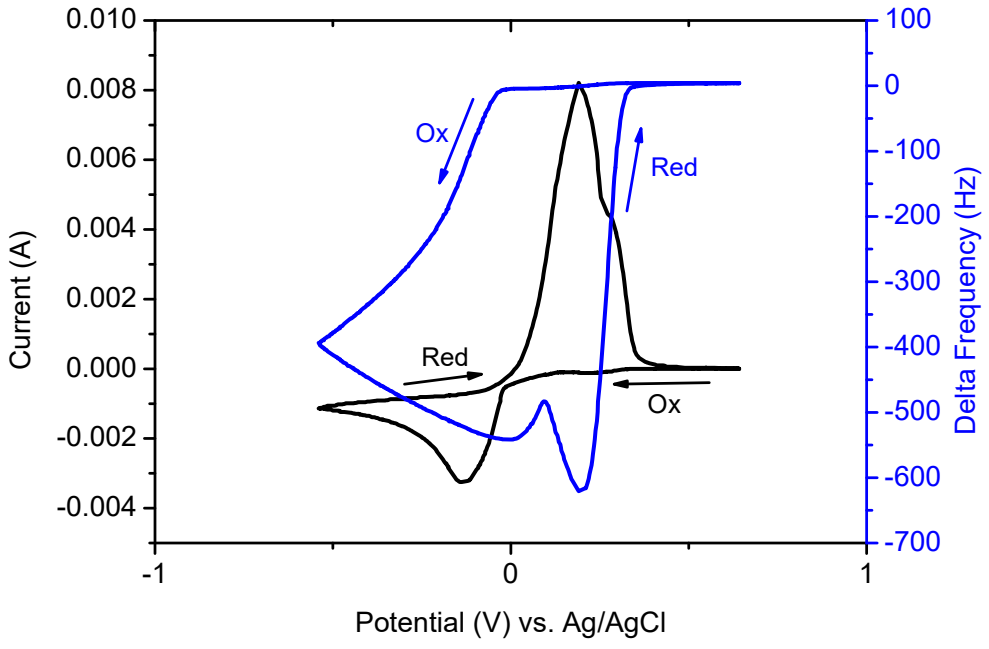

Figure 2-13 – Simultaneous CV and VM of a 10mmol dm^3 $CuSO_4$ and 100mmol dm^3 H_2SO_4 solution in distilled, deionised water recorded on an Au QCM crystal at 50m Vs^{-1}.

In order to determine the sensitivity of the QCM (as noted above), it is first necessary to calculate the number of moles of Cu electrochemically reduced at the electrode surface. This is then compared with

the frequency response data. The former is done by calculating the charge passed through the electrode during either the Cu metal deposition (cathodic current response in Figure 2-13) or dissolution (anodic current response in Figure 2-13) steps. The charge Q is calculated by integrating the current passed as a function of time:

$$Q = \int_0^t i(t) \tag{2.17}$$

Because the potential increment is small, it is possible to integrate this function into an Excel® spreadsheet using equation (2.18):

$$Q = \sum_j \left(\frac{i_j + i_{j-l}}{2} \right) \bullet \frac{\Delta E}{v} \tag{2.18}$$

Where Q is the total charge in C, i_j is the current for data point j in A, ΔE is the potential step in V, and v is the scan rate of the experiment in V s^{-1}.

During the reduction going sweep of Figure 2-13, the mass change is entirely due to the deposition of Cu metal. Therefore, dividing the value obtained for the charge passed by the Faraday constant F gives access to the number of moles of electrons used to reduce Cu^{2+} ions to Cu metal. As the reaction is a two-electron process, the mass of Cu deposited on the QCM electrode can easily be calculated using the atomic weight of Cu. Finally by dividing the calculated mass of Cu deposited on the electrode by the total frequency change recorded by the QCM gives the mass sensitivity of the crystal.

For the data set presented in Figure 2-13, the mass sensitivity calculated for all scans was found to be 0.059 ng Hz^{-1} cm^{-2}, the standard deviation being 6.1% wt., which is in good agreement with the theoretically predicted sensitivity constant of 0.056 ng Hz^{-1} cm^{-2}.

2.3.1.3 QCM – Experimental Setup

EQCM experiments were carried out using a quartz crystal microbalance from Maxtek (5980 Lakeshore Drive, Cypress, CA, USA) and a Q-Sense open module (Gothenburg, Sweden) with a combined Autolab PGSTAT20 potentiostat from Windsor Scientific Ltd and driven by GPES 4.9 software (Eco Chemie,

The Netherlands). QCM piezoelectrodes were left to equilibrate for 1 hour in air and then 1 hour in solution, at open circuit potential, prior to each electrochemical measurement. To prevent electromagnetic interference from the surroundings the electrochemical cell was placed in a Faraday cage. Current and mass-response profiles were always recorded simultaneously. After frequency equilibration, linear sweep voltammetry and potential step measurements were performed in 1.5 mL (1.5 cm^3) solutions of 5 – 35% wt. The current transients were compared to those for 316L SS to assess the suitability of SS2343 as an analogue. Previous work by Donik *et al* has shown 316L SS and SS2343 to have almost identical potentiodynamic/electrochemical properties [149].

2.3.1.3.1 Potential Step Studies

Using the EQCM, chronoamperometric-microgravimetric measurements were made by means of a potential 'staircase' experiment, Figure 2-14, in which the potential was stepped at 0.15 V intervals from an initial value of -0.2 to 1.15 V. At each step, *t*, on the 'staircase' the potential was held for 45 minutes and the resultant current transient and change in electrode mass was recorded.

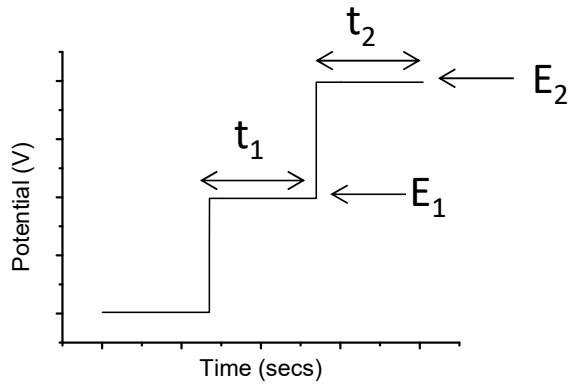

Figure 2-14 –Schematic showing the applied potential sequence. A potential (E_1) was applied for a time (t_1) then stepped to a higher potential (E_2) to a time (t_2).

2.4 Hydrodynamic Studies on Stainless Steels in Nitric Acid

2.4.1 The Rotating Disk Electrode

In the absence of fluid turbulence, mass transfer can be accomplished in three different ways [150]:

1. Migration – the movement of charged particles in an electric field
2. Diffusion – the movement of species against a concentration gradient
3. Convection – the movement of species induced by stirring or a density gradient

The effects of migration can be discounted in the experiments reported here because the concentration of the supporting electrolyte (in this case HNO_3) is sufficiently high to negate any effects of migration in the electrolyte [151], [152]. The effects of convection, which is deliberately introduced to the system in Rotating Disk Electrode (RDE) studies, are discussed below.

A RDE is a hydrodynamic working electrode. The electrode rotates during experiments inducing a flux of analyte to the electrode surface. Hydrodynamic working electrodes are used in electrochemical studies when investigating reaction mechanisms related to the coupling of redox chemistry to mass transfer and preceding or following chemical steps [153]. The main advantage of hydrodynamic electrodes over static electrodes is that steady state can be reached readily and measurements can be made with high precision, i.e the increased transport of electroactive species to the electrode, leads to a higher recorded current and therefore greater sensitivity and reproducibility [55], [60].

The rotation of a rotating disk electrode is expressed in terms of angular velocity (rad s^{-1}), or, more commonly, full rotation per second (s^{-1} or Hz) or rotation speed (where 1 Hz equates to 2π rad s^{-1} [154]). As the disk turns it acts as a convective pump, drawing solution up towards the electrode surface. The result is a laminar flow of solution towards and across the electrode. The rate of the solution flow can be controlled by the electrode's rotation speed and can be modelled mathematically. This flow can quickly achieve conditions in which the steady-state current is controlled by the solution flow and so convectively assisted mass transport to the electrode surface. This is another advantage over static experiments where

the sole mode of mass transport supporting the steady-state current is the slower non-convectively assisted diffusion [60], [153].

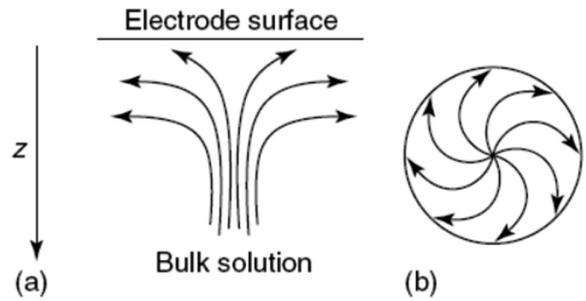

Figure 2-15 -Solution flow for RDE (a) along z-axis and (b) near disc surface [153].

Even when the electrode is rotating, near the electrode surface there is a thin diffusion layer of electrolyte in which there is no tendency for movement normal to or across the electrode (see Figure 2-15). Here, the only means of mass transport is diffusion across this so-called "diffusion layer". The thickness of this layer, δ. varies inversely with rotation speed and is given by [153]:

$$\delta = 0.643 D^{1/2} v^{1/6} \omega^{-1/2} \tag{2.19}$$

Where D is the diffusion coefficient, ω is the rotation speed (Hz) and ν is the kinematic viscosity ($cm^2\ s^{-1}$) i.e. the viscosity divided by the density.

The advantages of using electrodes with controlled hydrodynamics over static electrodes may be more easily understood by considering the general scheme for electrochemical reactions:

$$R_{bulk} \xrightarrow[k_{mt}]{} R_{surf} \xrightarrow[k_e \pm ne^-]{} Pn^-/n^+ \tag{2.20}$$

Where R is the reactant which is converted to the product, P at an electrode surface by accepting or donating electrons (i.e. reduction or oxidation). The overall reaction requires mass transport of R from the bulk of the solution to the electrode, the rate of which can be considered to be governed by a first order rate constant k_{mt} in cm s^{-1}. The rate of mass transfer is then given by the flux of species to the electrode surface (mol $cm^{-2}\ s^{-1}$), j_{mt} [153]:

$$j_{mt} = k_{mt}(c_\infty - c_0) \tag{2.21}$$

Where c is the concentration, mol cm^{-2}, of R in the bulk (at near infinite distance from the electrode) or at the electrode surface (at distance, 0 cm, from the electrode). When the rate of mass transport is relatively slow (i.e. the electrode is not rotating) and, therefore, rate limiting, the overall flux is given by:

$$j_{mt} = k_{mt}c_\infty \tag{2.22}$$

At the electrode, the electrochemical reaction then occurs governed by the first-order electrochemical rate constant k_e. Under steady state conditions, the electrochemical flux is equal to the overall flux, that is:

$$j_e = k_e c_o = j = j_{mt} \tag{2.23}$$

In a simple voltammetric experiment, reproducible currents can only be obtained in systems in which k_{mt} and k_e can be controlled. k_e is easily controlled by controlling the electrode potential. However, in stagnant solutions k_{mt} is not constant and is time dependant. The extent of which the reactant has depleted near the electrode governs the rate of mass transfer and therefore mass transfer is time dependent. This leads to irregular, unpredictable currents. Hydrodynamic electrodes generate reproducible and predictable solution convection currents through mechanical stirring.

Thus, by running linear sweep voltammetry and other experiments at various rotation rates, different electrochemical phenomena can be investigated, including multi-electron transfer, the kinetics of a slow electron transfer, adsorption/desorption steps, and electrochemical reaction mechanisms.

2.4.2 Construction of a Stainless Steel Rotating Disk Electrode

Generally an RDE is constructed by imbedding the working electrode as a rod of material in Teflon, epoxy resin or another plastic. This construct is then attached to a motor directly by a chuck and is rotated at certain frequency, ω (revolutions per second) [55], as shown in Figure 2-16.

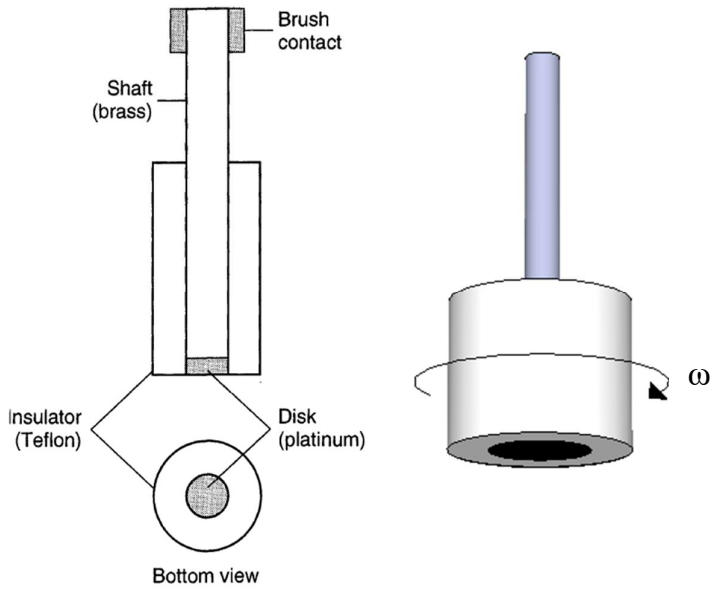

Figure 2-16 – Schematic of a rotating disk electrode [155].

For the work described here, the steel RDE was constructed using a cylindrical brass section as its core. A 10 mm diameter circular stainless steel tip (316L, Advent Research Materials Ltd, Eynsham, Oxford, UK) was attached to the brass section using a silver loaded epoxy adhesive (Stock no. 186-3616, RS Components Ltd, Corby, Northhants, UK). The entire electrode was then sealed in a resin layer (HY1300 and CY1300, Aeropia Ltd, Newton Road, Crawley, UK) moulded into a cylindrical shape (Figure 2-17). Finally the stainless steel tip was polished using a series of abrasives with decreasing size/grade of grit. Specifically, sandpaper grades 240-1200 and diamond abrasive compounds (Marcon, Codicote, Hitchin, Herts, UK) of 6 and 1 micron.

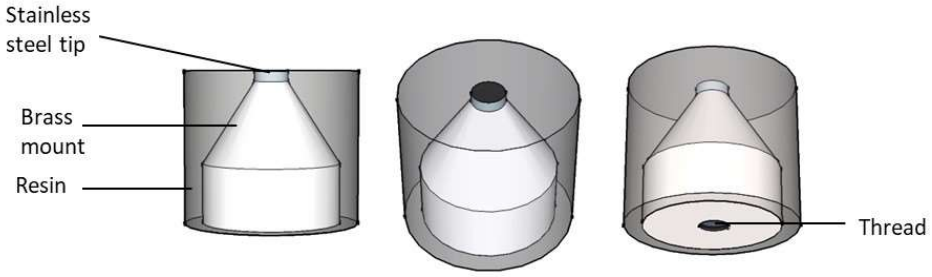

Figure 2-17 – Diagrammatic representation of a 316L SS rotating disk electrode.

2.4.3 Levich Study on 316L SS Rotating Disk Electrodes

A Levich-type experiment was conducted using an Autolab PGSTAT20 potentiostat. Rotation speed was controlled by a rotating disk electrode rotator controller (Princeton Applied Research, Farnborough, UK). As before, the stainless steel rotating disk working electrode pre-treatment consisted of polishing on emery paper up to 1200 grade followed in turn by polishes using 6 and 1 micron diamond paste. The electrodes were then degreased in acetone and rinsed with purified water. The RDE was used in a three electrode system with a platinum mesh auxiliary and SCE reference electrode, as shown in Figure 2-18.

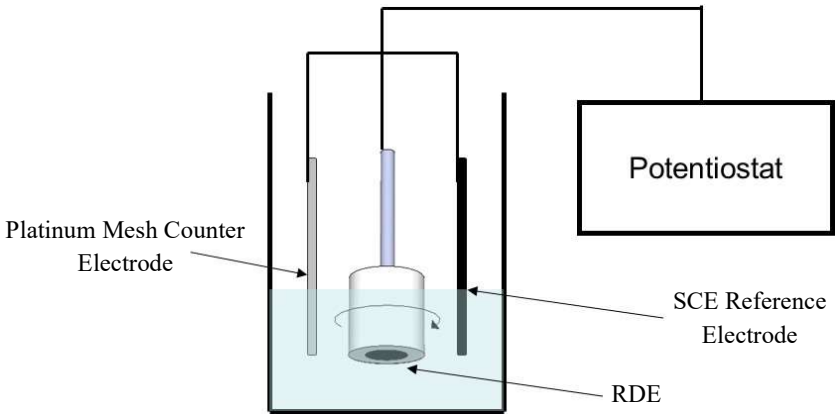

Figure 2-18 –Schematic of RDE experimental setup.

Before the Levich experiment was conducted, the open circuit potential of the system was monitored until it reached steady state (approximately 1 hour). Potential was then swept, at a scan rate of 10 mV s^{-1}, from 1 V down to the potential of interest (see Chapter 4). This potential is within the transpassive region for the 316L SS however the focus of this experiment was not the corrosion behaviour of stainless steel, but the reduction chemistry of HNO_3. The potential was then held whilst the rotation of the electrode was varied from 100-3000 rpm. The current was recorded and allowed to stabilise for 5 minutes at each rotation speed before the rotation speed was increased.

2.5 Surface Analysis Studies of Stainless Steel Oxide Layers

2.5.1 X-ray Photoelectron Spectroscopy

2.5.1.1 Introduction

X-ray Photoelectron Spectroscopy (XPS), also known as Electron Spectroscopy for Chemical Analysis (ESCA) is a widely used surface analysis technique. XPS utilises x-ray photons to ionise surface atoms. When an atom absorbs an X-Ray photon, an electron can be ejected (Figure 2-19b). The kinetic energy (KE) depends on the photo energy (hv) and the binding energy (BE) of the electron (the energy required to remove the electron from the surface). Measuring the kinetic energy of the so-liberated electron provides information on: (1) the oxidation state of an element/elements, (2) the chemical state of a metal/metal oxide film and (3) the elemental profile through a material. A general schematic of XPS is shown in Figure 2-19a [156].

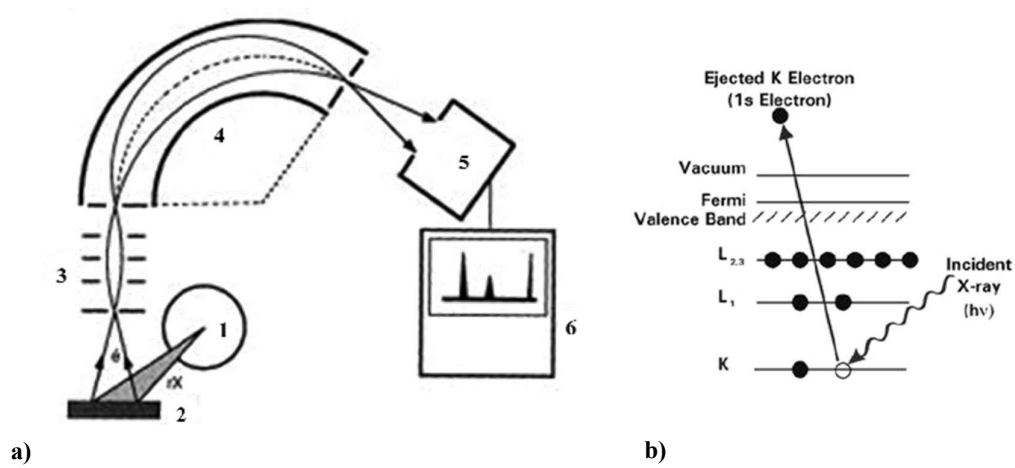

Figure 2-19 – a) Schematic of X-Ray photo electron spectroscopy showing (1) X-ray source, (2) sample, (3) electronic focusing system, (4) spectrometer, (5) electron detector or channeltron and (6) data acquisition system. b) The photoemission process involved for XPS surface analysis. The discs represent electrons and the bars represent energy levels within the material being analysed.[156]–[158].

In the analytical chamber the specimen (2) is bombarded by the x-ray photon source (1) and the ejected photoelectrons are focused on to the entrance slit of an electrostatic analyser by an electromagnetic lens system (3). The ejected electrons then pass through the analyser. Within the analyser, electrons pass between a pair of electrodes. Between the electrodes and the electrons is a series of lenses, which are used to reduce the kinetic energy of the electrons, only electrons of a specific energy are allowed to pass through to the detector, the 'pass energy', PE. (4). The electrons then arrive at the detector and are counted using an electron multiplier, usually a channel electron multiplier (channeltron) (5) [159], [160].

2.5.1.2 Sample Preparation

Surface passivation was induced by electrochemical polarisation of stainless steel planchet samples in an electrolyte consisting of 5% wt. and 25% wt. HNO_3. In order to determine the interaction of europium (analogue for americium), cerium (analogue for plutonium) and uranium with stainless steel sample, passivation experiments were also performed in solutions of 1 mmol dm^{-3} europium (III) nitrate, 30 mmol dm^{-3} cerium (III) nitrate hexahydrate or 10 mmol dm^{-3} uranyl nitrate, at both 5 and 25% wt. nitric acid concentrations. All solutions were degassed using nitrogen for 15 minutes prior to use.

Polarisation measurements were performed using an Autolab PGSTAT20 potentiostat and three electrode cell detailed previously. As described for LSV experiments in section 2.2.1.1, polished 316L stainless steel planchets were placed in a QCM electrode holder so that only the electrode face was exposed to solution. These were prepared prior to use by rinsing the steel with acetone to remove any organic contaminants. Polarisation was performed at 0.2, 0.5 and 0.8 V vs. SCE respectively, for 20 min. After polarisation, the samples were taken out of solution with the potential switched on and quickly dipped in deionised water before immediately drying using nitrogen gas. Samples were then rapidly transferred to the ultrahigh vacuum chamber necessary to perform XPS in order to minimise the effects of environmental oxidation of the steel surface.

2.5.1.3 Typical XPS Analysis Scheme

X-ray photoelectron spectroscopy (XPS) analysis was carried out at the Nanotechnology & Integrated BioEngineering Centre (NIBEC) at the University of Ulster and the Surface Interface Analysis Centre at

the University of Bristol. At the University of Ulster, XPS analysis was performed on 316L SS after polarisation of the electrode in HNO_3 concentrations of 5 and 25% wt. at 0.2 and 0.8 V vs. SCE. 316L SS was also analysed after being exposed to europium (III) nitrate and cerium (III) nitrate solutions under the same conditions. At the University of Bristol, XPS analysis was performed on 316L SS after polarisation in 5 and 25 wt. % wt. HNO_3 at 0.2, 0.5 and 0.8 V vs. SCE as this was considered a more representative range for analysing compositional changes in the passive film. 316L SS samples were also analysed after being exposed to uranyl nitrate solutions under the same conditions.

2.5.1.3.1 XPS Analysis Scheme at the University of Ulster

XPS was carried out using a Kratos Axis Ultra DLD spectrometer (Kratos, UK) at $<5 \times 10^{-8}$ Torr. Measurements were made using a monochromated Al Kα X-ray (1486.6 eV) source operating at an anode voltage of 15 kV and current of 10 mA. A magnetic immersion lens was used to neutralise charging effects. Binding energy (BE) positions were calibrated to hydrocarbon (C1s) signal, set at 285.00 eV [161]. Initial wide energy survey scans (1–1300 eV) were recorded at a pass energy of 160 eV with subsequent high resolution spectra recorded at 20 eV.

Quantitative analysis of three separate areas of each sample type, reported as relative atomic percentage (at.% wt.), was achieved using CasaXPS software (Casa software, UK) after subtraction of a linear background. Spectra were curve fitted after linear background subtraction using a mixed Gaussian–Lorentzian (70:30) function [162].

2.5.1.3.2 Analysis Scheme at the University of Bristol

A Thermo Fisher Scientific (East Grinstead, UK) Escasope equipped with a dual anode X-ray source (AlKα 1486.6 eV and MgKα 1253.6 eV) was used for XPS analysis. Samples were analysed under high vacuum ($<5x10^{-8}$ mbar) with AlKα radiation at 250W (12.5 kV; 20 mA). Following the acquisition of survey spectra over a wide binding energy range, the C1s, O1s, Cr2p and Fe2p3 spectral regions were then scanned at a higher energy resolution such that valence state determinations could be made for each element. High resolution scans were acquired using 100 eV pass energy and 750 ms dwell times.

Data analysis was carried out using CasaXPS software (Casa software, UK) after subtraction of a linear background. Spectra were curve fitted after shirley background subtraction using a mixed Gaussian–Lorentzian (70:30) function [162].

Shirley background subtraction requires choosing two points, one at a kinetic energy and another below the peak. This leads to a simple, iteratively calculated background in which the background intensity at a given energy is directly proportional to the intrinsic peak area at the high kinetic energy side [163], [164].

The data collected at the University of Bristol appears to be contaminated (this was confirmed by Bristol University, although the source of contamination is unknown). Elements such as lead and fluorine were found to be present which was unexpected. This will be taken into account during analysis.

2.5.1.4 XPS Limitations

While XPS is a widely used technique there are limitations to its use [160], [165], [166]:

- XPS equipment requires specialist training and years of experience in its use.
- XPS requires an Ultra High Vacuum (UHV), typically in the range of 10^{-8} – 10^{-10} Torr.
- The lateral resolution is limited to a range of a few to 100µm.
- Sample size is restricted to a few cm^2 and a few mm thick. Although, in some cases, e.g. radioisotope contamination studies, where there may be other restrictions (dose etc.), a small sample size is of benefit as only a small amount of material is required for analysis.
- Depth resolution is only a few (~5) nm. Again, this could be regarded as advantageous in thin film studies, such as those carried out in this work.
- XPS detection limits range from 0.1 to 1 atom % [167]. Figure 2-20, overleaf, shows how this relates to other spectroscopic techniques.

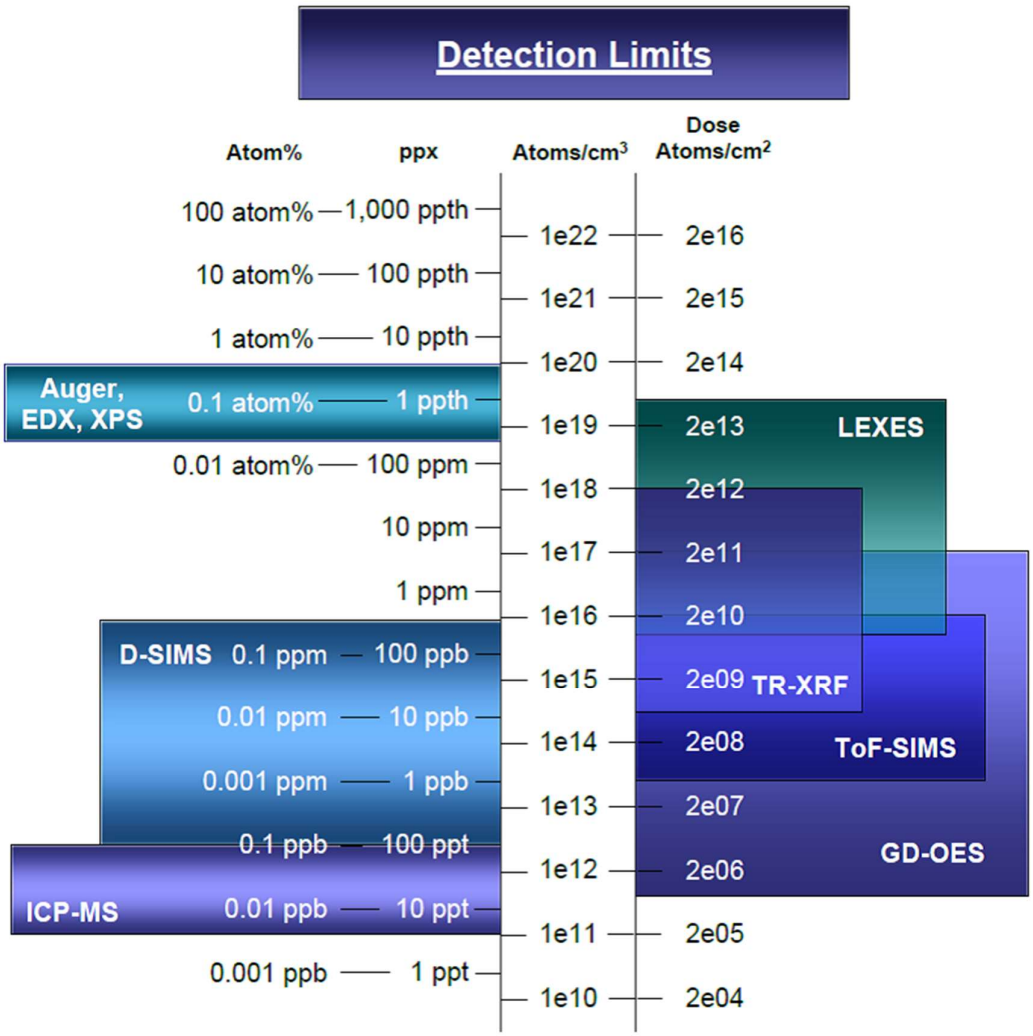

Figure 2-20 – Detection limits of different Spectroscopic Techniques [168].

Chapter 3

Electrochemical, Microgravimetric and Surface Characterisation of 316L Stainless Steel Behaviour in Nitric Acid ≤15% wt.

3 ELECTROCHEMICAL, MICROGRAVIMETRIC AND SURFACE CHARACTERISATION OF 316L STAINLESS STEEL BEHAVIOUR IN NITRIC ACID CONCENTRATIONS ≤15% wt.

This work is primarily interested in entrainment of radionuclides in steel under conditions typical of those found in nuclear reprocessing. However, an investigation into the baseline mechanistic changes of the corrosion behaviour of process steels in varying HNO_3 concentrations and in the absence of potential contaminant radionuclides may, in itself, lead to a better understanding of how steels passivate/freely corrode in HNO_3 – and therefore uncover the processes by which contaminants may become trapped. Furthermore, as described in Chapter 1, whilst the electrochemical reduction of HNO_3 on inert electrodes, such as Pt, is well understood [6], [7], [87], [89]–[91], [8], [80]–[86] the electrochemical reduction of HNO_3 concentration > 5% wt. (>1.13 mol dm^{-3}) has not been extensively explored on 316L SS.

As such, this chapter focuses on baseline electrochemical experiments conducted on 316L SS in HNO_3 concentrations ≤15% wt. (≤3.38 mol dm^{-3}), typical of HNO_3 concentrations found in primary separation cycles and fission product scrubbing [19].

3.1 Linear Sweep Voltammetry

In order to provide a preliminary assessment of what effect 'low' HNO_3 concentrations (for the purposes of this work, this is defined as $[HNO_3] \geq 5\%$ wt. but $\leq 15\%$ wt.) have on the electrochemical behaviour of 316L SS, linear sweep voltammetry was used to identify the point at which the steel corrodes, passivates and then transpassively dissolves in increasing HNO_3 concentrations, for the purpose of this work, this is defined as $[HNO_3]$.

Figure 3-1 shows the measurements from LSV experiments for 316L SS electrodes recorded in solutions with HNO_3 concentrations ranging from 5 – 15% wt. (1.13 – 3.38 mol dm^{-3}) over the potential range -0.5 – 1.5V.

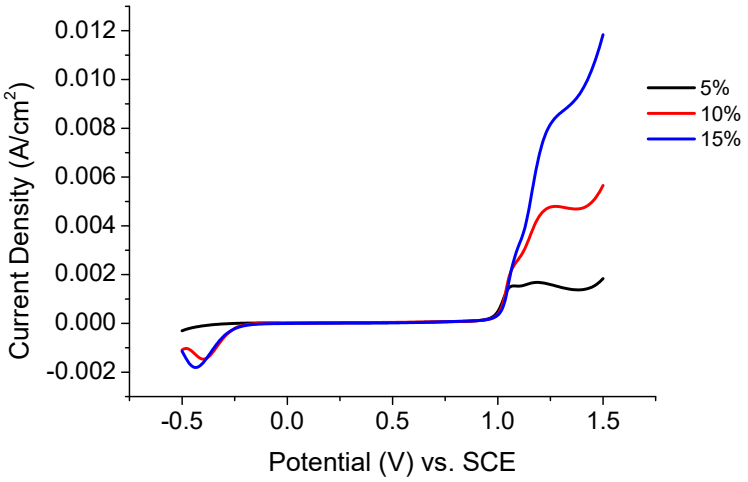

Figure 3-1 – Linear Sweep Voltammograms for 316L SS in 5-15% wt. HNO_3 at room temperature (20 ±2°C). Plots were measured in the potential range -0.5 to 1.5 V (sweep rate, 10 mV s^{-1}).

The change in behaviour with increasing HNO_3 concentration is seen in Figure 3-1. However, more information can be gathered from these measurements when the log of the current density is plotted against potential. Figure 3-2a shows potentiodynamic polarisation curves (log current density plotted against potential) for 316L SS electrodes recorded in solutions with HNO_3 concentrations ranging from 5 – 15% wt. (1.13 – 3.38 mol dm^{-3}) over the potential range -0.5 – 1.5V.

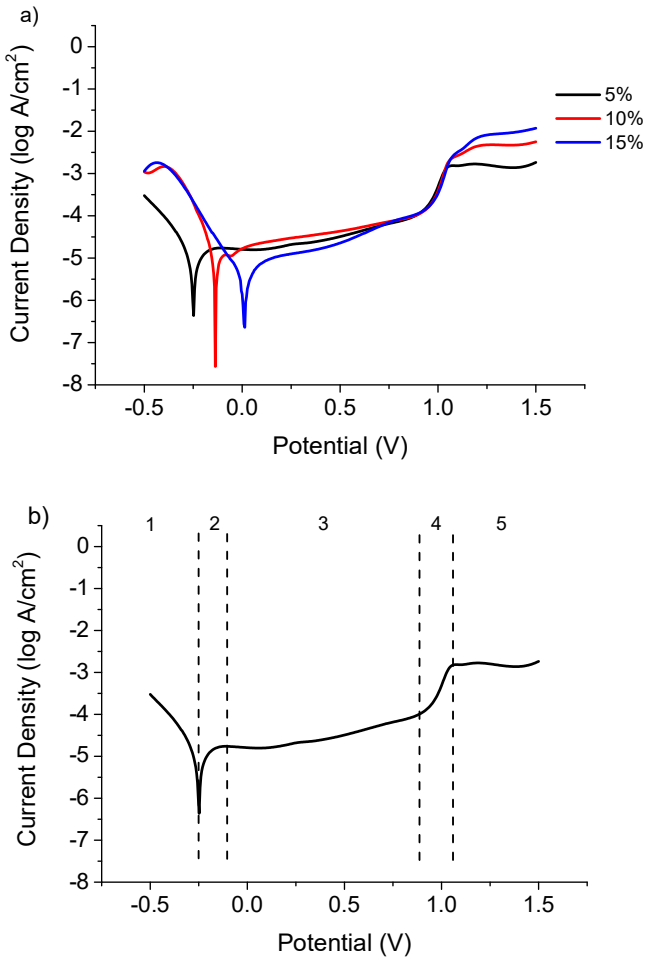

Figure 3-2 - a) Potentiodynamic polarisation curves for 316L SS in 5-15% wt. HNO_3 at room temperature (20 ±2°C). Plots were measured in the potential range -0.5 to 1.5 V (sweep rate, 10 mV s^{-1}) b) Polarisation curve for 5% wt. HNO_3, zones 1-5 are described in text.

From Figure 3-2a it can be seen that five distinct regions may be identified at all HNO_3 concentrations studied which, for the sake of illustrative clarity, are indicated on the annotated curve recorded at 5% wt. nitric acid, Figure 3-2b. These regions correspond to (1) hydrogen evolution/water reduction (2) active dissolution/onset of passivation, (3) passivity, (4) transpassive dissolution and (5) secondary passivation. Region 5 is a region that has been previously described by Betova [74] as being associated with the formation of a supplementary Fe(III) rich oxide layer, before oxygen evolution at ~1.3 V [169].

Returning to Figure 3-2a it can be seen that the corrosion potential (E_{corr}) gradually increases between 5 and 15% wt. (1.13 and 3.38 mol dm^{-3}) HNO_3. This could be due to a greater availability of H^+ for reduction to H_2 at the higher acidities or increased prevalence of HNO_2 reduction. The latter may be

explained as follows. According to Fauvet *et al.* and as discussed in detail in section 1.3.4 above, the corrosion potential of the 316L SS surface in the presence of HNO_3 is controlled by the concentration of HNO_2, present as a result of the thermal decomposition of HNO_3 and disproportionation of NO_2 [77], [78]:

$$4HNO_3 \rightleftarrows 4NO_2 + 2H_2O + O_2 \tag{1.12}$$

$$2NO_2 + H_2O \rightleftarrows HNO_2 + HNO_3 \tag{1.13}$$

Thus, HNO_2 is available to interact with the steel surface, as shown by reaction 1.22) [6]:

$$HNO_{2(el)} + H^+ + e^- \rightleftarrows NO_{ads} + H_2O \tag{1.22}$$

An increase in HNO_3 concentration results in the observed slow increase in corrosion potential, as the availability of HNO_2 for reaction 1.22 increases, resulting in further electron transfer from the steel.

Considering now the anodic end of the polarisation curve of Figure 3-1a, once the metal has entered the transpassive dissolution region, ~0.9 V to ~1 V. The absolute current increases with increasing HNO_3 concentration. This is likely due to the increased availability of HNO_3 increasing the acidity of the solution, driving the rapid transpassive dissolution of the Cr(III) rich passive film which has been oxidised to the more soluble Cr(VI). The increased acidity is also likely to inhibit secondary passivation of Fe_2O_3, this is described in more detail below.

Moving further anodically into the region of secondary passivation (~1.1 V), from Figure 3-2a it can be seen that such passivation is most quickly established in 5% wt. HNO_3, occurring at E >1 V and log i > -3. At 10% wt. HNO_3 the system fully passivates at both a higher potential, E> 1.2 V, and a higher transpassive current, log i > -2.5. This suggests that the onset of secondary passivation is restricted, presumably through the increased solubility of Fe_2O_3 with increasing HNO_3 concentration. This trend is continued at 15% wt. HNO_3 where full passivation is only achieved at E>1.3 V and log i > -2.

3.1.1 E_{corr} and i_{corr} Analysis.

Corrosion potential (E_{corr}) and corrosion current density (i_{corr}) were calculated using Tafel extrapolation of the linear segments of the measured potential-current density curves of Figure 3-2a, in the vicinity of

E_{corr}. E_{corr} and i_{corr} are dependent on the autocatalytic reduction of nitric acid and increased availability of HNO_2, as described above or the greater availability of H_2. Both E_{corr} and i_{corr} are known to increase with higher autocatalytic contribution via reactions 1.22 and 1.29 (which increases with increasing HNO_3 concentration), which together describe the global reduction of HNO_3 [157]:

$$HNO_3 + 2NO_{ads} + H_2O \rightleftarrows 3HNO_{2(el)} \tag{1.29}$$

Figure 3-3a shows calculated E_{corr} values obtained at 5 - 15% wt. HNO_3 concentrations. From which it can be seen that E_{corr} increases near linearly with HNO_3 concentration.

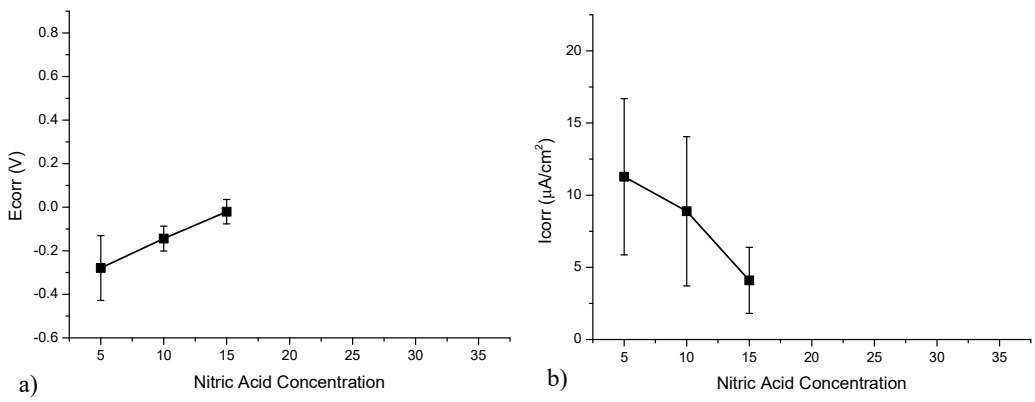

Figure 3-3 - a) Corrosion potential, E_{corr}, values vs. HNO_3 concentration b) Corrosion current density, i_{corr}, values vs. HNO_3 concentration and associated error bars calculated from Figure 3-2a for 316L SS in 5 - 15% wt. nitric acid. NOTE: Higher concentrations of HNO_3 have been left on the x-axis and will be filled in in Chapter 4.

Figure 3-3b shows the i_{corr} values for 5 – 15% wt. HNO_3. At the HNO_3 concentrations seen here, i_{corr} values decrease. The decrease in i_{corr} suggests the formation of a stable passivating oxide film which then reduces the availability of surface sites for reaction (1.22). This is consistent with the observed increase in E_{corr}, into the passive potential range of Figure 3-2b. This, in turn, suggests that system behaviour is governed by the coupling of the steel surface oxidation and nitrous acid catalysed nitric acid reduction half reactions. As HNO_3 concentration increases, H^+ or NO_3^- reduction also increases leading to an increase in E_{corr}, a greater extent of stainless steel oxidation and the formation of a thicker passive layer, leading to a lower i_{corr} at equilibrium.

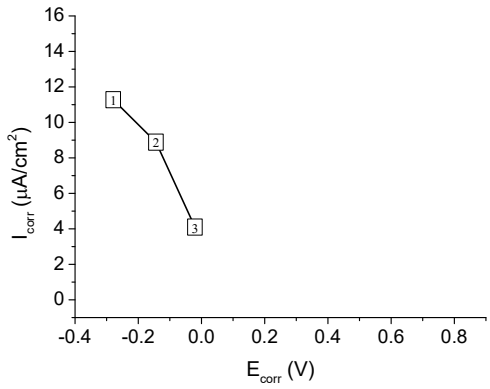

Figure 3-4 - i_{corr} vs. E_{corr} (data points minus error bars for clarity) calculated from LSV results in Figure 3-2a for 316L SS in 5 - 15% wt. (1-3 respectively) nitric acid. NOTE: Higher concentrations of HNO_3 have been left on the x-axis and will be filled in in Chapter 4.

Figure 3-4 shows a plot of i_{corr} vs. E_{corr} values calculated from LSV results of Figure 3-2a and initially shown in Figure 3-3. As discussed above, i_{corr} decreases as E_{corr} increases into the passive potential region. This shift into the passive region leads to a greater extent of stainless steel oxidation and the formation a thicker passive layer which, in turn, leads to a reduced i_{corr}. Thus, overall, corrosion rate counter-intuitively decreases with increase in HNO_3 concentration in the range of 5-15% wt. This behaviour will be further examined below using other electrochemical techniques such as; Electrochemical Impedance Spectroscopy and Electrochemical Quartz Crystal Microgravimetry.

In summary, i_{corr} decreases with an increase in HNO_3 concentration as E_{corr} increases with an increase in HNO_3 concentration. This indicates that the increase in HNO_3 is allowing for higher cathodic currents to be accessed, either via H^+ or NO_3^- reduction which, through galvanic coupling, allows for higher anodic current to be supported. This leads to an E_{corr} that resides deeper into the passive range and, in turn, thicker passive layers and lower i_{corr} values at equilibrium. The increase in HNO_3 is leading to an increase in E_{corr}, which moves the system further into the steel's passive region.

Importantly, the LSV results indicate that in order to artificially 'grow' oxide layers on 316L SS surfaces in HNO_3 concentrations of ≤15% wt. the applied potential needs to be <1 V to avoid transpassive dissolution of the Fe-Cr oxide film, and >-0 V to allow passivation to occur. Thus, differences in oxide layer growth modes in the passive region as a function of HNO_3 concentrations are now investigated in further detail using Electrochemical Impedance Spectroscopy.

3.2 Electrochemical Impedance Spectroscopy (EI S) Studies on 316L SS in Nitric Acid

EIS is a very useful technique when assessing small changes at the metal solution interface which may indicate passive film growth. 316L SS was analysed in the same potential region (-0.5 to 1.5 V vs. SCE) and HNO_3 concentrations (5-15% wt.) as the LSV studies in the previous section to allow for direct comparison with these results. Results detailed in this section are first presented using the raw experimental data, in the form of nyquist plots and E vs. Z' plots, at low frequencies. The data is then modelled using physically relevant equivalent circuits in Z-View2 impedance software, with the results presented alongside LSV results from the previous section. Z-View2 is based on the method of nonlinear least squares, which allows non-ideal electrochemical behaviour (elements that exhibit a combination resistive, capacitive or inductive behaviours) to be modelled [170], [171].

3.2.1 Nyquist Plots

Figure 3-5 to Figure 3-7 shows Nyquist plots for 316L SS in 5-15% wt. HNO_3, at potentials across the entire LSV range (-0.4 V, 0 V, 0.4 V, 0.8 V and 1.2 V).

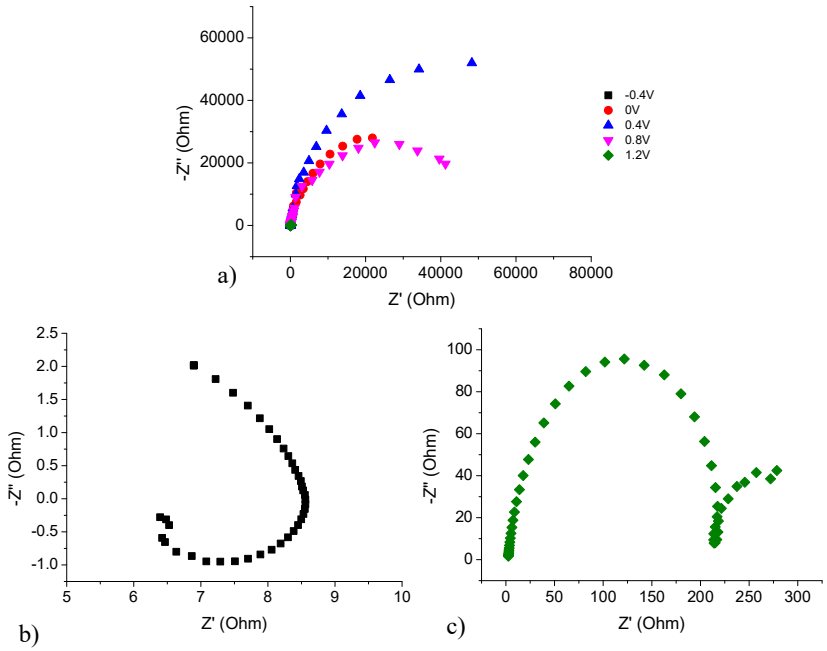

Figure 3-5 – Nyquist plots for 316L SS in 5% wt. HNO_3 solution at a) -0.4-1.2 V, b) -0.4 V and c) 1.2 V. -0.4 V and 1.2 V have been extracted for clarity. Axis scales have been altered to maximise variability visibility.

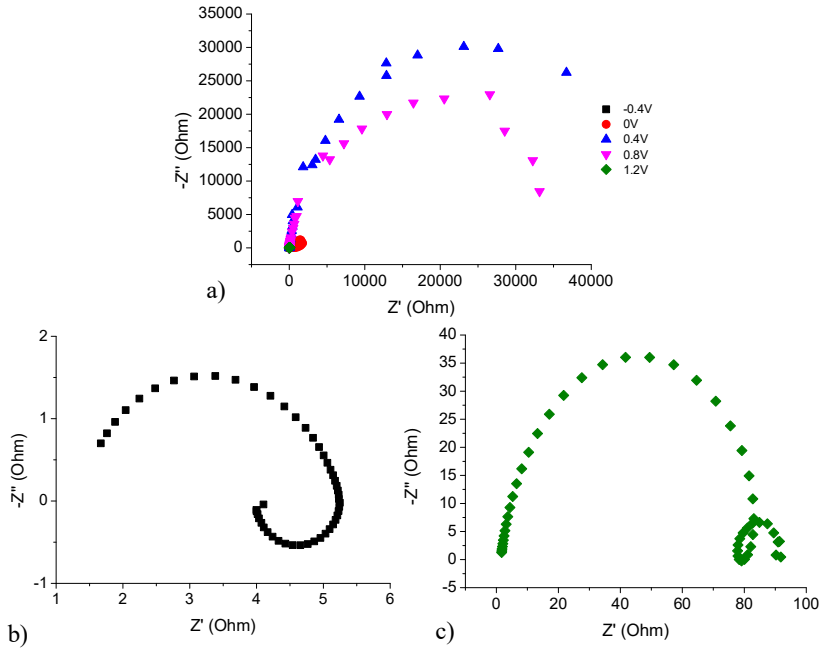

Figure 3-6 – Nyquist plots for 316L SS in 10% wt. HNO_3 solution at a) -0.4-1.2 V, b) -0.4 V and c) 1.2 V. -0.4 V and 1.2 V have been extracted for clarity. Axis scales have been altered to maximise variability visibility.

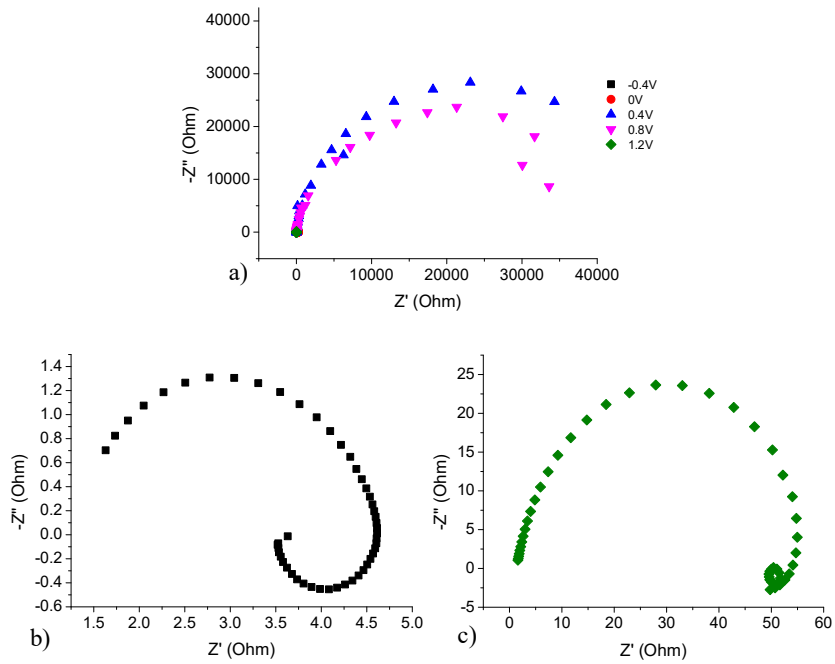

Figure 3-7 – Nyquist plots for 316L SS in 15% wt. HNO_3 solution at a) -0.4-1.2 V, b) -0.4 V and c) 1.2 V. -0.4 V and 1.2 V have been extracted for clarity. Axis scales have been altered to maximise variability visibility.

As discussed in Chapter 2, the resistive elements in the equivalent circuit can be estimated from the values at which the Nyquist plot crossed the real impedance axis (Z`). At potentials of -0.4V and 1.2V, representative of areas of hydrogen evolution and transpassive dissolution respectively, real impedance values are estimated to be very low, indicating the surface of the steel is freely reacting/dissolving. This is in line with equivalent LSV measurements shown in Figure 3-2a. At potentials within the passive region, 0V, 0.4V and 0.8V, impedance values are several orders of magnitude higher, indicating that a passivating film has formed on the steel surface, again in line with the LSV measurements of Figure 3-2a. However, at HNO_3 concentrations 10 and 15% wt. real impedance values at 0V are significantly lower than at 5% wt., as shown in Figure 3-8. LSV measurements indicate that 0V should still be within the passive range for 5% wt. HNO_3, at the onset of passivity for 10% wt. HNO_3 and just within the range for H_2 evolution for 15% wt. HNO_3 Thus, this decrease in real impedance values could be due to either an increase in H_2 evolution with increasing HNO_3 concentration or due to the surface being in the active corrosion region, although E_{corr} is below 0 V at 15% wt. HNO_3. This will be discussed further in Section 4.2.1.

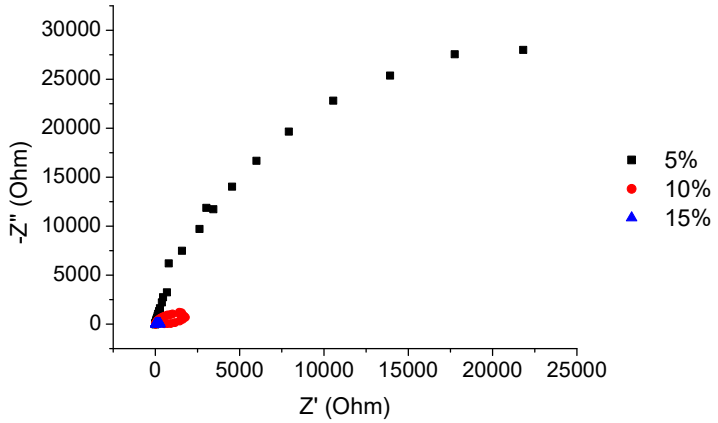

Figure 3-8 - Nyquist plots for 316L SS in 0-15% wt. HNO_3 solution at 0 V which has been extracted for clarity. Axis scales have been altered to maximise variability visibility.

Figure 3-9 shows the Nyquist plots for measurements within the range 0V to ~1V, which was identified in earlier experiments as the passive region and is described in section 3.1. Generally this region is characterised by higher impedance values than that which obtain under conditions of hydrogen evolution or transpassive dissolution. Impedance is highest at 0.4 and 0.6 V in 5% wt. HNO_3 indicating that this region is where the passive film is most developed. This is above the E_{corr} and i_{corr} values assessed in section 3.1.1 but is consistent with being well within the passive region indicated in Figure 3-2. Impedance values are also higher for 0, 0.2 and 0.8 V in 5% wt. HNO_3 than in 10 and 15% wt. HNO_3, where impedance values for 0 and 0.2 V are significantly lower. This shows that the passive film formed in these potential areas is more stable than that formed in 10 and 15% wt. HNO_3, This supports the observation in LSV studies of a decrease in the potential window of passivity (increase in E_{corr}) with increasing HNO_3 concentration.

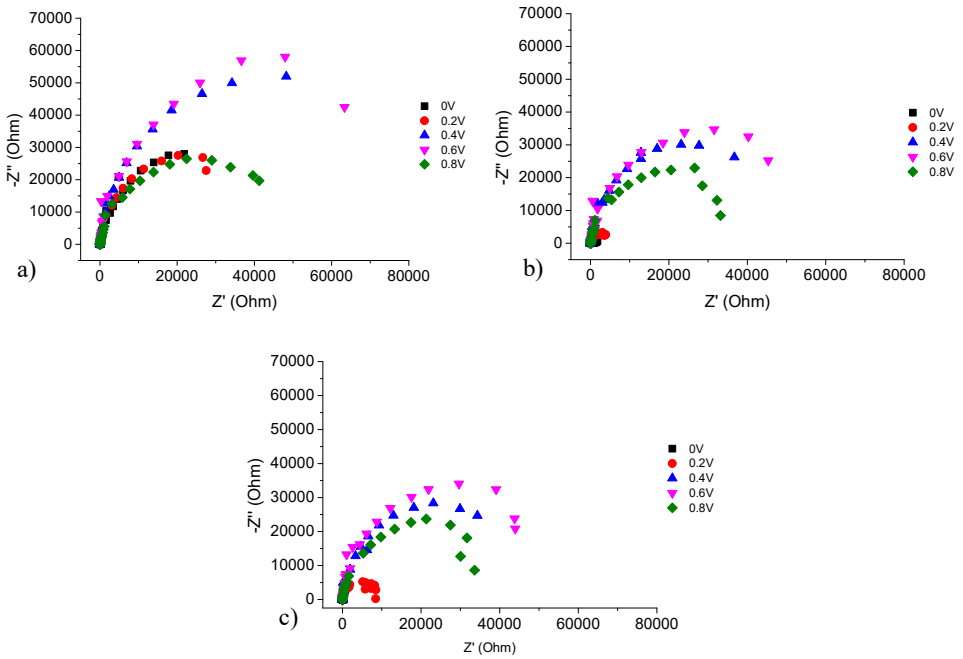

Figure 3-9 - Nyquist plots for 316L SS in a) 5% wt. HNO_3 solution, b) 10% wt. HNO_3 solution and c) 15% wt. HNO_3 as a function of film formation potential.

3.2.2 Impedance vs. Potential Plots

From the Nyquist plots in the previous section, it has been shown that differences in the real impedance, particularly in the low frequency region, may be directly related to resistive changes in the passivating layer on the steel. Thus, before applying equivalent circuit modelling to this data, simple real impedance vs. potential plots have been constructed and plotted alongside LSV data from the previous section in order to provide a broad semi-quantitative indication of system behaviour, as previously demonstrated by Fattah-alhosseini *et al* [76], [172]. Fattah-alhosseini *et al* [170] highlighted that the magnitude of impedance at low frequencies is several orders of magnitude higher than at high frequencies, thus any features are difficult to discern at higher frequencies [170]. Therefore, real impedance vs. potential plots are shown in Figure 3-10 for impedance data recorded at a low frequency value of 0.3 Hz.

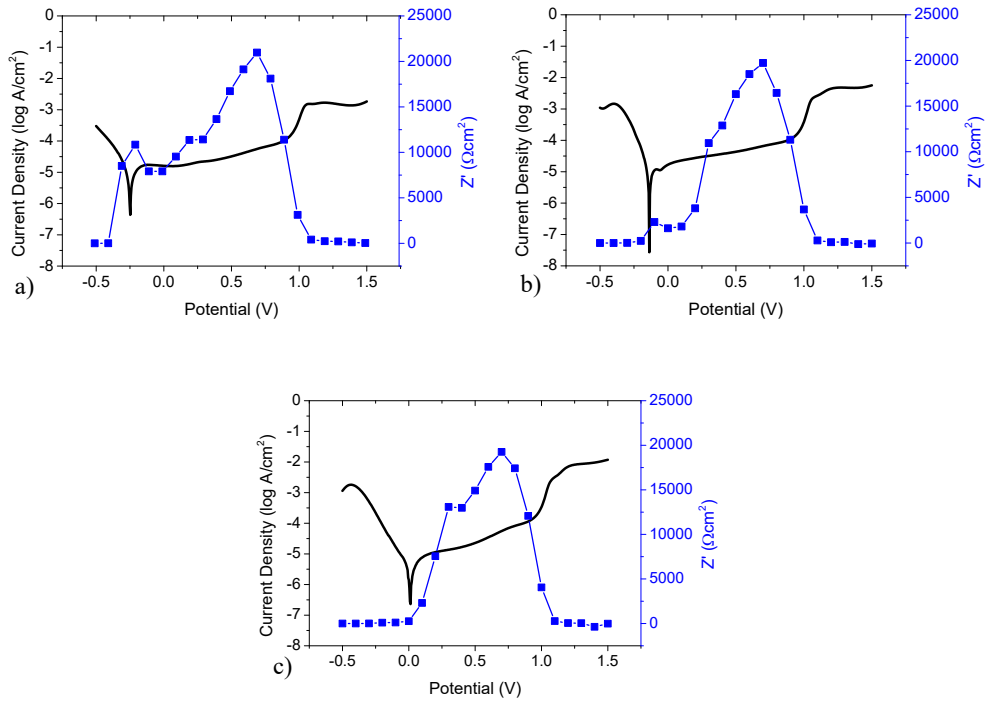

Figure 3-10 – Potentiodynamic polarisation curves plotted alongside low frequency impedance data for 316L SS in a) 5% wt. HNO_3 solution, b) 10% wt. HNO_3 solution and c) 15% wt. HNO_3 as a function of potential.

Considering first the results of Figure 3-10a, the impedance magnitude at 0.3 Hz, initially increases with potential, within the passive potential region, presumably as the passive magnetite/Cr_2O_3 film grows. This corresponds well with the increase in E_{corr} as HNO_3 concentrations is increase, identified in section 3.1.1. However, at a sufficiently high passive potential (E >0.7 V) the impedance magnitude decreases with increasing potential. This region, where the current begins to increase but breakdown potential is not reached, is associated with formation, and subsequent dissolution, of high valency Cr(VI) from the Cr(III) passive film [53], as described by Betova [74] and reviewed in section 1.3.3.3. Thus, as the film begins to slowly dissolve and breakdown, the impedance decreases accordingly. The lowest impedance values occur at potentials where total film dissolution occurs at > 1V, in good agreement with the LSVs of Figure 3-2.

Following the approach of Fattah-alhosseini *et al* [170], considering now the low potential region in more detail, smaller increases in impedance at potentials around E_{corr} are observed during experiments conducted at HNO_3 concentrations ≤ 10% wt. with the real impedance first rising to a low impedance in

line with increasing potential, before falling back and then increasing again at E> 0 V. This may be more easily observed by plotting low frequency impedance vs. potential traces for all HNO_3 concentrations on one plot. This is shown in Figure 3-11.

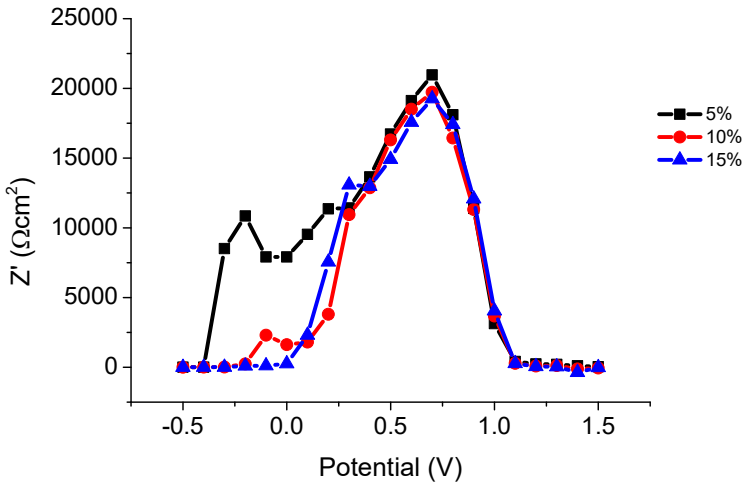

Figure 3-11 – Effect of film formation potential on impedance magnitude of 316L SS in 5-15% wt. HNO_3 at 0.3Hz.

Figure 3-11 shows that this effect is most obvious at 5% wt. HNO_3. As this occurs around E_{corr}, it may be due to the formation of a precursor Cr or Fe oxide layer, that is then converted at higher potentials to a full Cr(III) oxide passive layer. Drogowska *et al.* identified similar behaviour on 304 SS using EIS, with the formation of a low potential passive film which subsequently dissolved and a different higher potential passive film was then formed. The study was conducted in pH 8 carbonate solution so further investigation would be required to confirm this behaviour for this work [173].

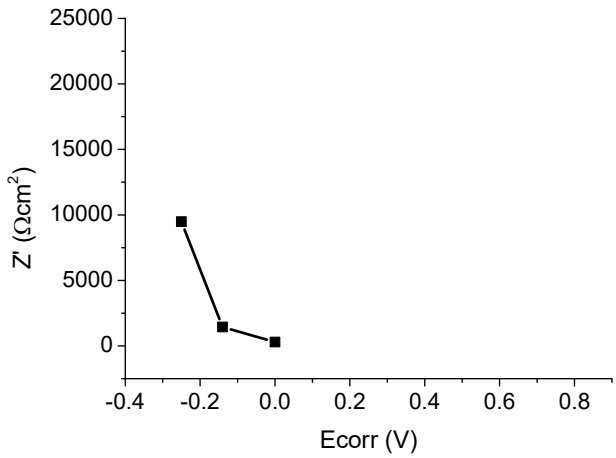

Figure 3-12 – Real impedance, Z', values at E_{corr} extrapolated from Figure 3-11 data. NOTE: Higher concentrations of HNO_3 have been left on the x-axis and will be filled in in Chapter 4.

Figure 3-12 shows real impedance values at E_{corr} for 5-15% wt. HNO_3. Impedance decreases with increasing HNO_3 concentration, indicating that the putative precursor film must presumably increase in solubility with increasing HNO_3 concentration, an effect akin to that described in LSV studies of secondary passivation in the transpassive region [74] (section 3.1). Observation of this precursor film formation in the LSV studies of section 3.1 is obscured as HNO_3 concentration increases due to the progressively more facile reduction of H^+ to H_2.

However, it is important to note that this interpretation using real impedance vs. potential data is a simplification and does not clearly define whether the change in impedance around E_{corr} is directly related to changes in the passive oxide film resistance, double layer capacitance or solution resistance. Therefore, the next section describes modelling the data using an equivalent circuit model to extract information on the oxide film resistance only.

3.2.3 Polarisation Resistance Measurements

3.2.3.1 Equivalent Circuit

Any electrochemical cell can be represented in terms of an equivalent electrical circuit that comprises a combination of resistances and capacitances. This circuit should contain at least four key components in

the case of a faradaic process occurring in the possible presence of a passivating film (which may itself result from the faradaic process) [60], [129], [132]:

1. A capacitive element representing the electrochemical double layer, this could be either;

    a. Double layer capacitance, C_{dl}, which best describes a system that approximates the behaviour of a simple parallel plate capacitor.

    b. A Constant Phase Element, CPE, which describes a system that approximates that of a distribution of capacitances. For example, surface inhomogeneity of a resistive film or variable thickness of that film across the electrode surface.

Thus, the double layer and the oxide layer grown at the steel surface can be described by either capacitive element, depending on the inhomogeneity/roughness at the electrode surface.

2. The resistance of the charge transfer process, R_{ct}

3. The resistance of any passive film formed, R_p

4. The resistance of the electrolyte solution between the working and reference electrodes, R_s

In our modelling of the 316L SS system, two simple equivalent circuits could be considered appropriate for the results presented in this work. For potentials ≤0 V and ≥1 V a 3 component model containing C_{dl}, a simple capacitor, and R_{ct} is considered the most accurate. The electrode is considered to be flatter and therefore behaves more like a parallel place capacitor. Whereas, at 0-1 V, the surface is passive and the more appropriate components would be CPE and R_p which better describe the behaviour of the protective oxide layer that forms in the passive region, as shown in Figure 3-13.

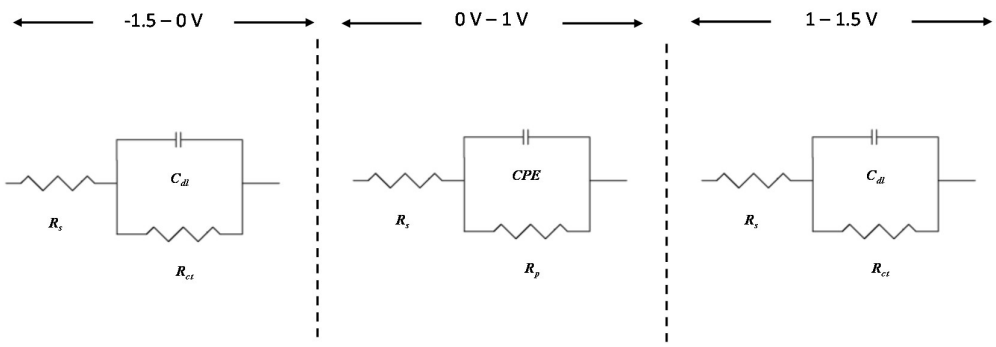

Figure 3-13 - Electrical equivalent circuit models used to represent an electrochemical interface undergoing corrosion at <0 V and >1 V and passivation in the region of 0-1 V. R_p is the polarization resistance, R_{ct} is the charge transfer resistance, C_{dl} is the double layer capacitance, CPE is the Constant Phase Element and R_s is the solution resistance.

However, as the main area of interest is the central passive region, the simplest model for characterising the metal-solution interface is the cell of Figure 2-13b. It includes the three essential parameters, R_s (solution resistance), CPE (the imperfect capacitance of the double layer) and R_p (the polarisation resistance) described above [130]. A simple model such as this is found to be appropriate for analysis here because the Nyquist plots of Figure 3-4 - Figure 3-6 exhibit a single time domain semi-circle, with no obvious inductor loops. Chi-squared values in the order of $1x10^{-2}$ - $3x10^{-2}$ were obtained when modelled using ZView2, as shown in Appendix 2.

3.2.3.2 Polarisation Resistance (R_p) Plots

Figure 3-14 (a-c) shows polarisation resistance, R_p, data obtained from the EIS data of Figure 3-5 - Figure 3-7, plotted with potentiodynamic polarisation curves for 316L SS in 5, 10 and 15% wt. HNO_3, over the potential range -0.5 – 1.5 V. R_p was calculated in ZView2, using the simple equivalent circuit model, shown in Figure 2-13b , described in section 3.2.3.1 to model the data (tabulated in Appendix 1). R_p represents the resistance of the passivating film that has been formed on the electrode surface. Thus, an increase in R_p is interpreted here as the formation, stabilisation and possible increase in the thickness of the surface oxide layer. Plotting R_p data alongside LSV data will allow for a direct comparison with LSV studies, this is shown in Figure 3-14.

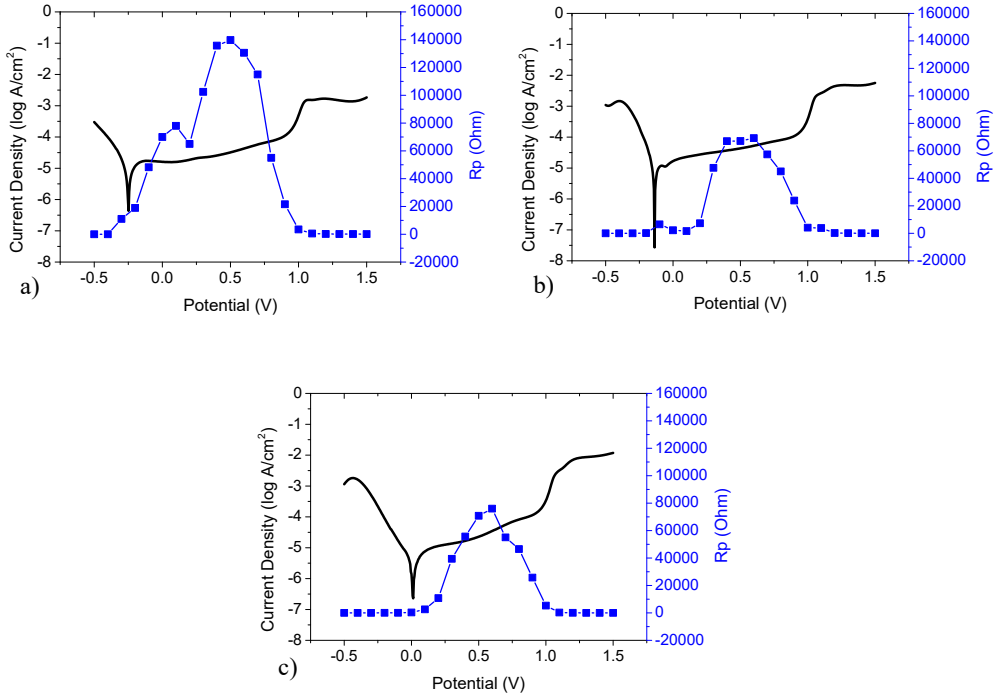

Figure 3-14 - Potentiodynamic polarisation curve plotted with impedance data for 316L SS in a) 5% wt. HNO_3 solution, b) 10% wt. HNO_3 solution and c) 15% wt. HNO_3 as a function of potential.

Consider first the cathodic region of the R_p vs. potential plots in Figure 3-14. As with plots of the real impedance vs. potential, at 5% wt. HNO_3 (Figure 3-14a) R_p increases rapidly as the metal enters the passive region at ~-0.25 V; however, there is a dip in R_p between 0.1 and 0.2 V. As the plotted parameter, R_p, is now, in principle, independent of double layer capacitance and solution resistance, the results of Figure 3-14, would suggest the previously theorised precursor layer of either Fe oxide or potentially $Cr(OH)_3$, formed before a Cr_2O_3 layer is fully formed at higher potentials, is real. As in Figures 3-10 and 3-11, the peak in the R_p value that occurs at ~0V in 5% HNO_3 disappears at $[HNO_3] > 10\%$. The above postulated precursor film must therefore presumably increase in solubility with increasing HNO_3 concentration. However, the reduction of H^+ could also be masking this feature and a precursor layer may still be present. One means by which to determine if this is the case if to obtain the capacitive parameter of the CPE. This will be derived from the capacitance of any passivating film present at the electrode surface in the passive range. Thus, Figure 3-15 shows polarisation curves plotted with both R_p and the capacitance parameter of the CPE. The presence of a thickening precursor film would lead to a decrease in the capacitance and this is clearly seen for 5% wt. HNO_3 (Figure 3-15a). Capacitance appears to decrease in line with increasing R_p for 10 and 15% wt. plots indicating that there is the potential for a

thinner/less efficient precursor film to have formed or no precursor film forming at all at slightly higher HNO_3 concentrations. The existence and potential composition of this film is returned to in the next chapter.

As the potential is increased to > ~0.5 V, the current observed in the LSV starts to gently increase in the passive region, behaviour which as discussed in the previous section has been linked with the formation of high valency chromium from Cr(III) which leads eventually to the onset of transpassive dissolution. This behaviour coincides with the levelling off and subsequent decrease of R_p. Again, as high valency chromium Cr(VI) is more soluble, this dissolution of Cr reduces the effectiveness of the protective film leading to a consequent reduction in film resistance. The reduction in film resistance (R_p) can be seen clearly to correlate with an increase in capacitance in Figure 3-15, suggesting that the passive layer is thinning.

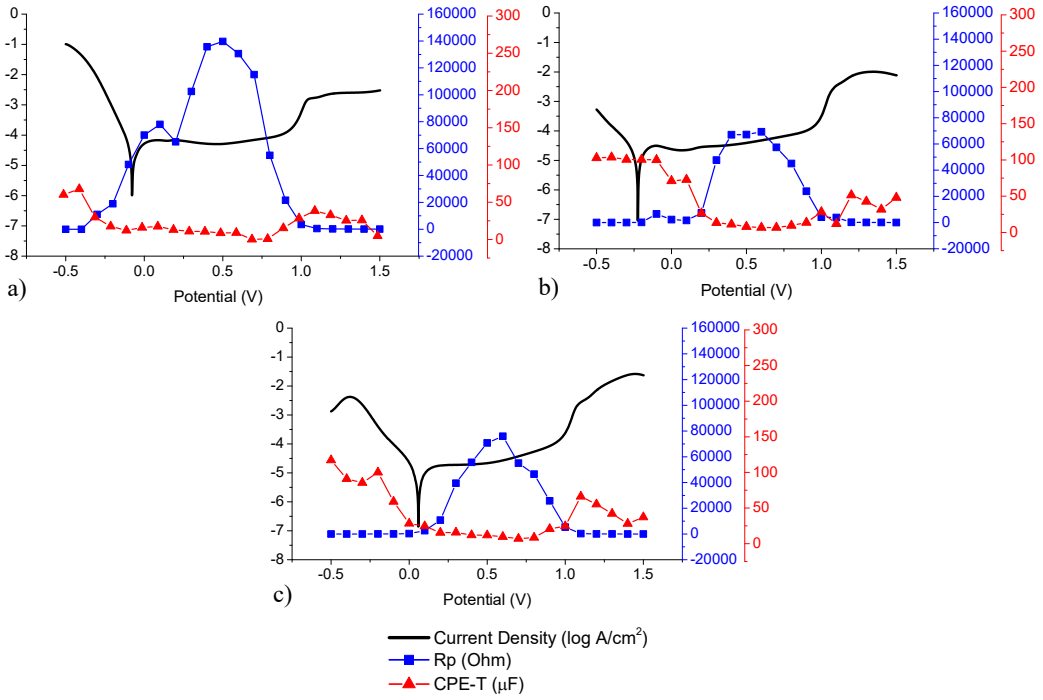

Figure 3-15 - Potentiodynamic polarisation curve plotted with impedance (blue) and the capacitance element of CPE (red) data for 316L SS in a) 5% wt. HNO_3 solution, b) 10% wt. HNO_3 solution and c) 15% wt. HNO_3 as a function of potential.

At ~1V high valency Cr is stripped from the passive film leading to the dissolution of underlying iron, observed as a consequent rapid reduction in R_p and increase in capacitance. It is interesting to note that

even though secondary passivation is apparent in the LSV results of Figure 3-2a, this behaviour is not shown clearly in the EIS results, with R_p remaining low at potentials >1V. Capacitance values do decrease at potentials >1.1V which may be indicative of the secondary passive film. However, capacitance values do not drop to values seen in the presence of the passive film 0.25 - 1V. These results suggest that the secondary film that forms above 1V may only be a thin film which is only partially passive in character [74].

R_p peak values in the passive range decrease with increasing HNO_3 concentration, indicating that the passive layer thickness is decreasing with increasing HNO_3 concentration. The next section will discuss film layer thickness further. Microgravimetric experiments assess mass changes on the electrode surface related to electrochemical changes in passive layer formation with increasing HNO_3 concentration.

3.3 In-situ Microgravimetric Studies of Passive Behaviour on SS2343 (316L Analogue) in Nitric Acid

3.3.1 Introduction

In the previous section the electrochemical behaviour of 316L SS in nitric acid concentrations ≤15% wt. was characterised using LSV and EIS. This section deals with microgravimetric measurements of SS2343 (316L SS equivalent, see Chapter 2) in nitric acid using the Electrochemical Quartz Crystal Microgravimetry (EQCM) and how recorded mass changes are related to the electrochemical behaviour of 316L SS in HNO_3.

3.3.2 Establishing 316L as a suitable analogue for 2343

3.3.2.1 Introduction

No 316L SS QCM crystals were not commercially available at the time of this study. The closest analogue was found to be SS2343. SS2343 may be regarded as a suitable analogue for 316L SS due to its similar chemical composition, Table 3-1. Work by Donik *et al* [149] compared the electrochemical and

potentiodynamic properties of 316L SS and SS2343 indicates that their corrosion behaviour is almost identical, only differing at high Cl^- concentrations.

Table 3-1 - Composition of various Stainless Steels (% wt.) [46]

Metals	Cr	Ni	C	Mn	Si	P	S	Mo	Nb
316L	16.6	10.03	0.016	1.49	0.48	0.03	0.002	2.5	0.004
SS2343	16.87	10.74	0.026	1.51	0.36	0.033	0.025	2.53	0.005

From Table 3-1 it can be seen that some compositional differences do exist between the two steels, SS2343 has slightly higher Cr, Ni, C, Mn and S content, whereas 316L has a higher Si content. Thus, it is necessary to briefly compare their electrochemical behaviour in 5% wt. HNO_3 electrolyte, in order to ensure the suitability of SS2343 as an analogue for 316L SS.

3.3.2.2 Comparison of the Electrochemical Behaviour of 316L SS and SS2343

Initial tests used linear sweep voltammetry across the same voltage window and at the same scan speed as that employed in LSV studies in section 3-1. The results of this experiment in the form of current density and log current density are shown in Figure 3-16.

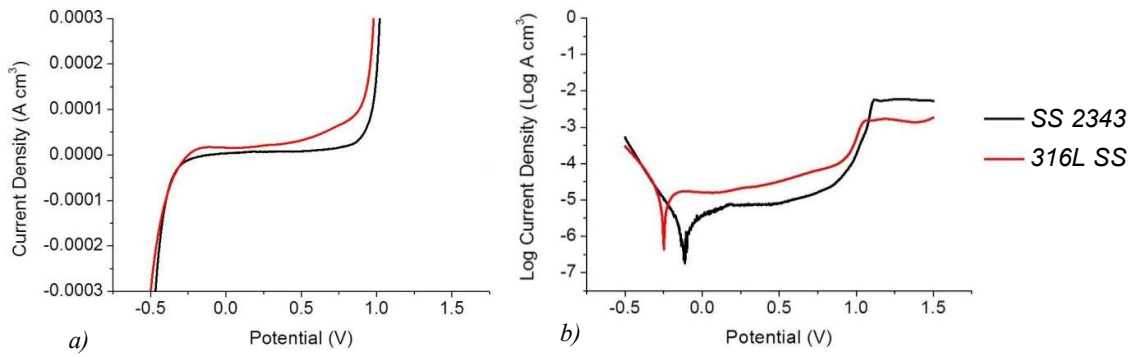

Figure 3-16 - Potentiodynamic polarisation curves showing a) potential vs. current density and b) potential vs. log current density of SS 2343 and 316L SS in 5% wt. HNO_3 (sweep rate, 10 mV s^{-1}).

The polarisation curves in Figure 3-16 broadly show that the two steels are electrochemically similar, with passivity and transpassivity occurring at approximately the same point. This suggests that SS2343 is suitable as an analogue for 316L SS in electrochemical experiments. However, there are slight differences between the two. In general, in Figure 3-16a, SS2343 has a lower current from ~-0.25 V to 1 V compared to that of 316L SS i.e. SS2342 appears to be more passive. In Figure 3-16b, E_{corr} is more positive (-0.17 compared to -0.25 V for 316L SS) and i_{corr} is lower (-5.5 Log A cm^{-3} compared to -5 Log A cm^{-3}). Onset of transpassive dissolution occurs at 1V for SS2343 and ~0.9 V for 316L SS. The general difference in current and E_{corr} is expected to be due to slight differences in the composition between the two steels.

Thus, in order to further compare the two steels a series of potential step experiments were performed, whereby the potential is stepped by 150 mV every 45 minutes while the current is measured. Figure 3-17 shows the results of this experiment in 5% wt. HNO_3.

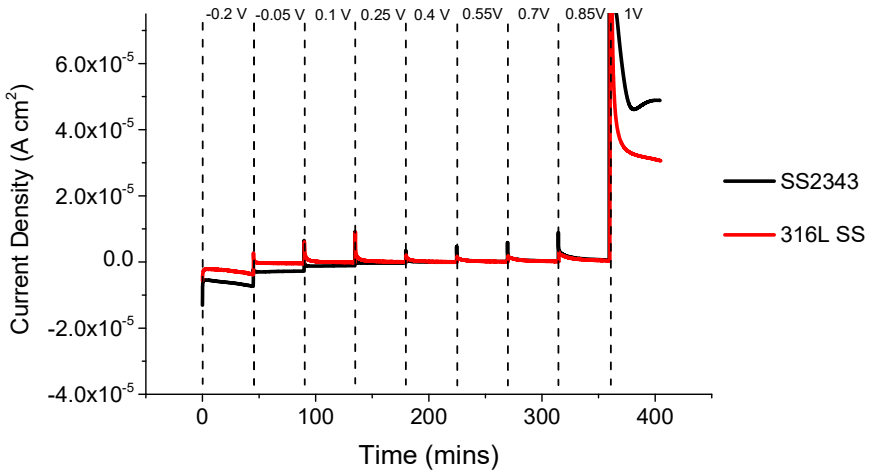

Figure 3-17 – Current measured over time during potential step measurements of SS 2343 and SS 316L in 5% wt. HNO_3.

Again, there is good electrochemical agreement between the two alloys, although, as noted for Figure 3-16, there are some minor differences at potentials <0.1 V and potentials >1 V. Specifically, current levels are lower for SS2343, again most likely due to slight compositional differences. However, these small differences aside, overall the results lead to the conclusion that SS2343 is a suitable analogue for 316L SS in terms of its electrochemical corrosion behaviour.

3.3.3 EQCM LSV/Voltamassogram studies

As described in Chapter 1, charge passed in linear sweep voltammograms may be related to mass changes at the electrode surface through application of Faraday's law. However, changes in current in LSVs may also be due to hydrogen or oxygen evolution processes or oxidation/reduction of solution species, for example the electrochemical conversion of nitric acid to nitrous acid. Thus, it is important to separate corrosion processes from other charge transfer processes. In order to do this the QCM, which provides *in situ* nanogram measurements of mass changes that accompany electrode processes, is coupled with a potentiostat to allow simultaneous monitoring of mass change and current passed during LSV measurements.

Using SS2343 piezoelectrodes, polarisation curves and simultaneous voltamassograms were recorded from 0 V (low passive potential) to 1 V (transpassive dissolution) at a scan rate of 10 mV s^{-1}. Figure 3-18a, Figure 3-19a and Figure 3-20a show the measured current density (A cm^2) and the corresponding mass change for SS2343 in 5% wt.-15% wt. nitric acid.

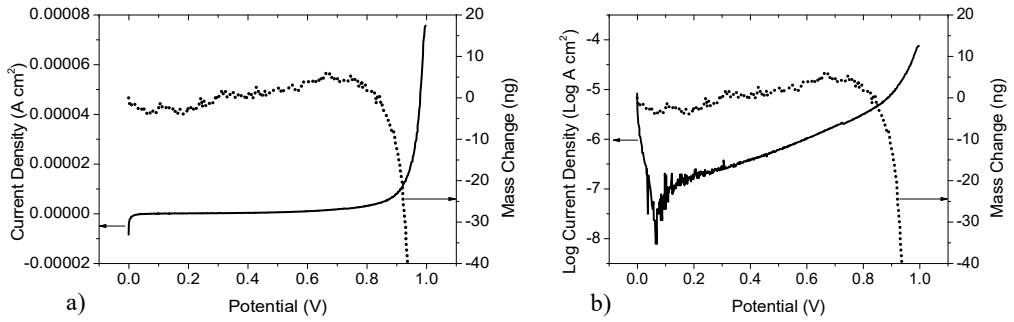

Figure 3-18 – a) Linear Sweep Voltammogram and b) Potentiodynamic polarisation curves of SS 2343 in 5% wt. HNO_3. Sweep rate = 10 mV s^{-1}.

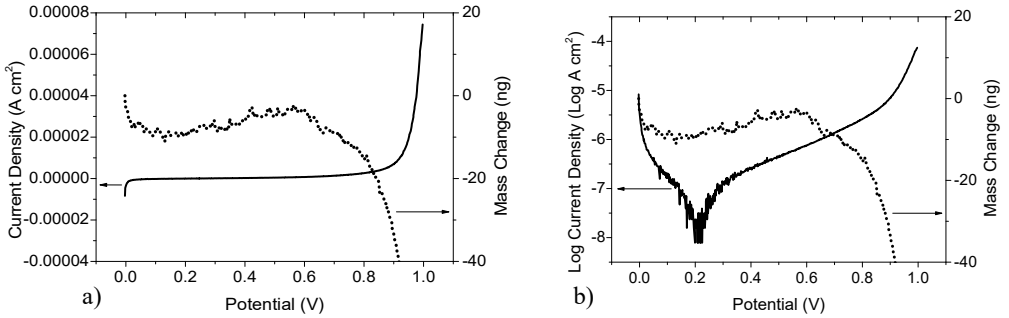

Figure 3-19 - a) Linear Sweep Voltammogram and b) Potentiodynamic polarisation curves of SS 2343 in 10% wt. HNO_3. Sweep rate = 10 mV s^{-1}.

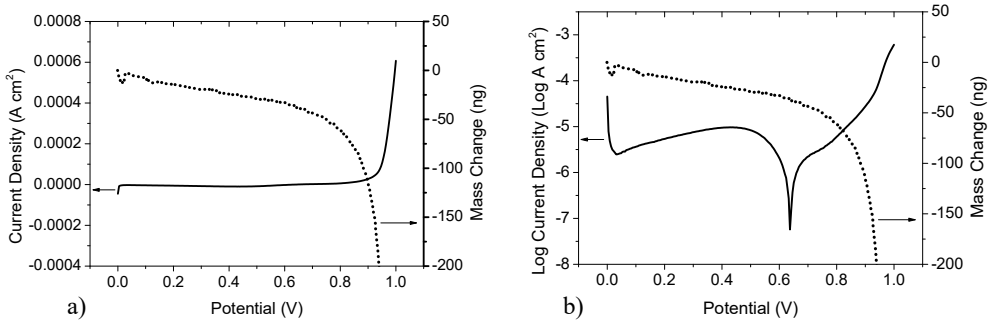

Figure 3-20 - a) Linear Sweep Voltammogram and b) Potentiodynamic polarisation curves of SS 2343 in 15% wt. HNO_3. Sweep rate = 10 mV s^{-1}.

Considering first the general relationship between the voltammogram and voltamassogram, using the lowest HNO_3 concentration data of Figure 3-18 (i.e. 5% HNO_3), at 0 V an initial small mass loss is observed with initiation of scanning. However, in the simultaneously recorded LSV it can be seen that the current decreases at this potential and this is more apparent in the log *I* vs. E data. This potential is below E_{corr} identified in section 3.1.1 and thus water reduction and hydrogen evolution is occurring as well as slow dissolution of the steel/air formed passive film. The majority of the observed mass loss is thus expected to be due to the dissolution of the steel/air formed passive film on the electrode surface. This mass loss is arrested at a potential of ~0.1 V and a mass increase is observed. The current also achieves steady state at this point indicating that the passive film is establishing itself. As the potential increases above ~0.1 V mass slowly begins to increase as the protective oxide layer grows and reinforces. However, as the potential is increased towards the transpassive region, mass increase slows and mass then starts to decrease at ~0.75 V. As previously discussed in sections 3.1 and 3.2, at this potential, chromium begins to switch valence states from Cr(III) to Cr(VI). Cr(VI) is more soluble in

this environment, leading to chromium dissolution from the oxide layer. Finally, above 0.8 V the chromium oxide layer destabilises and oxidative dissolution of the underlying iron surface occurs, as shown by the large decrease in mass and concurrent increase in oxidative current.

Differences between the voltammetric behaviour observed in 5%, 10% and 15% HNO_3 are shown in Figure 3-18, Figure 3-19 and Figure 3-20. These may be more easily understood by plotting the voltamassograms only for each concentration on one plot. This is shown in Figure 3-21.

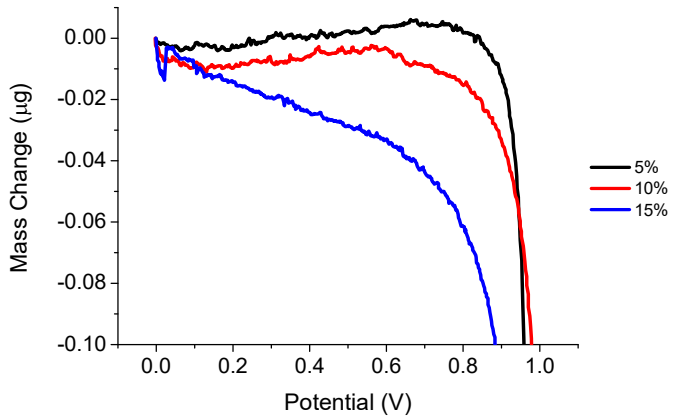

Figure 3-21 – Voltamassograms of SS2343 piezoelectrodes in 5-15% wt. HNO_3.

At 5 and 10% wt. HNO_3 the observed mass increase in the passive region is very similar, indicating that the film formation mechanism is the same in both concentrations. The main difference between these two concentrations is the earlier onset of Cr(III) oxidation (~0.6 V vs. ~0.75V), presumably due to the increased solubility of Cr oxides at a the lower pHs / higher HNO_3 concentrations.

At 15% wt. nitric acid the mass of the steel piezoelectrode slowly decreases at potentials > ~0.05V, which is quite different compared to the two lower concentrations (5 and 10% wt. HNO_3) where film formation and growth results in a mass increase. Interestingly the log *I* vs. E results of Figure 3-20 suggest that E_{corr} is significantly higher than at 5 and 10% wt. HNO_3 and higher than expected when compared to LSV results in Figure 3-2. EQCM LSV experiments were repeated and a similar E_{corr} was observed each time, the reason for this is currently unknown and will need to be investigated further. Even when the potential increases above E_{corr} the film on the steel surface continues to decrease in mass, quite contrary to the voltamassogram results discussed above. Schmutz & Landolt have identified similar behaviour in the passive region on QCM crystals sputtered with an iron-chromium alloy [73]. Schmutz & Landolt attributed this behaviour to continuous metal dissolution occurring alongside film formation with the

associated two currents essentially cancelling each other out. Essentially, the Cr passive layer takes on a semi-porous character due to deterioration from Cr(III) to Cr(VI) conversion, allowing low level dissolution of underlying Fe/Fe_3O_4 through the usually protective Cr oxide. A net mass loss is observed because the negative mass change from the dissolution of iron exceeds the positive mass change resulting from chromium oxide film growth. Schmutz & Landolt also suggest that a relative increase in Cr content in the passive film is not due to the selective oxidation of Cr rather it is due to the selective dissolution of Fe at the metal-oxide interface. This behaviour does not occur at lower HNO_3 concentrations, however, and thus appears to be HNO_3 concentration dependant. This is most likely due to an increase in the solubility of Fe with a decrease in pH.

EQCM and LSV have been used here as a rapid scanning technique. Whilst LSV is a useful electrochemical characterisation technique it does not allow for oxide layer growth kinetics to be determined, the primary area of interest for radionuclide uptake. Therefore, in the next section EQCM combined with slower potential-step measurements have been used to more fully understand Cr/Fe film formation and growth in the passive phase.

3.3.4 EQCM Potential Step Studies

Using the EQCM, chronoamperometric-microgravimetric measurements were made by means of a potential 'staircase' experiment in which the potential was stepped at 0.15 V intervals from an initial value of -0.2 to 1.15 V. At each step on the 'staircase' the potential was held for 45 minutes and the resultant current transient and change in electrode mass was recorded.

Figure 3-22 shows the time dependence of the changes in electrode mass (as determined by the use of the Sauerbrey equation, equations (2.15) and (2.16) above) [174]) that occur in response to the potential 'staircase' as a function of HNO_3 concentration, from a HNO_3 concentration of 5% wt. (Figure 3-22A) to 15% wt. (Figure 3-22C). As with the LSV studies of Figure 3-21, in general oxide layer growth decreases with increasing HNO_3 concentration, seen most convincingly from the mass measurements made at +0.55V However, more subtle observations as to differences between HNO_3 concentrations may be made based on the shapes of each of the mass traces in Figure 3-23.

Considering first the cathodic region: broadly net mass gains are observed in the potential range -0.2 to 0.25 V due to the formation of the Cr/Fe oxide passive film. Mass gains are higher at 5% wt. HNO_3 and decrease gradually with increasing HNO_3 concentration. It is interesting to note that in 15% wt. HNO_3 an increase in mass is observed, whereas in the previous LSV EQCM experiments an overall mass loss was recorded. This is most likely due to instabilities in the passive film formed in the low potential passive region at fast scan rates, with Cr(III) to Cr(VI) decreasing film stability, compared to slower scan rates in the potential step studies which allow the film to stabilise before a change in the environmental conditions.

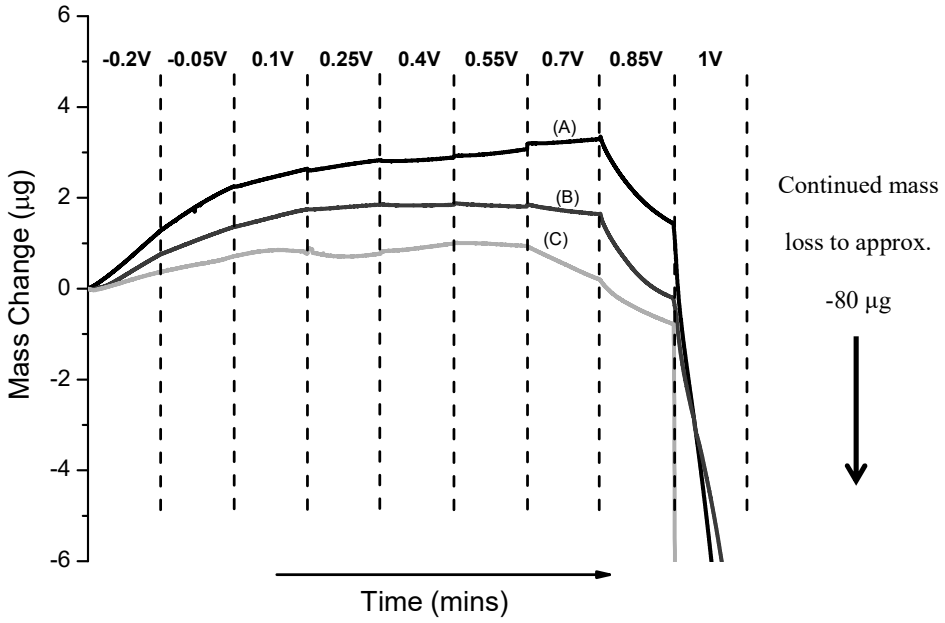

Figure 3-22 - Mass change of SS 2343 as a function of time during potential step experiments in 5-15% wt. (A-C respectively) HNO_3. Polarisation conditions: Start potential = -0.2 V, end potential = 1 V, potential step = 0.15 V, time between steps = 45 mins.

As the potential increases, no net mass losses or gains are observed from 0.4 and 0.7 V for 5 and 10% wt. HNO3 respectively and from 0.25 V for 15% wt. HNO_3. As discussed in the previous section, this change in behaviour corresponds to the region where it has been suggested that slow Cr(III) to Cr(VI) begins to occur at high potentials in the passive region, immediately prior to transpassivity [56,65], resulting in a balance of Cr passive film growth and dissolution. At 15% wt. HNO_3 this occurs at a much

lower potential in the passive region, presumably due to the increased concentration of HNO_3 (and therefore HNO_2 availability) and increased solubility of Fe/Cr precursor oxides (see section 3.2).

In 5 and 10% wt. HNO_3, a mass decrease is observed at higher potentials, ~0.85 to 1 V, indicating the early onset of transpassivity just before the breakdown potential (1 V) is reached and rapid dissolution of underlying iron occurs [65], [74]. In 15% wt. HNO_3 this mass decrease occurs earlier, ~0.7 V. As discussed in the previous section this is presumably due to the increased solubility of Fe oxides at a lower pH, allowing more rapid dissolution through a weakened, semi-porous, Cr oxide passive film.

In summary, EQCM studies have characterised passive film growth and stability in concentrations of $HNO_3 \leq 15\%$ wt. In 5 and 10% wt. HNO_3 film formation, stabilisation and dissolution occurs at similar potentials throughout. However, in general the overall film thickness is lower at 10% wt.% wt. HNO_3 than at 5% wt. HNO_3. In 15% wt. HNO_3, film formation behaviour differs, in fast scan LSV studies a mass loss is observed at all potentials. This has been attributed to the semi-porous behaviour of Cr oxide at this HNO_3 concentration, allowing the slow dissolution of underlying Fe, consequently resulting in an overall mass decrease. However, during potential step studies this behaviour is not observed. It is believed that the slower scan rate in the E-step studies allows the film to stabilise before any changes in environmental conditions occur. E-step studies observed a decrease in overall mass increase with increasing HNO_3 concentrations and this matches well with decreasing R_p peak values observed in EIS studies of section 3.2. The decrease in both mass and R_p values indicates that the passive layer thickness is decreasing with increasing HNO_3 concentration.

3.4 Compositional Analysis of the Passive Film Formed On 316L Stainless Steel in Nitric Acid

3.4.1 Introduction

In the preceding sections of this chapter we have electrochemically characterised the passive behaviour of 316L SS samples in HNO_3 concentrations from 5-15 % wt. We have demonstrated that E_{corr} increases with increasing HNO_3 concentration (LSV data, section 3.1) and that passive layer thickness decreases

with increasing HNO_3 concentrations (EQCM data, section 3.3). Passive oxide film formation slows at potentials ≥ 0.25 V vs. SCE due to a pre-passive Cr(III)/Cr(VI) dissolution reaction (EQCM data, section 3.3).

This chapter attempts to analytically determine, using X-ray Photoelectron Spectroscopy (XPS), any compositional changes that may occur in the so formed passive films as a function of applied potential in 5% wt. HNO_3. However, due to time and equipment access restrictions, measurements were only recorded in 5% wt. HNO_3 in the ≤15% wt. HNO_3 range. Nonetheless, the results do provide some useful information regarding layer composition changes as a function of applied potential.

XPS measures the surface elemental composition, empirical formula and chemical state of the sample under interrogation [175]. Thus, it is invaluable for understanding the composition of thin films, oxidation processes, passivity and the interaction of materials with different electrochemical environments. Importantly, XPS has been used previously in several studies to assess the accumulation of uranium on stainless steel surfaces [106], [107], [118] and has also been used to characterise depth, distribution and chemical state of various contaminants in the passive oxide layer formed on process stainless steels [103], [176].

Based on these previous studies, here we specifically report on binding energy shifts for the key components of the passive oxide layer of 316L only, chiefly the Cr $2p_{3/2}$, Fe $2p_{3/2}$ and O 1s elemental orbital signals.

3.4.2 Results

Figure 3-23 shows the initial XPS survey scan of a 316L planchet sample polarised in the passive region at 0.2 V in 5% wt. HNO_3.

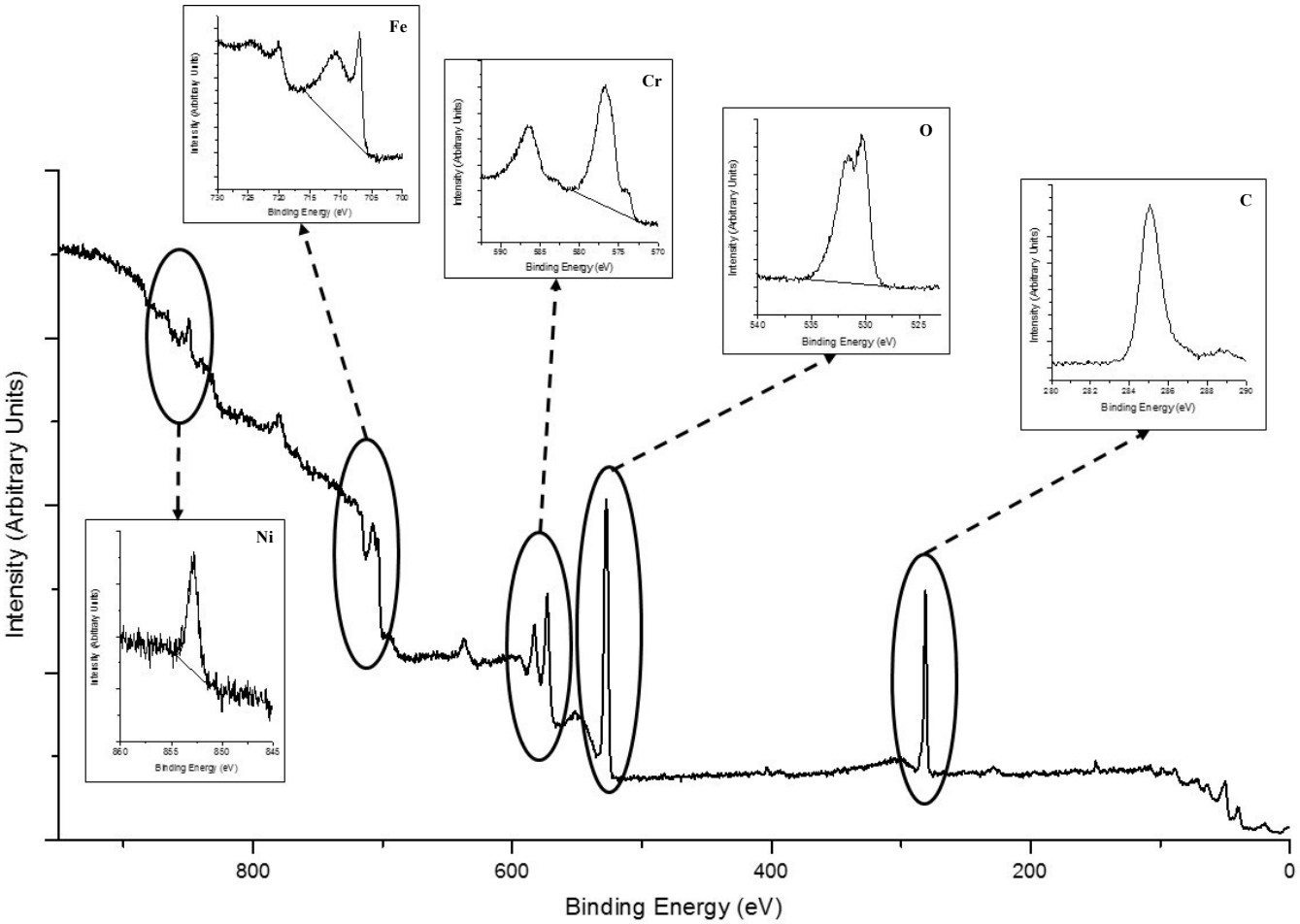

Figure 3-23 – Wide survey spectra (main) and high resolution spectra (insets) of the surface oxide layer of a 316L sample polarised at 0.2 V in 5% wt. HNO^3. All peaks were calibrated to hydrocarbon (C1s) signal, set at 285.00 eV.

The survey scan encompasses the entire energy range, showing characteristic peak intensities of all the elements that are present on the surface of the sample. After the initial survey scan high resolution scans of the chromium, iron and oxygen binding energy signals were taken in order to determine changes in their binding energy representative of oxide formation/dissolution. Examples of the high resolution spectra are shown in the insets of Figure 3-23.

It should be noted that nickel is not shown in the high resolution scans of Figure 3-23 as when the spectra for nickel was analysed it was concluded that no nickel oxide was present in the passive film on the steel surface, with the XPS signal only coming from Ni metal in the steel bulk, as shown in Figure 3-24. Therefore, during the following discussion nickel is omitted from analysis.

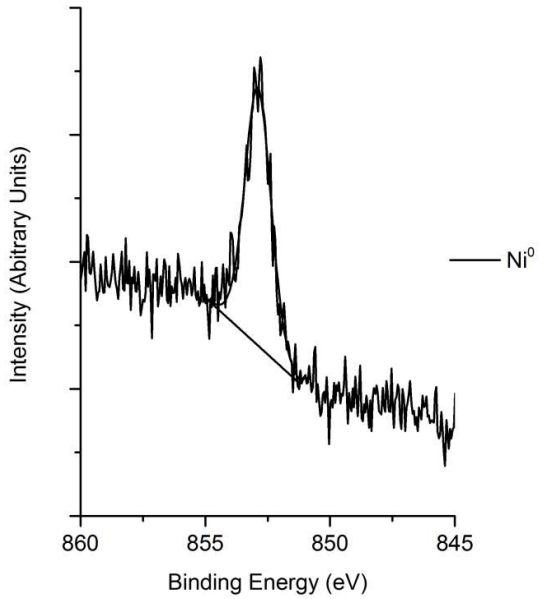

Figure 3-24 - XPS profile of Ni $2p_{3/2}$ after passivation of 316L SS at 0.2 V in 5% wt. HNO_3.

In order to determine the atomic percentage of the key elements shown in the high resolution spectra of Figure 3-23, curve fitting must be conducted to quantify and deconvolute the contribution of each chemical species to the recorded intensity. A typical curve fit of the Fe 2p region, assuming all possible iron species make up the observed intensity, is shown in Figure 3-25.

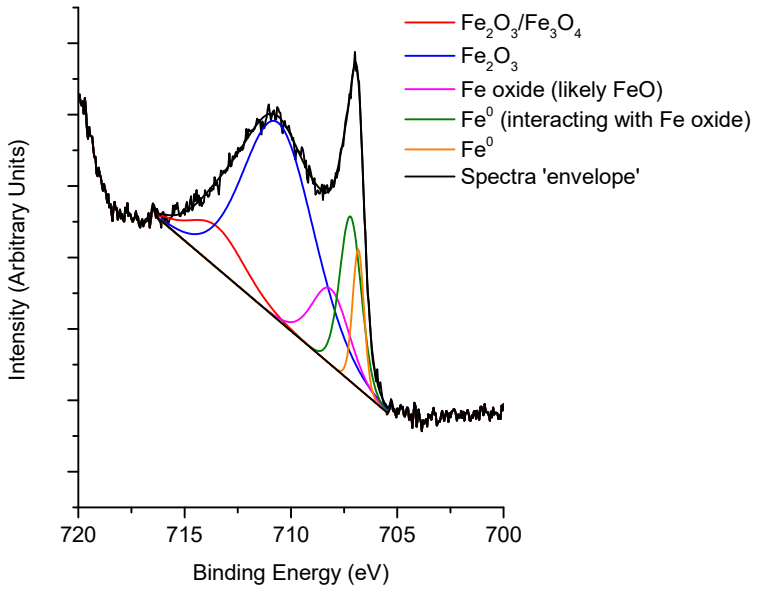

Figure 3-25 – Typical curve fitting for the Fe 2p region after applying linear background subtraction Fe 2p XPS profile after passivation of 316L SS at 0.2 V in 5% wt. HNO_3.

In the spectra shown above, curves for the iron species that are present in the Fe 2p region, metal (Fe^0) and various iron oxides (mainly Fe_2O_3), have been fitted to the recorded spectra using CasaXPS software (CASA Software Ltd.). The spectra 'envelope', essentially a line of best fit along the recorded spectra, fits very well using this species combination.

However, due to peak proximity, there is some difficulty in clearly classifying the contribution of each species to the identified peaks. The 4 layer model of Figure 1-33 showed how different oxides will be present simultaneously making it difficult to discern which peak can be attributed to which oxide. Therefore, to ease peak identification the Fe 2p spectra were fitted using only the two dominant Fe 2p components as illustrated in Figure 3-26.

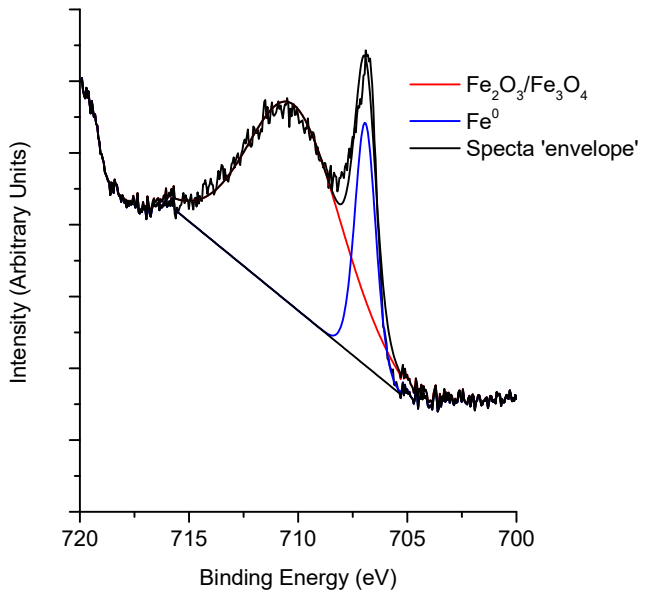

Figure 3-26 – Curve fit to the Fe $2p_{3/2}$ region with only two components. Fe 2p XPS profile after passivation of 316L SS at 0.2 V in 5% wt. HNO_3.

It can be seen from Figure 3-26 that using this simplified component analysis technique the spectra 'envelope' still maintained a good fit to the actual XPS spectra, validating the use of this type of reduced analysis.

Thus, for the high resolution spectra of Figure 3-23 the peak binding energy (E_b) parameters of each of the dominant components of Fe, Cr and O have been used. The average binding energy and full width half maximum (FWHM) for these dominant components is shown in Table 3-2. Due to uncertainty, an adjustment of ± 0.5 eV to peak position was applied.

Table 3-2 – Average peak positions and FWHM for Fe 2p, Cr 2p and O 1s curve fitted intensities.

Component	Assignment	Average Peak Position	FWHM
Fe 2p	Fe^0	706.96	1
	Fe_2O_3/Fe_3O_4	710.32	5.1
Cr 2p	Cr^0	573.97	1.13
	Cr_2O_3	575.82	0.7
	$Cr(OH)_3$	576.84	2.2
	CrO_3	578.60	2.5
O 1s	Fe_2O_3/Fe_3O_4/Cr2O3	530.11	1.2
	$Cr(OH)_3$	531.72	2.1
	H_2O/ O_2^0 ads	533.80	2

During analysis peak positions were kept constant for each element and linear background correction was used to determine spectral baseline and peaks. Furthermore where the full width half maximum (FWHM) was wider than average it was assumed that two phases were present with a similar binding energy. Based on the parameters of Table 3-2, curve fitted high resolution spectra of 316L SS samples in 5% wt. HNO_3 polarised at 0.2 and 0.8V respectively are shown in Figure 3-27.

Considering first the results of the samples polarised at 0.2 V, the iron profiles in Figure 3-27a show two peaks, the peak at 706.96 eV is due to elemental iron (Fe^0) and the peak around 710.32 eV is attributed to either iron (III) oxide (Fe_2O_3) or iron (II,III) oxide (Fe_3O_4) in 316L SS [177]. The FWHM for the Fe(III) peak is quite large, most likely due to a multiphase oxide of Fe_2O_3 and Fe_3O_4 and unfitted peaks of FeO and elemental Fe interacting with Fe oxide [178] as discussed above and shown in Figure 3-25. From the absence of hydroxide species, such as Geothite (FeO(OH)) or Lepidocrocite (γ-FeO(OH)) it is not unreasonable to conclude that little Fe is present at the direct interface between the alloy and the electrolyte, suggesting a Cr-rich passive film.

The chromium profiles in Figure 3-27b, show four peaks which are attributed to: Cr metal (573.97 eV), Chromium (III) oxide (Cr_2O_3) (575.82 eV), Chromium (III) hydroxide ($Cr(OH)_3$) (576.84 eV) and Chromium (VI) oxide (CrO_3) (578.60 eV).

Finally, the oxygen profile shown in Figure 3-27c. The O1s spectra of Figure 3-27c taken independently from iron and chromium is not enough to confirm the presence of these species due to convolution. It is, however, useful to confirm the presence of mixed Cr/Fe oxides/hydroxides on the metal surface [105].

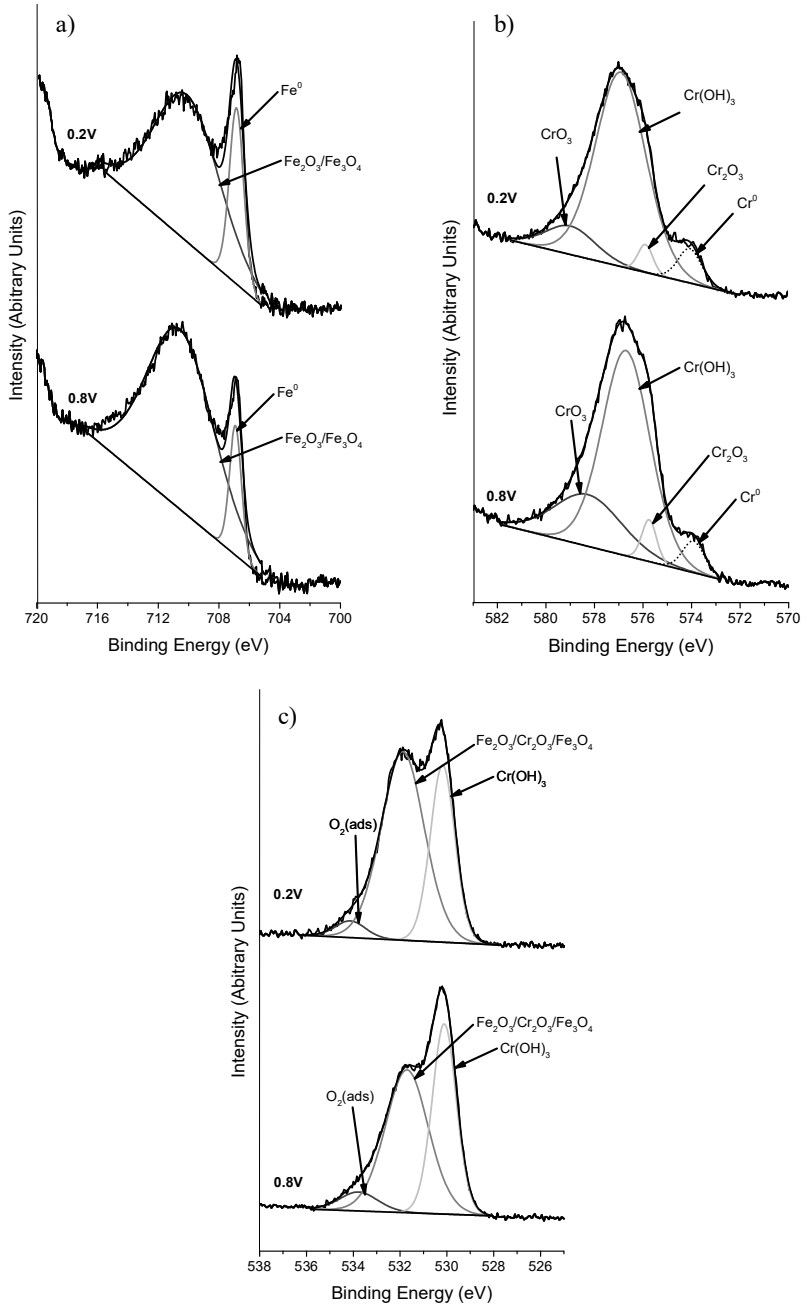

Figure 3-27 - XPS profile of a) Fe $2p_{3/2}$, b) Cr $2p_{3/2}$ and c) O 1s after passivation.

Due to the large number of species involved in Figure 3-27, and described above, compositional differences between the two potentials may be more easily understood by plotting the relative atomic percentages of each species for both the iron profiles of Figure 3-27a and the chromium profiles of Figure 3-27b. Such plots for both 0.2 and 0.8 V respectively are shown in Figure 3-28.

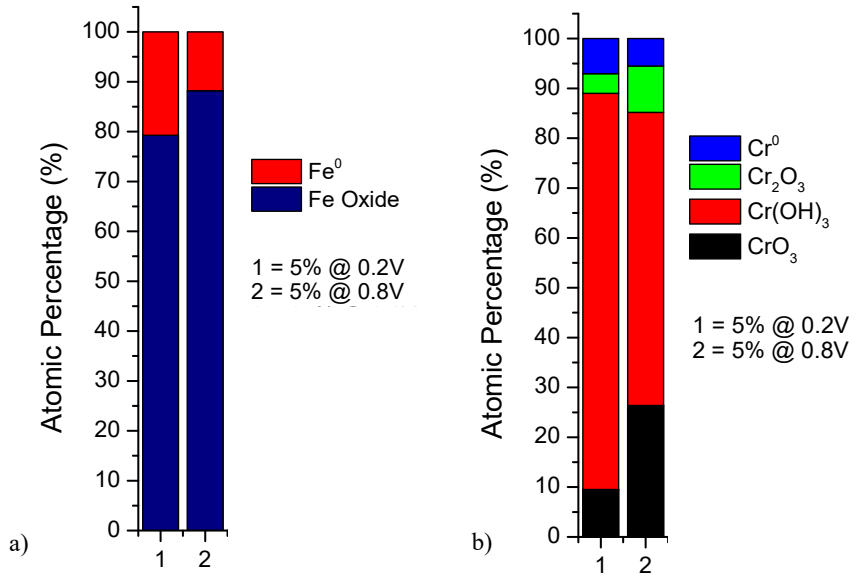

Figure 3-28 – Atomic Percentage data comparison for Fr (a) and Cr (b) results In both figures,, Bar 1 relates to data recorded at 0.2 V, Bar 2 relates to data recorded at 0.8V.

It can be seen from Figure 3-28 that increasing the potential to 0.8V leads to an increase in intensity of the Fe(III)/Fe(II/III) oxide peak at around 710.32 eV, suggesting an increase in Fe(III)/Fe(II/III) oxide concentration close to or at the steel surface.

It is important to note that at higher potentials Fe(II) is oxidised to Fe(III) [57], [178], [179]. The oxide composition at 0.8 V and above is therefore proportionally most likely dominated by Fe(III) oxide [57], [179].

Turning to the Cr results of Figure 3-28, it can be seen that increasing the potential to 0.8 V also increases the intensity of CrO_3 (Cr(VI)), whilst decreasing the intensity of the Cr^0 and $Cr(OH)_3$ signal. As discussed previously, and described by Padhy [65], Cr is more soluble in its Cr(VI) oxidation state, CrO_3, than its Cr(III) oxidation state Cr_2O_3/$Cr(OH)_3$ at this higher potential. The presence of Cr(VI) in the film is a necessary prerequisite prior to dissolution from the film. Ring disk electrode experiments by Betova *et al.* [180] show Cr(VI) dissolution at potentials >0.8V which is in agreement with EQCM results shown in Figure 3-22, where mass loss is observed at E≥0.85V. Thus, as with LSV, EIS and EQCM results, XPS results support the theory that an increase in potential to 0.8V leads to the oxidation of Cr(III) to Cr(VI) which will subsequently lead to dissolution of Cr(VI) from the film and a decrease in surface Cr^0/$Cr(OH)_3$

content as more chromium is converted to the higher valency state. Interestingly, while $Cr^0/Cr(OH)_3$ content decreases from 0.2 to 0.8 V, Cr_2O_3 content in the passive film increases from 0.2 to 0.8V. The origin of this increase is not described any further here, but in detail in the following chapter (section 4.5).

In conclusion, XPS investigation has shown that a passive film consisting of Cr hydroxide and Cr(III) oxide layers is formed at lower passive only potentials (0.2V), with said film having a higher concentration of Cr(VI) at potentials on the edge of the passive transpassive transition (0.8V), supporting previous results by Padhy [65] . The absence of a $Fe(OH)_3$/FeOOH signal in the iron profiles indicates that no Fe is present at the alloy/electrolyte interface further supporting the presence of a Cr-rich passive film.

3.5 Summary

In this chapter, the electrochemical behaviour of 316L SS in HNO_3 concentrations ≤15% wt. has been studied. LSV and EIS results indicate that in order to passivate 316L SS surfaces in HNO_3 concentrations of ≤15% wt. the applied potential needs to be <1 V to avoid transpassive dissolution of the Fe-Cr oxide film, and >-0.2 V to allow passivation to occur.

Using electrochemical techniques, we have established the viability of SS2343 as an analogue for 316L SS for EQCM studies. Further, using information gleaned from the LSV and EIS studies it has been shown that the EQCM can follow the *in-situ* mass change during electrochemically driven passivation and transpassive dissolution of a SS2343 piezoelectrode. Current and mass-response curves show that as a function of potential, while the current trace may suggest the steel is passive, in reality the film may not be fully formed or semi-porous and therefore will not provide full protection for the steel surface.

Through potential 'staircase' experiments, the potential was held for a longer time to assess mass change of SS 2343 as a function of HNO_3 concentration (5% wt. to 15% wt.). At HNO_3 concentration ≤15% wt., the maximum extent of oxide growth is observed at E=~0.55 V. Beyond this potential, transpassive processes, via either slow conversion of Cr(III) to Cr(VI) or full transpassive dissolution of $Cr(OH)_3/Cr_2O_3$ leads to a mass loss from the electrode surface.

XPS studies in 5% wt. HNO_3 have shown that at low potentials in the passive range (e.g. 0.2 V) a passive film consisting of Cr (III) hydroxide and Cr(III) oxide layers is predominant. At higher potentials on the edge of the passive-transpassive transition (0.8 V), the film shows a higher concentration of Cr(VI), in line with electrochemical and microgravimetric observations.

Having considered the electrochemical corrosion behaviour of 316L SS process steel at HNO_3 concentrations <15% wt., in the next chapter we now consider the behaviour of said steel in nitric acid concentrations >15% wt., typical of those found at head end fuel pin dissolution in a reprocessing process.

Chapter 4

Electrochemical, Microgravimetric and Surface Characterisation of 316L Stainless Steel Behaviour in Nitric Acid ≥20% wt.

4 ELECTROCHEMICAL, MICROGRAVIMETRIC AND SURFACE CHARACTERISATION OF 316L STAINLESS STEEL BEHAVIOUR IN NITRIC ACID CONCENTRATIONS ≥20% wt.

In the previous chapter, results from electrochemical and XPS experiments performed on 316L SS were analysed in HNO_3 concentrations ≤15% wt. Here, we examine the effect of HNO_3 at concentrations ≥20% wt. Such concentrations are common at head end dissolution of fuel rods, in highly active liquor evaporators and in initial uranium scrub and backwash steps. As with chapter 3, here we examine the corrosion behaviour of 316L SS under such conditions using: Linear Sweep Voltammetry, Electrochemical Impedance Spectroscopy, Microgravimetry and X-ray Photoelectron Spectroscopy.

4.1 Linear Sweep Voltammetry

In order to provide a preliminary assessment of what effect 'high' HNO_3 concentrations (≥20% wt. but ≤ 35% wt.) have on the electrochemical behaviour of 316L SS, linear sweep voltammetry was used to identify the point at which the steel corrodes, passivates and then transpassively dissolves in increasing HNO_3 concentrations.

Figure 4-1 shows the measurements from LSV experiments for 316L SS electrodes recorded in HNO_3 concentrations from 20-35% wt. (4.51 to 7.91 mol dm^{-3}) over the potential range -0.5 to 1.5 V. In order to provide comparison against lower HNO_3 concentrations, LSV results for 5-15% wt. HNO_3 have also been added to Figure 4-1.

A change in behaviour with increase in HNO_3 concentration is seen in Figure 4-1; however, due to the currents measured at higher HNO_3 concentrations it is difficult to make any comparisons. More information can be gathered from these measurements when the log of the current density is plotted against potential, as shown in Figure 4.2.

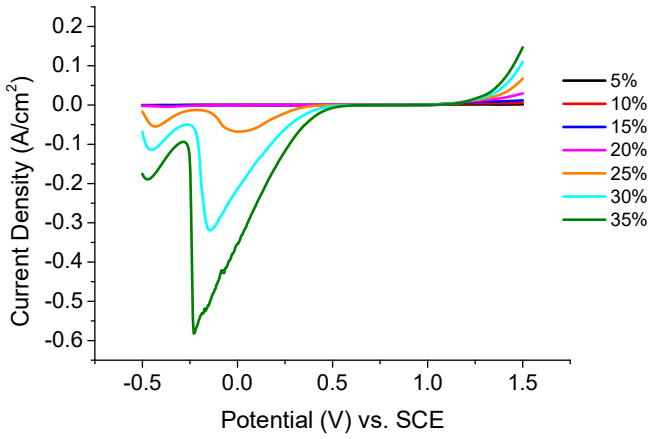

Figure 4-1 – Linear Sweep Voltammograms for 316L SS in 5-35% wt. HNO_3 at room temperature (20 ±2°C). Plots were measured in the potential range -0.5 to 1.5 V (sweep rate, 10 mV s^{-1}).

Figure 4-2 shows the potentiodynamic polarisation curves (log current density plotted against potential) for 316L SS electrodes recorded in HNO_3 concentrations from 5-35% wt. over the potential range -0.5 to 1.5 V.

From Figure 4-2, it can be seen that whilst there is a gradual increase in E_{corr} between 5% wt. and 15% wt. HNO_3,this increase dramatically accelerates between 15% wt. and 20% wt. (3.38 and 4.51 mol dm^{-3}) HNO_3. This is consistent with previous results reported by Otero [181], on 316L SS, and Whillock [182], on 304L SS, and may be explained as follows.

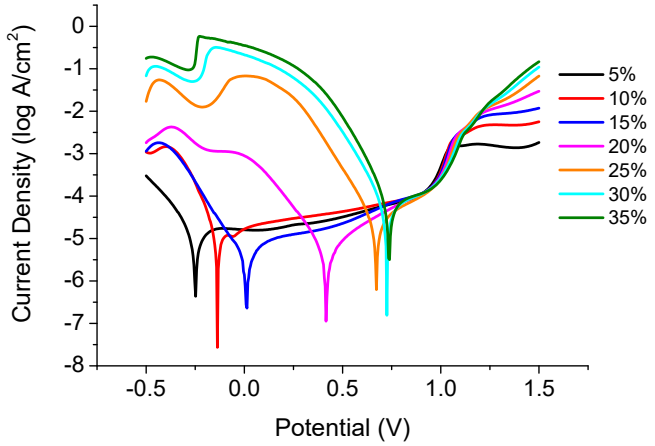

Figure 4-2 - Potentiodynamic polarisation plots of 316L SS in 5-35% wt. HNO_3 at room temperature (20 ±2°C). Plots were measured in the potential range -0.5 to 1.5 V (sweep rate, 10 mV s^{-1}).

As previously described in Chapter 3, the corrosion potential (E_{corr}) of the 316L SS surface in the presence of HNO_3 is controlled by the concentration of HNO_2 available to interact with the steel surface [6]. At low concentrations of HNO_3 (≤15% wt.) the autocatalytic regeneration of HNO_2, reaction (1.19) and (1.21) (if homogenous according to Schmid *et al.*) or reactions (1.22) and (1.24) (if heterogeneous according to Balbaud *et al.*), is slow due to the low HNO_3 concentration and associated low [HNO_2].

$$HNO_2 + H^+ + e^- \rightleftarrows NO + H_2O \tag{1.19}$$

$$2NO + HNO_3 + H_2O \rightleftarrows 3HNO_2 \tag{1.21}$$

However, at high HNO_3 concentrations (≥20% wt.) the regeneration of HNO_2 is fast due to the increased availability of HNO_3 driving reaction (1.23), and the increased thermodynamic stability of NO_2 at higher acidities [183].

$$HNO_3 + NO \rightleftarrows HNO_2 + NO_2 \tag{1.23}$$

Reaction 1.19 is believed by Balbaud *et al.* to be heterogeneous (see reaction (1.22)) at all acidities, something Lange *et al.* agrees with at high acidities (see reaction (1.30)). Both Balbaud *et al.* and Lange *et al.* agree that the reactions occurring after (1.19)/(1.22)/(1.30) have at least some heterogeneous character (see reactions (1.23), (1.24) and (1.32)-(1.35) although they differ in view as to their exact nature.

Nonetheless, the increase in HNO_3 concentration to >20% wt. HNO_3 leads to a change in the stoichiometric ratio for the reaction of (most likely adsorbed) NO with nitric acid from:

(i) $1NO_3^-$ to 2NO at [HNO_3] < 15% wt. (reaction (1.21)) to

(ii) $1NO_3^-$ to 1NO at [HNO_3] >20% wt. (reaction (1.23))

This means that HNO_2 regeneration is easier/quicker at higher HNO_3 concentrations as the ratio goes from 1:2 to 1:1.

Thus, charge transfer at the steel surface is not limited by the concentration of HNO_2, resulting in an increase in the observed corrosion potential and reduction in the window of passivation. The increased acidity may also lead to H^+ reduction, also leading to an increase in E_{corr}, whilst the surface of the steel may still be passive. This will be further investigated during EQCM, EIS and XPS experiments.

Considering now the region of transpassive dissolution, and specifically the region of secondary passivation (around 1 V in Figure 4-2), it can be seen that the thinning of the secondary passive Fe(III) oxide film demonstrated at 15% wt. HNO_3 continues at HNO_3 concentrations up to 25% wt. Secondary passivation is completely inhibited at HNO_3 concentrations ≥ 25% wt., as demonstrated by the almost completely linear current increase from the onset of transpassive dissolution (at ~0.9 V) to 1.5 V. As with our interpretation of this behaviour at 15% wt. HNO_3, this may be explained by the increased solubility of Fe(III) oxide in the presence of increasing HNO_3 and H^+ concentrations.

4.1.1 E_{corr} and i_{corr} Analysis.

Corrosion potential (E_{corr}) and corrosion current density (i_{corr}) were calculated using Tafel extrapolation of the linear segments of the measured potential-current density curves of Figure 4-2, in the vicinity of E_{corr}. Figure 4-3a shows E_{corr} values obtained at 5 - 35% wt. HNO_3 concentrations.

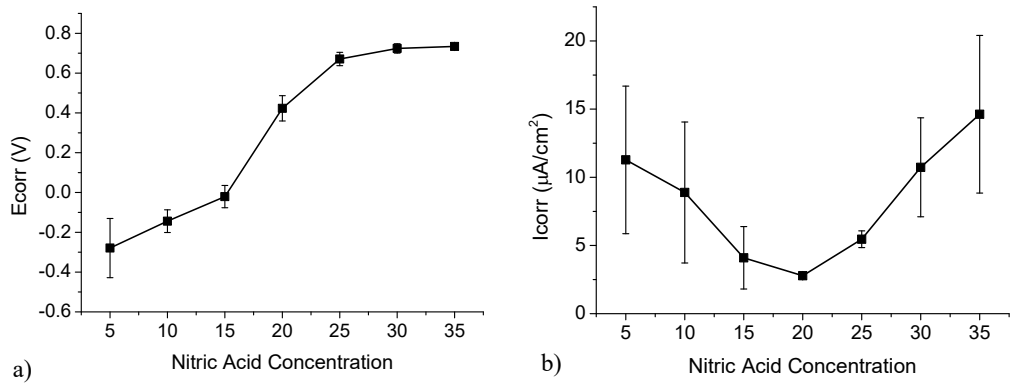

Figure 4-3 - a) Corrosion potential, E_{corr}, values vs. HNO_3 concentration b) Corrosion current density, i_{corr}. Values vs. HNO_3 concentration and associated error bars calculated from Figure 4-2a for 316L SS in 5 - 35% wt. nitric acid.

From Figure 4-3a it can be seen that E_{corr} varies sigmoidally with HNO_3 concentration, with E_{corr} increasing in the range 5 - 25% wt. HNO_3 (1.13 - 5.53 mol dm^{-3}) HNO_3, before plateauing at HNO_3 concentrations ≥25% wt. Again, this increase in E_{corr} may be explained by the increase in autocatalytic contribution of HNO_2 (due to the fewer number of surface adsorbed NO molecules required to react with HNO_3 at higher HNO_3 concentrations, see above) via reactions (1.33) to (1.35) at HNO_3 concentration ≥ 15% wt.

Figure 4-3b shows the calculated i_{corr} values for 5 – 35% wt. HNO_3. It can be seen from Figure 4-2b that i_{corr} values initially decrease with increasing HNO_3 at HNO_3 concentrations of ≤15% wt. Looking at Figure 4-2b it can be seen that the E_{corr} values associated with this decrease in i_{corr} increase with HNO_3 concentration. Assuming that E_{corr} = open circuit potential then comparison with Figure 4-3b would suggest that the decrease in i_{corr} with HNO_3 concentration may be associated with an increase in the thickness of the passivating oxide film (increase in E_{corr} into the passive region).

At HNO_3 concentrations ≥20% wt. (4.51 mol dm^{-3}) i_{corr} increases indicating that the passive oxide film on the surface of the steel is degrading resulting in an increase in the corrosion rate. Again assuming that E_{corr} = open circuit potential and comparing with Figure 4-3b such a potential would suggest that onset of Cr(III) to Cr(VI) oxidation is occurring (as shown by the small increase in current in Figure 4-3b). Such a passive-transpassive transition may be more easily understood through the construction of a pseudo-polarogram, whereby E_{corr} is plotted against i_{corr} for HNO_3 concentrations 5-35% wt. This is shown in Figure 4-4.

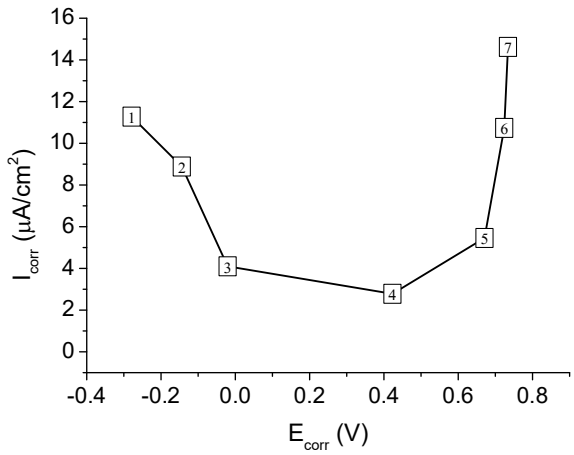

Figure 4-4 – Pseudo-polarogram of i_{corr} vs. E_{corr} (data points minus error bars for clarity) calculated from Figure 4-2a for 316L SS in 5 - 35% wt. (1-7 respectively) nitric acid.

Figure 4-4 shows that at HNO_3 concentrations of >20% wt., where E_{corr} >0.4 V, i_{corr} increases with increasing concentration of nitric acid as Cr(III) oxidises to soluble Cr(VI) in the passive film due to onset of early transpassive dissolution. The increase in E_{corr} and then i_{corr} due to chromium oxidation can also be linked to the autocatalytic regeneration of HNO_2. As described above, the increase in HNO_3 concentration to > 20% wt. changes the NO:HNO_3 stoichiometric ratio from 2:1 below 15% wt. to 1:1

above 20% wt. HNO_3 – meaning that nitrous regeneration is easier at the higher nitric concentration. In other words, HNO_2, which is now in abundance due to the stability of NO_2 at higher acidities, is no longer the limiting factor in the charge transfer at the steel surface, resulting in the increase in the observed corrosion potential. This passive to transpassive behaviour with increasing HNO_3 concentration is discussed in more detail in the following EIS and EQCM result sections.

4.2 Electrochemical Impedance Spectroscopy (EIS) Studies on 316L SS in Nitric Acid

In the previous chapter EIS was shown to be a useful technique when assessing small changes at the electrode surface, some of which may indicate passive film growth. Here, 316L SS in HNO_3 concentrations of $\geq$ 20% wt. were analysed in the same potential region (-0.5 to 1.5V vs. SCE) as the previous electrochemical studies in lower concentrations of HNO_3, to allow for comparison. Results obtained in this section are first presented using the raw experimental data in the form of Nyquist plots and E vs. Z' plots at low frequencies. The data is then modelled using Z-View2 impedance software and equivalent circuit, with the results are presented alongside LSV results.

4.2.1 Nyquist Plots

Figure 4-5 to Figure 4-11 shows resultant nyquist plots at -0.4, 0, 0.4, 0.8 and 1.2 V. As previously discussed in Chapter 3, at HNO_3 concentrations of $\leq$ 15% wt. the real impedance values obtained at potentials of -0.4V and 1.2V representative of the hydrogen evolution and transpassive dissolution regions of the steel are very low, indicating the surface of the steel is not fully passivated. However, at potentials of 0.4V and 0.8V, impedance values are several orders of magnitude higher indicating that a passive film has formed on the steel surface, as would be expected based on the LSV of Figure 4-2.

At HNO_3 concentrations $\geq$ 20% wt. impedance values in the passive region (0.4 and 0.8 V) decrease with increasing HNO_3 concentration. This is particularly apparent at nitric acid concentrations $\geq$25% wt., where the impedance values recorded at 0.4V decreases rapidly with increasing concentrations of HNO_3 in the range of 25-35% wt.

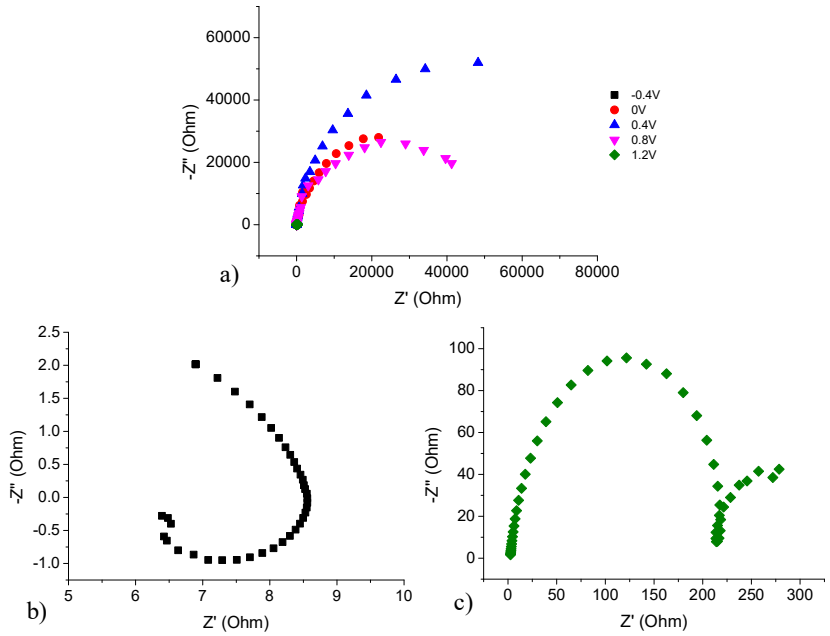

Figure 4-5 – Nyquist plots for 316L SS in 5% wt. HNO_3 solution at a) -0.4-1.2 V, b) -0.4 V and c) 1.2 V. -0.4 V and 1.2 V have been extracted for clarity. Axis scales have been altered to maximise variability visibility.

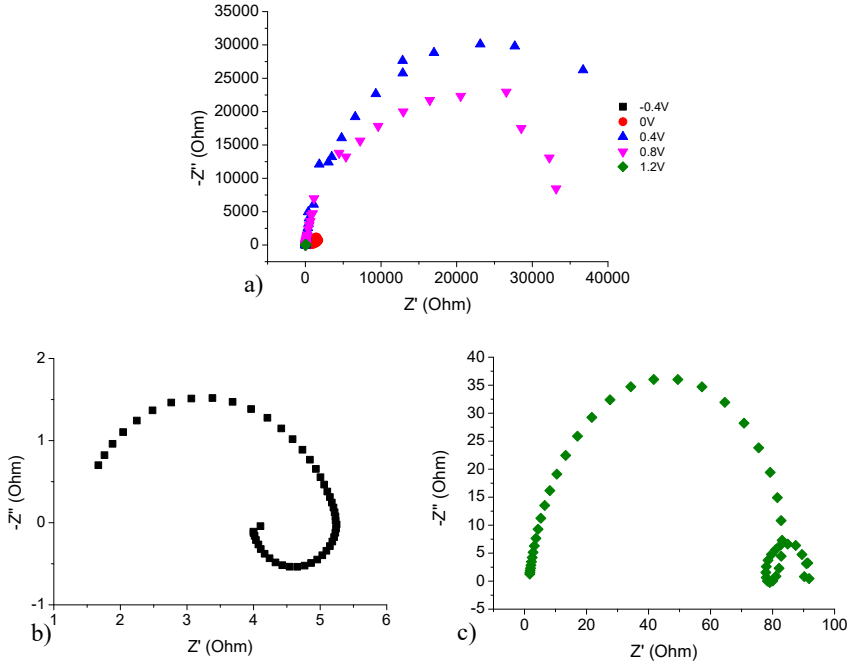

Figure 4-6 – Nyquist plots for 316L SS in 10% wt. HNO_3 solution at a) -0.4-1.2 V, b) -0.4 V and c) 1.2 V. -0.4 V and 1.2 V have been extracted for clarity. Axis scales have been altered to maximise variability visibility.

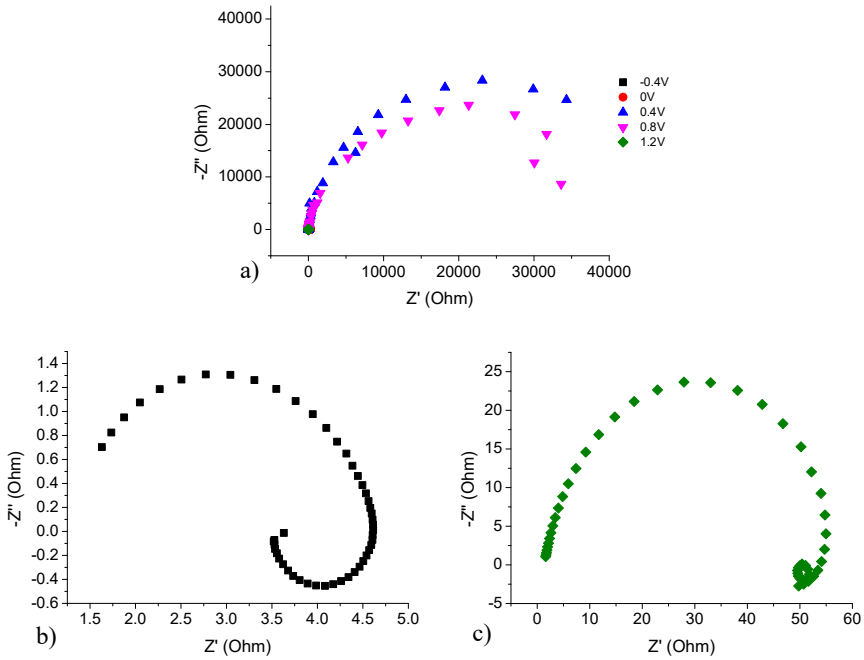

Figure 4-7 – Nyquist plots for 316L SS in 15% wt. HNO_3 solution at a) -0.4-1.2 V, b) -0.4 V and c) 1.2 V. -0.4 V and 1.2 V have been extracted for clarity. Axis scales have been altered to maximise variability visibility.

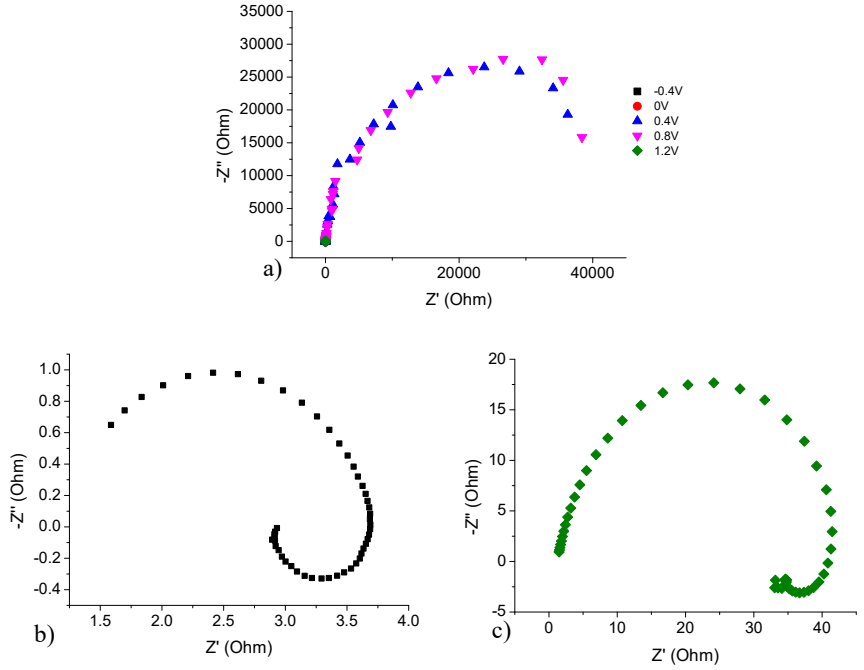

Figure 4-8 – Nyquist plots for 316L SS in 20% wt. HNO_3 solution at a) -0.4-1.2 V, b) -0.4 V and c) 1.2 V. -0.4 V and 1.2 V have been extracted for clarity. Axis scales have been altered to maximise variability visibility.

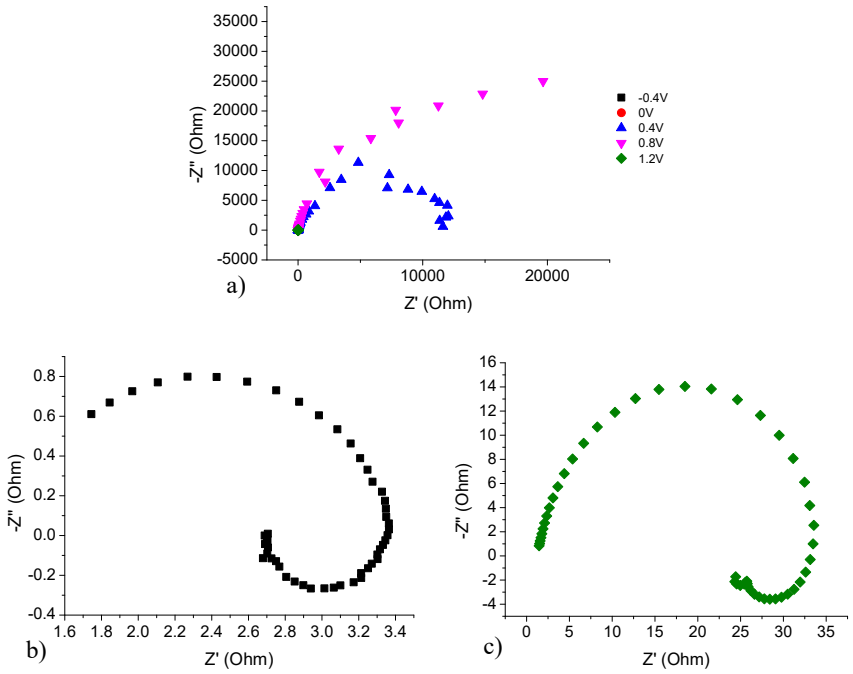

Figure 4-9 – Nyquist plots for 316L SS in 25% wt. HNO_3 solution at a) -0.4-1.2 V, b) -0.4 V and c) 1.2 V. -0.4 V and 1.2 V have been extracted for clarity. Axis scales have been altered to maximise variability visibility.

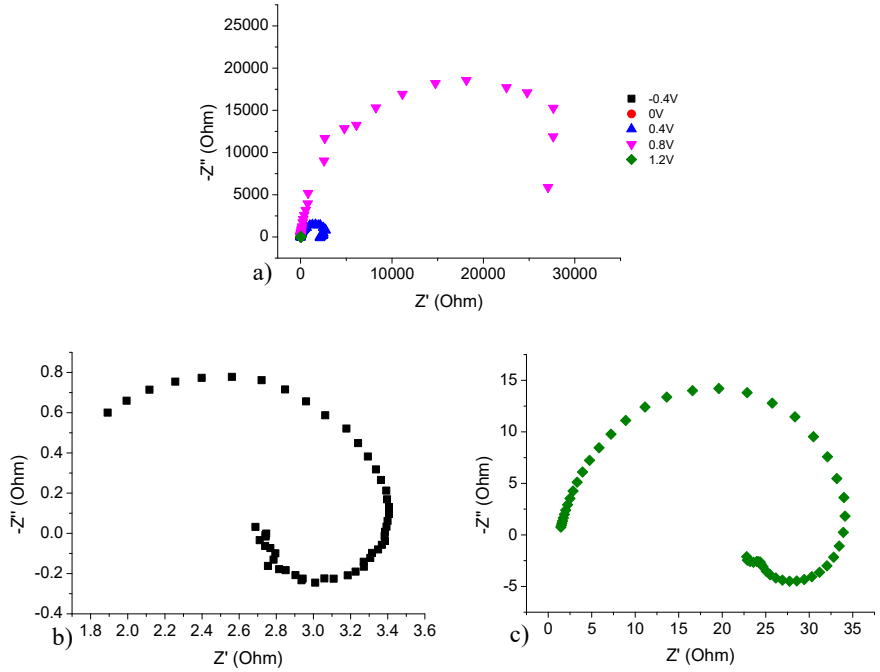

Figure 4-10 – Nyquist plots for 316L SS in 30% wt. HNO_3 solution at a) -0.4-1.2 V, b) -0.4 V and c) 1.2 V. -0.4 V and 1.2 V have been extracted for clarity. Axis scales have been altered to maximise variability visibility.

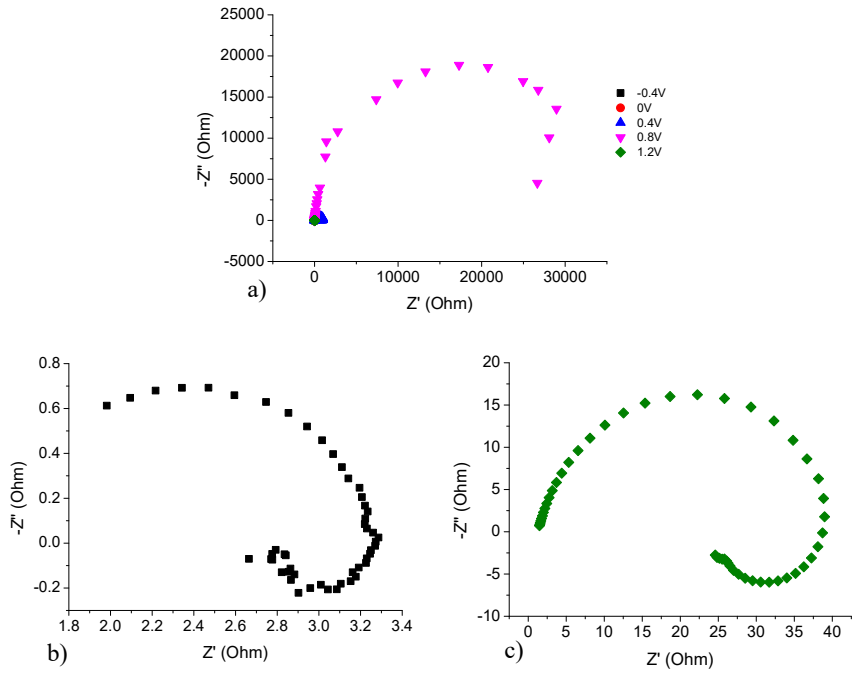

Figure 4-11 – Nyquist plots for 316L SS in 35% wt. HNO_3 solution at a) -0.4-1.2 V, b) -0.4 V and c) 1.2 V. -0.4 V and 1.2 V have been extracted for clarity. Axis scales have been altered to maximise variability visibility.

Impedance values also decrease with increasing HNO_3 concentration at potentials outside the normally passive region. As HNO_3 concentrations increase impedance values at 0V decrease significantly. At 10% wt. HNO_3, impedance values have a maximum of ~1000 Ohms whilst at 15% wt. values drop to ~150 Ohms. E_{corr} values are still below 0V (i.e. 0V is still within the passive range) therefore impedance values would be expected to be higher. One explanation for this, is it is possible that the increase in HNO_3 has led to an increase in H_2 evolution in the lower potential region. However, at higher HNO_3 concentrations, HNO_3 concentration ≥20% wt., E_{corr} is well above 0 V (i.e. 0V is in the nominally active region). Here, active corrosion/H_2 evolution leads to very low impedance values shown in Figure 4-12b.

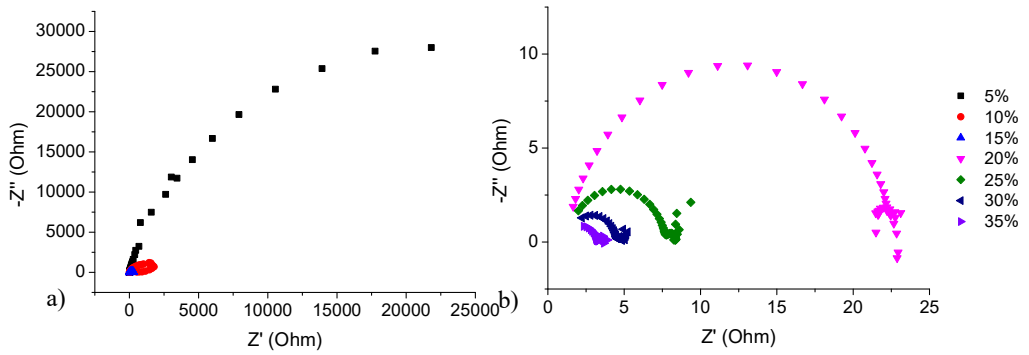

Figure 4-12 - Nyquist plots for 316L SS in a) 5-15% wt. HNO_3 solution and b) 20-25% wt. at 0V. Axis scales have been altered to maximise variability visibility.

Changes in what has been identified as the passive region at 5% wt. HNO_3 may be more easily assessed through analysis of impedance results taken in the passive region only (0, 0.2, 0.4, 0.6 and 0.8 V). Nyquist plots for these potentials are shown in Figure 4-13.

From Figure 4-13a it can be seen that high impedance values are measured at all potentials in 5% wt., indicating that the steel surface is passive in this potential region. As the HNO_3 concentration is increased to 10 and 15%, impedance values for 0 and 0.2 V decrease. The decrease in impedance at 0 V is discussed above; E_{corr} is lower than 0.2 V at 5-15% wt. HNO_3 (-0.25, -0.14 and 0 v respectively), yet the measured impedance follows the same pattern as that recorded at 0 V. It is unlikely that the steel surface is corroding at this potential, it is more likely that, the increased acidity at 10 and 15%, H_2 evolution is occurring at the surface of the steel leading to reduced impedance.

At HNO_3 concentrations ≥20% wt. the impedance values decrease more obviously at the lower potentials selected for study here (0, 0.2 and 0.4V), indicating a 'narrowing' of the passive film formation region. For example, at 0.4 V impedance values are high at 5-15% wt. HNO_3 at ~30,000-50,000 ohms. But as HNO_3 concentration is increased to 20% wt. the impedance drops to ~25,000 ohms. As HNO_3 concentrations increase above 20% wt. the impedance at 0.4V continues to drop to a few hundred ohms at 35% wt. At 20% E_{corr} is ~0.423 V, therefore, at 0.4 V the surface of the steel is likely to be actively corroding.

At HNO_3 concentrations ≥25% even impedance values recorded at 0.6 V are seen to decrease compared to those recorded at lower HNO_3 concentrations; here E_{corr} has risen to 0.67, with impedance values dropping from ~50,000 ohms to ~5,000 at 25% wt. to 35% wt. HNO_3 respectively. This region has been identified as the pre-transpassive region where Cr(III) is oxidised to Cr(VI) which subsequently dissolves into solution. The area is still passive but the passive film may not be fully formed leading to reduced impedance. This passive/transpassive transition will be addressed further in Polarisation Resistance plots in Section 4.2.3 and Microgravimetric studies in Section 4.4.

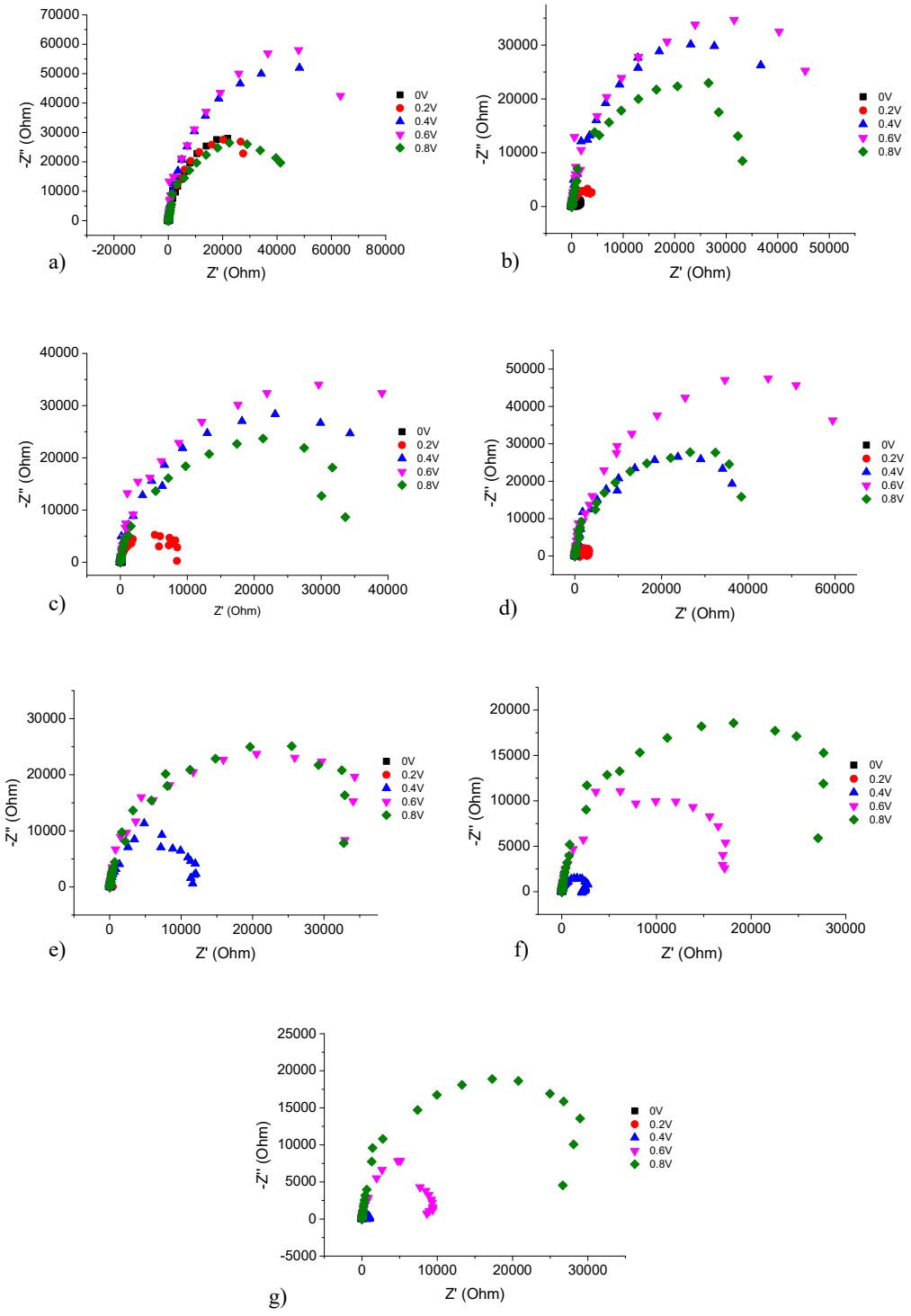

Figure 4-13 - Nyquist plots for 316L SS in 5-35% wt. HNO_3 (a-g) as a function of film formation potential. Axis Scales have been altered to maximise variability visibility.

4.2.2 Impedance vs. Potential Plots

As described in Chapter 3, differences in the real impedance, particularly in the low frequency region, may be tentatively related to changes in passivation of the steel. Thus, before applying equivalent circuit modelling to this data, simple real impedance vs. potential plots have been constructed and plotted alongside LSV data from the previous section. Such plots are shown in Figure 4-14 for impedance data recorded at a frequency of 0.3 Hz.

Considering first the plots at HNO_3 concentrations ≤ 15% wt. (a-c), as previously discussed in Section 3.2.2, impedance magnitude increases with potential as the passive region is entered and traversed. At 5 and 10% wt. HNO_3, there is an increase in impedance which then decreases before increasing into the main passive film. This is believed to be due to the formation of a precursor passive oxide film that is then converted at higher potentials to a full Cr(III) oxide passive film (see section 3.2.2 for a more detailed description).

Now looking at plots for HNO_3 concentrations > 15% wt. (d-g), while the passive window does decrease in width at higher HNO_3 concentrations (20 - 35% wt.), as shown in Figure 4-14 and summarised in Figure 4-15, passivation appears to be occurring at potentials below E_{corr}. For example, as can be seen from Figure 4-14d, for 20% wt. HNO_3 E_{corr} occurs at ~0.42 V whereas impedance is increasing at ~0.1 V. Also, at 35% wt. HNO_3 E_{corr} is at ~0.73 V but real impedance is increasing in magnitude at ~0.35 V. Such a result seems unrealistic considering the polarisation plots of Figure 4-2. Thus, as described previously, this result is most likely due to interpretation using real impedance vs. potential data being too much of a simplification and therefore not clearly defining whether the change in impedance around E_{corr} is directly related to changes in the passive oxide film resistance, double layer capacitance or solution resistance. For example, as discussed previously in Section 4.2.1, hydrogen evolution may have an effect on the real impedance values which may 'hide' the real behaviour of 316L SS in HNO_3. As such, the next section describes modelling the data using an equivalent circuit model to extract information on the oxide film resistance only.

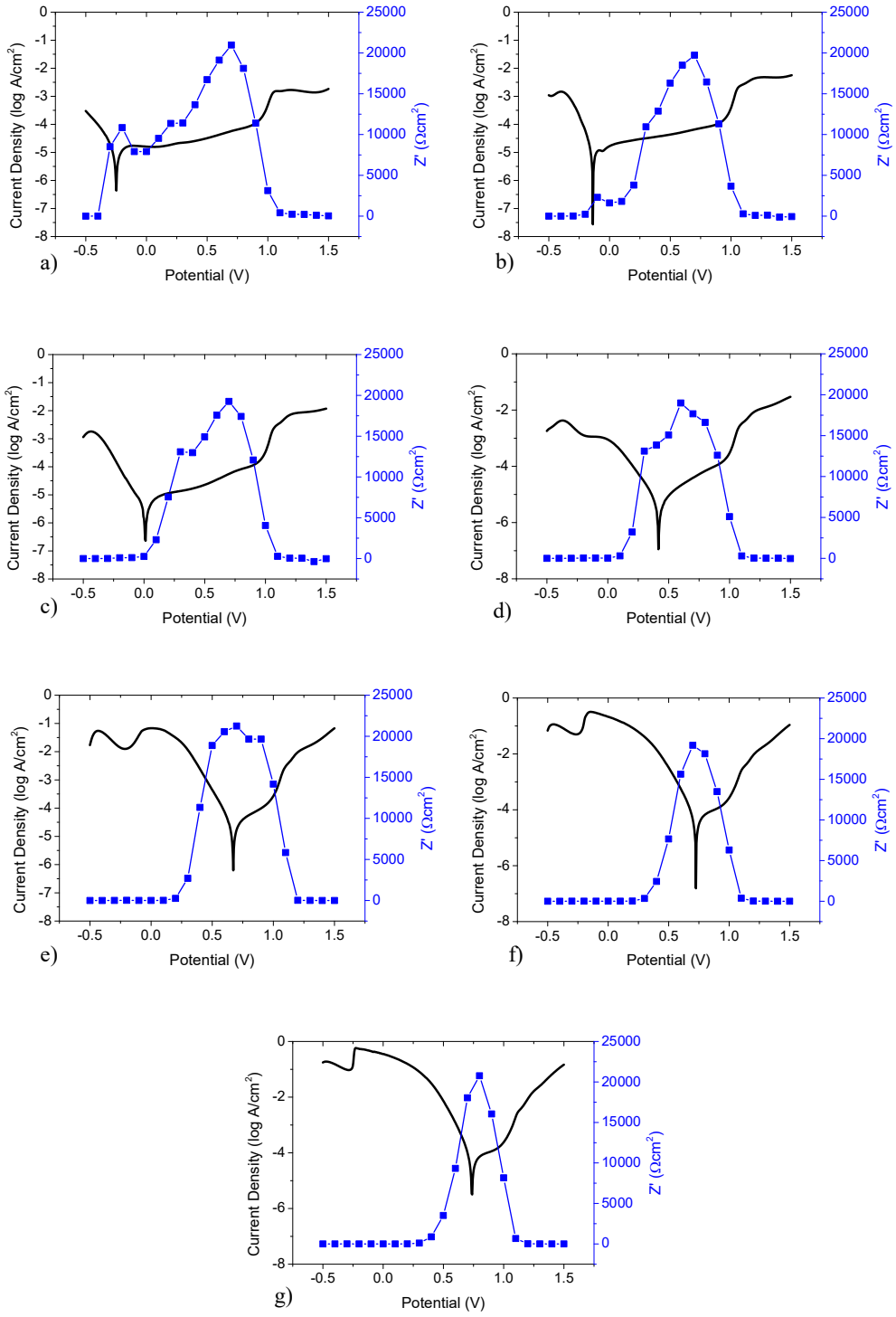

Figure 4-14 – Potentiodynamic polarisation curves plotted alongside low frequency impedance data for 316L SS in 5-35% wt. HNO_3 (a-g) as a function of potential.

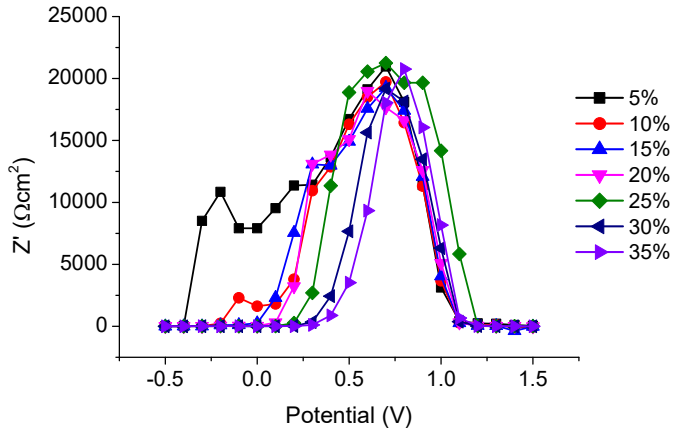

Figure 4-15 – Effect of potential on impedance magnitude of 316L in 5-35% wt. HNO_3 at 0.3 Hz.

4.2.3 Polarisation Resistance Measurements

4.2.3.1 Equivalent Circuit

Equivalent circuits were discussed fully in Section 3.2.3.1.

For lower HNO_3 concentrations (5-15% wt.), two equivalent circuits were considered to be appropriate for the results presented in Section 3.2.3. For potentials ≤0 V and ≥1 V a 3 component model containing C_{dl} and R_{ct} is considered the most accurate. The electrode is considered to be corroding, either actively or transpassively, therefore charge transfer at the electrode surface is occurring. At 0-1 V the surface is passive at these acid concentrations; thus, the more appropriate components would be CPE and R_p which measures the resistance and the imperfect capacitance of the surface formed passive film as shown in Figure 4-16.

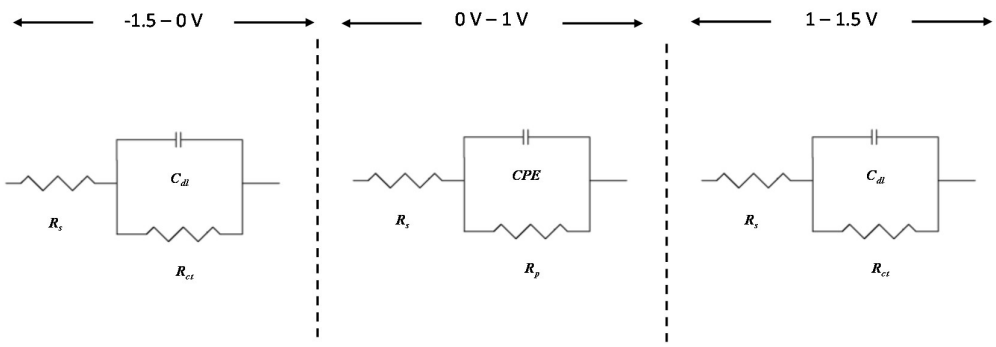

Figure 4-16 - Electrical equivalent circuit models used to represent an electrochemical interface undergoing corrosion at <0 V and >1 V and passivation in the region of 0-1 V. R_p is the polarization resistance, R_{ct} is the charge transfer resistance, C_{dl} is the double layer capacitance, CPE is the Constant Phase Element and R_s is the solution resistance.

For higher HNO_3 concentrations (20-35% wt.), three equivalent circuits were considered to be appropriate for the results presented here, as shown in Figure 4-17. Based on the work by Fattah-alhosseini *et al* [170], a number of complex equivalent circuit models were tested to describe the impedance / corrosion behaviour in lower (≤15% wt.) and higher (≥20% wt.) HNO_3 concentrations. The 3 component models shown in Figure 4-16 (≤15% wt. HNO_3) and Figure 4-17 (≥20% wt. HNO_3) gave the best fit for the data. In the model of Figure 4-17a, R_1 and R_2 represent the polarisation resistance at the electrode surface (R_1) and adsorption resistance (R_2) caused by adsorbed species at the electrode surface, such as H_2 or nitrate reduction species (e.g. NO). This model covers a wide potential range, from -1.5 V up to ~0.8 V.

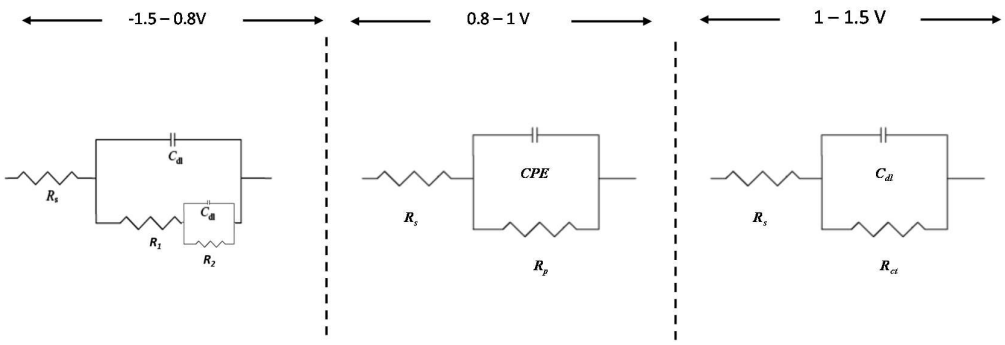

Figure 4-17 - Electrical equivalent circuit models used to represent an electrochemical interface undergoing corrosion at <0.8 V and >1 V and passivation in the region of 0.8 – 1 V. R_p is the polarization resistance, R_{ct} is the charge transfer resistance, C_{dl} is the double layer capacitance, CPE is the Constant Phase Element and R_s is the solution resistance.

However, as the main area of interest is still the central passive region, the simplest model for characterising the metal-solution interface is again the Randle cell of Figure 4-17b. As described in Chapter 2, Section 3.2.3.1, it includes the three essential parameters, R_s (solution resistance), CPE (the imperfect capacitance of the double layer) and R_p (the polarisation resistance) described above [130]. A simple model such as this is considered appropriate for analysis here because the Nyquist plots within the area of interest exhibit a single time domain semi-circle, with no obvious inductor loops. Chi-squared values of the order of $1x10^{-2}$ - $8x10^{-2}$ were obtained when modelling the data in Zview2, as shown in Appendix 2.

4.2.3.2 Polarisation Resistance (R_p) Plots

Figure 4-18(a-g) shows potentiodynamic polarisation curves plotted with calculated polarisation resistance (R_p) data for 316L SS in HNO_3 concentrations from 5-35% wt., over the potential range -0.5 – 1.5 V. The polarisation resistance (R_p) was again calculated in ZView2, using the simple equivalent circuit model, Figure 4-17b, described in section 4.2.3.1 to model the experimental impedance data. R_p represents the resistance of any passivating film that has been formed on the electrode surface. Thus, an increase in R_p is interpreted here as the formation, stabilisation and possible increase in the thickness of the surface oxide layer. Plotting R_p data alongside LSV data allows for a direct comparison with LSV

studies. This is shown in Figure 4-18, along with data for HNO_3 concentrations < 15% wt. from Chapter 3 for comparison.

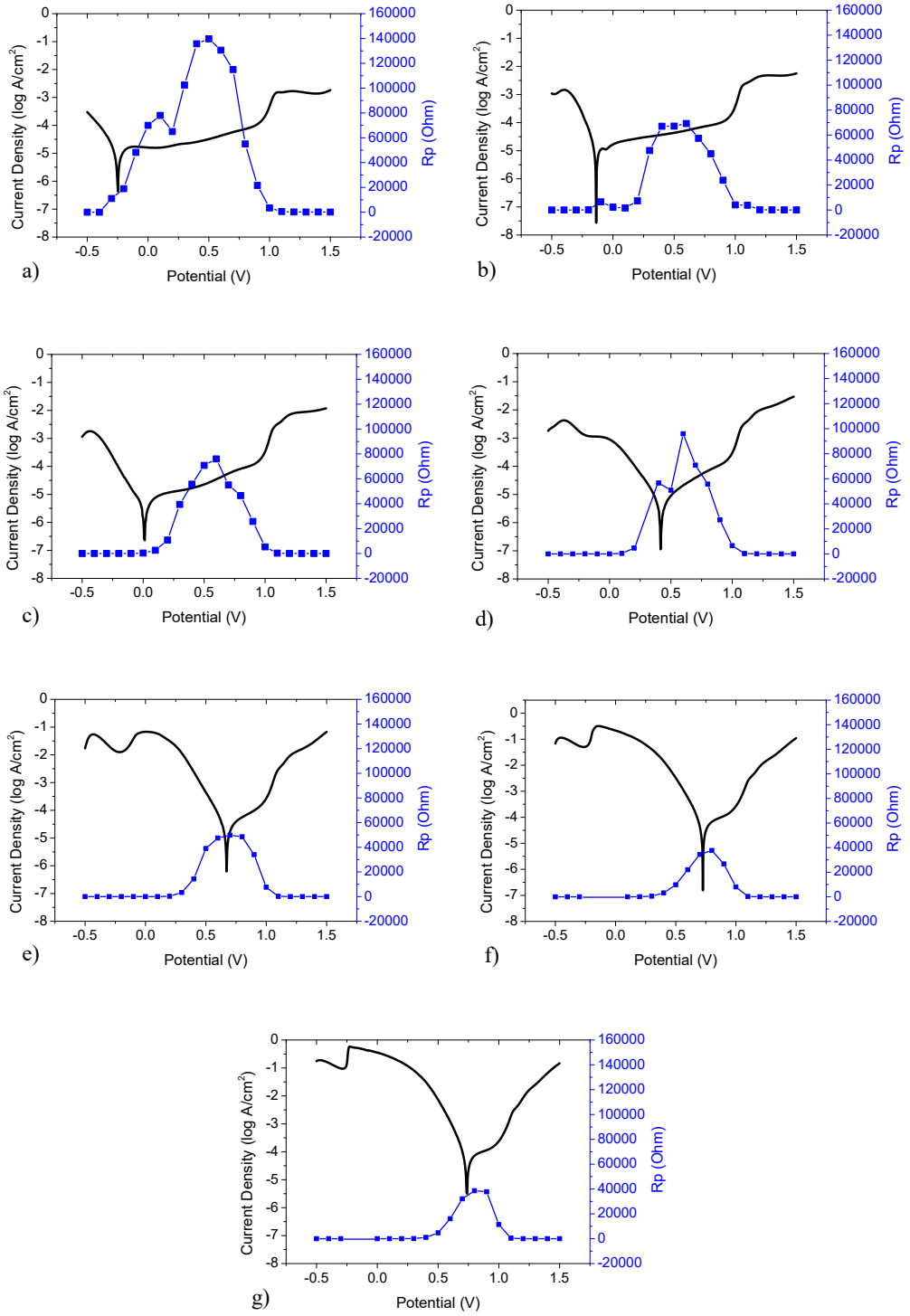

Figure 4-18 - Potentiodynamic polarisation curves from Figure 4-2 plotted with impedance data for 316L in 5-35% wt. (a-g respectively) nitric acid.

Consider first, the cathodic region of the R_p vs potential plots in Figure 4-18. Looking at the R_p vs potential plot obtained at 20% wt. HNO_3, Figure 4-18d, it can be seen that the initial onset of the increase of R_p with potential, and the breadth and height of the R_p peak are all very similar to those features recorded at 15% wt. HNO_3. Further, while the peak in the R_p plot still remains in the passive region at 20% wt. HNO_3, there appears to be some oxide growth just prior to E_{corr}, a feature not seen at HNO_3 concentration < 20% wt. Comparing Figure 4-18d with the pseudo-polarogram of Figure 4-4 reveals that actually i_{corr} (and thus the rate of corrosion) is low at 20% wt. HNO_3 compared to values of E_{corr} observed at > 20% wt. Thus, it is reasonable to conclude that 20% wt. HNO_3, considered the onset of NO_2 thermodynamic stability by Lange *et al.* [7], is a transition point where E_{corr} is increasing due to the increased participation of NO_2 in the mechanism associated with HNO_3 reduction (see Equations *(1.19)* - *(1.23)*, page 125). It should be noted that whilst this transition in NO_2 stability is occurring at 20% wt. HNO_3, its effect on passivity and corrosion rate at this acidity is minimal, a conclusion supported by the i_{corr} measurements of Figure 4-3b. Polarisation curves plotted with R_p and capacitance, shown in Figure 4-19, also support this conclusion. Capacitance values decrease at potentials well before E_{corr} values are reached at higher HNO_3 concentrations, behaviour typical to a thickening oxide layer. This, the HNO_3 reduction reaction and its products may be electrochemically masking passivation at HNO_3 concentrations ≥20% wt.

At ≥25% wt. HNO_3 the breath and height of the R_p peak in the R_p vs potential plot begins to decrease with respect to that seen at 20% wt. HNO_3 as E_{corr} shifts evermore positive and E_{corr} is pushed into the region of pre-transpassive dissolution. Such observations are in good agreement with the pseudo-polarogram of Figure 4-4.

The decrease in R_p at ~1 V in almost all of the R_p vs potential plots of Figure 4-19 has been previously attributed to the onset of transpassive dissolution. The oxidation of Cr(III) to Cr(VI) leads to the dissolution of the more soluble Cr(VI) subsequently reducing the effectiveness and effective thickness of the passive oxide film. This leads to the subsequent reduction in film resistance and simultaneous increase in capacitance, as shown in Figure 4-19.

The results of Figure 4-19 also indicate that a secondary film is possibly being formed at high potentials in high HNO_3 concentrations. Capacitance values decrease at ~1.25 V, a result that would be consistent with the thickening of a surface oxide film. This occurs in line with an increase in R_p values at >1V in

HNO_3 concentrations ≤15%. This is not clear in the polarisation curve plots or R_p plots at higher HNO_3 concentrations (≥20% HNO_3), this may be due to oxygen evolution masking the formation of this film in high HNO_3, high potential conditions and the secondary passive film not being as effective as passive films formed at lower potentials.

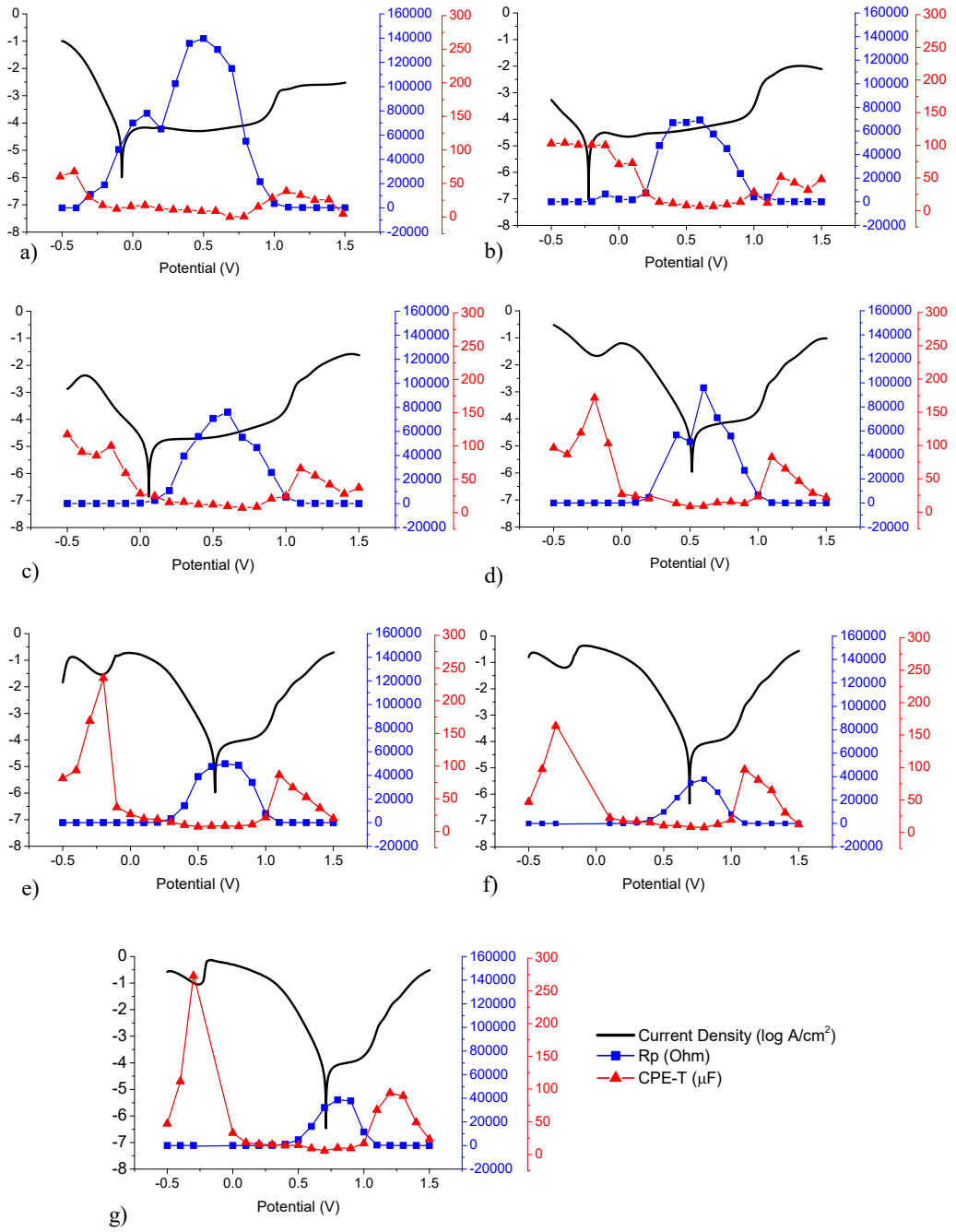

Figure 4-19 - Potentiodynamic polarisation curve plotted with impedance (blue) and capacitance (red) data for 316L SS in a-g (5-35% wt. HNO_3 solution) as a function of potential.

4.3 Analysis of the Nitric Acid Reduction Mechanism on 316L SS Using Rotating Disk Electrode Studies

We have shown in the preceding sections that there is a distinct change in 316L SS corrosion behaviour at HNO_3 concentrations ≥ 25% wt. This has been suggested to be due to the increased stability of the HNO_3 reduction product NO_2 at HNO_3 concentrations ≥ 25% wt., which, via a solution phase hydrolysis reaction (1.35) significantly increases the concentration of active corrosion reagent HNO_2. The electrochemical corrosion studies reported in this thesis have thus far been performed under stagnant conditions, where HNO_2 diffuses to the electrode surface and is reduced to NO during the concomitant oxidation of the steel. However, under reprocessing conditions continuous flow would be induced which would therefore have two effects on the reduction of HNO_2 and consequently the corrosion of the steel: (1) Increased diffusion of HNO_2 to the electrode surface and (2) increased formation of NO_{ads} via HNO_2 oxidation of the steel.

Therefore in order to investigate the effect of solution flow on the steel corrosion process and more closely examine the reduction of HNO_2 at the steel surface, Rotating Disk Electrode (RDE) studies were performed using 316L SS disks. Importantly, passive oxide formation has been shown to inhibit nitric acid reduction on the steel surface [6]. Thus, in order to study the HNO_3 reduction mechanism in more detail, polarisation curves were first run in reverse, scanning cathodically from the transpassive region, in order to remove, or at least compromise, the passivating layer on the steel first. Figure 4-20 shows an example of a non-rotating, cathodically scanned polarisation curve of 316L SS in a 5% wt. HNO_3 solution.

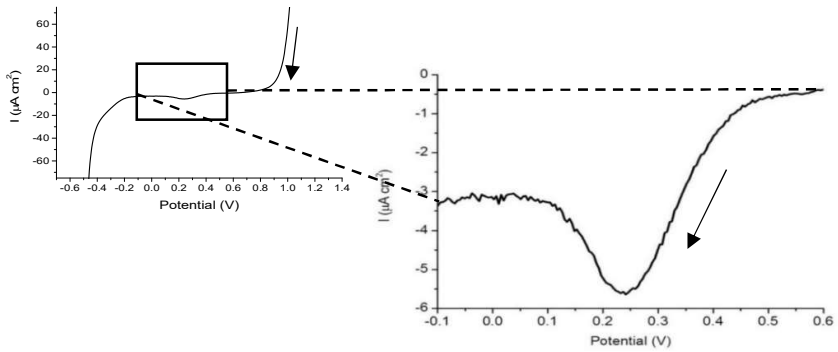

Figure 4-20 - Polarisation curve showing a cathodic scan of 316L SS in 5% wt. wt HNO_3. Plots were measured in the potential range 1.5 to -0.5 V nitric acid at a rate of 10 mV s^{-1}.

Figure 4-20 shows a cathodic scan of 316L SS in 5% wt. HNO_3. Importantly, a new current peak is observed in the 0.1 to 0.4 V region, which for the reader's convenience is shown in greater detail in the inset of Figure 4-20. This peak has been attributed to the surface electrode reaction from reactions 1.22 and 1.24 [7]:

$$HNO_{2(el)} + H^+ + e^- \rightleftarrows NO_{(ads)} + H_2O \tag{1.22}$$

$$2NO_{(ads)} + HNO_3 + H_2O \rightleftarrows 3HNO_{2(el)} \tag{1.24}$$

Where HNO_2 is reduced at the electrode to, in the first instance, Nitrogen Monoxide (NO) [7]. The decrease in the reduction current at potentials negative of the peak at 0.25 V has been attributed by Lange [7] to the further reduction of NO in a two-step mechanism to N_2O. As such the maximum current density for the main HNO_2 to NO reduction process observed at 0.25 V was selected as the applied potential for all subsequent rotation speed studies.

Moving now to rotating disk electrode studies, Figure 4-21 shows a plot of current density vs. angular velocity at 0.25 V in 5, 20 and 35% wt. nitric acid.

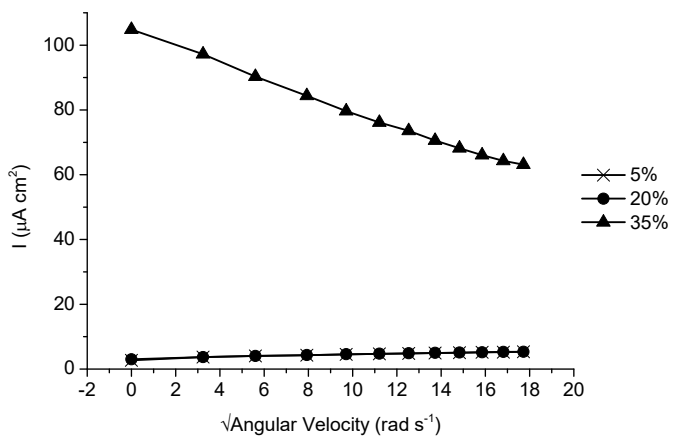

Figure 4-21 – Current Density vs. Angular Velocity at 0.25 V/SCE as a function of HNO_3 concentration.

Figure 4-21 shows that at nitric acid concentrations of 5 and 20% wt., current density is mostly independent of rotation speed. This indicates that the net HNO_3 reduction reaction of equations (1.22) and (1.24) is mediated by electroactive species that are entirely adsorbed at the electrode surface. At a concentration of 35% wt. HNO_3 the reduction current is substantially greater than that recorded at 5 and 20% wt. HNO_3 concentration and decreases with increasing rotation speed. This indicates that the

formation of the electroactive species (or precursor) must be occurring in the bulk solution phase for such a dependency to be apparent.

According to Abel & Schmid [89]–[91] and supported by Balbaud [5], Fauvet [6] and Lange [7] the electroactive species in this reaction is believed to be HNO_2. At 5 and 20% wt. (1.13 and 4.51 mol dm^{-3}) HNO_3, the observed current increases slightly with increasing rotation speed. This is most likely due to the increased flux of HNO_3 to the steel surface, allowing it to react with surface adsorbed NO via reaction (1.24). Compared to results recorded at 35% wt. HNO_3, electrode rotation at 5 and 20% wt., HNO_3 concentration has little influence because the reaction is following the Balbaud [5] and Fauvet [6] reaction mechanism of reactions (1.22) - (1.24), where the electroactive reaction intermediates, or their immediate precursors, are adsorbed at the electrode surface.

At 35% wt. (7.89 mol dm^{-3}) the rotation of the electrode leads to a decrease in the current density. This inverse dependence of the current density on rotation speed is consistent with the loss, due to the stirring, of the electroactive species, or the species that reacts with said electroactive species, such as NO, which subsequently slows down the kinetics of the process. At the higher HNO_3 concentration of 35% wt. NO_{ads} is rapidly produced at the electrode surface, the resultant excess of NO_{ads} leading to its subsequent desorption. This desorption allows NO_2 formed in solution via reactions (1.32) and (1.33) [7] to react and regenerate the electroactive species, HNO_2 via reaction (1.34).

$$HNO_{2(aq)} + H^+ \rightleftarrows NO^+_{(ads)} + H_2O \tag{1.29}$$

$$NO^+_{(ads)} + e^- \rightleftarrows NO_{(ads)} \tag{1.30}$$

$$NO_{(ads)} \rightleftarrows NO \qquad \{1.31)$$

$$HNO_2 + H^+ + NO_3^- \rightleftarrows 2N_2O_4 + H_2O \tag{1.32}$$

$$N_2O_4 \rightarrow 2NO_2 \tag{1.33}$$

$$NO_2 + NO + H_2O \rightleftarrows 2HNO_2 \tag{1.34}$$

As the angular velocity increases, the faster stirring of the solution leads to the dispersal of NO and NO_2 into the bulk solution, preventing the regeneration of HNO_2, thus, retarding the autocatalytic cycle and leading to the decrease in the current density observed in Figure 4-21 [80].

At 35% wt. HNO_3 the mechanism proposed by Balbaud [5] and Fauvet [6] for HNO_3 concentrations >20% wt., equations 1.22 and 1.23 (shown below), may still occur in parallel at the electrode surface with near-surface solution phase reactions [7], albeit more rapidly than at lower concentrations of nitric acid, due to the increased thermodynamic stability of NO_2 at this higher HNO_3 concentration.

$$HNO_{2(el)} + H^+ + e^- \rightleftarrows NO_{(ads)} + H_2O \tag{1.22}$$

$$HNO_3 + NO_{(ads)} \rightleftarrows HNO_{2(el)} + NO_{2(ads)} \tag{1.23}$$

Results from RDE studies on HNO_2 regeneration support LSV and EIS studies in sections 4.1 and 4.2. The shift in E_{corr}, i_{corr}, corrosion rate and the decrease in R_p peak size and maximum peak values observed at HNO_3 concentrations ≥20% wt. in section 4.1 can be explained by the increased stability and so ease of formation of NO_2 in the solution phase. The NO that is produced in reaction (1.29), and then desorbed, will react with the now stable NO_2 to produce more HNO_2, thereby increasing the corrosion rate at the electrode surface. This increases the oxidative power of the nitric acid media which leads to the increase in E_{corr}. With the introduction of 'stirring' the HNO_2 would be removed from the near-surface region of the electrode, reducing the corrosion rate.

4.4 In-situ Microgravimetric Studies of Passive Behaviour on SS2343 (316L Analogue) in Nitric Acid

4.4.1 Introduction

Through the previous LSV, EIS and RDE analysis we have now characterised the corrosion behaviour of 316L SS in HNO3 concentrations from 20-35% wt. However, we have only briefly studied the growth of the oxide film via EIS. Thus, the following EQCM and XPS sections focus on the passive region of the LSV's of section 4.1 and attempt to further understand the level of growth and character of the so

formed oxide layer. This first section (4.4.2) deals with the EQCM measured mass change of SS2343 (316L SS equivalent) in HNO_3 concentrations of ≥ 20% wt.

4.4.2 EQCM LSV/Voltamassogram studies

As per section 3.3.3, polarisation curves were recorded from 0 V (for comparison purposes, even though low passive potentials are higher at these HNO_3 concentrations) to 1 V (transpassive dissolution) using the SS2343 piezoelectrode with simultaneous measurement of the associated mass change via EQCM. Figure 4-22 – Figure 4-28 shows the recorded voltamassograms for 316L SS in 5-35% wt. HNO_3. Measurements performed at concentrations ≤15% wt. are previously discussed in Section 3.3.3, and are included here for comparison.

As discussed in Chapter 3 and briefly described again here, EQCM studies at lower HNO_3 concentrations (≤ 15% wt. HNO_3) reveal that, as can be seen in Figure 4-22 and Figure 4-23, at 5 and 10% wt. HNO_3 the observed mass increase in the passive region is very similar, indicating that the film formation mechanism is the same in both concentrations. The main difference between these two concentrations is the earlier onset of Cr(III) oxidation (~0.6 V vs. ~0.75V), presumably due to the increased solubility of Cr oxides at a lower pH.

At 15% wt. HNO_3 film formation behaviour changes with, as can be seen in Figure 4-24, the mass of the steel piezoelectrode slowly decreasing with increasing potential at potentials > ~0.05V. An overall mass loss occurs at all potentials, this mass loss has been attributed to a porous Cr oxide allowing the continuous dissolution of Fe while maintaining primary passivity. A net mass loss is observed because the negative mass change from the dissolution of iron exceeds the positive mass change resulting from chromium oxide film growth, a behaviour previously observed by by Schmutz and Landolt [73].

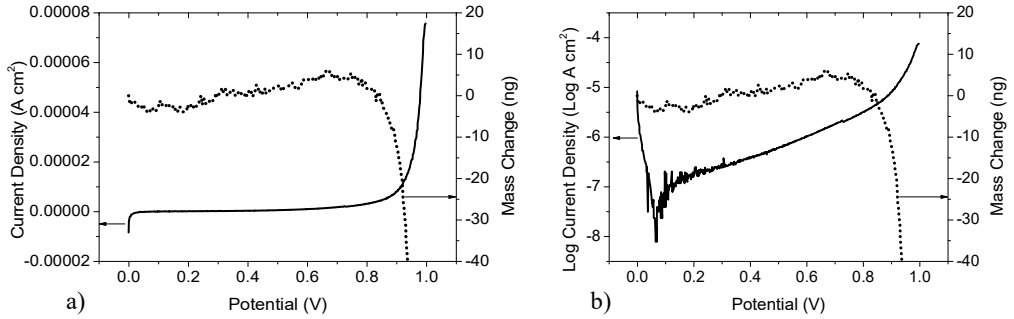

Figure 4-22 – a) Linear Sweep Voltammogram and b) Potentiodynamic polarisation curves of SS 2343 in 5% wt. HNO_3. Sweep rate = 10 mV s^{-1}.

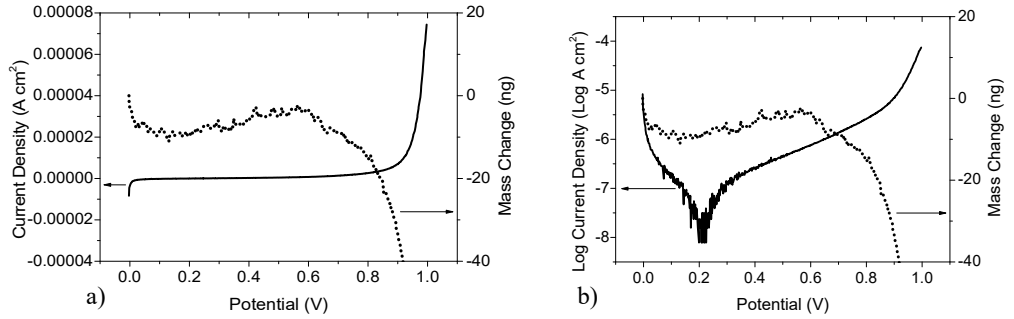

Figure 4-23 – a) Linear Sweep Voltammogram and b) Potentiodynamic polarisation curves of SS 2343 in 10% wt. HNO_3. Sweep rate = 10 mV s^{-1}.

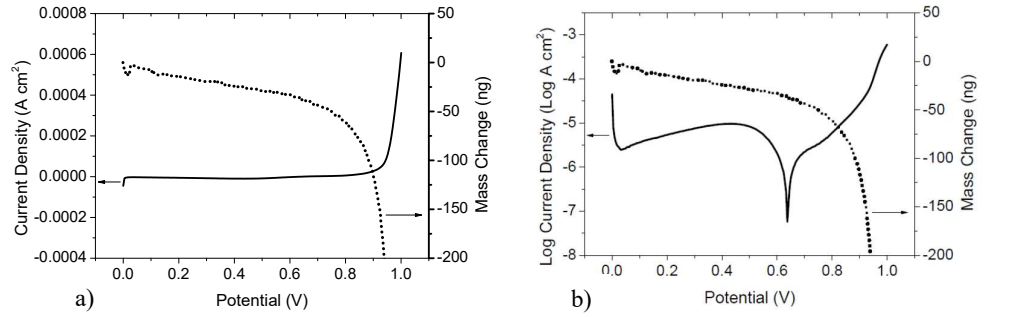

Figure 4-24 – a) Linear Sweep Voltammogram and b) Potentiodynamic polarisation curves of SS 2343 in 15% wt. HNO_3. Sweep rate = 10 mV s^{-1}.

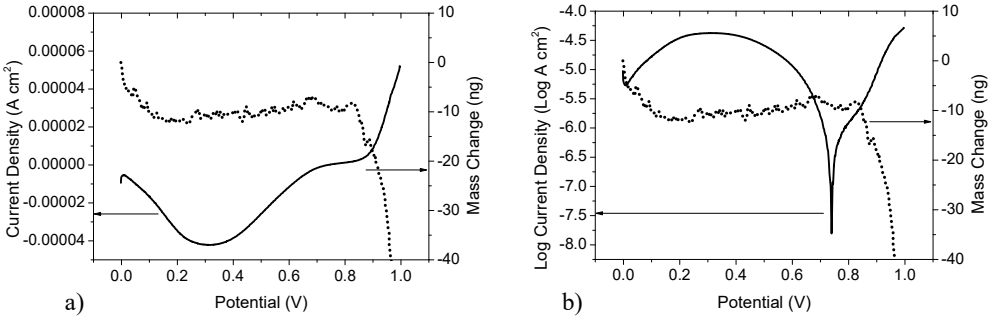

Figure 4-25 – a) Linear Sweep Voltammogram and b) Potentiodynamic polarisation curves of SS 2343 in 20% wt. HNO_3. Sweep rate = 10 mV s^{-1}.

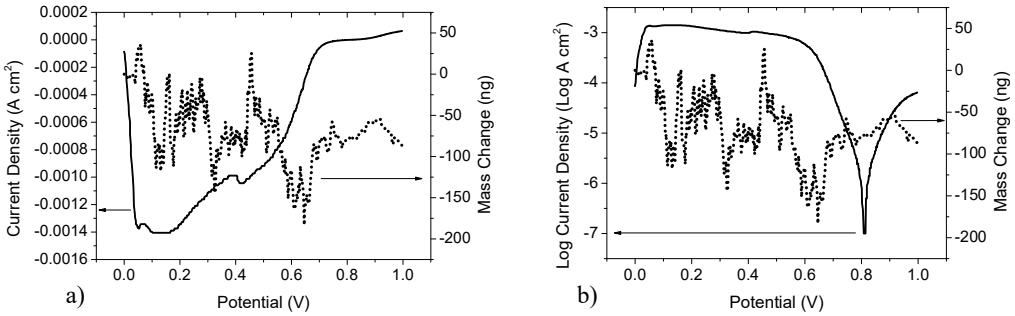

Figure 4-26 – a) Linear Sweep Voltammogram and b) Potentiodynamic polarisation curves of SS 2343 in 25% wt. HNO_3. Sweep rate = 10 mV s^{-1}.

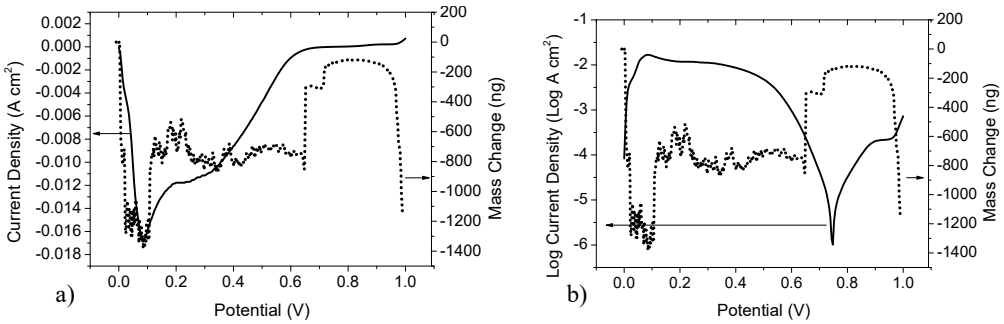

Figure 4-27 – a) Linear Sweep Voltammogram and b) Potentiodynamic polarisation curves of SS 2343 in 30% wt. HNO_3. Sweep rate = 10 mV s^{-1}.

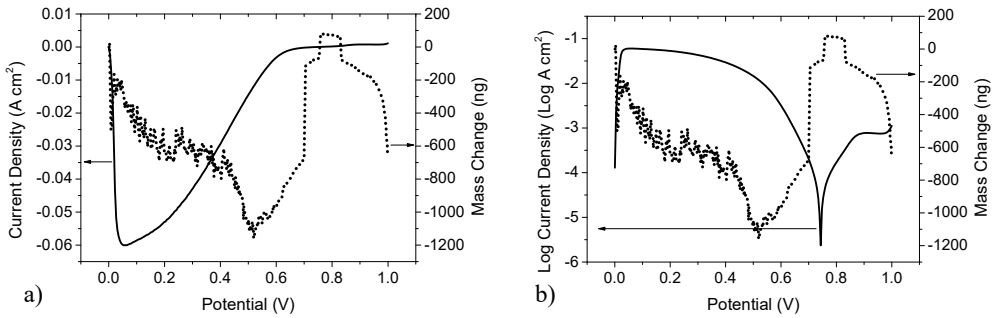

Figure 4-28 – a) Linear Sweep Voltammogram and b) Potentiodynamic polarisation curves of SS 2343 in 35% wt. HNO_3. Sweep rate = 10 mV s^{-1}.

At 20% wt. HNO_3 a change in current behaviour is observed (Figure 4-25). However, the mass change vs potential plot does not appear to be greatly affected compared to that seen at 15% wt.HNO_3 (Figure 4-24). It has previously been suggested, in sections 4.1 and 4.2, that 20% wt. HNO_3 is a transitional concentration. At 20% wt. HNO_3 the current behaviour alters due to a change in HNO_3 reduction mechanism which is linked to increased NO_2 thermodynamic stability in solution at higher HNO_3 concentrations. However, the effect on corrosion and, therefore, mass change is still minimal. At ~0.4 V, after an initial mass loss, mass begins to increase. This ties in well with LSV studies which show that in 20% wt. HNO_3 above this potential the steel is passive. Mass increases to ~0.7 V and starts to rapidly decrease at ~0.8 V. This is also in good agreement with LSV studies which show that in this region the passive film begins to dissolve as the steel enters the transpassive regime.

At HNO_3 concentrations ≥25% wt. both current and mass traces are substantially different to those recorded at HNO_3 concentrations ≤20% wt. However, both the current and mass trace then do not alter much at concentrations greater than 25% wt. Below E_{corr}, 0.671 (25% wt.), 0.724 (30% wt.) and 0.734 (35% wt.), each of the voltamassogram traces are very 'noisy' with large jumps between mass loss and mass gain. There are two processes that are potentially contributing to the 'noisy' voltamassograms 1) Hydrogen evolution and iron dissolution, with iron dissolution occurring below E_{corr} and hydrogen evolution obtaining to ever higher potentials with increasing acidity; and 2) Metastable pitting. The formation of metastable pits and then repassivation could cause rapid fluctuations in mass loss and gain. It is likely that a combination of the two processes described above are contributing to the 'noisy' voltamassogram rather than just one process, however, deconvolution of these two processes is difficult. The change in behaviour from a stable passive steel surface, to a less stable corroding steel surface nicely

matches data obtained in EIS studies in section 4.2, where R_p decreases suddenly at HNO_3 concentrations ≥25% wt. as shown in Figure 4-18. The formation of metastable pits on the surface of the stainless steel EQCM crystal will need to be investigated further to support these conclusions.

Above E_{corr}, HNO_3 concentrations ≥25% wt. show an increase in mass followed by a stabilisation in the mass oscillation. This suggests that above E_{corr} iron dissolution/hydrogen evolution and/or pitting corrosion has ceased and passive film formation has occurred. This supports observations made in LSV and EIS measurements that a thin passive film may form at higher HNO_3 concentrations, albeit in a much narrower potential range i.e. above E_{corr} but before transpassive dissolution.

Differences between HNO_3 concentrations shown in Figure 4-22 – Figure 4-28 may be more easily understood by plotting the voltamassograms for each concentration on a single plot. This is shown in Figure 4-29 below. There is a clear transition in behaviour in HNO_3 concentrations >20% wt. Mass plots become 'noisier' with less identifiable trends.

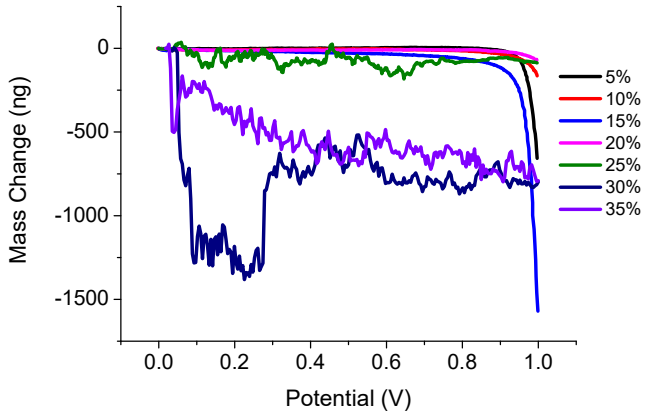

Figure 4-29 – Voltamassograms of SS2343 piezoelectrodes in 5-35% wt. HNO_3.

EQCM and LSV have been used here as a rapid scanning technique, whilst LSV is a useful technique it does not allow for slow oxide layer growth. Therefore, in the next section EQCM and potential-step measurement techniques have been used to more fully understand growth rates in the passive region at all HNO_3 concentrations.

4.4.3 Potential Step Studies

Using the EQCM, chronoamperometric-microgravimetric measurements were made by means of a potential 'staircase' experiment in which the potential was stepped at 0.15 V intervals from an initial value of -0.2 to 1.15 V. At each step on the 'staircase' the potential was held for 45 minutes and the resultant current transient and change in electrode mass was recorded. Figure 4-30 shows the time dependence of the changes in electrode mass that occur in response to the potential 'staircase' at a range of HNO_3 concentrations, from a HNO_3 concentration of 5 to 35% wt. (Figure 4-30).

Measurements performed at concentrations <20% wt. are previously discussed in Section 3.3.4, and are included here for comparison. However, briefly the general behaviour of 316L SS at these concentrations may be described thus. Net mass gains are observed in the potential range -0.2 to 0.25 V due to the formation of the Cr/Fe oxide passive film. The mass gain then slows between 0.4 and 0.7 V. This corresponds to the region where it has been suggested that slow Cr(III) to Cr(VI) begins to occur at high potentials in the passive region immediately prior to transpassivity [63], [76]. At higher potentials, ~0.85 to 1 V, a mass decrease is observed, indicating the onset of transpassivity, most likely due to faster formation of Cr(VI) ions and rapid dissolution [65], [74].

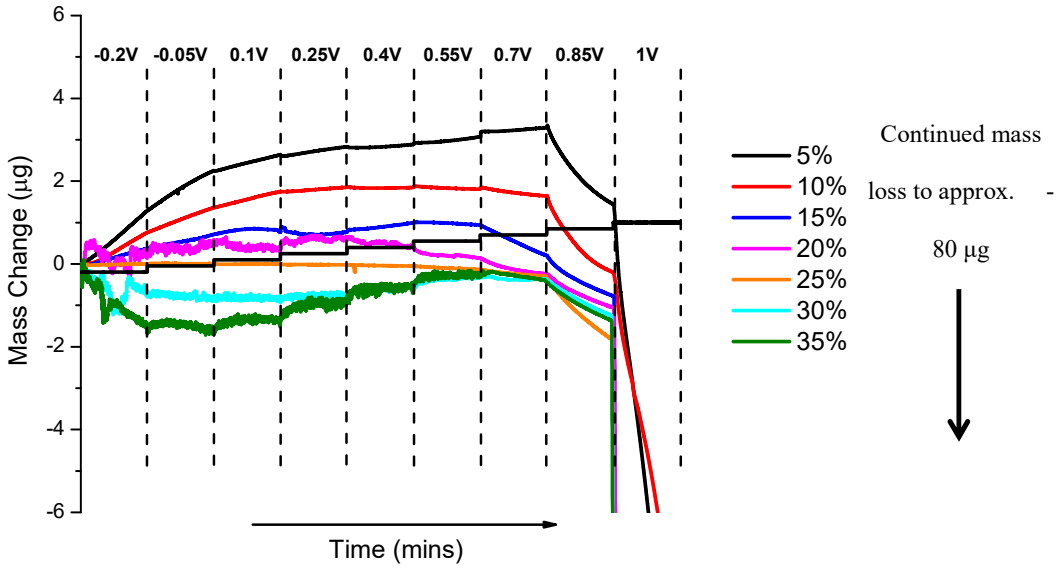

Figure 4-30 - Mass change of SS 2343 as a function of time during potential step experiments in 5-35% wt. HNO_3. Polarisation conditions: Start potential = -0.2 V, end potential = 1 V, potential step = 0.15 V, time between steps = 45 mins.

Consider now the mass change observed in response to the potential step staircase at a HNO_3 concentration of 20% wt. The pattern of mass change behaves in a similar manner to 5-15% wt. HNO_3. From the LSV and EIS data of sections 4.1 and 4.2 and initial EQCM experiments of section 4.4.2, we have previously shown that HNO_3 concentration 20% wt. is a transition point where behaviour starts to change due to the change in HNO_3 reduction mechanism. The potentials associated with the onset of oxidation current (an increase in E_{corr} values shown in Figure 4-3) and the onset of R_p value increases shift in a manner that indicates a change in HNO_3 reduction mechanism (previously discussed in more detail in sections 4.1 and 4.2). However, the effect on corrosion and, therefore, mass change was shown to be minimal. At potentials ≥0.4 V, mass decreases more quickly at 20% wt. HNO_3 than at lower HNO_3 concentrations and this is in good agreement with the pseudo-polarogram shown in Figure 4-4 which shows i_{corr} increasing over 20% wt. HNO_3 with E_{corr} rising above 0.4 V under these conditions.

The 'noisy' mass change behaviour observed at lower potentials at ≥25% wt. HNO_3, Figure 4-30, agrees with similar behaviour seen in rapid LSV studies on SS2343, Figure 4-28. As discussed in reference to Figure 4-26, under these high HNO_3 concentrations and low applied potential conditions, simultaneous hydrogen evolution, iron dissolution and/or metastable pitting leads to apparent rapid mass losses and gains ('noise') and a general decrease in mass due to the inhibition of a passive layer formation (potential < E_{corr}). Interestingly it can also be seen from the traces recorded at HNO_3 concentrations >30% wt., Figure 4-30, that at potentials ≥0.25 V there is a small net increase in mass. Again such mass increases are concurrent with the decrease in the current density in Figure 4-2a, suggesting some passive film formation over a significantly reduced potential window is occurring. Interestingly the smaller size of this mass increase compared to that obtained in the passive region at HNO_3 concentration < 25% wt. indicates either that: 1) a much thinner film is formed or 2) the film is still not fully formed and is only partially passive in character.

One consistent pattern of behaviour across all HNO_3 concentrations is the rapid decrease in mass at 1 V, corresponding to the passive-transpassive transition. This does not appear to be affected by the increase in HNO_3 concentration and is associated with the onset of transpassive dissolution of the passive film.

Results from EQCM studies (both LSV and E-step) relate well to LSV and EIS studies on 316L SS. At lower HNO_3 concentrations (≤15% wt.), where HNO_2 regeneration has been shown to occur slowly, oxide growth has been recorded using the QCM, said growth decreasing with increasing HNO_3 concentration.

At these HNO_3 concentrations LSV and EIS studies recorded E_{corr} values at ≤0 V, i_{corr} values are low and R_p values are high. Thus, under these conditions there is the potential for contaminant entrainment, with contaminants potentially being taken up into the so grown passive oxide film. This will be explored in Chapter 5 .

To summarise, 20% wt. HNO_3 has been identified as a transition point where at HNO_3 concentrations above this threshold, NO_2 plays a greater role in the mechanism associated with HNO_3 reduction. At 20% wt. HNO_3 E_{corr} is increasing compared to lower HNO_3 concentrations due to the associated NO_2 mechanism change, but the effect on passivity and corrosion rate is minimal, a conclusion supported by the i_{corr} measurements and R_p extrapolation.

At HNO_3 concentrations ≥20% wt. E_{corr} has been shown to shift to significantly higher potentials. EQCM studies showed that passive film formation does not occur below E_{corr}; this is most likely due to pitting/active dissolution/hydrogen evolution which is accessed at much lower potentials, significantly restricting oxide layer growth and the region of passivity. Above E_{corr} this behaviour stabilises and a mass gain is observed although the reduced scale of this mass increase compared to the mass measured in the passive region at HNO_3 concentrations < 25% wt. indicates either that: 1) a much thinner film is formed or 2) the film is still not fully formed and is only partially passive in character. Under these conditions, it is unlikely that contaminant entrainment will occur due to reduced ability to form a strong passive oxide film. This will be explored in section 4.5.

Whilst electrochemical techniques are a valuable tool for measuring changes in corrosion behaviour at the electrode surface, it provides no information on the compositional nature of the film that has formed on the stainless steel surface. As such, next section discusses XPS analysis of the surface film formed on 316L SS in 25% wt. HNO_3, said concentration chosen to represent the higher HNO_3 concentrations studied in this section, i.e. where NO_2 is thermodynamically stable.

4.5 Compositional Analysis of the Passive Film Formed On 316L Stainless Steel Nitric Acid

4.5.1 Introduction

This section attempts to analytically determine, using X-Ray Photoelectron Spectroscopy (XPS), any compositional changes that may occur in the so formed passive films as a function of HNO_3 concentration and applied potential. As described above, 20% wt. HNO_3 is the point at which a mechanism change can be seen to occur in the reduction of HNO_3. Said mechanism change significantly accelerates the rate of HNO_3 reduction and decreases the potential range over which passivity is observed at HNO_3 concentrations >20% wt. Thus, the following section presents XPS results recorded at 5 and 25% wt. HNO_3 as examples of system behaviour at HNO_3 concentrations below and above 20% wt. respectively. Results observed at 5% HNO_3 have already been discussed is detailed in section 3.4.2. Key findings are represented here for the convenience of the reader.

4.5.2 Results

Curve fitted high resolution spectra of 316L SS samples in 5% wt. (an example of low HNO_3 concentration) and 25% wt. (an example of high HNO_3 concentration) HNO_3 polarised at 0.2 (low passive potential) and 0.8 V (high passive potential) respectively are shown in Figure 4-31, Figure 4-32 and Figure 4-33.

Consider first the Fe, Cr and O species observed at low and high over potentials at both HNO_3 concentrations. The iron profiles in Figure 4-31 show two peaks: a peak at 706.96 eV, due to elemental iron (Fe^0); and a peak around 710.32 eV attributed to either iron (III) oxide (Fe_2O_3) or iron (II,III) oxide (Fe_3O_4) in 316L SS (see section 3.4.2 for the detail of this assignment).

The chromium profiles in Figure 4-32, show four peaks which can be attributed to: Cr metal (573.97 eV), Chromium (III) oxide (Cr_2O_3) (575.82 eV), Chromium (III) hydroxide (576.84 eV) and Chromium (VI) oxide (CrO_3) (578.60 eV).

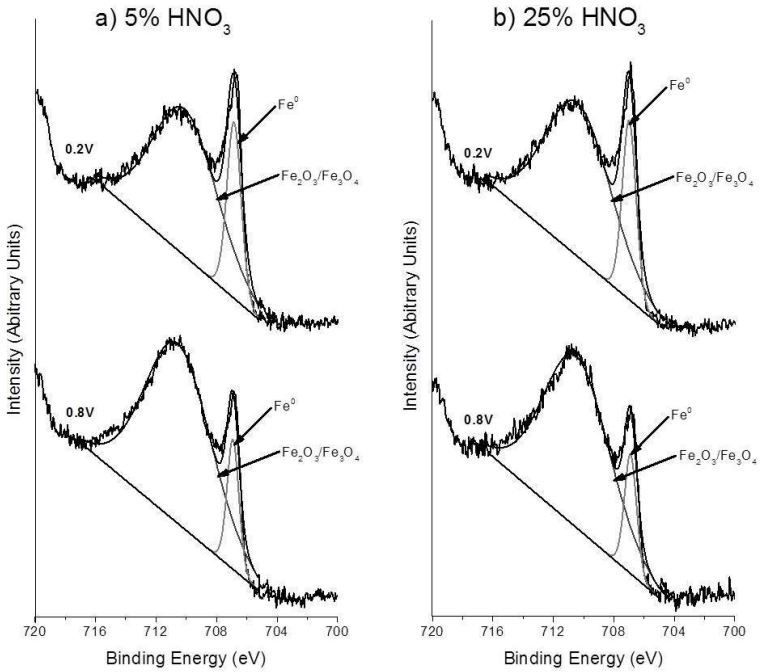

Figure 4-31 - XPS profile of Fe $2p_{3/2}$ after passivation of 316L SS in a) 5% wt. and b) 25% wt. HNO_3 at 0.2 and 0.8 V.

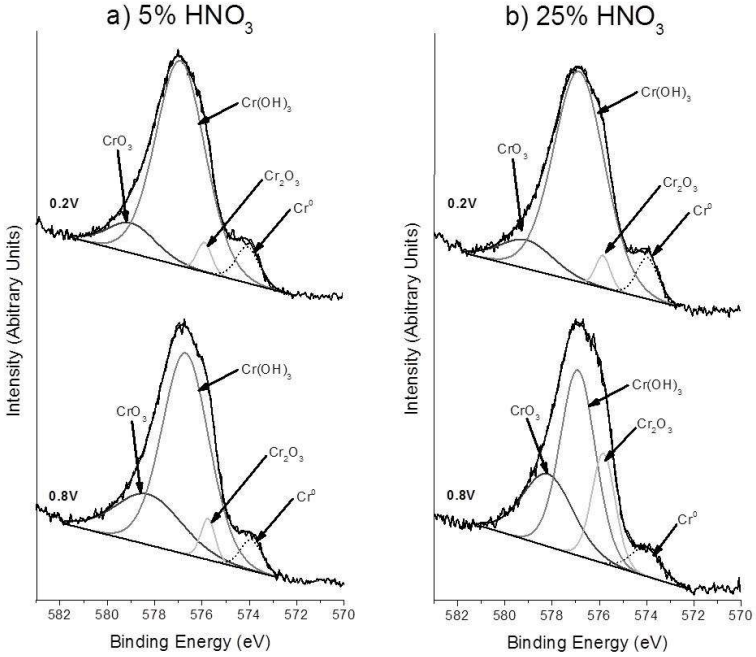

Figure 4-32 - XPS profile of Cr $2p_{3/2}$ after passivation of 316L SS in a) 5% wt. and b) 25% wt. HNO_3 at 0.2 and 0.8 V.

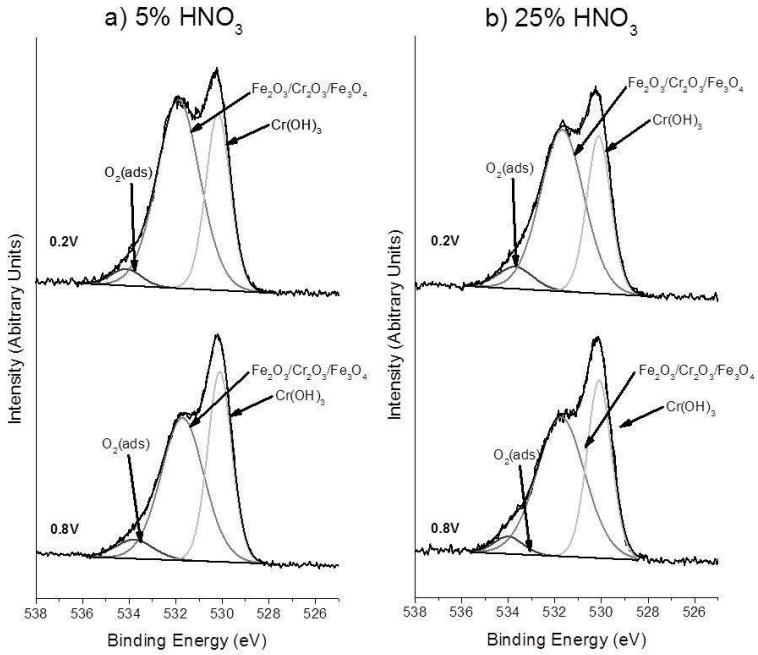

Figure 4-33 - XPS profile of O 1s after passivation of 316L SS in a) 5% wt. and b) 25% wt. HNO_3 at 0.2 and 0.8 V.

Two broad, compound peaks due to oxygen are observed at 530 and 532 eV, shown in Figure 4-33. In and of themselves, they are not enough to confirm speciation due to deconvolution issues. They are, however, useful to confirm the presence of mixed Fe/Cr oxides/hydroxides on the metal surface [105].

Due to the large number of species involved, steel surface compositional differences between the two nitric acid concentrations may be more easily understood by plotting the relative atomic percentages of each species for both the Fe profiles of Figure 4-31 and the chromium profiles of Figure 4-32. Such plots for both 5 and 25% wt. HNO_3 at 0.2 and 0.8 V respectively are shown in Figure 4-34.

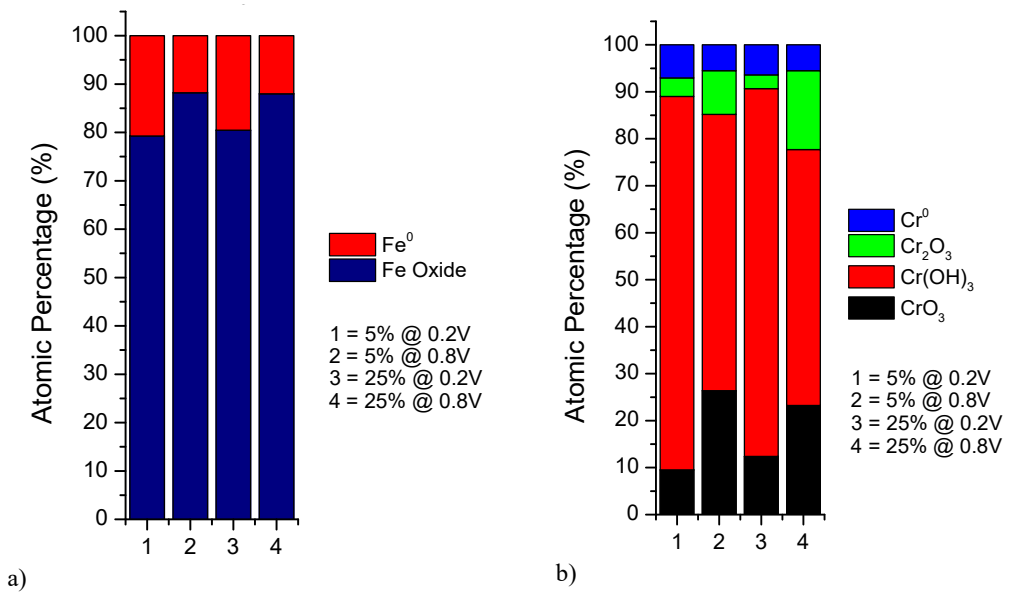

Figure 4-34 – Atomic Percentage data comparison for Fe (a) and Cr (b) results.

Considering first the iron profile of Figure 4-34a, at both HNO_3 concentrations increasing the potential from 0.2 V to 0.8V leads to an increase in intensity of the Fe_3O_4/Fe_2O_3 peak at around 710.32 eV, suggesting an increase in iron oxide concentration. Unfortunately due to signal quality it is impossible to identify the exact oxidation state of the iron oxide at each potential. However, electrochemically it is known that at higher potentials Fe(II) is oxidised to Fe(III), generating Fe_2O_3 (see Pourbaix diagram of Figure 1-12) [57], [178], [179]. As such, it is not unreasonable to assume that the iron oxide signal at 0.8V may be dominated by Fe(III) oxide (hematite, α-Fe_2O_3,or maghemite, γ- Fe_2O_3). Importantly there is little difference in atomic percentage between either 5% wt. or 25% wt., suggesting that it is differences in the Cr oxide film that is crucial to the observed electrochemical differences in corrosion behaviour.

Considering now the chromium profile of Figure 4-34b, at both HNO_3 concentrations increasing the potential from 0.2 to 0.8 V increases the intensity of Cr_2O_3 and CrO_3 peaks as well as decreasing the Cr^0 and $Cr(OH)_3$ peak intensities. As described in Chapter 3, this is due to chromium being more soluble in its Cr(VI) oxidation state (CrO_3) than its Cr(III) oxidation state ($Cr_2O_3/Cr(OH)_3$ [65]. Therefore, the increase in potential leads to the production of Cr(VI) within the film, which is a necessary prerequisite for dissolution of Cr(VI) from the film, and a decrease in $Cr^0/Cr(OH)_3$ as more chromium is converted to oxide/hydroxide and stripped out of the film.

From Figure 4-34 (b), the main difference between 5 and 25% wt. HNO_3 is the atomic percentage of Cr_2O_3 present in the passive film. At 0.8V. Cr_2O_3 is ~10% more intense in 25% wt. HNO_3 than in 5% wt. HNO_3. This may be explained as follows.

The formation of a chromium hydroxide/oxide passive layer on steel originates from the formation of Cr^{2+} ions and subsequent $Cr(OH)_2$ hydrate in the pre-passive stage (low potentials) [184]:

$$Cr_s \rightarrow Cr^{2+}_{(aq)} + 2e^- \tag{4.1}$$

$$Cr^{2+}_{(aq)} + 2H_2O \rightarrow Cr(OH)_{2(s)} + 2H^+ \tag{4.2}$$

With increasing potential towards passivation Cr^{2+} ions are converted to Cr^{3+} ions which subsequently form $Cr(OH)_3$:

$$Cr^{2+}_{(aq)} + e^- \rightarrow Cr^{3+}_{(aq)} \tag{4.3}$$

$$Cr^{3+}_{(aq)} + 3H_2O \rightarrow Cr(OH)_{3(s)} + 3H^+ \tag{4.4}$$

Thus, $Cr(OH)_3$ forms the stable passive layer in mild non-oxidising acidic environments and neutral alkaline conditions [157].

However, under oxidising acidic conditions $Cr(OH)_3$ may convert to chromium oxide, Cr_2O_3, via the following solid state reaction [185]:

$$Cr(OH)_{3(s)} + Cr_{(s)} \rightarrow Cr_2O_{3(s)} + 3H^+ + 3e^- \tag{4.5}$$

Thus, under the oxidising acidic conditions employed in Figure 4-34 it would be expected that in the passive region a significant portion of the stable $Cr(OH)_3$ film would be converted to Cr_2O_3. Focussing on Figure 4-34b it can be seen that this is indeed the case. However, at 0.2V, in both concentrations of HNO_3, the percentage of Cr_2O_3 is low (< 3%). The reason for this is described in more detail below.

Considering first 25% wt. HNO_3 at 0.2 V, it can be seen from the LSV and EQCM data of sections 4.1 and 4.4 that the surface is corroding actively, presumably through acid dissolution of the existing air formed $Cr(OH)_3$ passive layer. As such the potential is not positive of E_{corr}, a point which would allow

Cr_2O_3 formation, resulting in a lower atomic percentage of Cr_2O_3 compared to 5% wt. HNO_3, where both the potential is above E_{corr} and the pH are within the region of passivity.

Turning now to 5% wt. HNO_3 at 0.2V, the lack of comparative Cr_2O_3 may be due to the lack of a significantly oxidising environment to convert the more stable $Cr(OH)_3$ film into the less stable intermediate oxide, Cr_2O_3. Such an observation is in line with the EIS derived polarisation resistance measurements of Chapter 3. Here a small spike in R_p is observed at ~0.25V before the main passivation peak is apparent. Considering the XPS results described above this may be assumed to be a transition of $Cr(OH)_3$ to Cr_2O_3 in the passive layer as the applied potential becomes more oxidising. This is supported by observations that this spike disappears at HNO_3 concentrations > 10% wt., presumably because the environment has become too oxidising to support a pure or high percentage $Cr(OH)_3$ film.

Considering now the data for 5% wt. HNO_3 at 0.8V, it can be seen that in this pre-transpassive area a much higher percentage of Cr_2O_3 is present as well as CrO_3 from Cr(III) to Cr(VI) derived pre-transpassive dissolution. Again this supports the above analysis of transition from pure/near pure $Cr(OH)_3$ to a higher percentage Cr_2O_3 passive film at higher potentials (>0.25V) in 5% wt. HNO_3.

At 25% wt. HNO_3 at 0.8V the atomic percentage of Cr_2O_3 is greatly increased compared to 5% wt. HNO_3. Comparison with the LSV and EQCM traces of sections 4.1 and 4.4 reveals that this potential is within the limited range where a passive film can exist. Due to the much more oxidising environment generated by the higher HNO_2 present at higher nitric acid concentrations (due to NO_2 stability) the film here has a much higher Cr_2O_3 character, but is still in part $Cr(OH)_3$. The higher degree of Cr_2O_3 may also account for the limited oxide layer thickness in this region noted in the EQCM results of section 4.4 and EIS results of section 4.2. Single step oxidation of $Cr(OH)_3$ to CrO_3 is mechanistically more difficult than single step oxidation of Cr_2O_3 to CrO_3, the former usually involving oxidation to intermediate Cr_2O_3 first, i.e. $Cr(OH)_3$ to Cr_2O_3 to CrO_3 [157][186]. As such, unlike the much higher $Cr(OH)_3$ content primary passive layer formed in 5% wt. HNO_3, the primary passive layer formed in 25% wt. HNO_3 is thinner and potentially partially porous, as the high percentage Cr_2O_3 component is readily converted to CrO_3.

In summary, X-ray photoelectron spectroscopy investigation in the above concentrations and potentials has revealed the generation of a passive film consisting of hydroxide rich layer and oxide layers at lower potentials in both 5 and 25% wt. nitric acid.

With the transition from low to high concentrations of HNO_3 the Fe signal is believed to shift from a Fe(II) dominant oxide to a Fe(III) oxide with no observed change in concentration. This has led to the conclusion that Cr behaviour is more crucial to the electrochemical changes identified in sections 4.1 and 4.2 and the microgravimetric changes observed in section 4.4.

With an increase in potential and HNO_3 concentration, the Cr film shifts from a $Cr(OH)_3$ dominant film to a passive film consisting of hydroxide ($Cr(OH)_3$) and oxide (Cr_2O_3) layers. Cr_2O_3 concentrations increase greatly at higher potential due to the oxidation of $Cr(OH)_3$ in more oxidising conditions. At low HNO_3 and low potential the HNO_3 is not oxidising enough to convert the $Cr(OH)_3$ to Cr_2O_3 and at high HNO_3 and low potential the surface of the steel is below E_{corr} and is , therefore, not passive. CrO_3 increases in concentration when potential is increased due to the oxidation of Cr(III) species to Cr(VI).

The changes in Cr speciation described above may also account for the reduced film thickness observed in EQCM studies. Cr_2O_3 more readily converts to CrO_3 than $Cr(OH)_3$, therefore, at high HNO_3 concentrations where Cr_2O_3 is more prevalent, conversion to CrO_3 is likely to be easier leading to increased dissolution of Cr from the passive film. Reducing Cr from the passive film will reduce the efficacy of the film which also supports the decrease in R_p observed in EIS studies and the increase in i_{corr} observed in LSV studies.

4.6 Summary

In this chapter, we have described the electrochemical characterisation of 316L SS in HNO_3 concentrations ≥20% wt. alongside plots from 316L SS in HNO_3 concentrations ≤15% wt.

LSV studies have demonstrated that E_{corr} and i_{corr} increase with increasing HNO_3 concentration (shown in Figure 4-4). This is attributed to a change in the HNO_2 regeneration mechanism at ~20% wt. HNO_3. At lower concentrations, regeneration of HNO_2 is believed to occur primarily on the stainless steel surface. This is a slow process which is dependent on the diffusion of HNO_3 to the surface of the steel. At higher concentrations, the mechanism shifts to near-surface solution based regeneration. The abundance of HNO_3 and stability of NO_2 at higher HNO_3 concentrations leads to the rapid production of HNO_2 which results in the observed increase in E_{corr} and i_{corr}. EIS studies nicely support this assessment, with high R_p values over a wide range of potentials at lower concentrations (<20% wt.) and over a narrower range at

higher HNO_3 concentrations (>20% wt.). Onset of the R_p increase on the potential axis occurs at higher potentials in higher HNO_3 concentrations, following the increase in E_{corr} values observed in LSV studies. Lower R_p values coincide with an increase in i_{corr}, this is most likely due to increased production of HNO_2 with increased thermodynamic stability of NO_2 in solution. This leads to the increased oxidation of Cr(III) to Cr(VI), which is more soluble, and the subsequent dissolution of Cr(VI) reducing the efficacy of the passive film. Onset of transpassive dissolution occurred at ~1 V for a HNO_3 concentrations.

EQCM has been shown to follow the in-situ mass change of a passive stainless steel electrode resulting from the application of a potential. We have used EQCM to study the induced formation of the passive oxide layer at SS 2343 (a 316L analog). Polarisation curves were recorded on QCM crystals with simultaneous measurements of mass change. Current and mass-response curves show that at HNO_3 concentrations ≥20% wt., passive film formation does not occur below E_{corr}. Above E_{corr} mass traces were noisy showing large mass losses and gains. This is believed to be due to either hydrogen evolution with the concurrent stripping of iron from the electrode surface or metastable pitting. The rapid formation of metastable pits and then repassivation could cause rapid fluctuations in mass loss and gain. When the potential reached E_{corr} mass increased at each HNO_3 concentration and the mass trace stabilised. The narrower region of passivity agrees nicely with LSV and EIS studies which suggest that at HNO_3 concentrations ≥20% wt. a rapid autocatalytic regeneration of HNO_2 is occurring due to increased thermodynamic stability of NO_2 in solution and the increased rate of HNO_3 reduction. This, in turn, inhibits passive film formation and leads to an increase in E_{corr}.

In the potential 'staircase' EQCM experiments, the potential was held for a longer time to assess mass change of SS 2343 as a function of HNO_3 concentration (5% wt. to 35% wt.). At HNO_3 concentrations ≤15% wt., the maximum extent of oxide growth is observed at E=~0.55 V. Beyond this point, the transpassive processes lead to a mass loss from the electrode surface, the first time such a feature has been observed on passivated stainless steel. Oxide growth is significantly reduced at HNO_3 concentrations ≥20% wt., with all samples presenting substantial mass loss at E=0.7 V, a transpassive process also seen in the case of samples studied at ≤15% wt. This has repercussions for the use of stainless steels in highly oxidising environments, such as those that may occur in the concentrated HNO_3 highly active raffinate liquor solutions that are found in evaporators.

These studies have provided us with information that will allow us to artificially 'grow' oxide layers in any concentration of HNO_3. Overall it is more likely that contaminant entrainment is going to occur in lower concentrations of HNO_3 (<20% wt.) where a strong passive oxide film forms, rather than at higher HNO_3 concentrations (>20% wt.) where the ability to produce a passive oxide film appears greatly reduced.

XPS analysis showed that at low concentrations of HNO_3 and low potentials the passive layer formed is dominated by $Cr(OH)_3$. An increase in potential in low concentrations of HNO_3 leads to the conversion of $Cr(OH)_3$ to Cr_2O_3 in low concentrations of HNO_3. At high concentrations and potentials the passive layer shifts to a passive film consisting of $Cr(OH)_3$ and increased Cr_2O_3 content. At low HNO_3 concentrations and low potential the HNO_3 is not oxidising enough to convert the $Cr(OH)_3$ to Cr_2O_3 and at high HNO_3 concentrations and low potential the surface of the steel is below E_{corr} and is, therefore, not passive.

The changes in Cr speciation can be linked to the reduced film thickness observed in EQCM studies. Cr_2O_3 more readily converts to CrO_3 than $Cr(OH)_3$, therefore, at high HNO_3 concentrations where Cr_2O_3 is more prevalent, conversion to CrO_3 is likely to be easier, leading to increased dissolution of Cr from the passive film. Reducing the Cr content within the passive film will reduce the efficacy of the film which also supports the decrease in R_p observed in EIS studies and the increase in i_{corr} observed in LSV studies.

Having described the effect of HNO_3 only on 316L stainless steel dissolution at two different concentration regimes (i) ≤ 15% wt. typical of that found in reprocessing actinide 'strip' steps and (ii) > 15% wt. typical of that found in 'head end' fuel pin dissolution, highly active liquor evaporators and in initial uranium scrub and backwash steps, it is now of importance to describe the effect of radionuclides on SS316L corrosion behaviour and the incorporation of said radionuclides into the so formed passive film in both concentration regimes. Thus, the next chapter applies LSV and XPS analytical techniques used in both this and the previous chapter to HNO_3/316L SS systems in the presence of both active radionuclides (Uranium) and radionuclide surrogates (Europium/Cerium, acting as a surrogates for Americium/Plutonium respectively).

Chapter 5

Electrochemical and Compositional Analysis of the Passive Film Formed on 316L Stainless Steel in the Presence of Radioactive and Non-Radioactive Contaminants

5 ELECTROCHEMICAL AND COMPOSITIONAL ANALYSIS OF THE PASSIVE FILM FORMED ON 316L STAINLESS STEEL IN THE PRESENCE OF RADIOACTIVE AND NON-RADIOACTIVE CONTAMINANTS

5.1 Introduction

In the previous two chapters we have established, using LSV, EIS, EQCM and XPS, that a passive film forms on 316L SS when exposed to nitric acid. These experiments have provided us with detailed information on the passive potential region. Using EQCM we have demonstrated a level of 'controllability' for oxide growth on our steels within this passive region. Also, we have seen how different HNO_3 concentrations effect this growth and the composition of the so formed passive layer.

In this chapter we now take this approach a step further and introduce both non-active radionuclide surrogates (Eu and Ce) and actual radionuclides (U) into solution in order to attempt to determine their uptake into the steel passive film and to some extent their effect on the corrosion behaviour of said passive film.

5.2 Stainless Steel Passivation in the Presence of Non-Radioactive Surrogates

In this study Cerium (III) Nitrate Hexahydrate has been used as a non-radioactive a surrogate for Plutonium and Europium (III) Nitrate Pentahydrate as a non-radioactive surrogate for Americium. Both have been shown to be suitable surrogates for their respective radionuclides in previous studies [187], [188]. As with previous chapters, LSV is first used to determine any change in electrochemical behaviour/corrosion rate of SS316L in the presence of radioactive surrogates in the same concentration ranges of nitric acid described previously. After these initial electrochemical experiments, *ex situ* XPS is again used to determine the degree of uptake of the surrogates into the stainless steel passive film.

5.2.1 Stainless Steel Passivation in the Presence of Cerium (III) Nitrate

5.2.1.1 Polarisation Curve Results

Figure 5-1 shows potentiodynamic polarisation curves for 316L SS electrodes recorded in a) 5-35% wt. HNO_3 concentrations (from Chapters 3 and 4 respectively) and b) 5-35% wt. HNO_3 concentrations containing 30 mmol dm^3 $Ce(NO_3)_3 \cdot 6H_2O$ over the potential range -0.5 to 0.5 V.

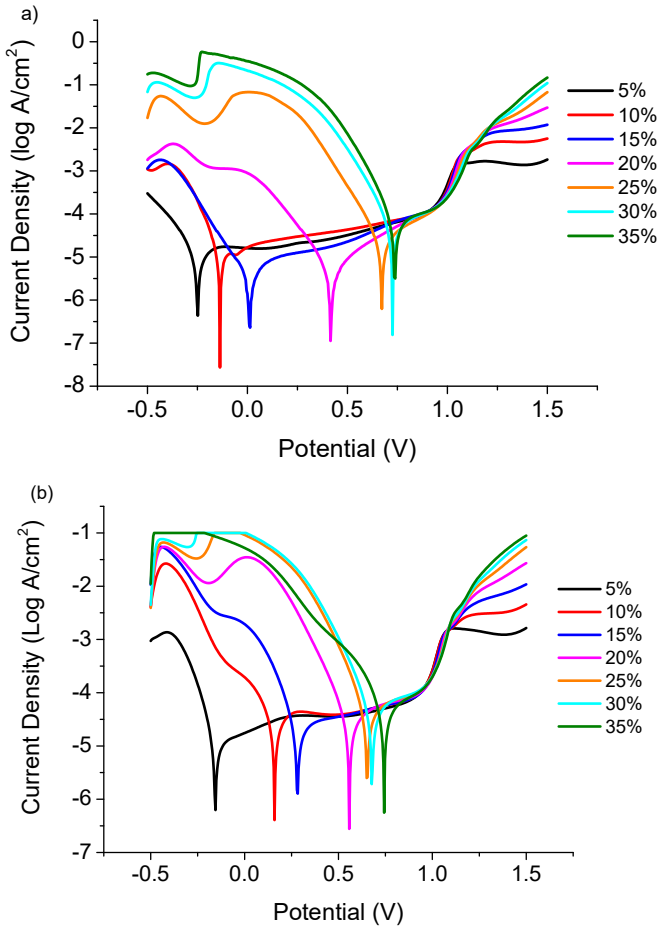

Figure 5-1 – Potentiodynamic polarisation plots of 316L SS in a) 5-35% wt. HNO_3 and b) 5-35% wt. HNO_3 containing 30mmol dm^3 $Ce(NO_3)_3 \cdot 6H_2O$ at room temperature (20±2°C). Plots were measured in the potential range -0.5-1.5 V (sweep rate, 10 mV s^{-1}).

From Figure 5-1b, it can be seen that the shift in behaviour between low (≤15% wt. HNO_3) and high (≥20% wt. HNO_3) HNO_3 concentrations, previously discussed in section 4.1, is less pronounced in the

presence of Ce(III) than in HNO_3-only solutions. This is because the addition of Ce(III) to the nitric acid media has led to a positive shift in corrosion potential for lower HNO_3 concentrations (5-20% wt.). Ce(III) salts are used as corrosion inhibitors to improve corrosion resistance in aluminium alloys. Ce(III) salts form an insoluble film at cathodic sites, whilst the exact mechanism may change in the presence of 316L SS, the switch from improving corrosion resistance to increasing corrosion was not expected. Previously, the positive shift in E_{corr} for HNO_3 was believed to be associated with the increased stability of NO_2 at higher HNO_3 concentrations, which led to an increase in HNO_2 content and therefore an increase in E_{corr}. The increase in E_{corr} at lower HNO_3 concentrations suggests that NO_2 stability is no longer the only factor influencing E_{corr}.

HNO_2 and NO_2 can both act as a reducing agents, as shown in equations (5.1) [189] and (5.2) [6], [111] respectively, which would ensure that Ce(III) would remain in its lower oxidation state, 3+.

$$NO_2^- + H_2O \rightarrow NO_3^- + 2e^- + 2H^+ \qquad E^0{}_{25^oC} = 0.558 \text{ V vs. SCE} \qquad (5.1)$$

$$2NO_2 + 2H_2O \leftrightarrow 2NO_3^- + 4H^+ + 2e^- \qquad E^0{}_{25^oC} = 0.553 \text{ V vs. SCE} \qquad (5.2)$$

If this was the case then at lower HNO_3 concentrations, where less HNO_2 and NO_2 are present, the oxidative power of the media may be higher than in the presence of HNO_2 and NO_2 [190]. In this situation Ce(III) would be oxidised to Ce(IV) in the following reaction:

$$Ce^{3+} \leftrightarrow Ce^{4+} + e^- \qquad E^0{}_{25^oC} = 1.365 \text{ V/SCE} \qquad (5.3)$$

Ce(IV) is known to act as a corrosion accelerant [190] which would explain the positive shift in E_{corr} in lower HNO_3 concentrations. Once the HNO_3 concentration is increased to >20% wt., and subsequently the NO_2 stability increases then the HNO_2 concentrations will increase sufficiently to reduce Ce(IV) to Ce(III).

Ce(III) has no significant impact on corrosion rate [190], leading to no change in behaviour at higher HNO_3 concentrations in the presence of Ce as Ce is no longer influencing E_{corr}.

A major flaw in this argument is the potential at which the Ce(III)/Ce(IV) couple reacts (1.365 V/SCE). However, Johnson *et al* [191] have reported the oxidation of Ce(III) in concentrated HNO_3, where E^0 for HNO_2 reduction (Equation (5.4)) is about +1.2V [192].

$$HNO_2 + H^+ + e^- \rightarrow H_2O + NO \tag{5.4}$$

E^0 for $Ce^{3+/4+}$ is approximately 1.4V, see equation (5.3) on the previous page, however as:

$$E = E^0 + \frac{RT}{nF} ln \frac{[Ce^{4+}]}{[Ce^{3+}]} \tag{5.5}$$

The initial lack of Ce(IV) in solution may reduce E to less than ~1.4 V, potentially as low as 1.2 V. E for the HNO_2/NO process may also increase above +1.2V due to the electrogeneration of HNO_2 at low applied potentials. These concentration induced changes in E for the Ce(IV)/Ce(III) couple and the HNO_2/NO couple may then result in Ce(III) reducing HNO_2, producing NO and Ce(IV). The latter may then act in its established manner as a steel corrosion accelerator, resulting in the increase in E_{corr} at low HNO_3 concentrations seen in Figure 5-1b.

Using equation (5.5) [27] we can calculate how much Ce(IV) would be required for the above shift in potential. The Nernst equation above (5.5) can be rearranged so:

$$ln \frac{[Ce^{4+}]}{[Ce^{3+}]} = (E - E^0) \frac{RT}{nF} \tag{5.6}$$

Where;

E=1.2V

E^0 = 1.4V

R (Universal Gas Constant) = 8.314 J K^{-1} mol^{-1}

T (Temperature) = 298 K

n (number of electrons) = 1

F (Faraday Constant) = 96,485 C mol^{-1}

The concentration of Ce(IV) required would be approximately 29.99 mmol dm^3. It is unrealistic to assume that >99% of the available Ce in solution will be oxidised to Ce(IV) in the above scenario. Therefore, something else is either oxidising Ce(III) to Ce(IV) or causing the increase in corrosion rate. Further experimentation is required to confirm whether any Ce(IV) is present and, if so, what the cause is.

A detailed analysis on the effect on E_{corr} is discussed in the next section.

5.2.1.2 E_{corr} and i_{corr} Analysis

The corrosion potential (E_{corr}) and corrosion current density (i_{corr}) were calculated using Tafel extrapolation in the vicinity of E_{corr} of the linear segments of the measured potential-current density curves of Figure 5-1b. Results of E_{corr} and i_{corr} vs. HNO_3 concentration are shown in Figure 5-2:

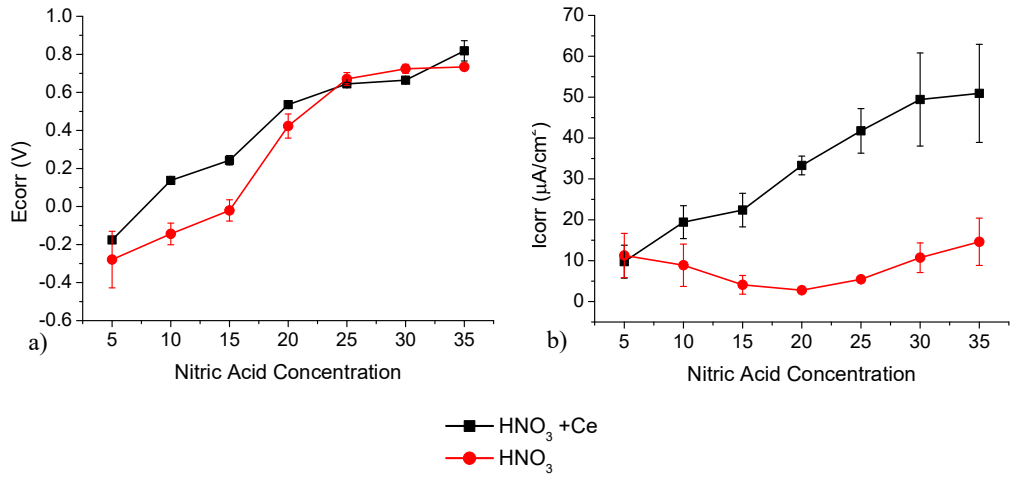

Figure 5-2 –a) Corrosion potential, E_{corr}, values and associated error bars vs. HNO_3 concentration b) Corrosion current density, i_{corr}. values and associated error bars vs. HNO_3 concentration calculated from Figure 5-1a for 316L SS in 5 - 35% wt. HNO_3 and Figure 5-1b for 316L SS in 5 - 35% wt. HNO_3 containing 30mmol dm^3 $Ce(NO_3)_3 \cdot 6H_2O$.

From Figure 5-2a it can be seen that, in the presence of cerium, E_{corr} increases in a near-linear fashion with increasing HNO_3 concentration and, for most HNO_3 concentrations, is greater in the presence of cerium than in its absence. In both the absence and presence of Ce, E_{corr} plateaus at approximately the same HNO_3 concentration value of ≥25% wt. As described in previous chapters, in HNO_3 only media, the increase in E_{corr} with increasing HNO_3 concentration is directly related to the greater availability of the electrochemically active species HNO_2 arising from the increased stability of NO_2. As discussed in the previous section, the increase in E_{corr} at lower HNO_3 concentrations in the presence of cerium can be attributed to the increased oxidative power of the nitric media due to the presence of Ce(IV) [44], [190]. At higher HNO_3 concentrations, the increased concentration of HNO_2 and, particularly NO_2 (due to the dual, concentration-dependant roles that HNO_2 plays in Ce(III) oxidation and Ce(IV) reduction) reduces

Ce(IV) to Ce(III), in accordance with the reverse of equation (5.3), the latter species being known to not significantly affect corrosion. Therefore, at higher HNO_3 concentrations, E_{corr} is being only being influenced by HNO_2 as with HNO_3 only media.

Figure 5-2b shows the calculated i_{corr} values for 5-35% wt. in both the absence and presence of 30 mmol dm^3 Ce(III) (as $Ce(NO_3)_3 \cdot 6H_2O$). It can be seen from Figure 5-2b that i_{corr} values increases linearly with increasing HNO_3 concentration in the presence of Ce, with no clear transition between behaviour at low and high HNO_3 concentrations. i_{corr} values are higher than in HNO_3 only media, indicating a higher corrosion rate in the presence of cerium – presumably due, at least in part, to cerium (VI)'s role as a corrosion accelerator on steel as described above. At higher HNO_3 concentrations, in the presence of Ce, i_{corr} values plateau whilst the corresponding E_{corr} values continuing to increase with increasing nitric concentration, albeit more slowly than at lower nitric concentrations. The values of E_{corr} in this higher HNO_3 concentration range indicate that, at HNO_3 concentrations ≥25% wt, the passive film is dissolving and intergranular corrosion is ongoing. This behaviour may be more easily understood through the pseudo-polarogram plot shown in Figure 5-3, where E_{corr} is plotted against i_{corr} for HNO_3 concentrations 5-35% wt. for both HNO_3 only solutions and solutions containing Ce.

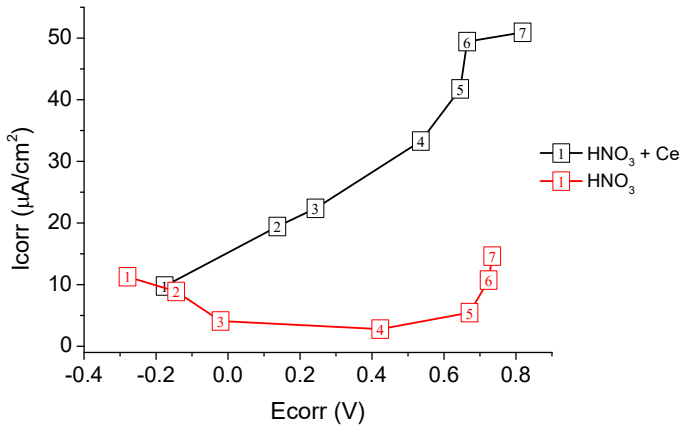

Figure 5-3 – Pseudo-polarogram of i_{corr} vs. E_{corr} (data points minus error bars for clarity) calculated from Figure 5-1a for 316L SS in 5 - 35% wt. HNO_3 and Figure 5-1b for 316L SS in 5 - 35% wt. HNO_3 containing 30mmol dm^3 $Ce(NO_3)_3 \cdot 6H_2O$.

Figure 5-3 shows that, in the presence of Ce, i_{corr} increases linearly with increasing E_{corr} in the range -0.1 V to +0.6 V. This is in contrast to HNO_3-only solutions where i_{corr} only increases when E_{corr} >0.4 V. This

indicates that passivity is limited in the presence of cerium and may be breaking down at HNO_3 concentrations <25% wt.

The results of Figure 5-3 also show that, in the presence of cerium, the corrosion rate is higher than in HNO_3 only solutions. As previously discussed, this may be due to the oxidation of Ce(III) to Ce(IV) in lower HNO_3 (≤20% wt.) concentrations, the presence of Ce(IV) then accelerating corrosion. At higher HNO_3 concentrations (>20% wt.) the increased presence of HNO_2 and stability of NO_2 leads to the reduction of Ce(IV) back to Ce(III) . The corrosion rate is now being influenced by the remaining HNO_2 which is lower in concentration than in HNO_3 only media, due to its role in the reduction of Ce(IV). Thus, the corrosion rate is slightly lower at higher HNO_3 concentrations in the presence of Ce.

Further experimentation is required to confirm whether any Ce(IV) is present due to electrogenerated HNO_3 in lower potentials and why, for example, the use of *in situ* UV-vis spectroscopy.

Whilst electrochemical techniques are a valuable tool for measuring changes in corrosion behaviour at the electrode surface but they provide no information on the compositional nature of the film that has formed on the stainless steel surface. The next section discusses XPS analysis of the surface film formed on 316L SS in 5 and 25% wt. HNO_3, said concentrations have been chosen to represent the lower and higher HNO_3 concentrations studied in this section i.e. where NO_2 is not present and where NO_2 is stable.

5.2.1.3 XPS analysis of 316L SS in Nitric Acid Media Containing Cerium Nitrate

Curve fitted high resolution spectra of 316L SS samples in 5% wt. HNO_3, with 30mmol dm^3 Ce(III) (as $Ce(NO_3)_3 \cdot 6H_2O$), polarised at 0.2 and 0.8 V are shown in Figure 5-4, Figure 5-5 and Figure 5-6.

The iron profiles in Figure 5-4 show two peaks, the peak at 706.9 eV is due to elemental iron (Fe^0) and the peak around 710.7 eV is attributed to either iron (III) oxide (Fe_2O_3) or iron (II,III) oxide (Fe_3O_4), the same as the iron profiles under nitric acid only conditions described in Chapter 3 and 4.

The chromium profiles in Figure 5-5, show four peaks which based on previous analysis can be attributed to: Cr metal (573.9 eV), Chromium (III) oxide (Cr_2O_3) (575.7 eV), Chromium (III) hydroxide (576.8 eV) and Chromium (VI) oxide (CrO_3) (578.8 eV).

Two broad, compound peaks due to oxygen are observed at 530 and 532 eV, shown in Figure 5-6. As in chapter 4, in and of themselves they are not enough to confirm speciation due to deconvolution issues. They are, however, useful to confirm the presence of mixed Fe/Cr oxides/hydroxides on the metal surface [105].

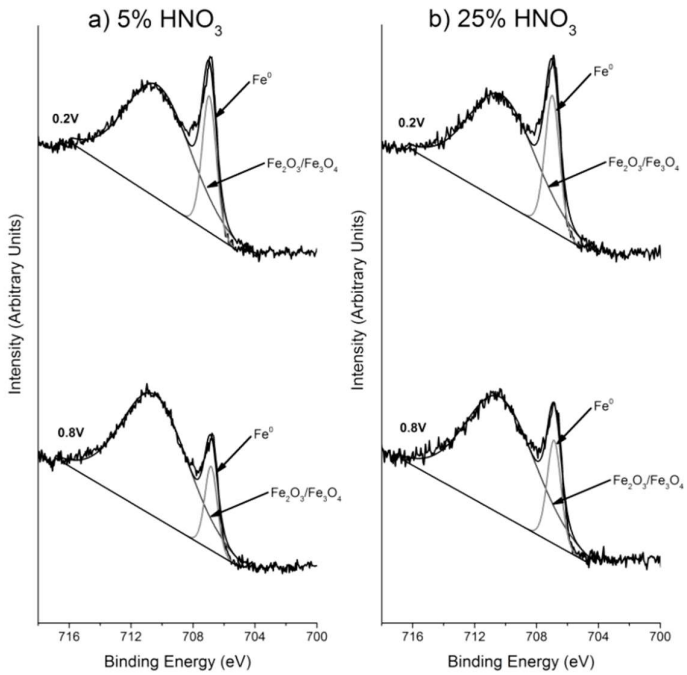

Figure 5-4 – XPS profile of Fe $2p_{3/2}$ after passivation of 316L SS in a) 5% wt. and b) 25% wt. HNO_3, both with 30mmol dm^3 of 30mmol dm^3 $Ce(NO_3)_3 \cdot 6H_2O$, at 0.2 and 0.8 V.

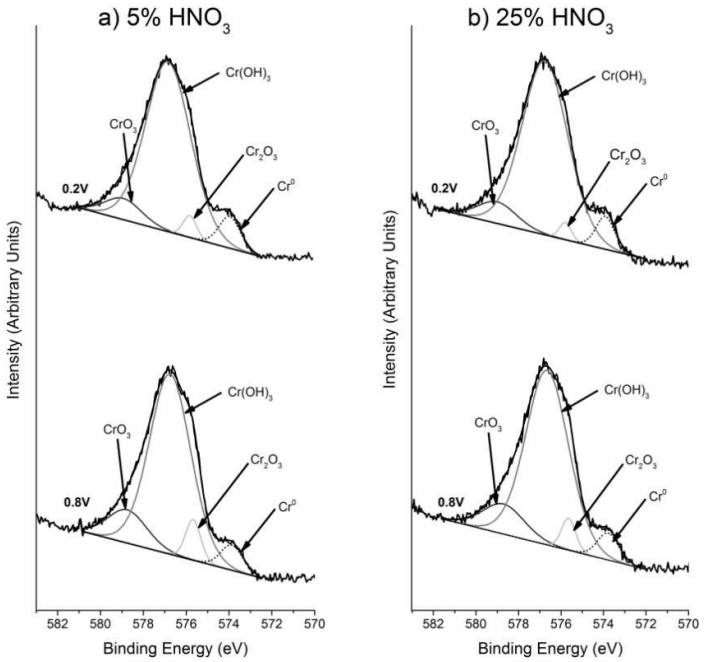

Figure 5-5 - XPS profile of Cr $2p_{3/2}$ after passivation of 316L SS in a) 5% wt. and b) 25% wt. HNO_3, both with 30mmol dm^3 $Ce(NO_3)_3 \cdot 6H_2O$, at 0.2 and 0.8 V.

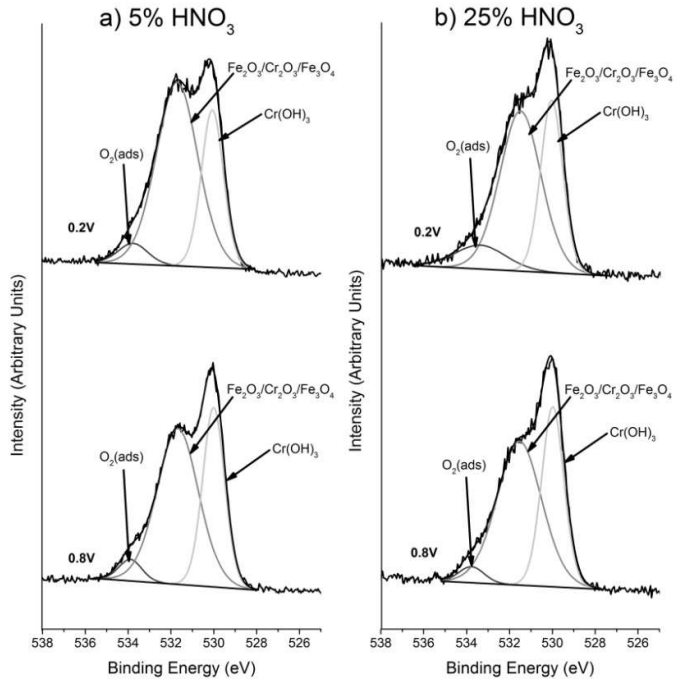

Figure 5-6 - XPS profile of O 1s after passivation of 316L SS in a) 5% wt. and b) 25% wt. HNO_3, both with 30mmol dm^3 $Ce(NO_3)_3 \cdot 6H_2O$., at 0.2 and 0.8 V.

Due to the number of species involved, and the presence of different radionuclide surrogates, the data of Figure 5-4 to Figure 5-6 may be more easily understood by plotting the relative atomic percentage of each species. For the Fe profiles of Figure 5-4, the relative atomic percentage plot is shown in Figure 5-7. For the Cr profiles of Figure 5-5 for Ce, the relative atomic percentage plot is shown in Figure 5-8. Results from section 4.5 on 316L SS in HNO_3 only media have been included for comparison purposes.

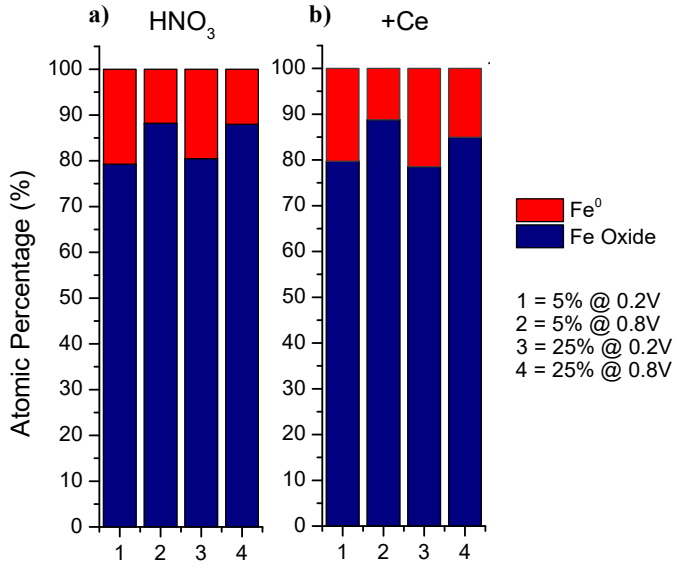

Figure 5-7 –Iron XPS component concentrations for a) HNO_3 solutions, b) HNO_3 solutions containing 30mmol dm^3 $Ce(NO_3)_3 \cdot 6H_2O$.

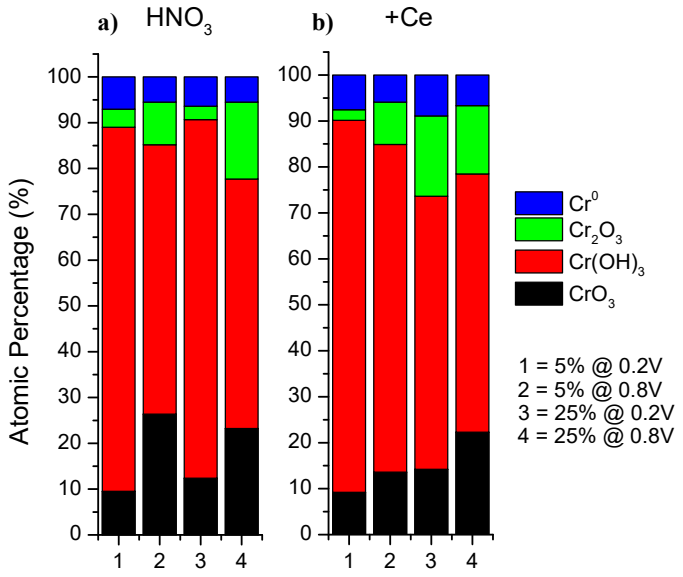

Figure 5-8 –Chromium XPS component concentrations for a) HNO_3 solutions, b) HNO_3 solutions containing 30mmol dm^3 $Ce(NO_3)_3 \cdot 6H_2O$.

Considering first the iron percentages of Figure 5-7. Increasing the HNO_3 concentration from 5% wt. to 25% wt. does not affect the iron oxide composition significantly at 0.2 or 0.8V. As discussed in Chapter 4, electrochemically it is known that at higher potentials Fe(II) is oxidised to Fe(III), generating Fe_2O_3 [57], [178], [179]. As such, the iron oxide signal at 0.8 V may be assumed to be dominated by Fe(III) oxide (hematite, α-Fe_2O_3,or maghemite, γ-Fe_2O_3). Importantly, there is little difference in atomic percentage between either 5% wt. or 25% wt., suggesting that it is differences in the Cr oxide film that are crucial to the observed electrochemical differences in corrosion behaviour. Furthermore, the effect of Ce on the iron component of the passive film is also minimal, with no significant differences in wt. % compared to experiments in HNO_3 only. This is consistent with the conclusion that it is the chromium in the film that mainly determines the overall electrochemical / corrosion behaviour of the steel surface.

Consider now the chromium profiles for HNO_3 in Figure 5-11. As with the HNO_3 only results, increasing the potential from 0.2 to 0.8 V increases the intensity of the CrO_3 peak as well as decreasing the intensity of the Cr^0 and $Cr(OH)_3$ peaks. As previously described in Chapters 3 and 4, this is due to chromium oxidising from its Cr(III) oxidation state (Cr_2O_3/$Cr(OH)_3$) to its more soluble Cr(VI) oxidation state (CrO_3). The increase in potential leads to the dissolution of Cr(VI) from the film and a decrease in Cr^0/$Cr(OH)_3$ as more Cr is converted to oxide/hydroxide and stripped out of the film.

In HNO_3-only solutions, the Cr speciation profiles obtained at 0.2 V are similar for both nitric acid concentrations studied i.e. 5 and 25% wt.

In the presence of Ce, there is a large difference in the composition of the Cr profile for 0.2 V in 25% wt. when compared to that of 5% wt. HNO_3 – the composition observed at 0.2 V at 5% wt. nitric in the presence of Ce being broadly similar to that recorded in the absence of Ce. The change at 25% wt is likely due to the formation of Ce(IV) at this HNO_3 concentration in accordance with the mechanism suggested above. The absence of any analogous difference in behaviour in the absence and presence of cerium at 0.2 V in 5% wt. HNO_3 indicates no Ce(IV) is formed at this HNO_3 concentration, a conclusion in keeping with Figure 5-1 - wherein a shift in E_{corr} in the presence of Ce is only observed at HNO_3 concentrations $\geq$10% wt., suggesting that the Ce(IV) generation mechanism described above only operates at HNO_3 concentrations greater than 10% wt.

Turning now to measurements at 0.8 V, the increase in Cr(VI) (in the presence and absence of Ce) in 5% wt. HNO_3 at this potential compared to 0.2 V is likely due to the increasing the oxidative stress on the electrode, therefore, increasing the likelihood that Cr(III) will oxidise to Cr(VI) (as explained above, see section 4.5.2). Increasing the HNO_3 concentration to 25% wt. leads to oxidation of Cr(III) to Cr(VI) either via electrochemical or Ce mediated means which will cause the passive film that has formed to undergo transpassive dissolution.

While the above analysis describes the effect Ce on the passive film, whether Ce is incorporated as part of their action on the Cr film has not been addressed. As such high resolution spectra of the cerium region, 860-900 eV in each set of respective experiments were taken. Figure 5-9 shows the XPS profile for cerium in 5 and 25% wt. HNO_3 at 0.2 and 0.8 V.

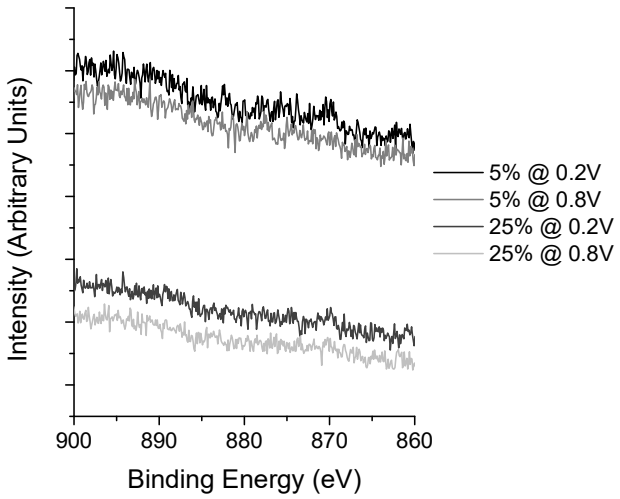

Figure 5-9 - XPS profile of Ce $3d_{5/2}$ after passivation of 316L SS in 5 and 25% wt. HNO_3, with 30mmol dm^3 $Ce(NO_3)_3 \cdot 6H_2O$, at 0.2 and 0.8 V.

A peak for Ce should occur within the 883 to 884 eV region. The spectra clearly show no Ce has been detected on the surface of the 316L SS electrode at both HNO_3 concentrations and potential ranges studied indicating that either no incorporation of Ce has occurred or that any Ce that has been incorporated is below the limit of detection of the XPS (0.1 atom%). This is most likely due to the Ce increasing the oxidative power of the media, as demonstrated by the higher E_{corr} values in the LSV studies, which leads to Cr(III) oxidation to Cr(VI) and film dissolution. As Cr is the primary component of the passive film formed at the steel surface at these pHs (see above) any effect that causes the dissolution of that film will

suppress Ce absorption/incorporation into that film. In this case, Ce appears to be working against itself, especially at 25% wt. HNO_3 when the conversion to Ce(III) to Ce(IV) is at its greatest (see Figure 5-1)

Overall, the work in this section has highlighted the possibility that the presence of Pu in nitric acid media may lead to an increase in corrosion especially at HNO_3 concentrations of 10% wt. or greater. This may affect the overall lifetime of the pipework in reprocessing plants. However, Pu is not likely to be taken up into the passive film, indicating that contamination of pipework by Pu is unlikely.

The next section discusses the influence of Am surrogate Eu on the behaviour of 316L SS in HNO_3 media.

5.2.2 Stainless Steel Passivation in the Presence of Europium Nitrate

5.2.2.1 Polarisation Curve Results

Eu has been used extensively as a surrogate for Am; studies tend to focus on the extraction of Eu/Am from reprocessing streams and improvement of vitrification techniques [188], [193]. Investigation of the effect of the presence of Eu/Am on stainless steel corrosion in reprocessing conditions has not been explored. The work here will serve as a brief investigation into the effect of the presence of Eu in HNO_3 on passivation in nitric acid media and whether Eu, and therefore Am, will become entrained in the passive film formed on 316L SS in XPS experiments.

Figure 5-10 shows potentiodynamic polarisation curves for 316L SS electrodes recorded in a) 5-35% wt. HNO_3 concentrations and b) 5-35% wt. HNO_3 concentrations containing 10mmol dm^3 $Eu(NO_3)_3 \cdot 5H_2O$ over the potential range -0.5 to 1.5 V.

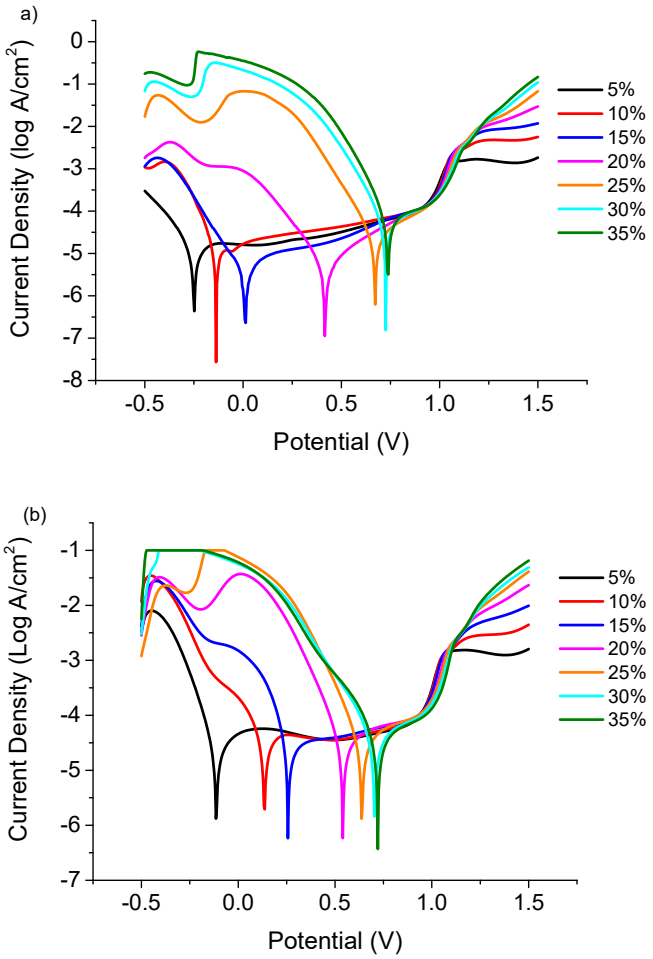

Figure 5-10 – Potentiodynamic polarisation plots of 316L SS in a) 5-35% wt. HNO_3 and b) 5-35% wt. HNO_3 containing 10mmol dm^3 $Eu(NO_3)_3{\cdot}5H_2O$ at room temperature (20±2°C). Plots were measured in the potential range -0.5-1.5 V (sweep rate, 10 mV s^{-1}).

From Figure 5-10b it can be seen that the shift in behaviour between high and low HNO_3 concentrations (15 and 20% wt), previously discussed in section 4.1, is less distinct in the presence of Eu. Overall lower concentrations of HNO_3 (5-20% wt.) have shifted E_{corr} to slightly more positive potentials in the presence of Eu, as shown in Figure 5-11. In HNO_3-only studies this region was shown to be passive. This would initially suggest that the presence of Eu may increase the metal's tendency to passivate at these HNO_3 concentrations.

5.2.2.2 E_{corr} and i_{corr} Analysis

Corrosion potential (E_{corr}) and corrosion current density (i_{corr}) were calculated using Tafel extrapolation of the linear segments of the measured potential-current density curves of Figure 5-10b, in the vicinity of E_{corr}. Figure 5-11a shows E_{corr} values obtained at 5 - 35% wt. HNO_3 concentrations in the presence of Eu.

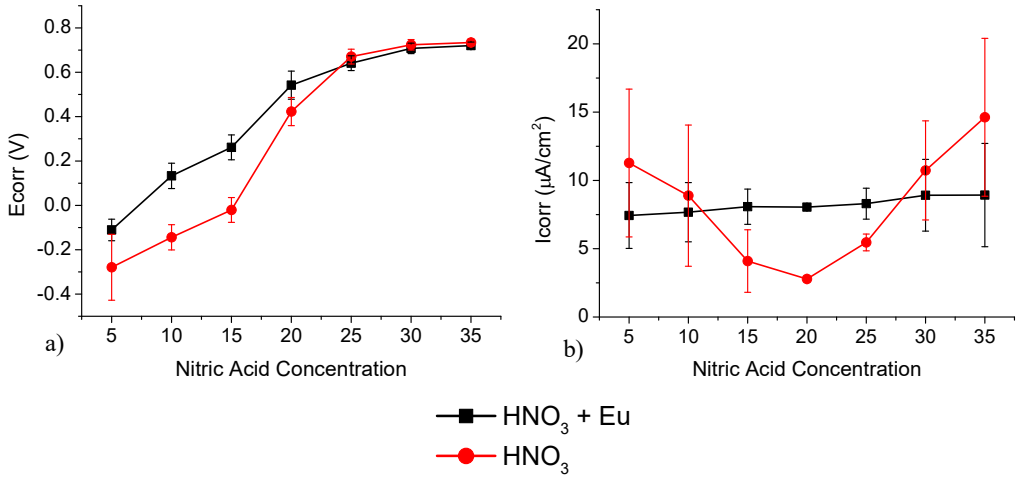

Figure 5-11 – a) Corrosion potential, E_{corr}, values and associated error bars vs. HNO_3 concentration b) Corrosion current density, i_{corr}. values and associated error bars vs. HNO_3 concentration calculated from Figure 5-10a for 316L SS in 5 - 35% wt. HNO_3 and Figure 5-10b for 316L SS in 5 - 35% wt. HNO_3 containing 10mmol dm^3 $Eu(NO_3)_3 \cdot 5H_2O$.

From Figure 5-11a it can be seen that E_{corr} variation with HNO_3 concentration at HNO_3 concentrations <25% wt. is more linear with increasing HNO_3 concentration in the presence of Eu than in HNO_3-only solutions, before plateauing at HNO_3 concentrations ≥25% wt. In HNO_3-only media this increase in E_{corr} was attributed to the increased HNO_2 content, leading eventually to transpassive dissolution of the passive film. However, in the presence of Eu, the more positive E_{corr} values at lower concentrations may be attributed to the steel entering into its passive region more rapidly at lower concentrations. This is supported by i_{corr} values in Figure 5-11b which, unlike 316L SS in HNO_3-only, do not show a rapid increase with HNO_3 concentrations ≥20% wt. Instead, they show a small slow increase with increasing

HNO_3 concentrations. Interestingly i_{corr} values are higher at HNO_3 concentrations < 30% wt. and >10% wt. in the presence of Eu than in HNO_3 only media.

It is possible that in the presence of Eu, 316L SS passivity is wider than in HNO_3-only solutions due to an alteration in the composition of the passive film, i.e. the film that is forming is less effective as a protective film, resulting in higher i_{corr} values, but provides a greater resistance to corrosion in highly oxidising conditions that corresponds to the pre-transpassive region of the polarisation curve i.e. E > ~+0.5 V. Previous analysis of LSV and XPS results (Sections 4.1 and 4.5) showed that the rapid increase in i_{corr} was due to the oxidation of Cr(III) to Cr(VI) which subsequently led to transpassive dissolution of the protective passive film. Previous studies have investigated the use of Lanthanides, such as cerium, lanthanum and samarium, as possible corrosion inhibitors[194], [195]. It has been suggested that lanthanides act as a thin barrier, by forming an insoluble film ($La(OH)_3$) on the surface of the stainless steel [194], [196]–[198]. However, no specific reference was found referring to Eu as a corrosion inhibitor, neither in the transpassive or pre-transpassive regions or otherwise..

From the results shown here it is possible that Eu is acting as a corrosion inhibitor under the conditions studied, most especially the transpassive and pre-transpassive regions. Further investigation into this is required. The presence of Eu on the surface of the steel will be further investigated in the XPS analysis in section 5.2.2.3.

Returning to the behaviour of 316L SS in HNO_3 in the presence of Eu, E_{corr}/i_{corr} variations may be more easily understood through the pseudo-polarogram plot shown in Figure 5-12, where E_{corr} is plotted against i_{corr} for HNO_3 concentrations 5-35% wt. for both HNO_3 only solutions and solutions containing Eu.

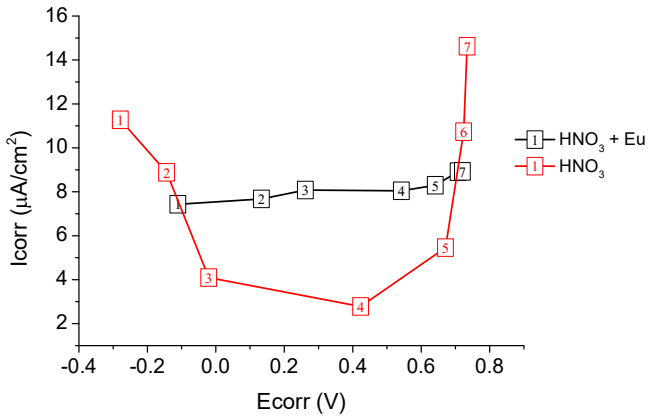

Figure 5-12 - Pseudo-polarogram of i_{corr} vs. E_{corr} calculated from Figure 5-10a (red) for 316L SS in 5 - 35% wt. HNO_3 and Figure 5-10b (black) for 316L SS in 5 - 35% wt. HNO_3 containing 10mmol dm^3 $Eu(NO_3)_3 \cdot 5H_2O$.

Figure 5-12 shows that compared to i_{corr} values recorded for 316L SS in the presence of HNO_3 only, in the presence of Eu three major differences are apparent: Firstly, at E_{corr} <0.6 V and >0 V, i_{corr} values are higher in the presence of Eu that in HNO_3 alone. Previously, an increase in i_{corr} has been linked to a change in passive film composition which has led to a less efficient protective film on the surface of the steel. As mentioned previously, lanthanide species are known to be good corrosion inhibitors [194], [196]–[198]. Lanthanide species form an insoluble film on the surface of metal, allowing them to act as a diffusion barrier, hindering the corrosion process. 316L SS already contains species which form an effective passive film, in particular Cr. By hindering corrosion it is possible that an insoluble Eu film, likely $Eu(OH)_3$ or similar [198], is also hindering the metals own passivation process. Therefore i_{corr} does not increase with increasing E_{corr} because the metal is passive, but *via* formation of a different passive film leads to higher i_{corr} values.

Secondly, when compared to i_{corr} measurements in HNO_3 only, i_{corr} values measured in the presence of Eu show only a small increase with increasing E_{corr}. As mentioned above, it is likely that the Eu in solution acting as a corrosion inhibitor by forming an insoluble film which is preventing corrosion on the surface of the metal. The so formed film is passive at a wider range than the passive film formed on 316L SS in HNO_3 only, therefore i_{corr} remains lower at higher HNO_3 concentrations.

Finally, unlike i_{corr} measurements in HNO_3 only, there is no rapid increase in i_{corr} at HNO_3 concentrations ≥ 30% wt. This behaviour suggests that the Eu layer that is formed on the 316L SS surface is more

effective at higher potentials (i.e. in the pre-transpassive and transpassive regions) and HNO_3 concentrations than the Cr film that forms in HNO_3 solutions.

Whilst electrochemical techniques are a valuable tool for measuring changes in corrosion behaviour at the electrode surface, it provides no information on the compositional nature of the film that has formed on the stainless steel surface. As such, next section discusses XPS analysis of the surface film formed on 316L SS in 5 and 25% wt. HNO_3. These concentrations have been chosen to represent the lower and higher range of HNO_3 concentrations that stainless steels are exposed to in reprocessing streams.

5.2.2.3 XPS analysis of 316L SS in Nitric Acid Media Containing Europium Nitrate

Curve fitted high resolution spectra of 316L SS samples in 5% wt. HNO_3 and 10mmol dm^3 $Eu(NO_3)_3 \cdot 5H_2O$ polarised at 0.2 and 0.8 V are shown in Figure 5-13, Figure 5-14 and Figure 5-15.

The iron profiles in Figure 5-13 show two peaks, the peak at 706.9 eV is due to elemental iron (Fe^0) and the peak around 710.7 eV is attributed to either iron (III) oxide (Fe_2O_3) or iron (II,III) oxide (Fe_3O_4), the same as the iron profiles under nitric acid only conditions described in Chapter 3 and 4.

The chromium profiles in Figure 5-14, shows four peaks which based on previous analysis can be attributed to: Cr metal (573.9 eV), Chromium (III) oxide (Cr_2O_3) (575.7 eV), Chromium (III) hydroxide (576.8 eV) and Chromium (VI) oxide (CrO_3) (578.8 eV).

Two broad, compound peaks due to oxygen are observed at 530 and 532 eV, shown in Figure 5-15. As in chapter 4, in and of themselves they are not enough to confirm speciation due to deconvolution issues. They are, however, useful to confirm the presence of mixed Fe/Cr oxides/hydroxides on the metal surface [105].

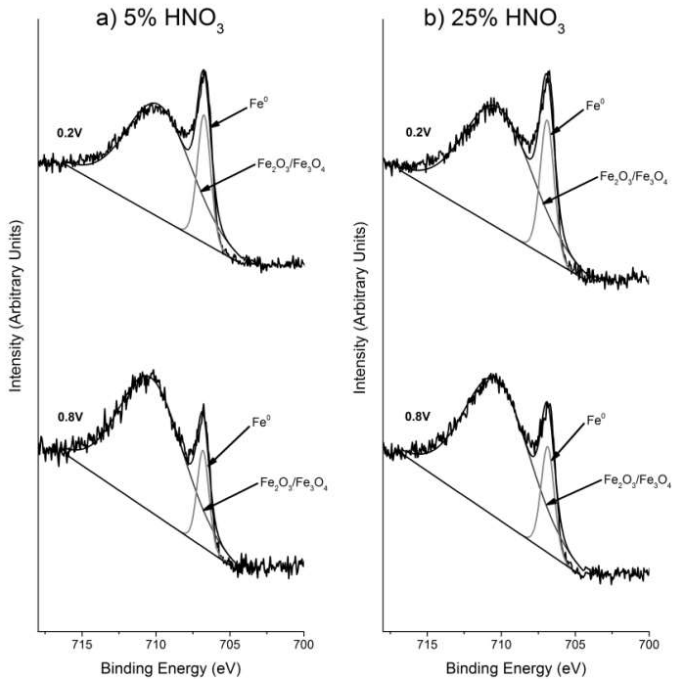

Figure 5-13 - XPS profile of Fe $2p_{3/2}$ after passivation of 316L SS in a) 5% wt. and b) 25% wt. HNO_3, both with 10mmol dm^3 $Eu(NO_3)_3 \cdot 5H_2O$, at 0.2 and 0.8 V.

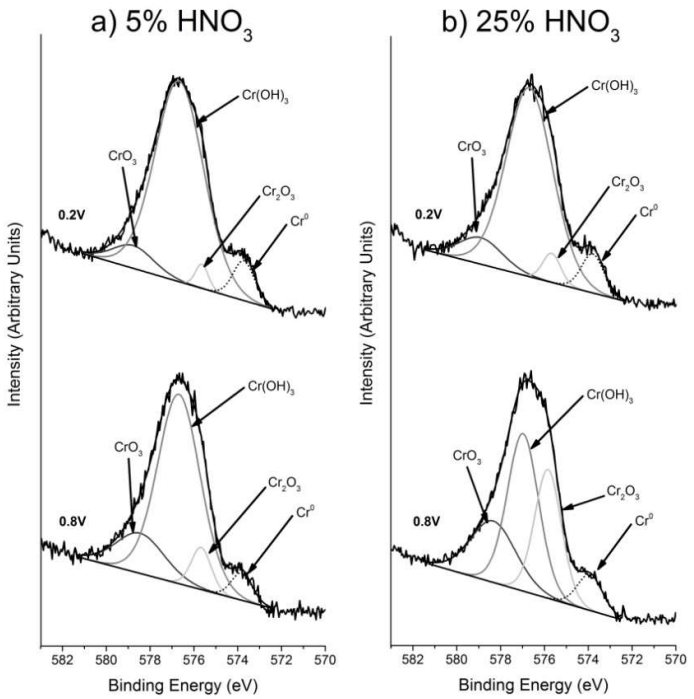

Figure 5-14 - XPS profile of Cr $2p_{3/2}$ after passivation of 316L SS in a) 5% wt. and b) 25% wt. HNO_3, both with 10mmol dm^3 $Eu(NO_3)_3 \cdot 5H_2O$, at 0.2 and 0.8 V.

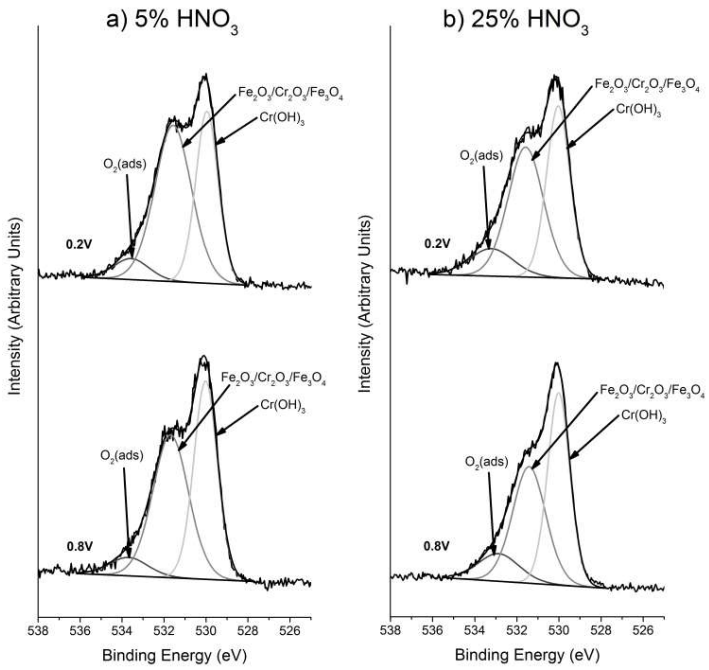

Figure 5-15 - XPS profile of O 1s after passivation of 316L SS in a) 5% wt. and b) 25% wt. HNO_3, both with 10mmol dm^3 $Eu(NO_3)_3{\cdot}5H_2O$, at 0.2 and 0.8 V.

Due to the number of species involved, and the presence of different radionuclide surrogates, the data of Figure 5-13 to Figure 5-15 may be more easily understood by plotting the relative atomic percentage of each species. For the Fe profiles of Figure 5-13, the relative atomic percentage plot is shown in Figure 5-16. For the Cr profiles of Figure 5-14, the relative atomic percentage plot is shown in Figure 5-17. Results from section 4.5 on 316L SS in HNO_3 only media are also included to aid in the readers comparison.

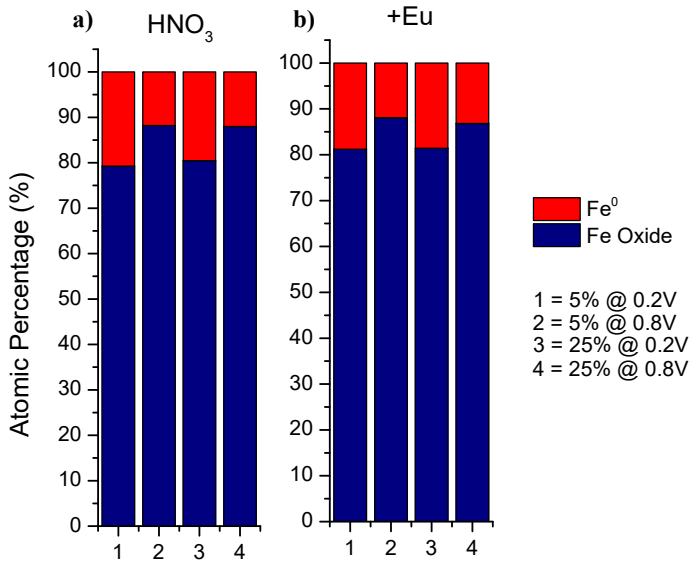

Figure 5-16 –Iron XPS component concentrations for a) HNO_3 solutions, b) HNO_3 solutions containing 10mmol dm^3 $Eu(NO_3)_3 \cdot 5H_2O$.

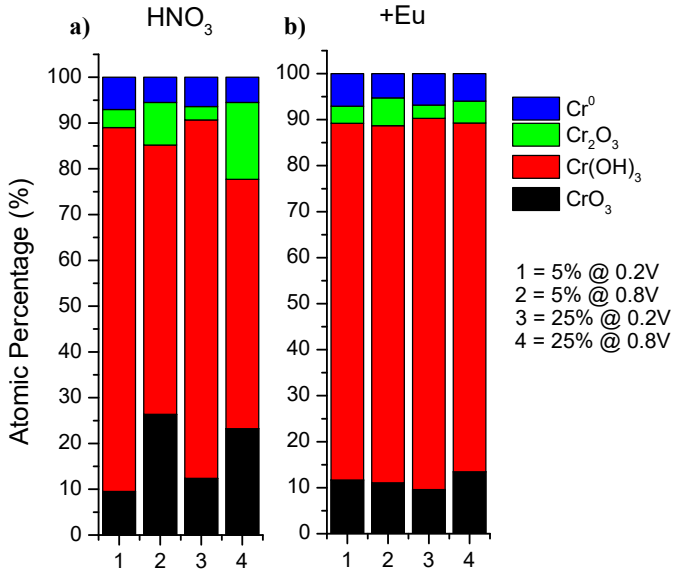

Figure 5-17 –Chromium XPS component concentrations for a) HNO_3 solutions, b) HNO_3 solutions containing 10mmol dm^3 $Eu(NO_3)_3 \cdot 5H_2O$.

Considering first the Fe percentages of Figure 5-16, increasing the HNO_3 concentration from 5% wt. to 25% wt. does not affect the iron oxide composition significantly at 0.2 or 0.8V. As discussed in Chapter 4, electrochemically it is known that at higher potentials Fe(II) is oxidised to Fe(III), generating Fe_2O_3 [57], [178], [179]. As such, the iron oxide signal at 0.8 V may be assumed to be dominated by Fe(III) oxide (hematite, α-Fe_2O_3,or maghemite, γ-Fe_2O_3). Furthermore, there is little difference in atomic

percentage between either 5% wt. or 25% wt., suggesting, as also described in Chapters 3 and 4, that it is differences in the Cr oxide composition that control the observed electrochemical differences in corrosion behaviour. Again, this is consistent with the conclusion that the primary constituent of the film determining electrochemical behaviour at these pHs is chromium, Importantly, the effect of Eu on the iron component of the passive film is also minimal, with no significant differences in wt. % compared to experiments in HNO3 only. This suggests that no mixed Fe/Eu oxide/hydroxide is being formed on the surface of the steel and that Eu is forming a separate film on the surface of the metal, either as a single component Eu oxide film or as a mixed metal oxide film with chromium..

Considering now the chromium profiles for HNO_3 containing 10 mmol dm^{-3} Eu(III) (as $Eu(NO_3)_3 \cdot 5H_2O$) in Figure 5-17b, the behaviour is different to that of Figure 5-17a containing HNO_3 only. In the presence of Eu, there is only a small decrease in Cr^0 content and a small increase in Cr_2O_3 content at both 5 and 25% wt. nitric acid concentrations when increasing the potential from 0.2 to 0.8 V. CrO_3 does not increase with potential in the lower concentration of nitric acid. However, it does increase at 0.8 V from 0.2 V in 25% wt. nitric acid concentration.

In comparison to the Eu free system, these results indicate that chromium and Cr(III) in particular being more stable towards oxidation in the presence of Eu, with Cr (III) not rapidly oxidising to Cr (VI). Thus, the passive film is more stable as chromium is less likely to dissolve. The electrochemical results suggested that Eu was forming a protective layer on the surface of the metal at the expense of the Cr passive film. It has been suggested that the Eu film hindered corrosion but also the regular passivation process, it is possible that the film that is being measured here is the initial air formed film on the surface of the steel which is then being protected by the Eu passive layer. The lack of increase in Cr(VI) content suggest that the surface is not being attacked by HNO_3 and thus not going transpassive; this is in agreement with LSV results which showed little increase in i_{corr} at higher potentials.

While the above analysis describes the effect of Eu on the Cr passive film, whether a detectable Eu film is present on the surface has not been addressed. As such high resolution spectra of the europium region, 1115-1150 eV, for each experiment shown in Figure 5-17a were taken, with results shown in Figure 5-18.

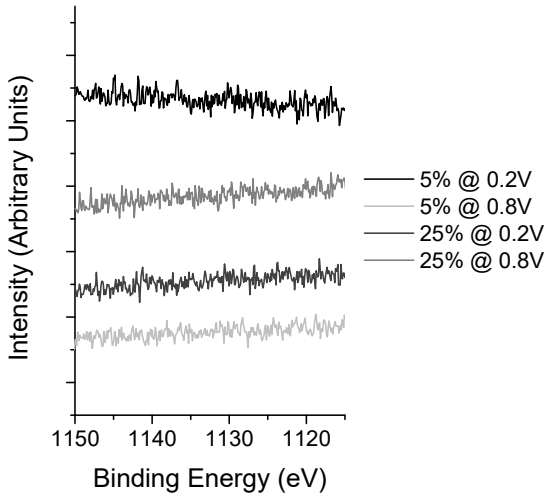

Figure 5-18 - XPS profile of Eu $3d_{5/2}$ after passivation of 316L SS in 5 and 25% wt. HNO_3, with 10mmol dm^3 $Eu(NO_3)_3 \cdot 5H_2O$, at 0.2 and 0.8 V.

A peak for Eu should occur within the 1135 eV region. The spectra clearly show no Eu has been detected on the surface of the 316L SS electrode at both HNO_3 concentrations and potential ranges studied indicating that no incorporation of Eu has occurred or that any Eu that has been incorporated is below the limit of detection of the XPS (0.1 atom%).. Studies on lanthanides as corrosion inhibitors indicated they form thin films in the surface of the metal they are protecting. It is likely that the thin Eu film was only loosely adsorbed on the steel surface and that the film was washed off or fell off in the sample preparation process for XPS analysis, leaving the steel surface analysed here. Further *in situ* investigation will be needed to determine what whether a thin Eu film does indeed form on the surface of 316L SS and that this is what has reduced corrosion in high HNO_3 concentrations.

5.3 Stainless Steel Passivation in the Presence of Uranyl Nitrate

Having discussed the effect of radionuclide surrogates on process steel corrosion and their degree of uptake within the passive film, we now discuss preliminary studies using an actual radionuclide contaminant, uranium. As with surrogate studies, we first describe the electrochemical behaviour of 316L SS in the presence of uranyl nitrate using LSV before analysing the surface passive film using XPS.

5.3.1 Polarisation Curve Results

Figure 5-19b shows the potentiodynamic polarisation curves for 316L SS electrodes recorded in 10 mmol dm^{-3} uranyl nitrate in HNO_3 concentrations from 5% wt. to 35% wt. For the reader's convenience polarisation curves for 316L SS electrodes in 5-35% wt. HNO_3, previously shown in Figure 4-1, are shown in Figure 5-19a.

From Figure 5-19b it can be seen that E_{corr} shows little shift at lower HNO_3 concentrations of 5-20% wt. before increasing to more positive potentials at ≥25% wt. This is in contrast to 316L SS in HNO_3 only, Figure 5-19a, where E_{corr} shifts to more positive potentials between 15 and 20% wt. HNO_3.

It is apparent from Figure 5-19 that the addition of uranyl is, in some way, inhibiting the nitrous mediated reduction of nitrate at 15 and 20% wt. HNO_3. At these concentrations of HNO_3, the higher concentration HNO_3 mechanism starts to obtain due to greater stability of NO_2 at higher acidities. This, in turn, regenerates the HNO_2, allowing the catalytic cycle to continue. This is shown below in equations (1.22) and (1.23).

$$HNO_{2(el)} + H^+ + e^- \rightleftarrows NO_{ads} + H_2O \tag{1.22}$$

$$HNO_3 + NO_{(ads)} \rightleftarrows HNO_{2(el)} + NO_{2(ads)} \tag{1.23}$$

There are two ways that uranyl can interrupt this cycle.

- Reaction with HNO_2
- Reaction with NO

Work by Chimes [199] investigated HNO_2 behaviour in uranyl nitrate solution and observed no reaction of any note. This is not surprising as, if uranyl did scavenge HNO_2 then there would be no need to add hydrazine to the PUREX process in order scavenge HNO_2 and so stabilise U(IV) and Pu(III) to nitrous-driven oxidation to U(VI) and Pu(IV) [200].

With regard to NO, the NO/NO^+ couple has an E_0 of ~0.6 V vs NHE (0.36 V vs SCE) [192]. Comparison of this E^0 with the Pourbaix diagram for uranium [201] indicates that this E_0 sits right at the UO_2^{2+}/U^{4+} boundary. There is thus the potential for uranyl to react with NO, disrupting the catalytic cycle in equations (1.22) and (1.23) and thus preventing the catalytic regeneration of HNO_2 and so supressing the reduction of nitrate.

Thus, at low HNO_3 concentrations the scavenging of NO by uranyl may interfere with the global reduction of HNO_3 to HNO_2, previously discussed in Chapters 3 & 4, causing the lack of shift in E_{corr}. However, once the HNO_3 concentration increases sufficiently, the abundance of HNO_3 and stability of NO_2 at higher HNO_3 concentrations leads to the rapid production of HNO_2 which results in the observed increase in E_{corr} and i_{corr} at higher HNO_3 concentrations.

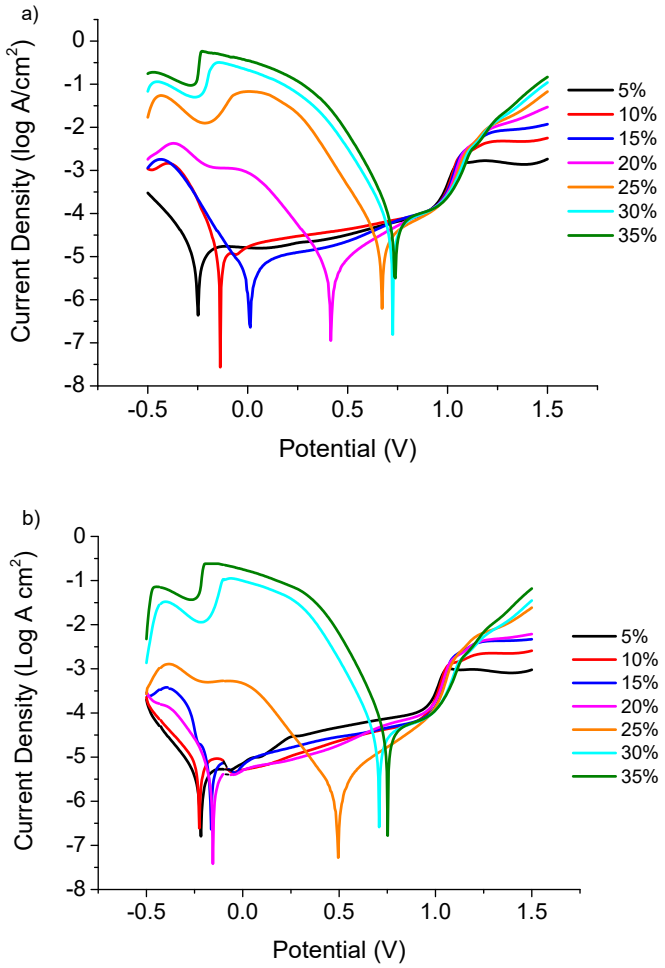

Figure 5-19 - Potentiodynamic polarisation plots of 316L SS in a) 5-35% wt. HNO_3 and b) 5-35% wt. HNO_3 containing 10 mmol dm^{-3} uranyl nitrate at room temperature (20 ±2°C). Plots were measured in the potential range -0.5 to 1.5 V (sweep rate, 10 mV s^{-1}).

The presence of uranyl has no effect on the transpassive behaviour of 316L SS, with the onset of transpassive dissolution occurring at ~1 V in Figure 5-19b, the same as that for HNO_3 only shown in Figure 5-19a.

More information will be gleaned from this data by extracting E_{corr} and i_{corr} values from the polarograms shown in Figure 5-20.

5.3.2 E_{corr} and i_{corr} Analysis

Corrosion potential (E_{corr}) and corrosion current density (i_{corr}) plots for Figure 5-19 were calculated using Tafel extrapolation of the linear segments of the measured potential-current density curves in the vicinity of E_{corr}. Both plots are shown in Figure 5-20.

As HNO_3 concentration increases, E_{corr} increases sigmoidally for both HNO_3 only solutions and HNO_3 solutions containing uranyl. In uranyl containing colutions, E_{corr} remains steady from 5 – 20% wt. HNO_3 and increases in between 20 and 25% wt. HNO_3 before plateauing at 30% wt. HNO_3. Generallly, these E_{corr} values are lower in the presence of uranyl for HNO_3 concentrations 10-25% wt. than in HNO_3 only. This supports the idea that the uranyl cation is interfering with the reduction of HNO_3, potentially by scavenging the surface adsorbed NO intermediate in HNO_3 reduction so reducing the HNO_2 content and therefore E_{corr} and i_{corr}. As previously mentioned, when the HNO_3 concentration increases sufficiently the abundance of HNO_3 and stability of NO_2 at higher HNO_3 concentrations leads to the rapid production of HNO_2 which results in the observed increase in E_{corr} and i_{corr}, albeit at higher HNO_3 concentrations that HNO_3 only conditions.

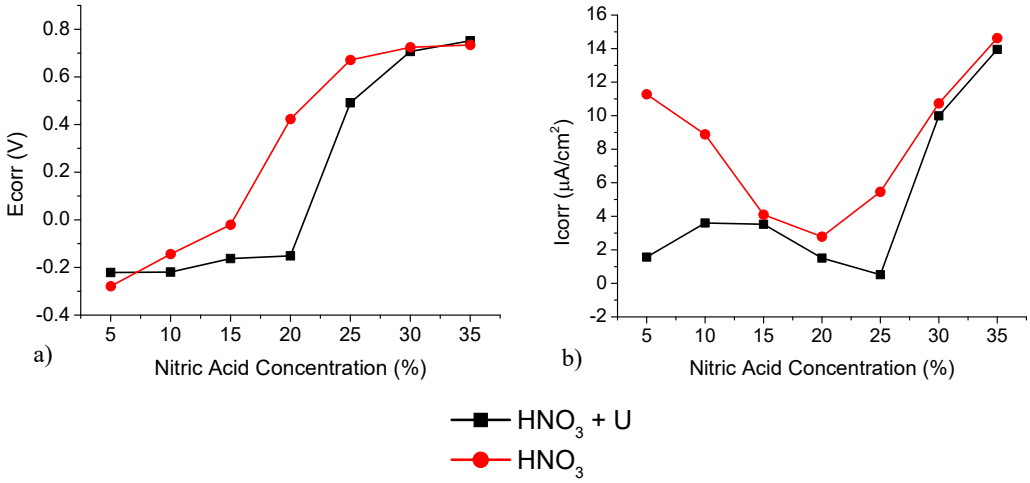

Figure 5-20 - a) Corrosion potential, E_{corr}, values vs. HNO_3 concentration b) Corrosion current density, i_{corr}. Values vs. HNO_3 concentration calculated from Figure 5-19a for 316L SS in 5 - 35% wt. HNO_3 and Figure 5-19b for 316L SS in 5 - 35% wt. HNO_3 containing 10 mmol dm^{-3} uranyl nitrate. NOTE: Uranyl nitrate experiments were only performed once, therefore no error bars are presented.

Figure 5-21 shows a pseudo-polarogram with E_{corr} plotted against i_{corr} for 316L SS in 10 mmol dm^{-3} uranyl nitrate and 5 - 35% wt. HNO_3. Figure 5-21 shows, overall, that 316L SS behaves in a similar manner in HNO_3 only media and in the presence of uranyl. What is apparent from looking at Figure 5-21 is that there is a more significant jump in E_{corr} in the presence of uranyl and then a rapid increase in i_{corr} after this jump in E_{corr} further supporting the conclusion that reaction with uranyl is interfering with HNO_3 reduction and HNO_2 cycling in lower HNO_3 concentrations which is only overridden once there is sufficient HNO_3 available.

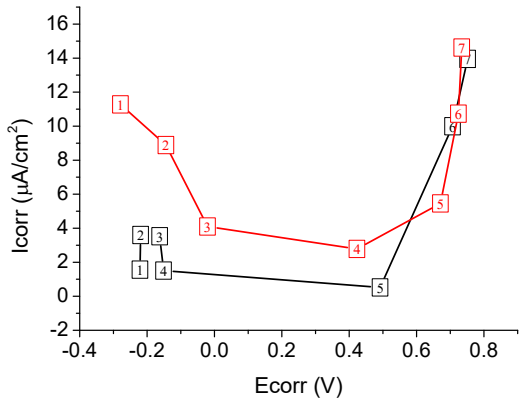

Figure 5-21 – Pseudo-polarogram of i_{corr} vs. E_{corr} calculated from Figure 5-19a (red) for 316L SS in 5 - 35% wt. HNO_3 and Figure 5-19b (black) for 316L SS in 5 - 35% wt. HNO_3 containing 10 mmol dm^{-3} uranyl nitrate.

As previously discussed, whilst electrochemical techniques are a valuable tool for measuring changes in corrosion behaviour at the electrode surface, it provides no information on the compositional nature of the film that has formed on the stainless steel surface. As such, next section discusses XPS analysis of the surface film formed on 316L SS in 5 and 25% wt. HNO_3. These concentrations have been chosen to represent the lower and higher range of HNO_3 concentrations that stainless steels are exposed to in reprocessing streams.

It is anticipated that U is more likely to be incorporated into the passive film in lower concentrations of HNO_3. From the LSV results and E_{corr} and i_{corr} analysis, it is possible that U, if incorporated at all, may even be present in 25% wt. HNO_3. XPS will be used in the following sections to assess the changes in composition of the passive film on the electrode surface.

5.4 XPS analysis of 316L in Nitric Acid Media Containing Uranyl Nitrate

Previous XPS spectra were recorded at the Nanotechnology and Integrated Bioengineering Centre (NIBEC), Ulster. Because of the use of uranium in the experiments described in this section, all subsequent XPS spectra were recorded in the uranium active labs at the University of Bristol.

Figure 5-22 shows the multiplet peaks for Cr $2p_{1/2}$ and Cr $2p_{3/2}$ after passivation in 25% wt. HNO_3 at 0.5 V. Multiplet splitting arises when an atom contains unpaired electrons [160]. An additional peak at 572-574 eV, which is not associated with the Cr multiplet peak, has been identified; there are two possible explanations for this peak, both associated with potential contaminants. 1) The peak is a Cu LMM auger transition [202], the peak matches the CuF_2 auger signal, ~571 eV BE, however there are no strong XPS peaks for Cu making this unlikely. 2) The peak is possibly Ag (~572-574 eV BE) [203], Ag also has secondary peaks which makes this a more likely candidate. However, without performing a survey scan using a Mg X-Ray source it is impossible to say for certain.

What is apparent is that the presence of foreign contaminants is evidence that the samples have been contaminated during sample preparation or whilst in storage awaiting analysis at Bristol University and subsequently confirmed by them. This has been taken into account during the assessment.

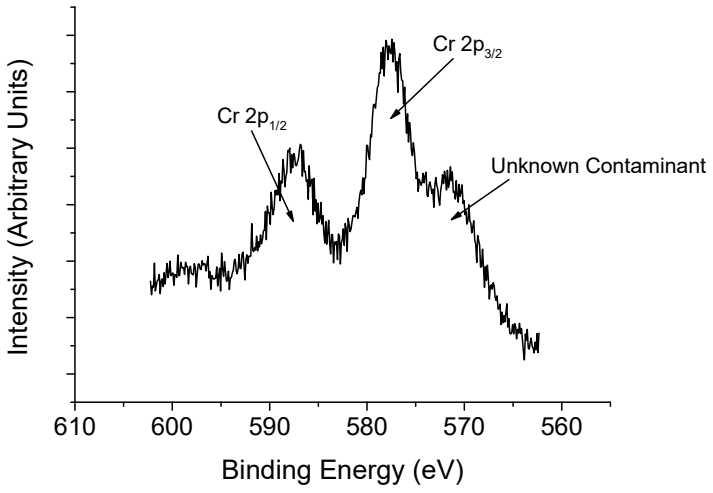

Figure 5-22 - XPS profile of Cr $2p_{1/2}$ and $2p_{3/2}$ after passivation of 316L SS in 25% wt. HNO_3 at 0.5 V.

Figure 5-23a shows the profiles for Cr $2p_{3/2}$ after passivation of 316L SS in 5 and 25% wt. HNO_3 at 0.2, 0.5 and 0.8 V. Figure 5-23b shows the profiles for Cr $2p_{3/2}$ after passivation of 316L SS in 5 and 25% wt. HNO_3 with 10 mmol dm^{-3} of U, at 0.2, 0.5 and 0.8 V. The chromium profiles in Figure 5-23a, shows one peak which is attributed to a combined Chromium (III) oxide/hydroxide peak (~578 eV). Previously in e.g. Figure 4-33 and all subsequent XPS of the chromium region in chapters 4 and 5, this peak was resolved into three peaks – two minor peaks at 578.6 eV and 575.82 eV, attributed to CrO_3 and Cr_2O_3 respectively, and a major peak at 576.84 eV, attributed to $Cr(OH)_3$ – see Table 3.2 for detailed assignment. Such deconvolution is not attempted for the data of Figure 5-23 due to the presence of the above-mentioned contaminant peak at 572-574 eV that **is** believed to mask the Cr_2O_3 peak at 575.82 eV– as well as the separate peak for metallic Cr^0 that, on the basis of Figure 4-33, might be expected at 573.97 eV.

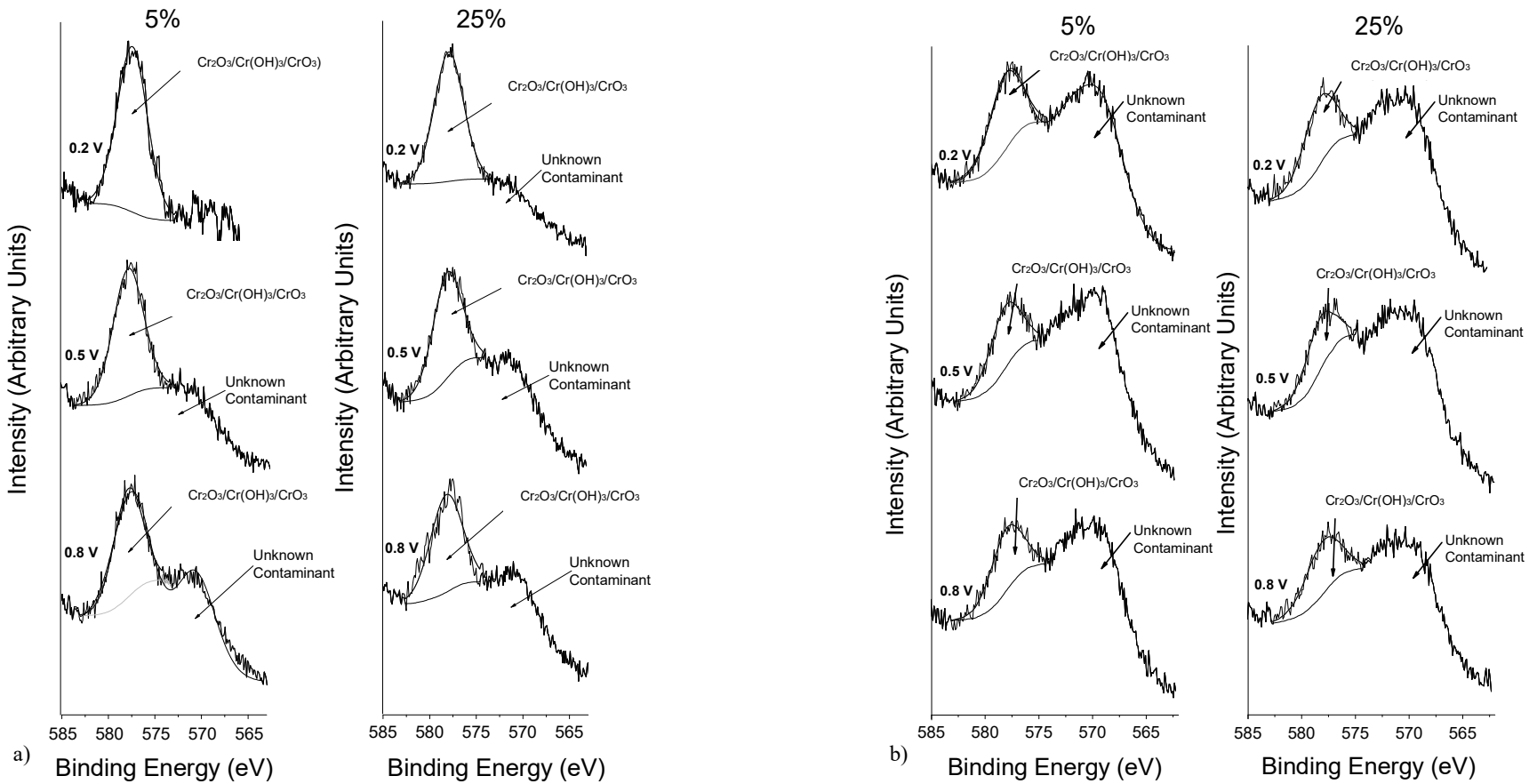

Figure 5-23 - XPS profiles of Cr $2p_{3/2}$ after passivation of 316L SS in 5 and 25% wt. HNO_3 at 0.2, 0.5 and 0.8 V, with a) containing HNO_3 only and b) with 10 mmol dm^{-3} of uranyl nitrate.

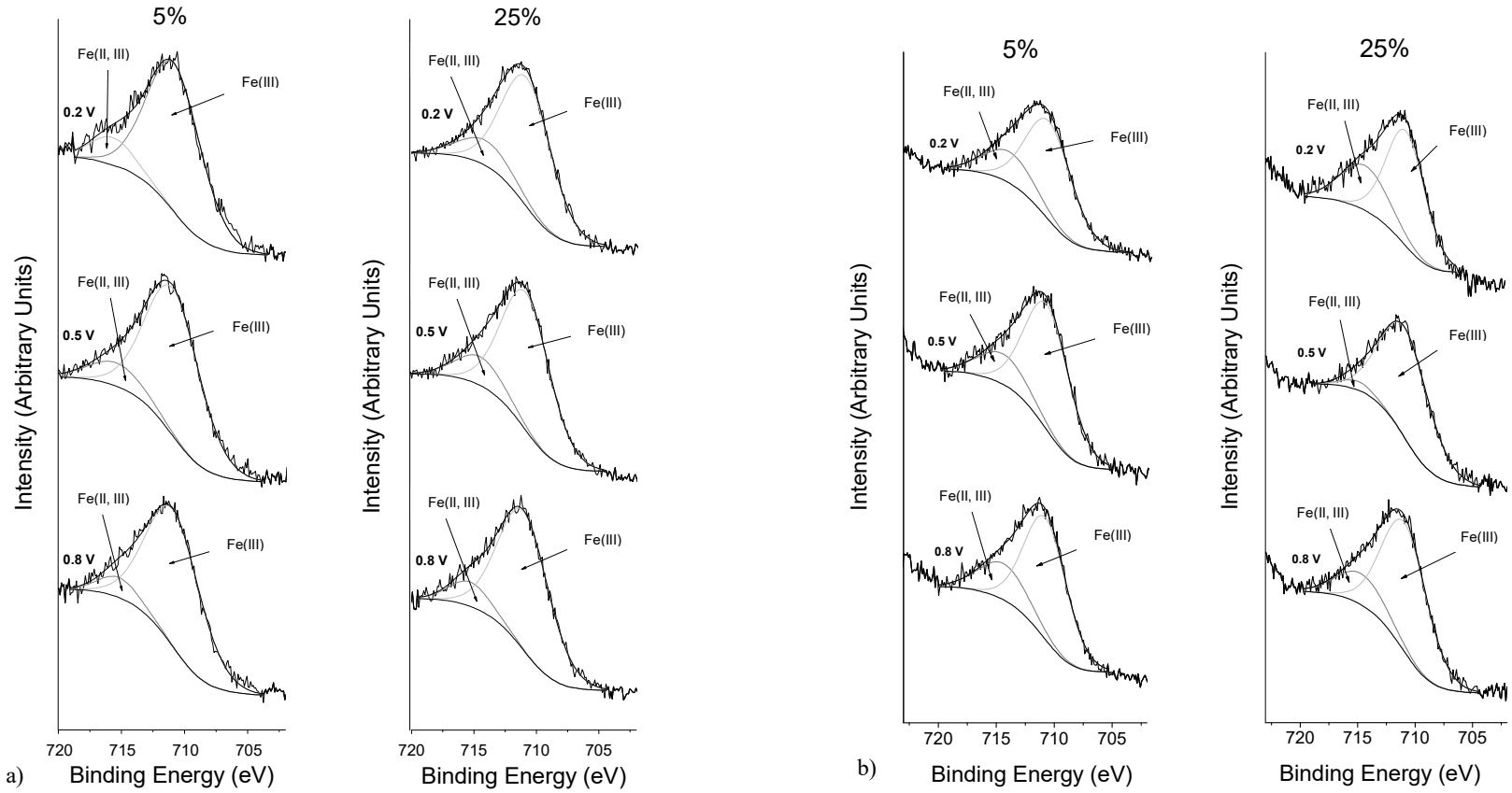

Figure 5-24 - XPS profiles of Fe $2p_{3/2}$ after passivation of 316L SS in 5 and 25% wt. HNO_3 at 0.2, 0.5 and 0.8 V, with a) containing HNO_3 only and b) with 10 mmol dm^{-3} of uranyl nitrate.

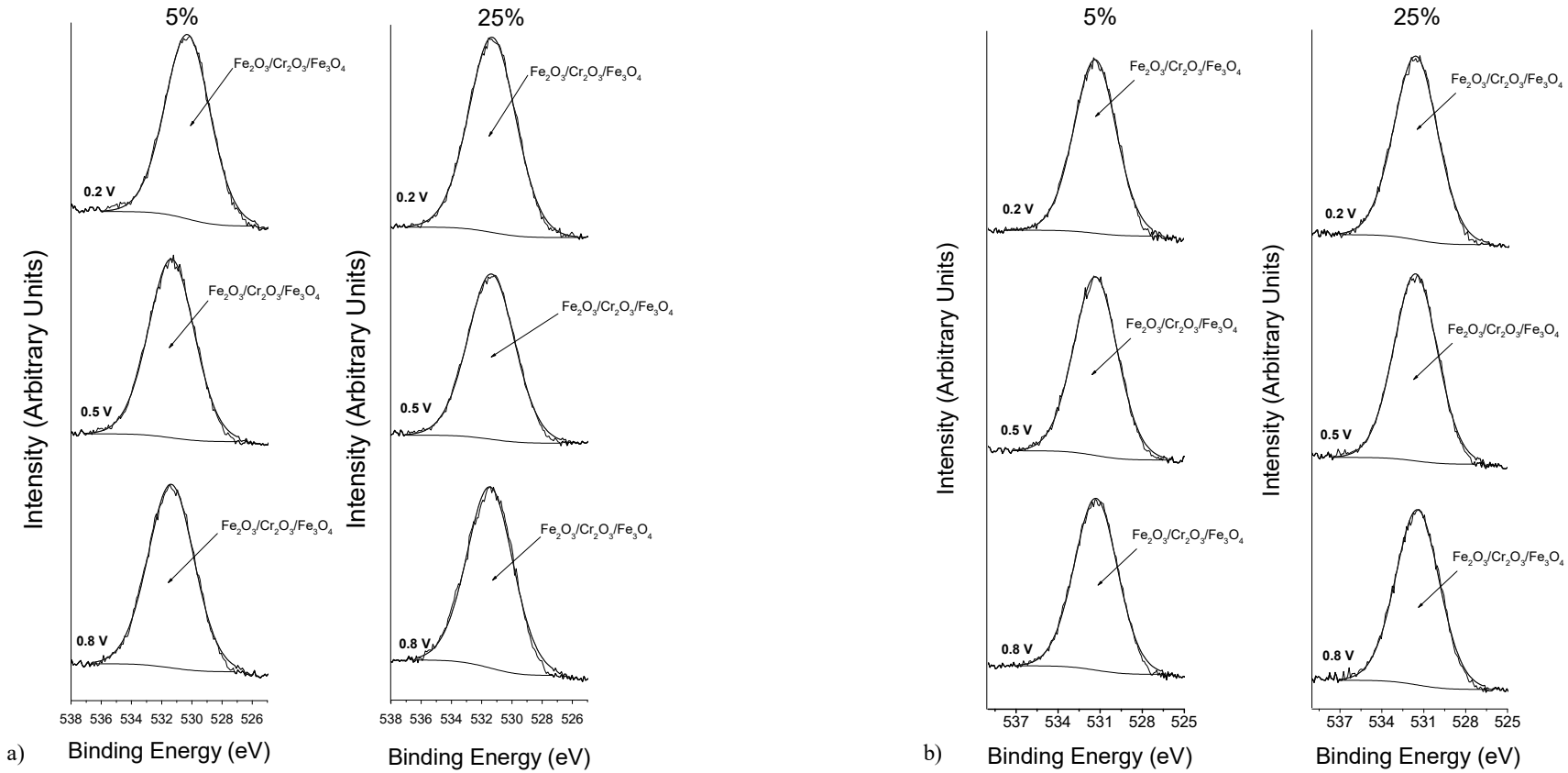

Figure 5-25 - XPS profiles of O 1s after passivation of 316L SS in 5 and 25% wt. HNO_3 at 0.2, 0.5 and 0.8 V, with a) containing HNO_3 only and b) with 10 mmol dm^{-3} of uranyl nitrate.

Figure 5-24a shows profiles for Fe $2p_{3/2}$ after passivation of 316L SS in 5 and 25% wt. HNO_3 at 0.2, 0.5 and 0.8 V. Figure 5-24b shows profiles for Fe $2p_{3/2}$ after passivation of 316L SS in 5 and 25% wt. HNO_3 with 10 mmol dm^{-3} of U, at 0.2, 0.5 and 0.8 V. All spectra of Figure 5-24 show one peak at ~711 eV. This is in agreement with earlier spectra recorded under similar conditions e.g. Figure 3-26 *et seq*. wherein the peak was assigned to a compound feature primarily associated with Fe_2O_3 / Fe_3O_4. The data of Figure 5-24 allow for this peak to be similarly broken down into two contributions: one peak associated with the Fe(II, III) ions of Fe_2O_3 and Fe_3O_4, centred at ~715 eV, and a second peak associated with the Fe(III) ions of Fe_2O_3 centred at ~711 eV. Noticable by its absence from Figure 5-24 is a peak at 706.96 eV, due to elemental iron (Fe^0) previously observed in earlier spectra recorded under similar conditions e.g. Figure 4-32 *et seq*. The XPS machines at the Universities of Bristol and Ulster used the same monochromated λ = 1486.6 eV / 0.83 nm X-ray source and thus both machines will have similar 3λ penetration depth of 2.5 nm. The absence of the Fe^0 peak in the data of Figure 5-24 therefore suggests that oxide layer on those samples is thicker than on those studied in the earlier spectra, so masking the uncorroded alloy beneath. This is surprising as all samples sent for study by XPS underwent exactly the same sample preparation i.e. 20 mins polarisation at the potential in question in the solution under study. The absence of the elemental Fe^0 peak at 706.96 eV leads to concerns regarding the validity of the data. As previously mentioned, the samples were contaminated during sample preparation or, most likely, whilst in storage awaiting analysis at Bristol University. Analysis and conclusions in previous sections show that the passive film formed on 316L SS is dominated by chromium and its behaviour, therefore it is not unreasonable to conclude that further analysis of the Fe spectra is unnecessary. In addition, the proximity of peaks shown in Figure 5-24 shows how different oxides will be present simultaneously making it difficult to discern which peak can be attributed to which oxide. Clearly classifying the contribution of each species to the identified peaks is considered to be unreliable and therefore the Fe $2p_{3/2}$ profiles will not be analysed any further.

Again reflecting the poorer quality of the XPS data presented in Figures 5-23 to 5-25 compared to that in the rest of this thesis, the oxygen profiles shown in Figure 5-25 are comprised of one single broad feature centred at 531 eV, rather than the two overlapping peaks seen at 530 and 532 eV in all other spectra recorded in this region using the same samples presented elsewhere in this thesis. As for the two peak oxygen spectra, the single peak spectra of Figure 5-25 are not enough to confirm speciation due to

deconvolution issues. They are, however, useful to confirm the presence of mixed Fe/Cr oxides/hydroxides on the metal surface [103].

As previously mentioned, the samples are believed to have been contaminated during analysis. Further analysis of uncontaminated samples is necessary in the future to confirm the behaviour of Cr in the presence of U.

The main objective of this work was to assess the presence of U in oxide films, Figure 5-26 shows the XPS profile for U in 5 and 25% wt. HNO_3 at 0.2, 0.5 and 0.8 V. A peak for U should occur in the 379 to 381 eV region. The spectra shows no clear U peak detected under any of the conditions studied, indicating that there is no incorporation of U when 316L SS is passivated in HNO_3 under these conditions.

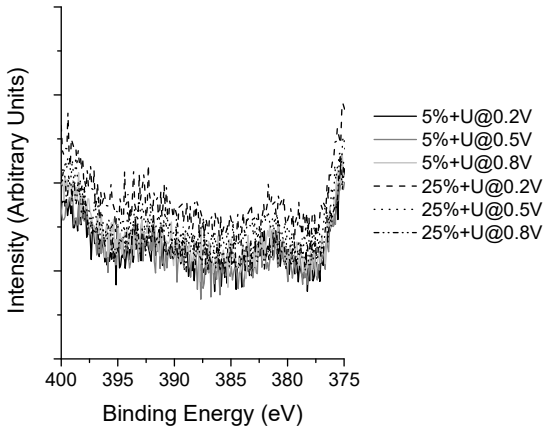

Figure 5-26 – XPS profile of U $4f_{7/2}$ after passivation of 316L SS in 5 and 25% wt. HNO_3, with 10 mmol dm^{-3} of uranyl nitrate, at 0.2 and 0.8 V.

5.5 Summary

In this chapter, we have described the electrochemical and surface compositional characterisation of 316L SS electrode in HNO_3 at various concentrations containing non-radioactive surrogate's cerium nitrate and europium nitrate and radioactive surrogate uranyl nitrate.

LSV studies in the presence of non-radioactive surrogate Ce, showed that the corrosion rate is higher than in HNO_3 only solutions. In the presence of Ce, at lower HNO_3 concentrations (<20% wt.), the corrosion

rate is significantly higher than in HNO_3 only solutions. It is believed that under these conditions, Ce(III) is oxidised to Ce(IV) which is a corrosion accelerator, thus leading to an increase in E_{corr}, i_{corr} and corrosion rate.

HNO_2 and NO_2 can both behave as reducing agents. The increase in HNO_3 concentration (≥20% wt.) increases the concentration of HNO_2 and the presence of NO_2, which is more stable in higher HNO_3 concentrations. Ce(IV) is reduced by these reducing agents to Ce(III) which has no effect on the corrosion rate. Thus, at higher HNO_3 concentrations it is HNO_2 and NO_2 that once again influence E_{corr}, i_{corr} and corrosion rate.

XPS spectra showed that no Ce was detected on the surface of the 316L SS electrode at both HNO_3 concentrations and potential ranges studied, suggesting that no incorporation of Ce occurs under these conditions. Again, this is most likely due to Ce increasing the oxidative power of the media in lower concentrations, as demonstrated by the higher E_{corr} values in the LSV studies, rather than being incorporated into the film. At higher concentrations Ce(III) has no influence on film formation and, therefore, also does not become entrained within the film.

These results have significant repercussions for Pu in HNO_3 media in reprocessing environments. The presence of Pu in nitric acid media may lead to an increase in corrosion at lower HNO_3 concentrations, affecting the overall lifetime of the pipework in reprocessing plants. However, Pu is not likely to be taken up into the passive film, indicating that contamination of pipework by Pu is unlikely and would not need to be considered during post operational clean out.

In the presence of Eu, the corrosion rate only increases slightly with HNO_3 concentration leading to the conclusion that Eu may be acting as a corrosion inhibitor. It has been suggested in previous studies that lanthanides make good corrosion inhibitors. Here, i_{corr} was higher in lower concentrations of HNO_3 than in HNO_3 only media. This suggests the formation of a passive film that is completely different to the one formed in HNO_3 only solutions, namely a Eu hydroxide which forms a thin protective layer on the surface of 316L SS. XPS spectra showed that no Eu was detected on the surface of the 316L SS electrode at both HNO_3 concentrations and potential ranges studied. This suggests that the film was loosely adsorbed on the surface of the steel rather than incorporated into a pre-existing film. Further *in-situ* investigation will

be required to define the effect Eu, and therefore Am, has on the formation of the passive film formed on 316L SS in HNO_3.

LSV studies showed in the presence of uranyl, that E_{corr} values were lower in the presence of uranyl for HNO_3 concentrations 10-25% wt. than in HNO_3 only. Corrosion rates were lower in 15-25% wt. HNO_3 in the presence or uranyl. It was concluded that uranyl ion, UO_2^{2+} is likely scavenging NO and interfering with the global reduction of HNO to HNO_2, causing the lack of shift in E_{corr}, i_{corr} and corrosion rate. However, once the HNO_3 concentration increased sufficiently, the abundance of HNO_3 and stability of NO_2 at higher HNO_3 concentrations will lead to the rapid production of HNO_2 which results in the observed increase in E_{corr} and i_{corr} at higher HNO_3 concentrations. The presence of U in solution had no effect on the onset of transpassive dissolution, which occurs at ~1 V.

XPS analysis was carried out on 5 and 25% wt. nitric acid containing 10mmol dm^{-3} uranyl nitrate at 0.2, 0.5 and 0.8 V and acid containing 30 mmol dm^{-3} Cerium (III) nitrate and 10mmol dm^{-3} Europium (III) nitrate at 0.2 and 0.8 V. Results showed that for HNO_3 solutions containing Ce and Eu, Fe oxide levels increased with an increase in potential in all solutions. At higher potentials Cr(III) will be oxidised to Cr(VI), which is more soluble. The dissolution of Cr(VI) will lead to a relative increase in iron content in the passive film which is observed here. This behaviour could not be identified in the spectra in the presence of uranyl, where a peak for Fe metal could not be identified.

Overall, Cr hydroxide dominated the passive film in lower potentials and HNO_3 concentrations and increase in both potential and HNO_3 led to the formation of a more oxide rich layer. As potentials increased further the Cr(III) is oxidised to Cr(VI). The dissolution of Cr(VI) and oxidation of Cr(III) reduced the efficacy of the passive film which leads it's subsequent transpassive dissolution. However, In HNO_3 solutions containing Eu the oxidation of Cr(III) to Cr(VI) appears reduced, indicating continued stability of the passive film at the potentials and HNO_3 concentrations studied. Ce increased the oxidation of Cr(III) to Cr(VI) at higher potentials. Within this chapter we were unable to fully analyse the U data due to the contamination of the U samples. Further analysis is necessary to fully understand the behaviour of oxides in the presence of U.

The results from this chapter suggest that there is no incorporation of radionuclide surrogate contaminants in the passive film formed on 316L SS. This implies that steel types that are chosen specifically for their

passivity for use in extreme acid environments in the presents of radionuclide contaminants may not be contaminated within their passive film. There are a wide range of radionuclides within reprocessing streams and the detection range of XPS (0.1 to 1 atomic %) may not be sensitive enough to detect the radionuclide surrogate contaminants studied here. Therefore, further *in-situ* investigation is required to ascertain whether this inference is correct. This is discussed further in section 6.3.

Chapter 6

Conclusions and Further Work

6 CONCLUSIONS AND FURTHER WORK

6.1 Project Objectives

The key objective of this project was to assess the possibility of contaminant entrainment in passive oxide films formed on stainless steel surfaces in HNO_3 conditions representative of reprocessing flow sheet. Entrainment of radionuclide contaminants in corrosion products had been extensively studied. Mainly nuclear plant materials, such as coolant circuits, or geological repository environments, such as corroding steel canisters. However, studies have not looked at the possibility of contaminant sorption/co-deposition on passive oxide films formed in HNO_3 conditions representative of reprocessing.

6.2 Conclusions

Initial experiments have focused on the characterisation of 316L SS in HNO_3 concentrations ≤15% wt. Regions for active dissolution, onset of passivation, passivity, transpassive dissolution and secondary passivation/oxygen evolution were identified.

LSV studies showed that E_{corr} and i_{corr} increased with increasing HNO_3 concentration. This behaviour has been attributed to a change in the HNO_2 regeneration mechanism. At lower concentrations, regeneration of HNO_2 is believed to occur on the stainless steel surface. This is a slow process which is dependent on the diffusion of HNO_3 to the surface of the steel. At higher concentrations, the mechanism shifts to near surface dominated based regeneration. The abundance of HNO_3 and stability of NO_2 at higher HNO_3 concentrations leads to the rapid production of HNO_2 which results in the observed increase in E_{corr} and i_{corr}.

EIS studies nicely support this assessment, with wide R_p peaks and high R_p values at lower concentrations (<20% wt.) and narrower peaks and lower R_p values at higher HNO_3 concentrations (>20% wt.). Onset of R_p increase occurs at higher potentials in higher HNO_3 concentrations, following the increase in E_{corr} observed in LSV studies. Lower R_p values coincide with an increase in i_{corr} values, this is most likely due to the oxidation of Cr(III) to Cr(VI), which is more soluble, and the subsequent dissolution of Cr(VI) reducing the efficacy of the passive film. Onset of transpassive dissolution occurred at ~1 V for a HNO_3 concentrations.

Figure 6-1a, produced by Fauvet *et al.* [6], shows a comparison between the domains of stability of 316L SS and 304L SS and 310L SS in nitric acid as a function of concentration and temperature (originally shown in Section 1.2.2.2.3). Figure 6-1a shows 316L SS with no region of stability above 3mol/L. The LSV and EIS work presented here has shown that 316L SS actually has a narrow region of passivity in HNO_3 up to 8mol/L at room temperature (25ºC). Figure 6-1a has been updated to include this region and is shown in Figure 6-1b.

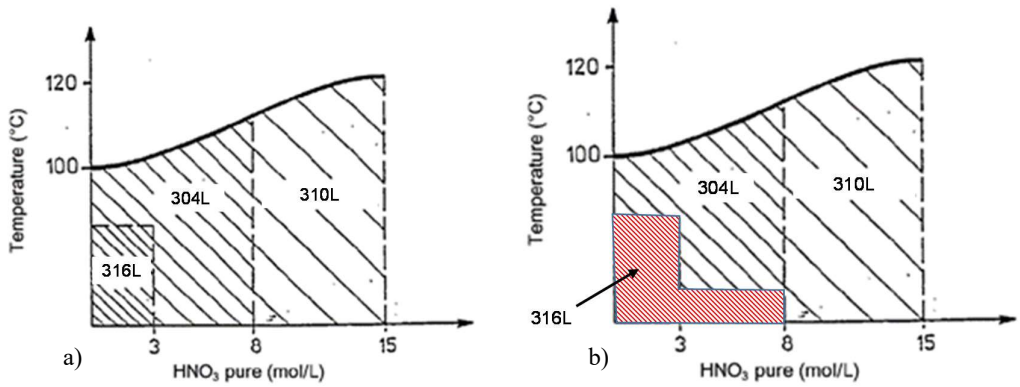

Figure 6-1 – a) Comparison between the domains of stability of a Mo containing steel (316L SS) and two low Mo steels is (304L SS and 310L SS) in nitric acid as a function of concentration and temperature [6] *b) an updated figure to include information gathered in the work presented here..*

The HNO_3 reduction mechanism was investigated using 316L SS Rotating Disk Electrodes. The HNO_3 reduction mechanism description can be found in Section 1.3.4.

RDE studies indicate two forms of Schmid's mechanism obtain on steels: 1) At HNO_3 concentrations ≤20% wt., the reaction of surface adsorbed intermediates such as NO and NO_2 dominate (as proposed by Balbaud [5] and Fauvet [6]) and the associated reduction current then shows no dependence on electrode rotation speed. 2) At HNO_3 concentration ≥20% wt., the reaction of NO and NO_2 intermediates in the solution near the electrode surface dominate (proposed by Lange [7], and Carta & Pigford [8]) and the associated reduction current then decreases with increasing rotation speed.

The latter behaviour is important when considering stainless steel pipework within nuclear environments that contain high concentrations of HNO_3. At higher concentrations any stagnation or reduction in the flow rate may lead to an increase in the autocatalytic reduction process of nitric acid which, in turn, will lead to an

increase in the corrosion potential, moving towards transpassive behaviour. This will over time lead to intergranular corrosion and subsequent pipework failure.

EQCM has been shown to follow the in-situ mass change of a passive stainless steel electrode resulting from the application of a potential. We have used EQCM to study the induced formation of the passive oxide layer at SS 2343 (a 316L analog). Using electrochemical techniques, we have established the viability of SS2343 as an analogue for 316L SS. Polarisation curves were recorded on QCM crystals with simultaneous measurements of mass change. Current and mass-response curves show that at HNO_3 concentrations ≤15% wt. the current trace may suggest that the steel is passive, however, the mass loss in the mass trace indicates that, at low potentials, the film may not be fully formed and therefore will not provide full protection for the steel surface. At higher potentials mass increases indicating stable passive film formation. At HNO_3 concentrations ≥20% wt., passive film formation does not occur below E_{corr}. Below E_{corr} mass traces were noisy showing large mass losses and gains. This is believed to be mainly due to hydrogen evolution at the electrode surface. When the potential reached E_{corr} mass increased at each HNO_3 concentration and the mass trace stabilised. The narrower region of passivity agrees nicely with LSV and EIS studies which suggest that at HNO_3 concentrations ≥20% wt. a rapid autocatalytic regeneration of HNO_2 is occurring in solution. This inhibits passive film formation and leads to an increase in E_{corr}.

In the potential 'staircase' experiments, the potential was held for a longer time to assess mass change of SS 2343 as a function of HNO_3 concentration (5% wt. to 35% wt.). At HNO_3 concentrations ≤15% wt., the maximum extent of oxide growth is observed at E=~0.55 V. Beyond this point, the transpassive processes leads to a mass loss from the electrode surface, the first time such a feature has been observed on passivated stainless steel. Oxide growth is not seen at HNO_3 ≥20% wt., with all samples presenting substantial mass loss at E=0.7 V, a transpassive process also seen in the case of samples studied at ≤15% wt. This has repercussions for the use of stainless steels in highly oxidising environments, such as those that may occur in the concentrated HNO_3 highly active raffinate liquor solutions that are found in evaporators.

These studies provided us with information that will allow us to artificially 'grow' oxide layers in any concentration of HNO_3 for XPS studies. Overall it is more likely that contaminant entrainment is going to occur in lower concentrations of HNO_3 (<20% wt.) where a strong passive oxide film forms, rather than at higher HNO_3 concentrations (>20% wt.) where the ability to produce a passive oxide film appears greatly reduced.

XPS analysis showed that in both 5 and 25% wt. HNO_3 the passivation of 316L SS formed a passive film consisting of hydroxide rich layer and oxide layers at lower potentials. Fe is believed to shift from an Fe(II) dominant oxide to Fe(III), no discernible shift was identified therefore Cr is believed to play a more crucial role in the electrochemical changes observed. With an increase in potential and HNO_3 concentration the passive film shifted to a relatively more dominant Cr oxide layer due the preferential formation of Cr_2O_3 from $Cr(OH)_3$ at low pH. At higher HNO_3 concentrations this leads to an increase in the formation Cr(VI), at high potentials Cr(VI) intensity decreased, this has been attributed to rapid dissolution into solution.

Electrochemical studies exhibited a shift in behaviour between 15 and 25% wt. nitric acid. It was expected that this would affect the composition of the passive film. Further studies on 316L SS in HNO_3 using XPS will allow for clarification as to why this occurs. It is likely that the shift in electrochemical behaviour is mostly due to the nitric acid autocatalytic reduction interactions with 316L SS but the exact mechanism has yet to be determined.

The effect of HNO_3 on 316L stainless steel dissolution at two different concentration regimes, ≤ 15% wt. typical of that found in reprocessing actinide 'strip' steps and > 15% wt. typical of that found in 'head end' fuel pin dissolution, highly active liquor evaporators and in initial uranium scrub and backwash steps was established. The effect of radionuclides on 316L SS corrosion behaviour and the incorporation of said radionuclides into the so formed passive film in both concentration regimes was investigated. Using the same electrochemical and analytical analysis techniques were used on HNO_3/316L SS systems but in the presence of both radionuclide surrogates (Europium/Cerium, acting as a surrogates for Americium/Plutonium respectively) and non-active radionuclides (Uranium).

LSV studies in the presence of non-radioactive surrogate Ce, showed that the corrosion rate is higher than in HNO_3 only solutions. In the presence of Ce, at lower HNO_3 concentrations (<20% wt.), the corrosion rate is significantly higher than in HNO_3 only solutions. It is believed that under these conditions, Ce(III) is oxidised to Ce(IV) which is a corrosion accelerator, thus leading to an increase in E_{corr}, i_{corr} and corrosion rate. Further experimentation will be required to confirm the presence of Ce(IV) within solution in the conditions described above.

HNO_2 and NO_2 can both behave as reducing agents. The increase in HNO_3 concentration (≥20% wt.) increases the concentration of HNO_2 and the presence of NO_2, which is more stable in higher HNO_3 concentrations.

Ce(IV) is reduced by these reducing agents to Ce(III) which has no effect on the corrosion rate. Thus, at higher HNO_3 concentrations it is HNO_2 and NO_2 that once again influence E_{corr}, i_{corr} and corrosion rate.

XPS spectra showed that no Ce was detected on the surface of the 316L SS electrode at both HNO_3 concentrations and potential ranges studied, indicating that no incorporation of Ce occurs under these conditions. Again, this is most likely due to Ce increasing the oxidative power of the media in lower concentrations, as demonstrated by the higher E_{corr} values in the LSV studies, rather than being incorporated into the film. At higher concentrations Ce(III) has no influence on film formation and, therefore, also does not become entrained within the film.

The results here have significant repercussions for Pu in HNO_3 media in reprocessing environments. The presence of Pu in nitric acid media may lead to an increase in corrosion at lower HNO_3 concentrations, affecting the overall lifetime of the pipework in reprocessing plants. However, Pu is not likely to be taken up into the passive film, indicating that contamination of pipework by Pu is unlikely and would not need to be considered during post operational clean out.

In the presence of Eu, the corrosion rate only increases slightly with HNO_3 concentration leading to the conclusion that Eu may be acting as a corrosion inhibitor. It has been suggested in previous studies that lanthanides make good corrosion inhibitors. Here, i_{corr} was higher in lower concentrations of HNO_3 than in HNO_3 only media. This suggests the formation of a passive film that is completely different to the one formed in HNO_3 only solutions, namely a Eu hydroxide which forms a thin protective layer on the surface of 316L SS. XPS spectra showed that no Eu was detected on the surface of the 316L SS electrode at both HNO_3 concentrations and potential ranges studied. This suggests that the film was loosely adsorbed on the surface of the steel rather than incorporated into a pre-existing film. Further *in-situ* investigation will be required to define the effect Eu, and therefore Am, has on the formation of the passive film formed on 316L SS in HNO_3.

LSV studies showed in the presence of uranyl, that E_{corr} values were lower in the presence of uranyl for HNO_3 concentrations 10-25% wt. than in HNO_3 only. Corrosion rates were lower in 15-25% wt. HNO_3 in the presence or uranyl. It was concluded that at the uranyl ion, UO_2^{2+} is likely to be scavenging NO and thus interfering with the global reduction of HNO_3 to HNO_2, causing the lack of shift in E_{corr}, i_{corr} and corrosion rate. However, once the HNO_3 concentration increased sufficiently, the abundance of HNO_3 and stability of NO_2 at higher HNO_3 concentrations will lead to the rapid production of HNO_2 which results in the observed

increase in E_{corr} and i_{corr} at higher HNO_3 concentrations. The presence of U in solution had no effect on the onset of transpassive dissolution, which occurs at ~1 V.

XPS analysis was carried out on 5 and 25% wt. nitric acid containing 10mmol dm^{-3} uranyl nitrate at 0.2, 0.5 and 0.8 V and acid containing 30 mmol dm^{-3} Cerium (III) nitrate and 10mmol dm^{-3} Europium (III) nitrate at 0.2 and 0.8 V. Results showed that for HNO_3 solutions containing Ce and Eu, Fe oxide levels increased with an increase in potential in all solutions. At higher potentials Cr(III) will be oxidised to Cr(VI), which is more soluble. The dissolution of Cr(VI) will lead to a relative increase in iron content in the passive film which is observed here. This behaviour could not be identified in the spectra in the presence of uranyl, where a peak for Fe metal could not be identified. Contamination of the samples prevented further assessment of the data.

Overall, Cr hydroxide dominated the passive film in lower potentials and HNO_3 concentrations and increase in both potential and HNO_3 led to the formation of a more oxide rich layer. As potentials increased further the Cr(III) is oxidised to Cr(VI). The dissolution of Cr(VI) and oxidation of Cr(III) reduced the efficacy of the passive film which leads it's subsequent transpassive dissolution. However, In HNO_3 solutions containing Eu the oxidation of Cr(III) to Cr(VI) appears reduced, indicating continued stability of the passive film at the potentials and HNO_3 concentrations studied. Ce and U both increased the oxidation of Cr(III) to Cr(VI) at higher potentials.

Overall the results have shown that HNO_3 concentration, and subsequently the HNO_2 regeneration mechanism, plays a key role in the formation and composition of the passive film on 316L SS. No contaminants were detected in the passive films formed on the steel in passive conditions indicating that if the steel remains passive in HNO_3 conditions representative of reprocessing that the risk of contaminant uptake is low. HNO_3 RDE studies show that stagnation of HNO_3 could lead to the intergranular corrosion and subsequent failure of the pipework.

There are many avenues of research to be explored to help supplement this theory which will be discussed in 6.3.

6.3 Further work

Whilst initial work has been carried out to electrochemically characterise 316L SS in a range of HNO_3 concentrations that are representative of nuclear reprocessing streams and to analyse surface composition of the passive film formed under these conditions in the presence of radionuclide surrogates. Further exploration into the electrochemical behaviour of steel in HNO_3 and in the presence of radionuclides is required. This can be separated into four key areas of study: (i) further investigation in the effect of HNO_3 on the passivation of 316L SS. (ii) further investigation into the effect of the addition of single radionuclide surrogates into HNO_3 media, (iii) use of electrochemistry to characterise the behaviour of stainless steel types in the presence of reprocessing stream simulants and (iv) temperature dependency on the formation of the passive film in HNO_3 and in the presence of radionuclides.

In the first (i), there are several key fields identified:

- Further development of the EQCM for use in passive film formation studies on steels. The EQCM has been shown to be a viable tool for measuring film formation on steel piezoelectrodes. Improvement in the experimental setup may allow for the measurement of film formation under flowing solution, more closely simulating pipework conditions.

- Investigation into the secondary passivation of 316L SS with focus on film composition, using XPS and other suitable techniques (potentially those with a greater detection limit, as shown in Figure 2-20), and investigations into Fe oxide formation and solubility at high potentials and HNO_3 concentrations.

- The use of detailed XPS and other suitable techniques (potentially those with a greater detection limit, as shown in Figure 2-20) at various HNO_3 concentrations and potentials to investigate HNO_3 reduction behaviour 'shift' and the effect this has on passive film formation. Work in Chapter 4 investigated film formation at high HNO_3 concentration and low HNO_3 concentrations at high and low passive potentials. More detailed studies into wider potential regions, in particular at E_{corr} where current increases with increasing HNO_3 concentration and the region of secondary passivation at potentials >1 V.

- Further investigation into HNO_3 reduction kinetics using koutecky-levich analysis to allow for a complete numerical treatment of all processes taking place at the metal/solution interface. With particular interest on the HNO_3 reduction mechanism 'shift' from surface based to a solution based mechanism.

For the second (ii), further electrochemical characterisation of stainless steels in the presence of radionuclide surrogates in HNO_3. Further use of techniques such as: Linear Sweep Voltammetry, Electrochemical Impedance Spectroscopy, Quartz Crystal Microgravimetry, X-ray Photoelectron Spectroscopy and *in-situ* spectroscopic techniques, such as Raman Spectroscopy and UV-vis Spectroscopy, will be used to investigate the inhibitive effects of Am and Eu. *In-situ* techniques will be useful for investigation of the formation of inhibitive films on the surface of 316L SS and the presence of these species in solution. Also, further investigation into the apparent corrosive behaviour of Ce in high HNO_3 concentrations on 316L SS.

For the third (iii), electrochemical characterisation of stainless steels used in reprocessing using techniques such as: Linear Sweep Voltammetry, Electrochemical Impedance Spectroscopy, Quartz Crystal Microgravimetry and X-ray Photoelectron Spectroscopy. Rather than using HNO_3 solutions with a single radionuclide surrogate, a solution representative of reprocessing stream liquors should be used to allow for any accumulative effects or other influential behaviour to be taken into account.

Finally, for the fourth (iv), investigation into the effect of temperature on the formation of the passive film in HNO_3 and in the presence of radionuclide surrogates. Work by Armstrong [204] suggests that i_{corr} increases with increasing temperature. This has clear implications for passivation of stainless steel types used in reprocessing. If i_{corr} increases this could lead to a decrease in passivity, followed by corrosion of the steel surface. This could lead to pipe or vessel failure for liquors containing high HNO_3 concentration liquors with a wide range of radionuclide contaminants.

Chapter 7

References

7 REFERENCES

[1] H. Steele, "Chemical Modelling of Steel Surface Contamination," Nexia Solutions, 2006.

[2] F. Rouppert, A. Ivoallan, and C. Argeron, "Reliability and Consistancy of Surface Contamination Measurements," 2002.

[3] C. Boxall, "Application for NDA Doctoral Bursary - Mechanisms of Fixed Contamination of Commonly Engineered Surfaces." 2008.

[4] A. J. Francis, C. J. Dodge, J. B. Gillow, G. P. Halada, and C. R. Clayton, "Mechanisms of Radionuclide-Hyroxycarboxylic Acid Interactions for Decontamination of Metallic Surfaces." pp. 1–21, 2001.

[5] F. Balbaud, G. Sanchez, P. Fauvet, G. Santarini, and G. Picard, "Mechanism of corrosion of AISI 304L stainless steel in the presence of nitric acid condensates," *Corros. Sci.*, vol. 42, no. 10, pp. 1685–1707, 2000.

[6] P. Fauvet, F. Balbaud, R. Robin, Q. T. Tran, A. Mugnier, and D. Espinoux, "Corrosion mechanisms of austenitic stainless steels in nitric media used in reprocessing plants," *J. Nucl. Mater.*, vol. 375, pp. 52–64, 2008.

[7] R. Lange, E. Maisonhaute, R. Robin, and V. Vivier, "On the kinetics of the nitrate reduction in concentrated nitric acid," *Electrochem. commun.*, vol. 29, no. 2, pp. 25–28, Apr. 2013.

[8] G. Carta and R. Pigford, "Absorption of nitric oxide in nitric acid and water," *Ind. Eng. Chem. ...*, vol. 329, no. 6, pp. 329–335, 1983.

[9] WNA, "World Energy Needs and Nuclear Power," *World Nuclear Association*, 2016. [Online]. Available: http://www.world-nuclear.org/information-library/current-and-future-generation/world-energy-needs-and-nuclear-power.aspx. [Accessed: 24-Jan-2016].

[10] WNA, "Nuclear Power in the United Kingdom," *World Nuclear Association*, 2017. [Online]. Available: http://www.world-nuclear.org/info/Country-Profiles/Countries-T-Z/United-Kingdom/. [Accessed: 24-Jan-2017].

[11] D. W. Keogh, "Actinides: Inorganic & Coordination Chemistry," in *Encyclopedia of Inorganic Chemistry*, R. B. King, Ed. Wiley, 2005, pp. 1–31.

[12] J. L. Robertson, "Chapter 9 - Nuclear Fuel Reprocessing," NTEC, 2011.

[13] Sellafield Ltd., "Magnox Reprocessing," 2013. [Online]. Available: http://www.sellafieldsites.com/solution/spent-fuel-management/magnox-reprocessing/. [Accessed: 27-Jun-2013].

[14] WNA, "Processing of Used Nuclear Fuel," *World Nuclear Association*, 2013. [Online]. Available: http://www.world-nuclear.org/info/Nuclear-Fuel-Cycle/Fuel-Recycling/Processing-of-Used-Nuclear-Fuel/#.UdFKRPmkruo. [Accessed: 01-Jul-2013].

[15] Sellafield Ltd., "Thorp Reprocessing," 2013. [Online]. Available: http://www.sellafieldsites.com/solution/spent-fuel-management/thorp-reprocessing/. [Accessed: 27-Jun-2013].

[16] C. H. Castano, "Nuclear Fuel Reprocessing," in *Nuclear Energy Encyclopedia: Science, Technology and Applications*, S. B. Krivit, J. H. Lehr, and T. B. Kingery, Eds. John Wiley & Sons Inc, 2011, pp. 121–126.

[17] IAEA, "Current Trends in Nuclear Fuel for Power Reactors," Vienna, 2007.

[18] C. Burrows, C. Phillips, and A. Milliken, "The Thermal Oxide Reprocessing Plant at Sellafield-Lessons Learned from 10 Years of Hot Operations and their Applicability to the DOE Environment Managment Program," *Waste Manag. Conf.*, pp. 1–17, 2006.

[19] D. M. F. Simpson and J. D. Law, "Nuclear Fuel Reprocessing," Idaho, 2010.

[20] T. Abram, "Nuclear Fuel Cycle Technology," University of Manchester, 2008.

[21] A. D. Wright, "Nitrate Ion Effects on Uranium Chemistry in the Tributylphosphate-Dodecane System," University of Nevada, 2008.

[22] J. D. Seader, E. J. Henley, and D. K. Rope, *Separation Process Principles: Chemical and Biochemical Operations*. John Wiley & Sons, Inc, 2011.

[23] D. D. Sood and S. K. Patil, "Chemistry of nuclear fuel reprocessing: current status," *J. Radioanal. Nucl. Chem.*, vol. 203, no. 2, pp. 547–573, 1996.

[24] J. M. Mckibben, "Chemistry of the PUREX Process," *Radiochim. Acta*, vol. 36, pp. 3–15, 1984.

[25] K. J. Moody, *Nuclear Forensic Analysis*. Taylor & Francis, 2005.

[26] B. D. Craig and D. S. Anderson, *Handbook of Corrosion Data*. USA : ASM International, 1995.

[27] E. Mattsson, *Basic Corrosion Technology for Scientists and Engineers*. London: IOM Communications Ltd, 2001.

[28] EnmaxLtd, "Stainless Steekin the UK Nuclear Fuel Reprocessing Industry," *Stainl. Steels '96*, 1996.

[29] N. Parvathavarthini, U. Kamachi Mudali, L. Nenova, C. Andreev, and B. Raj, "Sensitization and Intergranular Corrosion Behavior of High Nitrogen Type 304LN Stainless Steels for Reprocessing and Waste Management Applications," *Metall. Mater. Trans. A*, vol. 43, no. 6, pp. 2069–2084, Jan. 2012.

[30] L. Carrick, "Fabrication of Pipelines for Nuclear Fuel Reprocessing Plant," in *Welding and fabrication in the nuclear industry. Proceedings of the conference held in London, 3-5 April 1979*, 1979, pp. 263–264.

[31] R. A. Covert and A. H. Tuthill, "Stainless Steels : An Introduction to Their Metallurgy and Corrosion Resistance," *Dairy, Food Environ. Sanit.*, vol. 20, no. 7, pp. 506–517, 2000.

[32] E. A. Avellone, T. Baumeister, and H. Saunders, *Marks Standard Handbook for Mechanical Engineers*, vol. 115, no. 1. 1993.

[33] A. J. Sedricks, *Corrosion of Stainless Steels*. New York: John Wiley & Sons, Inc., 1996.

[34] ChaseAlloys, "Effects of Alloying Elements in Steels," 2013. [Online]. Available: http://www.chasealloys.co.uk/steel/alloying-elements-in-steel/. [Accessed: 20-Jun-2013].

[35] Petersonsteel, "Effects of Alloying Elements in Metal," 2011. [Online]. Available: http://www.petersonsteel.com/wp-content/uploads/2011/03/Elements.pdf. [Accessed: 20-Jun-2013].

[36] H. S. Khatak and B. Raj, *Corrosion of Austenitic Stainless Steel; Mechanism, Mitigation and Monitoring*. Narosa Publishing House, 2002.

[37] M. A. Streicher, "General and Intergranular Corrosion of Austenitic Stainless Steels in Acids," *J. Electrochem. Soc.*, vol. 106, no. 3, pp. 161–180, Mar. 1959.

[38] L. L. Shreir, R. A. Jarman, and G. T. Burstein, *Corrosion Vol. 1: Metal/Environment Reactions*. Oxford: Butterworth-Heineman Ltd., 1994.

[39] L. L. Shreir, R. A. Jarman, and G. T. Burstein, *Corrosion Vol. 2: Corrosion Control*. Oxford: Butterworth-Heineman Ltd., 1994.

[40] R. D. Shaw, "Corrosion Prevention and Control at Sellafield Nuclear Fuel Reprocessing Plant," *Br. Corros. J.*, vol. 25, no. 2, pp. 97–107, 1990.

[41] G. O. H. Whillock, S. E. Worthington, and C. J. Donohoe, "Localized Corrosion of Stainless Steel in a Nuclear Waste Cooling Water System— Part 1: Crevice Corrosion Studies," *Corrosion*, vol. 68, no. 8, pp. 677–687, May 2012.

[42] D. Henderson, "Stainless Steel Fabrication in Nuclear and Other High Intergrity Industries." Sellafield Ltd., 2008.

[43] S. Ningshen, U. Kamachi Mudali, G. Amarendra, and B. Raj, "Corrosion assessment of nitric acid grade austenitic stainless steels," *Corros. Sci.*, vol. 51, no. 2, pp. 322–329, 2009.

[44] J. P. Caire, S. Cullie, F. Dalard, J. M. Fulconis, and H. Delagrange, "AISI 304L stainless steel decontamination by a corrosion process using cerium IV regenerated by ozone; Part I: study of the accelerated corrosion process," *J. Appl. Electrochem.*, vol. 33, pp. 703–708, 2003.

[45] M. Danielson and S. Pitman, "Corrosion Test of 316L and Hastelloy C-22 in simulated Tank Waste Solutions." BNFL,Inc., Washington, 2000.

[46] F. Tehovnik, B. Arzensek, and B. Ark, "Tensile Tests on Stainless Steel in Temperature Range 800 to 1200 o C," *Metalurgija*, vol. 47, no. 2, pp. 75–79, 2008.

[47] G. O. H. Whillock and B. F. Dunnett, "Intergranular corrosion testing of austenitic stainless steels in nitric acid solutions." EUROCORR 2004: long term prediction and modeling of corrosion, 2004.

[48] J. Y. Jeng, B. E. Quayle, P. J. Modern, W. M. Steen, and B. D. Bastow, "Laser surface treatments to improve the intergranular corrosion resistance of 18/13/Nb and 304L in nitric acid," *Corros. Sci.*, vol. 35, no. 5–8, pp. 1289–1296, 1993.

[49] J. Decours, J. C. Decugis, R. Demay, M. Pelras, and G. Turluer, "Austenitic Stainless Steels: Assessment of Progress in Materials Performance for Reprocessing Applications," in *Proceedings of a Technical Committee Meeting on Materials Reliability in the Back End of the Nuclear Fuel Cycle*, 1986, pp. 117–127.

[50] ISO, "Corrosion of metals and alloys - Basic Terms and definitions," *ISO 8044:1999(en)*, 1999. .

[51] P. W. Atkins, *Physical Chemistry*, 5th ed. Oxford: Oxford University Press, 1994.

[52] G. S. Frankel and D. Landolt, "Fundementals of Corrosion," in *Encyclopedia of Electrochemistry - Volume 4: Corrosion and Oxide Films*, A. J. Bard and M. Stratmann, Eds. Wiley-VCH, 2007, pp. 3–8.

[53] D. Landolt, *Corrosion and Surface Chemistry of Metals*. EFPL Press, 2007.

[54] P. R. Roberge, *Corrosion Engineering: Principles and Practice*. USA: McGraw-Hill Companies Inc., 2008.

[55] A. J. Bard and L. R. Faulkner, *Electrochemical Methods: Fundamentals and Applications*. New York: John Wiley & Sons, 2001.

[56] N. D. Greene and A. deS Brasunas, "Corrosion-Related Chemistry and Electrochemistry," St Louis: NACE, 1970, p. 3–1–3.19.

[57] M. Pourbaix, *Atlas of electrochemical equilibria in aqueous solutions*. New York: Pergamon Press, 1966.

[58] J. A. Davis, *Corrosion: Understanding the Basics*. ASM International, 2000.

[59] C. R. Crow, *Principles and Applications of Electrochemistry*, 4th ed. London: Chapman and Hall, 1994.

[60] C. M. A. Brett and A. M. O. Brett, *Electrochemistry: Principles, Methods and Applications*. New York: Oxford University Press Inc., 1993.

[61] D. B. Hibbert, *Introduction to Electrochemistry*. London : The Macmillan Press LTD., 1993.

[62] T. L. S. L. Wijesinghe and D. J. Blackwood, "Characterisation of passive films on 300 series stainless steels," *Appl. Surf. Sci.*, vol. 253, no. 2, pp. 1006–1009, Nov. 2006.

[63] C.-O. A. Olsson and D. Landolt, "Passive films on stainless steels--chemistry, structure and growth," *Electrochim. Acta*, vol. 48, no. 9, pp. 1093–1104, Apr. 2003.

[64] B. Gwinner, M. Auroy, D. Mas, a. Saint-Jevin, and S. Pasquier-Tilliette, "Impact of the use of the ferritic/martensitic ODS steels cladding on the fuel reprocessing PUREX process," *J. Nucl. Mater.*, pp. 1–7, Nov. 2011.

[65] N. Padhy, R. Paul, U. Kamachi Mudali, and B. Raj, "Morphological and compositional analysis of passive film on austenitic stainless steel in nitric acid medium," *Appl. Surf. Sci.*, vol. 257, no. 11, pp. 5088–5097, Mar. 2011.

[66] D. Hamm, C.-O. A. Olsson, and D. Landolt, "Effect of chromium content and sweep rate on passive

film growth on iron-chromium alloys studied by EQCM and XPS," *Corros. Sci.*, vol. 44, no. 5, pp. 1009–1025, May 2002.

[67] C.-O. A. Olsson, D. Hamm, and D. Landolt, "Electrochemical Quartz Crystal Microbalance Studies of the Passive Behavior of Cr in a Sulfuric Acid Solution," *J. Electrochem. Soc.*, vol. 147, no. 7, pp. 2563–2571, Jul. 2000.

[68] C.-O. A. Olsson, D. Hamm, and D. Landolt, "Evaluation of Passive Film Growth Models with the Electrochemical Quartz Crystal Microbalance on PVD Deposited Cr," *J. Electrochem. Soc.*, vol. 147, no. 11, pp. 4093–4102, Nov. 2000.

[69] D. D. Macdonald, "The Point Defect Model for the Passive State," *J. Electrochem. Soc.*, vol. 139, no. 12, pp. 3434–3449, Dec. 1992.

[70] C. Y. Chao, L. F. Lin, and D. D. Macdonald, "A Point Defect Model for Anodic Passive Films I. Film Growth Kinetics," *J. Electrochem. Soc.*, vol. 128, no. 6, pp. 1187–1194, Jun. 1981.

[71] L. F. Lin, C. Y. Chao, and D. D. Macdonald, "A Point Defect Model for Anodic Passive Films II. Chemical Breakdown and Pit Initiation," *J. Electrochem. Soc.*, vol. 128, no. 6, pp. 1194–1198, Jun. 1981.

[72] C. Y. Chao, L. F. Lin, and D. D. Macdonald, "A Point Defect Model for Anodic Passive Films III. Impedance Response," *J. Electrochem. Soc.*, vol. 129, no. 9, pp. 1874–1879, Sep. 1982.

[73] P. Schmutz and D. Landolt, "Electrochemical quartz crystal microbalance study of the transient response of passive Fe---25Cr alloy," *Electrochim. Acta*, vol. 45, no. 6, pp. 899–911, Dec. 1999.

[74] I. Betova, M. Bojinov, T. Laitinen, K. Makela, P. Pohjanne, and T. Saario, "The transpassive dissolution mechanism of highly alloyed stainless steels: I. Experimental results and modelling procedure," *Corros. Sci.*, vol. 44, no. 12, pp. 2675–2697, Dec. 2002.

[75] V. Bague, S. Chachoua, Q. T. Tran, and P. Fauvet, "Determination of the long-term intergranular corrosion rate of stainless steel in concentrated nitric acid," *J. Nucl. Mater.*, vol. 392, no. 3, pp. 396–404, 2009.

[76] A. Fattah-alhosseini, A. Saatchi, M. A. Golozar, and K. Raeissi, "The transpassive dissolution mechanism of 316L stainless steel," *Electrochim. Acta*, vol. 54, no. 13, pp. 3645–3650, May 2009.

[77] R. Svensson and E. Ljungström, "A kinetic study of the decomposition of HNO3 and its reaction with NO," *Int. J. Chem. Kinet.*, vol. 20, no. 11, pp. 857–866, 1988.

[78] Y. Kameoka and R. L. Pigford, "Absorption of Nitrogen Dioxide into Water, Sulfuric Acid, Sodium Hydroxide, and Alkaline Sodium Sulfite Aqueous Solutions," *Ind. Eng. Chem. Fundam.*, vol. 16, no. 1, pp. 163–169, Feb. 1977.

[79] N. Padhy, S. Ningshen, U. Kamachi Mudali, and B. Raj, "In situ surface investigation of austenitic stainless steel in nitric acid medium using electrochemical atomic force microscopy," *Scr. Mater.*, vol. 62, no. 1, pp. 45–48, Jan. 2010.

[80] F. Balbaud, G. Sanchez, G. Santarini, and G. Picard, "Cathodic Reactions Involved in Corrosion Processes Occurring in Concentrated Nitric Acid at 100 øC," *Eur. J. Inorg. Chem.*, vol. 2000, no. 4, pp. 665–674, 2000.

[81] K. Vetter, "No Title," *Z. Phys. Chem*, vol. 194, pp. 199–206, 1950.

[82] K. Vetter, "No Title," *Z. Phys. Chem*, vol. 194, pp. 284–296, 1950.

[83] K. Vetter, "No Title," *Z. Elektrochem., Ber. Bunsenges. Phys. Chem*, vol. 63, pp. 1189–1191, 1959.

[84] G. Schmid, "No Title," *Z. Elektrochem., Ber. Bunsenges. Phys. Chem*, vol. 63, pp. 1192–1188, 1959.

[85] G. Schmid, "No Title," *Z. Elektrochem., Ber. Bunsenges. Phys. Chem*, vol. 63, pp. 1192–1197, 1959.

[86] G. Schmid and G. Krichel, "No Title," *Z. Elektrochem., Ber. Bunsenges. Phys. Chem*, vol. 68, pp. 677–688, 1964.

[87] G. Schmid and M. A. Lobeck, "No Title," *Z. Elektrochem., Ber. Bunsenges. Phys. Chem*, vol. 73, pp. 89–199, 1969.

[88] D. Sicsic, F. Balbaud-Célérier, and B. Tribollet, "Mechanism of Nitric Acid Reduction and Kinetic Modelling," *Eur. J. Inorg. Chem.*, vol. 2014, no. 36, pp. 6174–6184, 2014.

[89] E. Abel and H. Schmid, "No Title," *Z. Phys. Chem*, vol. 132, no. 56, p. 64.

[90] E. Abel and H. Schmid, "No Title," *Z. Phys. Chem1*, vol. 734, p. 279.

[91] E. Abel and H. Schmid, "No Title," *Z. Phys. Chem*, vol. 136, no. 153, p. 419.

[92] G. Gottstein and L. S. Shvindlerman, *Grain Boundary Migration in Metals: Thermodynamics, Kinetics, Applications*. CRC Press, 1999.

[93] R. W. Revie, *Uhlig's Corrosion Handbook*, 2nd ed. Wiley Interscience, 2000.

[94] R. P. V. Cruz, A. Nishikata, and T. Tsuru, "AC impedance monitoring of pitting corrosion of stainless steel under a wet-dry cyclic condition in chloride-containing environment," *Corros. Sci.*, vol. 38, no. 8, pp. 1397–1406, Aug. 1996.

[95] G. O. H. Whillock, T. J. Binks, and C. J. Donohoe, "Localized Corrosion of Stainless Steel in a Nuclear Waste Cooling Water System—Part 3: Development of a Large Artificial Pit," *Corrosion*, vol. 68, no. 10, pp. 859–871, Jun. 2012.

[96] D. D. Macdonald, "Passivity - the key to our metals-based cilvilization," *Pure Appl. Chem.*, vol. 71, no. 6, pp. 951–978, 1999.

[97] P. Marcus, V. Maurice, and H. H. Strehblow, "Localized corrosion (pitting): A model of passivity breakdown including the role of the oxide layer nanostructure," *Corros. Sci.*, vol. 50, no. 9, pp. 2698–2704, 2008.

[98] E. McCafferty, *Introduction to Corrosion Science*. Springer, 2010.

[99] NACE, "Crevice Corrosion," *NACE*, 2014. [Online]. Available: http://www.nace.org/Corrosion-Central/Corrosion-101/Crevice-Corrosion/. [Accessed: 14-Oct-2014].

[100] A. Aruntunow and K. Darowicki, "DEIS assessment of AISI 304 stainless steel dissolution process in conditions of intergranular corrosion," *Electrochim. Acta*, vol. 53, pp. 4387–4395, 2008.

[101] D. Lopez, N. A. Falleiros, and A. P. Tschiptschin, "Corrosion-erosion behaviour of austenitic and martensitic high nitrogen stainless steels," *Wear*, vol. 263, pp. 347–354, 2007.

[102] L. N. Moyes *et al.*, "Uranium Uptake from Aqueous Solution by Interaction with Goethite, Lepidocrocite, Muscovite, and Mackinawite: An X-ray Absorption Spectroscopy Study," *Environ. Sci. Technol.*, vol. 34, no. 6, pp. 1062–1068, 2000.

[103] G. Hirschberg *et al.*, "Accumulation of radioactive corrosion products on steel surfaces of VVER type nuclear reactors . I . 110m Ag," *J. Nucl. Mater.*, vol. 265, pp. 273–284, 1999.

[104] C. J. Dodge, A. J. Francis, J. B. Gillow, G. P. Halada, C. Eng, and C. R. Clayton, "Association of Uranium with Iron Oxides Typically Formed on Corroding Steel Surfaces," *Environ. Sci. Technol.*, vol. 36, no. 16, pp. 3504–3511, 2002.

[105] C. Eng, G. P. Halada, A. J. Francis, C. J. Dodge, and J. B. Gillow, "Uranium association with corroding carbon steel surfaces," *Surf. Interface Anal.*, vol. 35, pp. 525–535, 2003.

[106] P. Dombovari *et al.*, "Accumulation of uranium on austenitic stainless steel surfaces," *Electrochim. Acta*, vol. 52, pp. 2542–2551, 2006.

[107] P. Kádár, K. Varga, Z. N,meth, N. Vajda, T. Pint,r, and J. Schunk, "Accumulation of uranium, transuranium and fission products on stainless steel surfaces. I. A comprehensive view of the experimental parameters influencing the extent and character of the contamination," *J. Radioanal. Nucl. Chem.*, vol. 284, no. 2, pp. 303–308, 2010.

[108] L. Morss and L. B. Asprey, "Actinoid element," *Britannica*, 2018. [Online]. Available: https://www.britannica.com/science/actinoid-element. [Accessed: 23-Jul-2018].

[109] J. J. Katz, L. R. Morss, N. M. Edelstein, and J. Fuger, "Introduction," in *The Chemistry of the Actinide and Transactinide Elements*, 4th ed., vol. 3rd, Dordrecht: Springer, 2010, pp. 1–17.

[110] F. A. Cotton, G. Wilkinson, and P. L. Gaus, *Basic Inorganic Chemistry*. New York: John Wiley &

Sons, Inc.0, 1995.

[111] A. J. Bard, R. Parsons, and J. Jordan, *Standard Potentials in Aqueous Solution*. New York: Marcel Dekker, Inc., 1985.

[112] H. Vandenhove, C. Hurtgen, and T. E. Payne, "Uranium: Radionuclides," in *Encyclopedia of Inorganic and Bioinorganic Chemistry*, John Wiley & Sons, Ltd, 2011.

[113] R. J. M. Konings, L. R. Morss, and J. Fuger, "Thermodynamic Properties of Actinides and Actinide Compounds," in *The Chemistry of the Actinide and Transactinide Elements*, 4th ed., L. R. Morss, N. M. Edelstein, and J. Fuger, Eds. Springer, 2011, pp. 2113–2224.

[114] D. L. Clark, S. S. Hecker, G. D. Jarvinen, and M. P. Neu, "Plutonium," in *The Chemistry of the Actinide and Transactinide Elements*, 4th ed., L. R. Morss, N. M. Morss Edelstein, and L. R. Fuger, J., Eds. Springer, 2011, pp. 813–1264.

[115] G. Le Guran, "The application of colloidal photocatalysis in actinide photoredox chemistry," University of Central Lancashire, 2003.

[116] Z. Yoshida, S. G. Johnson, T. Kimura, and J. R. Krsul, "Neptunium," in *The Chemistry of the Actinide and Transactinide Elements*, 4th ed., L. R. Morss, N. M. Edelstein, and J. Fuger, Eds. 2011, pp. 699–812.

[117] Harvard Environmental Health and Safety, "Radiation Survey Information," *http://www.ehs.harvard.edu/sites/ehs.harvard.edu/files/radiation_survey_information.pdf*, 2012. .

[118] P. Kádár *et al.*, "Accumulation of uranium, transuranium and fission products on stainless steel surfaces II. Sorption studies in a laboratory model system," *J. Radioanal. Nucl. Chem.*, vol. 288, no. 3, pp. 943–954, Mar. 2011.

[119] R. Répánszki, Z. Kerner, and G. Nagy, "Adsorption of fission products on stainless steel and zirconium," *Adsorption*, vol. 13, no. 3–4, pp. 201–207, Oct. 2007.

[120] R. Répánszki and Z. Kerner, "Kinetics of fission products accumulation on structural materials," *J. Radioanal. Nucl. Chem.*, vol. 288, no. 3, pp. 729–733, Feb. 2011.

[121] C. W. Eng, G. P. Halada, A. J. Francis, and C. J. Dodge, "Spectroscopic study of decontaminated corroded carbon steel surfaces," *Surf. Interface Anal.*, vol. 36, pp. 1516–1522, 2004.

[122] Nuclear Energy Agency Organisation for the Economic Co-operation and Development Co-operative Programme for Exchange of Scientific and Technical Information Concerning Nuclear Installations Decommissioning Projects, "Decontamination Techniques Used in Decommissioning Activites," Paris, 1999.

[123] L. E. Boing, "Decontamination of Nuclear Facilities: Decontamination Technologies." IAEA, Manila, Phillipines, 2006.

[124] Co-ordination Network on Decommissioning, "Dismantling Techniques, Decontamination Techniques, Dissemination of Best Practise, Experience and Know-how," 2009.

[125] M. Ponnet, "Metal Decontamination Techniques used in Decommissioning Activities," in *Conference Proceedings for EUNDETRAF Session 9 - Thursday 21 November 2002*, 2002.

[126] C. R. Bayliss and K. F. Langley, "Decontamination Techniques," in *Nuclear Decommissioning, Waste Management and Environmental Site Remediation*, Burlington: Elsevier, 2003, pp. 89–97.

[127] B. Speiser, "Liner Sweep and Cyclic Voltammetry," in *Encyclopedia of Electrochemistry - Volume 3: Instrumentation and Electroanalytical Chemistry*, A. J. Bard and M. Stratmann, Eds. Wiley-VCH, 2007, pp. 81–104.

[128] I. Gamry, "Review on the Electrochemical Basis of Corrosion." 2010.

[129] I. Gamry, "Basics of Electrochemical Impedance Spectroscopy," 2010. [Online]. Available: https://www.gamry.com/application-notes/EIS/basics-of-electrochemical-impedance-spectroscopy/. [Accessed: 05-Mar-2017].

[130] R. W. Revie and H. H. Uhlig, *Corrosion and Corrosion Control; An Introduction to Corrosion Science and Engineering*. Hoboken New Jersey: John Wiley & Sons Inc, 2008.

[131] J. R. Macdonald, “Fundementals of Impedance Spectroscopy,” in *Impedance Spectroscopy; Theory, Experiment and Applications*, 2nd ed., E. Barsoukov and J. R. Macdonald, Eds. Hoboken: John Wiley & Sons Inc, 2005, pp. 1–26.

[132] S. Krause, “Impedance Methods,” in *Encyclopedia of Electrochemistry - Volume 3: Instrumentation and Electroanalytical Chemistry*, vol. 3, A. J. Bard Stratmann, M., Unwin, P.R., Ed. Wiley-Vch Verlag Gmbh, 2003, pp. 196–229.

[133] H. Cesiulis, N. Tsyntsaru, A. Ramanavicius, and G. Ragolsha, “The Study of Thin Films by Electrochemical Impedance Spectroscopy,” in *Nanostructures and Thin Films for Multifunctional Applications: Technology, Properties and Devices*, I. Tiginyanu, P. Topala, and V. Ursaki, Eds. Springer Internation Publishing, 2016, pp. 3–42.

[134] R. Greef and C. Department of, “A. C. Techniques,” Southampton: Southampton University, 1982, pp. 232–261.

[135] E. Katz and I. Willner, “Probing Biomolecular Interactions at Conductive and Semiconductive Surfaces by Impedance Spectroscopy: Routes to Impedimetric Immunosensors, DNA-Sensors, and Enzyme Biosensors,” *Electroanalysis*, vol. 15, no. 11, pp. 913–947, Jul. 2003.

[136] J. R. Scully, D. C. Silverman, and M. W. Kendig, *Electrichemical Impedance: Analysis and Interpretation*. ASTM, 1993.

[137] A. W. Bott, “Characterization of Films Immobilized on an Electrode Surface Using the Electrochemical Quartz Crystal Microbalance,” *Curr. Sep.*, vol. 18, no. 3, pp. 79–83, 1999.

[138] P. Schmutz and D. Landolt, “In-situ microgravimetric studies of passive alloys: potential sweep and potential step experiments with Fe-25Cr and Fe-17Cr-33Mo in acid and alkaline solution,” *Corros. Sci.*, vol. 41, no. 11, pp. 2143–2163, Nov. 1999.

[139] M. Itagaki, H. Nakazawa, K. Watanabe, and K. Noda, “Study of dissolution mechanisms of nickel in sulfuric acid solution by electrochemical quartz crystal microbalance,” *Corros. Sci.*, vol. 39, no. 5, pp. 901–911, May 1997.

[140] C.-O. A. Olsson and D. Landolt, “Film Growth during Anodic Polarization in the Passive Region on 304 Stainless Steels with Cr, Mo, or W Additions Studied with EQCM and XPS,” *J. Electrochem. Soc.*, vol. 148, no. 11, pp. B438–B449, Nov. 2001.

[141] D. A. Buttry, “Applications of the Quartz Crystal Microbalance to Electrochemistry,” *Electroanal. Chem.*, pp. 1–85, 1991.

[142] D. A. Buttry, “The Quartz Crystal Microbalance as an In-Situ Tool in Electrochemistry,” in *Electrochemical Interfaces: Modern Techniques for In-Situ Interface Characterisation*, H. D. Abruna, Ed. VHC Publishers Inc., 1991, pp. 529–566.

[143] M. R. Deakin and D. A. Buttry, “Electrochemical applications of the quartz crystal microbalance,” *Anal. Chem.*, vol. 61, no. 20, p. 1147A–1154A, 2008.

[144] Testbourne, “Quatrz Sensor Crystals,” 2013. [Online]. Available: http://www.testbourne.com/instruments/quartz-sensor-crystals/. [Accessed: 05-Sep-2013].

[145] D. A. Buttry and M. A. Ward, “Measurement of Interfacial Processes at Electrode Surfaces with the Electrochemical Quartz Crystal Microbalance,” *Chem. Rev.*, vol. 92, pp. 1355–1379, 1992.

[146] C. Gabrielli, M. Keddam, and R. Torresi, “Calibration of the Electrochemical Quartz Crystal Microbalance,” *J. Electrochem. Soc.*, vol. 138, no. 9, pp. 2657–2660, Sep. 1991.

[147] G. L. Borges, K. K. Kanazawa, J. G. Gordon II, K. Ashley, and J. Richer, “An in-situ electrochemical quartz crystal microbalance study of the underpotential deposition of copper on Au(111) electrodes,” *J. Electroanal. Chem.*, vol. 364, no. 1–2, pp. 281–284, Jan. 1994.

[148] F. P. L. Andrieux, “The micro-optical ring elextrode: development of a novel thin ring based device for spectrophotoelectrocheimstry and its application to the study of rose bengal,” University of Central Lancashire, 2004.

[149] C. Donik, I. Paulin, and M. Jenko, “Influence of MnS inclusions on the corrosion of austenitic stainless steels,” *Mater. Technol.*, vol. 44, no. 2, pp. 67–72, 2010.

[150] C. G. Zoski, *Handbook of Electrochemistry*. Amsterdam: Elsevier, 2007.

[151] J. Luo, W. Olthuis, B. H. Van Der Schoot, P. Bergveld, M. Bos, and W. E. Van Der Linden, "Modelling of the migration effect occurring at an ISFET-based coulometric sensor-actuator system," *Anal. Chim. Acta*, vol. 237, pp. 72–81, 1990.

[152] N. P. C. Stevens and A. M. Bond, "The influence of migration on cyclic and rotating disk voltammograms," *J. Electroanal. Chem.*, vol. 538–539, pp. 25–33, 2002.

[153] A. R. Mount, "Hydrodynamic Electrodes," in *Encyclopedia of Electrochemistry - Volume 3: Instrumentation and Electroanalytical Chemistry*, no. 3, A. J. Bard Stratmann, M., Unwin, P.R., Ed. Wiley, 2007, pp. 134–159.

[154] J. M. Hollas, *Modern Spectroscopy*, 4th ed. Wiley, 2004.

[155] R. S. Nicholson, "Theory and Application of Cyclic Voltammetry for Measurement of Electrode Reaction Kinetics," *Anal. Chem.*, vol. 37, no. 11, pp. 1351–1355, 1965.

[156] T. Scientific, "What is X-Ray Photoelectron Spectroscopy?," 2016. [Online]. Available: http://xpssimplified.com/whatisxps.php. [Accessed: 10-Apr-2017].

[157] N. Padhy, "Role of Passivity and Surface Modification on the Corrosion Behaviour of AISI 304L Stainless Steel in Nitric Acid Medium," Homi Bhabha National Institute, University of Mumbai, 2010.

[158] T. L. Barr, *Modern ESCA: The Principles and Practise of X-Ray Photoelectron Spectroscopy*. CRC Press, Inc., 1994.

[159] P. E. J. Flewitt and R. K. Wild, *Physical methods for materials characterisation*, 2nd ed. Bristol: Institute of Physics, 2003.

[160] J. Watts, J. Wolstenholme, and J. Wiley, *An introduction to surface analysis by XPS and AES*. 2003.

[161] J. Chastain, *Handbook of X-ray photoelectron spectroscopy*. Minnesota: Perkin-Elmer Corporation, 1992.

[162] R. A. D'Sa, J. Raj, M. A. S. McMahon, D. A. McDowell, G. A. Burke, and B. J. Meenan, "Atmospheric pressure plasma induced grafting of poly(ethylene glycol) onto silicone elastomers for controlling biological response," *J. Colloid Interface Sci.*, vol. 375, no. 1, pp. 193–202, Jun. 2012.

[163] A. Herrera-Gomez, "The Peak-Shirley Background," *Intern. Rep. Last Updat.*, no. 2, 2012.

[164] M. Aronniemi, J. Lahtinen, and P. Hautojärvi, "Characterization of iron oxide thin films," *Surf. Interface Anal.*, vol. 36, no. 8, pp. 1004–1006, Aug. 2004.

[165] W. Fredriksson, "Depth Profiling of the Passive Layer on Stainless Steel using Photoelectron Spectroscopy," Uppsla University, 2012.

[166] K. Janssens, "Chapter 2. X-Ray Photoelectron and Auger Electron Spectroscopy." Micro Trace Analysis Centre (MiTAC), University of Antwerp, Antwerp, Belgium, 2012.

[167] A. G. Shard, "Detection limits in XPS for more than 6000 binary systems using Al and Mg Kα X-rays," *Surf. Interface Anal.*, vol. 46, no. 3, pp. 175–185, Mar. 2014.

[168] X. International, "X-ray Photoelectron Spectroscopy," 2007. [Online]. Available: http://www.xpsdata.com/Technique_limits_p1.pdf. [Accessed: 09-Aug-2018].

[169] M. Bojinov, I. Betova, and R. Raicheff, "Influence of molybdenum on the transpassivity of a Fe + 12%Cr alloy in H2SO4 solutions," *J. Electroanal. Chem.*, vol. 430, no. 1–2, pp. 169–178, Jun. 1997.

[170] A. Fattah-alhosseini, S. Taheri Shoja, B. Heydari Zebardast, and P. Mohamadian Samim, "An Electrochemical Impedance Spectroscopic Study of the Passive State on AISI 304 Stainless Steel," *Int. J. Electrochem. Sci.*, vol. 152143, 2011.

[171] S. Sangwine, *Electronic Components and Technology*, 3rd ed. CRC Press, 2007.

[172] A. Fattah-Alhosseini, M. Mosavi, and A. Allahdadi, "An Electrochemical Impedance Study of AISI 321 Stainless Steel in 0.5 M H_2SO_4," *Int. J. Electrochem.*, vol. 2011, pp. 1–10, 2011.

[173] M. Drogowska, H. Menard, A. Lasia, and L. Brossard, “Impedance study of the passive film on stainless steel 304 in pH 8 carbonate solution,” *J. Appl. Electrochem.*, vol. 26, no. 11, pp. 1169–1177, 1996.

[174] *RQCM: Research Quartz Crystal Microbalance; operation and service manual*, Maxtek Inc. 2002.

[175] D. Briggs and M. P. Seah, *Practical Surface Analysis: by auger and x-ray photoelectron spectroscopy*. John Wiley & Sons Ltd., 1983.

[176] K. Varga, G. Hirschberg, Z. Nemeth, G. Myburg, J. Schunk, and P. Tilky, “Accumulation of radioactive corrosion products on steel surfaces of VVER type nuclear reactors. II. 60 Co,” *J. Nucl. Mater.*, vol. 298, pp. 231–238, 2001.

[177] R. Benoit, “XPS: Element or Energy,” *ThermoFisher Scientific*, 2012. [Online]. Available: http://www.lasurface.com/database/elementxps.php. [Accessed: 10-Sep-2012].

[178] R. M. Cornell and U. Schwertmann, *The Iron Oxides: Structure, Properties, Reaction Occurance and Uses*, 2nd ed. Wiley VHC GmbH & Co., 2003.

[179] B. Beverskog and I. Puigdomenech, “Revised pourbaix diagrams for iron at 25-300 ÝC,” *Corros. Sci.*, vol. 38, no. 12, pp. 2121–2135, 1996.

[180] I. Betova, M. Bojinov, T. Laitinen, K. Makela, P. Pohjanne, and T. Saario, “The transpassive dissolution mechanism of highly alloyed stainless steels: II. Effect of pH and solution anion on the kinetics,” *Corros. Sci.*, vol. 44, no. 12, pp. 2699–2723, Dec. 2002.

[181] E. Otero, A. Pardo, E. Sáenz, M. V Utrilla, and P. Hierro, “A study of the influence of nitric acid concentration on the corrosion resistance of sintered austenitic stainless steel,” *Corros. Sci.*, vol. 38, no. 9, pp. 1485–1493, 1996.

[182] G. O. H. Whillock, T. J. Binks, and C. J. Donohoe, “Localized Corrosion of Stainless Steel in a Nuclear Waste Cooling Water System—Part 4: Artificial Pit Investigation of Nitrate Inhibition,” *Corrosion*, vol. 68, no. 11, pp. 967–981, Jul. 2012.

[183] R. C. Woodhouse, C. Boxall, and R. J. Wilbraham, “Nitric Acid Reduction on 316L Stainless Steel Under Conditions Representative of Reprocessing,” *ECS Trans*, vol. 53, no. 21, pp. 25–32, 2013.

[184] V. Maurice, “X-Ray Photoelectron Spectroscopy and Scanning Tunneling Microscopy Study of Passive Films Formed on (100) Fe-18Cr-13Ni Single-Crystal Surfaces,” *J. Electrochem. Soc.*, vol. 145, no. 3, p. 909, 1998.

[185] A. Machet *et al.*, “XPS and STM study of the growth and structure of passive films in high temperature water on a nickel-base alloy,” *Electrochim. Acta*, vol. 49, no. 22–23, pp. 3957–3964, Sep. 2004.

[186] A. D. Apte, V. Tare, and P. Bose, “Extent of oxidation of Cr(III) to Cr(VI) under various conditions pertaining to natural environment,” *J. Hazard. Mater.*, vol. 128, no. 2–3, pp. 164–174, 2006.

[187] M. V Zamoryanskaya and B. E. Burakov, “Feasibility Limits in Using Cerium as a Surrogate for Plutonium Incorporation in Zircon, Zirconia and Pyrochlore,” *MRS Online Proc. Libr.*, vol. 663, 2000.

[188] R. S. Herbst *et al.*, “Integrated AMP-PAN, TRUEX, and SREX Flowsheet Test to Remove Cesium, Surrogate Actinide Elements, and Strontium from INEEL Tank Waste Using Sorbent Columns and Centrifugal Contactors,” 2000.

[189] D. N. Singh, *Basic Concepts of Inorganic Chemistry*. Delhi: Pearson, 2011.

[190] I. D. Nickson, C. Boxall, a Jackson, and G. O. H. Whillock, “A spectrophotometric study of cerium IV and chromium VI species in nuclear fuel reprocessing process streams,” *IOP Conf. Ser. Mater. Sci. Eng.*, vol. 9, p. 012011, Mar. 2010.

[191] R. W. Johnson and D. S. Jr. Martin, *Kinetics of the oxidation of cerium(III) by concentrated nitric acid*, vol. 10. 1959.

[192] M. Chimes, C. Boxall, S. Edwards, M. Sarsfield, R. J. Taylor, and D. Woodhead, “Reduction Reactions of Neptunium & Neptunium Analogues with Nitrogen Oxide Species,” *Prog. Nucl. Sci. Technol.*, 2017.

[193] T. S. Rudisill, "Pretreatment of Americium/Curium Solutions for Vitrification (U)," WSRC-TR-96-0074, 1996.

[194] M. Bethencourt, F. J. Botana, J. J. Calvino, M. Marcos, and M. a. Rodríguez-Chacón, "Lanthanide compounds as environmentally-friendly corrosion inhibitors of aluminium alloys: A review," *Corros. Sci.*, vol. 40, no. 11, pp. 1803–1819, 1998.

[195] B. Hinton and M. Forsyth, *Rare Earth-Based Corrosion Inhibitors*. Suffolk, UK: Woodhead Publishing, 2014.

[196] M. Van Soestbergen, S. J. F. Erich, H. P. Huinink, and O. C. G. Adan, "Inhibition of pH fronts in corrosion cells due to the formation of cerium hydroxide," *Electrochim. Acta*, vol. 110, pp. 491–500, 2013.

[197] C. Jeyaprabha, S. Sathiyanarayanan, and G. Venkatachari, "Effect of cerium ions on corrosion inhibition of PANI for iron in 0.5 M H2SO4," *Appl. Surf. Sci.*, vol. 253, no. 2, pp. 432–438, 2006.

[198] A. S. Fouda, H. Megahed, and D. M. Ead, "Lanthanides as environmentally friendly corrosion inhibitors of iron in 3.5% NaCl solution," *Desalin. Water Treat.*, vol. 51, no. 16–18, pp. 3164–3178, 2013.

[199] C. Boxall and M. Chimes, "HNO2 experiments in uranyl solution." Personal Communication, 2017.

[200] K. S. Kumar, "Evaluation of consequence due to higher hydrazine content in partitioning stream of PUREX process," *Radiochimica Acta*, vol. 104. p. 701, 2016.

[201] H.-H. Huang, "The Eh-pH Diagram and Its Advances," *Metals (Basel).*, vol. 6, no. 3, p. 23, 2016.

[202] T. Waechtler *et al.*, "Copper Oxide Films Grown by Atomic Layer Deposition from Bis(tri-n-butylphosphane)copper(I)acetylacetonate on Ta, TaN, Ru, and SiO[sub 2]," *J. Electrochem. Soc.*, vol. 156, no. 6, p. H453, 2009.

[203] S. Hüfner, G. K. Wertheim, and J. H. Wernick, "XPS core line asymmetries in metals," *Solid State Commun.*, vol. 17, no. 4, pp. 417–422, Aug. 1975.

[204] R. D. Armstrong, G. E. Cleland, and G. O. H. Whillock, "Effect of dissolved chromium species on the corrosion of stainless steel in nitric acid," *J. Appl. Electrochem.*, vol. 28, no. 11, pp. 1205–1211, 1998.

[205] R. C. Woodhouse, R. J. Wilbraham, and C. Boxall, "Fixed Contamination on Steel Sturfaces - First Use of QCM to Measure Oxide Growth on Process Steels Under Conditions Typical of Nuclear Reprocessing," *Mater. Res. Soc. Symp. Proc.*, vol. 1383, 2012.

Chapter 8

Appendices

Appendix 1

Electrochemical Impedance Spectroscopy (EIS) Zview Data

Table 8-1 – Best fit parameters of 316L SS surface at various potentials in 5% HNO_3 solution.

mV	Rs (ohm)	Rp (ohm)	CPE-T	CPE-P
-500	1.439	2.649	6.02E-05	0.8057
-400	2.8	3.658	6.77E-05	0.7348
-300	2.5	11060	2.97E-05	0.85098
-200	2.612	18948	1.76E-05	0.9243
-100	2.907	48186	1.21E-05	0.98496
0	2.578	70011	1.59E-05	0.93879
100	2.5	78000	1.75E-05	0.90961
200	2.7	65000	1.31E-05	0.925
300	2.8	102490	1.09E-05	0.95
400	2.644	135720	1.06E-05	0.9312
500	2.644	139720	8.66E-06	0.97769
600	2.644	130600	9.05E-06	0.97115
700	2.5	115000	7.42E-09	0.95
800	2.6	55013	7.14E-07	0.95
900	2.5	21583	1.53E-05	0.92045
1000	2.3	3497	2.84E-05	0.89626
1100	2.335	505.1	3.85E-05	0.88345
1200	2.321	224.5	3.28E-05	0.89179
1300	2.241	166.6	2.55E-05	0.89486
1400	2.211	139.4	2.58E-05	0.88249
1500	2.304	112.4	4.76E-06	0.83783

Table 8-2 – Best fit parameters of 316L SS surface at various potentials in 10% HNO_3 solution.

mV	Rs (ohm)	Rp (ohm)	CPE-T	CPE-P
-500	1.278	1.317	0.00010286	0.8347
-400	1.332	2.694	0.0001037	0.84628
-300	1.503	9.798	0.00010061	0.8461
-200	1.802	244.4	0.00010057	0.82
-100	1.619	6544	1.63E-04	0.70696
0	1.5	2253	7.12E-05	0.80509
100	2.796	1606	7.28E-05	0.89997
200	1.393	7311	2.65E-05	0.89956
300	1.654	47622	1.35E-05	0.96253
400	1.66	67056	1.12E-05	0.96832
500	1.643	67184	8.07E-06	0.99588
600	1.63	69269	6.81E-06	1.001
700	1.6	57409	6.82E-06	0.99601
800	1.601	45033	9.68E-06	0.96115
900	1.644	23859	1.37E-05	0.94143
1000	1.628	4097	2.83E-05	0.89124
1100	1.5	3850	1.19E-05	1.014
1200	1.457	231	5.15E-05	0.87384
1300	1.477	81.9	4.28E-05	0.89071
1400	1.461	42.14	3.19E-05	0.89907
1500	1.423	33.54	4.81E-05	0.83335

Table 8-3 – Best fit parameters of 316L SS surface at various potentials in 15% HNO_3 solution.

.

mV	Rs (ohm)	Rp (ohm)	CPE-T	CPE-P
-500	1.156	1.163	0.00011712	0.80622
-400	1.283	2.268	9.09E-05	0.85489
-300	1.487	7.456	8.56E-05	0.86089
-200	1.719	72.08	0.00010007	0.81989
-100	1.049	59.45	5.90E-05	0.81297
0	1.288	295.6	2.84E-05	0.89097
100	1.459	2570	2.47E-05	0.91055
200	1.72	10775	1.55E-05	0.96197
300	1.536	39431	1.58E-05	0.94554
400	1.639	55694	1.20E-05	0.96935
500	1.49	70793	1.19E-05	0.95411
600	1.888	75974	9.69E-06	0.95
700	1.864	55078	7.00E-05	1.002
800	1.841	46514	8.51E-06	0.98541
900	1.869	25758	2.08E-05	0.97869
1000	1.433	5310	2.46E-05	0.91002
1100	1.448	250.6	6.63E-05	0.86738
1200	1.463	48.59	5.53E-06	0.88567
1300	1.406	19.11	4.21E-05	0.89492
1400	1.508	9.501	2.81E-05	0.91267
1500	1.464	10.3	3.72E-05	0.86996

Table 8-4 – Best fit parameters of 316L SS surface at various potentials in 20% HNO_3 solution/

mV	Rs (ohm)	Rp (ohm)	CPE-T	CPE-P
-500	1.158	0.86608	9.66E-05	0.83752
-400	1.237	1.693	8.67E-05	0.86292
-300	1.406	5.121	0.00011931	0.82138
-200	1.192	39.43	0.00017178	0.74621
-100	0.98948	25.28	0.00010306	0.75278
0	1.119	21.33	2.70E-05	0.89002
100	1.253	444.9	2.39E-05	0.90871
200	1.319	4663	2.02E-05	0.9263
300				
400	1.451	56615	1.30E-05	0.96067
500	1.61	50898	8.42E-06	1.002
600	1.502	95921	9.21E-06	0.97543
700	1.507	70899	1.41E-05	1
800	1.419	55718	1.53E-05	0.99261
900	1.5	27153	1.28E-05	0.95946
1000	1.279	6553	2.32E-05	0.90861
1100	1.329	267.1	8.24E-05	0.85905
1200	1.335	32.83	6.51E-05	0.88143
1300	1.349	10.85	4.66E-05	0.91027
1400	1.434	3.989	2.85E-05	0.94745
1500	1.488	2.596	2.20E-05	0.95967

Table 8-5 – Best fit parameters of 316L SS surface at various potentials in 25% HNO_3 solution.

mV	Rs (ohm)	Rp (ohm)	CPE-T	CPE-P
-500	1.23	0.72492	8.14E-05	0.8619
-400	1.375	0.86195	9.34E-05	0.86195
-300	1.246	4.444	0.00016924	0.75981
-200	0.6859	22.15	0.00023458	0.69438
-100	1.026	5.358	3.70E-05	0.85143
0	1.136	6.731	2.66E-05	0.88707
100	1.203	17.96	1.94E-05	0.92361
200	1.263	283.5	1.87E-05	0.93169
300	1.379	3318	1.45E-05	0.95446
400	1.578	14290	1.01E-05	0.98759
500	1.36	39000	7.36E-06	0.96
600	1.492	47536	8.58E-06	0.98186
700	1.437	49781	8.60E-06	0.97315
800	1.568	48539	8.04E-06	0.98168
900	1.456	34008	1.07E-05	0.95
1000	1.367	7614	2.15E-05	0.90518
1100	1.334	218.9	8.65E-05	0.86267
1200	1.342	23.79	6.71E-05	0.88791
1300	1.378	6.909	5.25E-05	0.92225
1400	1.408	2.376	3.56E-05	0.95849
1500	1.494	1.215	1.99E-05	1.017

Table 8-6 – Best fit parameters of 316L SS surface at various potentials in 30% HNO_3 solution.

mV	Rs (ohm)	Rp (ohm)	CPE-T	CPE-P
-500	1.341	0.85483	4.68E-05	0.95576
-400	1.488	1.31	9.75E-05	0.85492
-300	1.347	4.997	0.0001637	0.76522
-200				
-100				
0				
100	1.138	6.147	2.26E-05	0.90314
200	1.212	30.04	1.75E-05	0.93433
300	1.243	487.8	1.71E-05	0.93519
400	1.268	3154	1.50E-05	0.94196
500	1.511	9811	1.04E-05	0.97885
600	1.315	22003	1.09E-05	0.95
700	1.304	34455	8.28E-06	0.98642
800	1.35	37699	7.49E-06	0.99569
900	1.311	26759	1.23E-05	0.94701
1000	1.35	8036	1.93E-05	0.92668
1100	1.331	241.4	9.67E-05	0.86063
1200	1.348	22.36	8.10E-05	0.88112
1300	1.378	6.066	6.47E-05	0.92039
1400	1.458	1.896	3.03E-05	1
1500	1.565	0.87766	1.23E-05	1.098

Table 8-7 – Best fit parameters of 316L SS surface at various potentials in 35% HNO_3 solution.

mV	Rs (ohm)	Rp (ohm)	CPE-T	CPE-P
-500	1.349	0.94102	4.69E-05	0.94102
-400	1.457	1.358	0.00011168	0.82547
-300	0.98659	5.106	0.00027304	0.68604
-200				
-100				
0	0.61508	2.64	3.29E-05	0.80275
100	1.231	3.125	1.83E-05	0.91797
200	1.226	7.117	1.57E-05	0.93789
300	1.311	112.4	1.49E-05	0.94338
400	1.318	1073	1.35E-05	0.94682
500	1.445	4735	1.41E-05	0.96961
600	1.431	16125	9.23E-06	0.9534
700	1.3	32092	5.54E-06	0.99057
800	1.4	38608	9.83E-06	0.97197
900	1.468	37781	9.29E-06	0.96904
1000	1.333	11413	1.68E-05	0.92244
1100	1.364	404.8	6.80E-05	0.88048
1200	1.374	24.08	9.39E-05	0.8717
1300	1.366	4.769	8.94E-05	0.90022
1400	1.429	1.601	4.89E-05	0.97626
1500	1.516	0.7773	2.35E-05	0.7773

Appendix 2

Electrochemical Impedance Spectroscopy Zview2
Modelling Example Chi Square Values

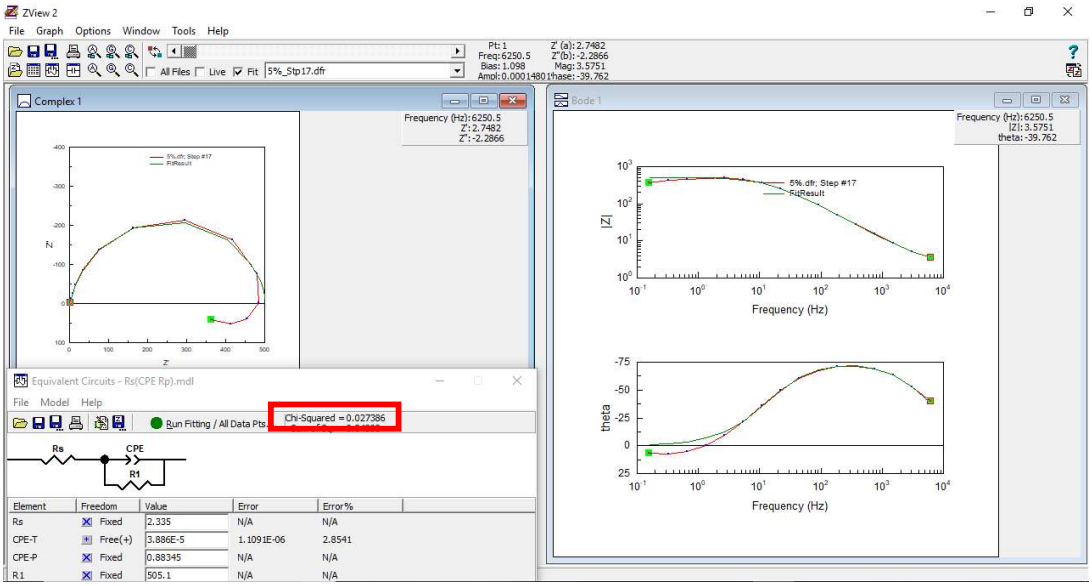

Figure 8-1 – Screenshot of Zview2 EIS analysis of 316L in 5% wt. nitric acid at 1.1V vs. SCE. Chi-Squared value highlighted in red.

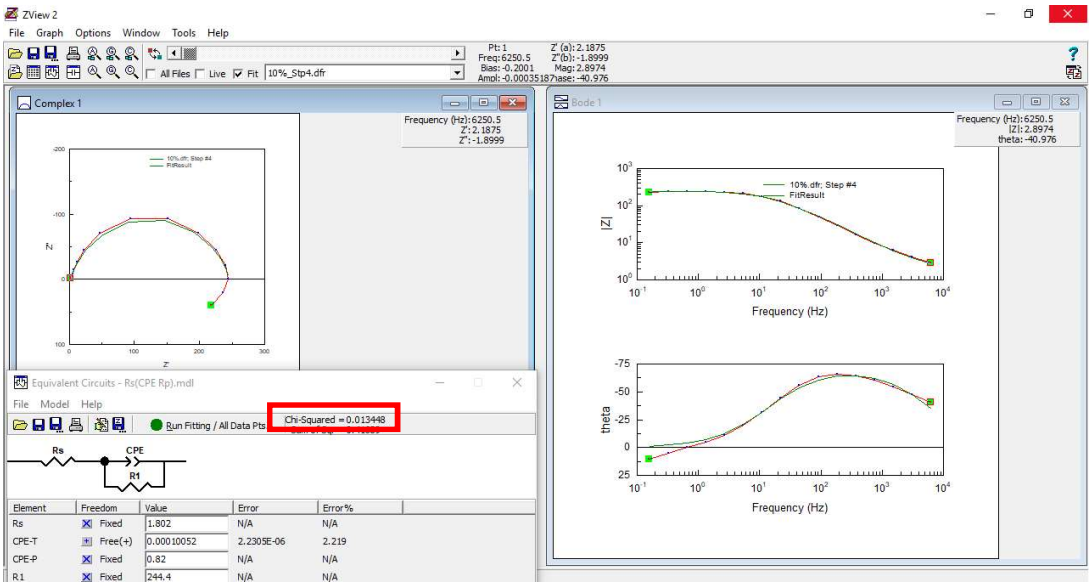

Figure 8-2 – Screenshot of Zview2 EIS analysis of 316L in 10% wt. nitric acid at -0.2V vs. SCE. Chi-Squared value highlighted in red.

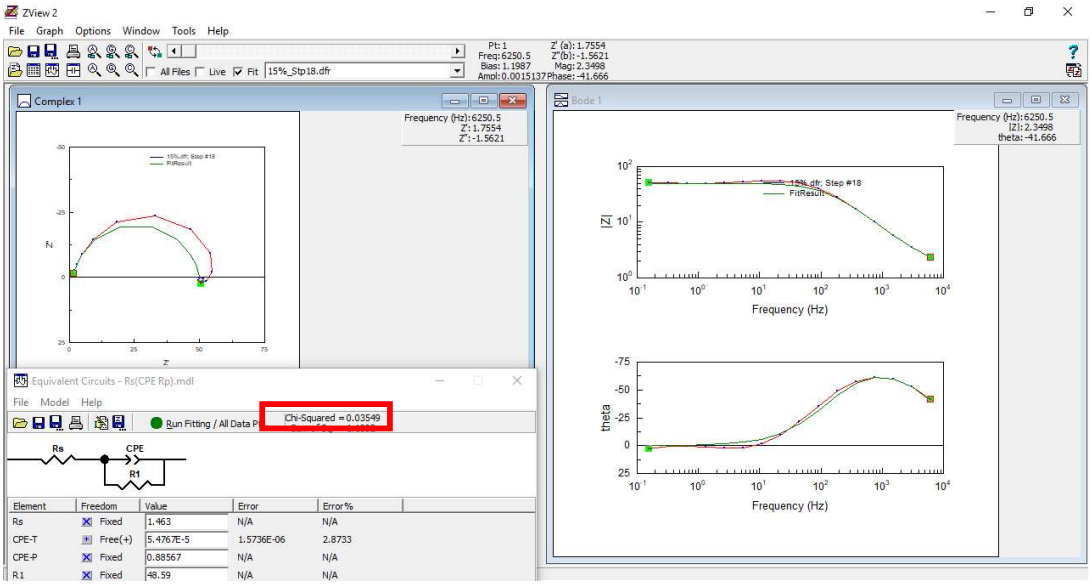

Figure 8-3 – Screenshot of Zview2 EIS analysis of 316L in 15% wt. nitric acid at 1.2V vs. SCE. Chi-Squared value highlighted in red.

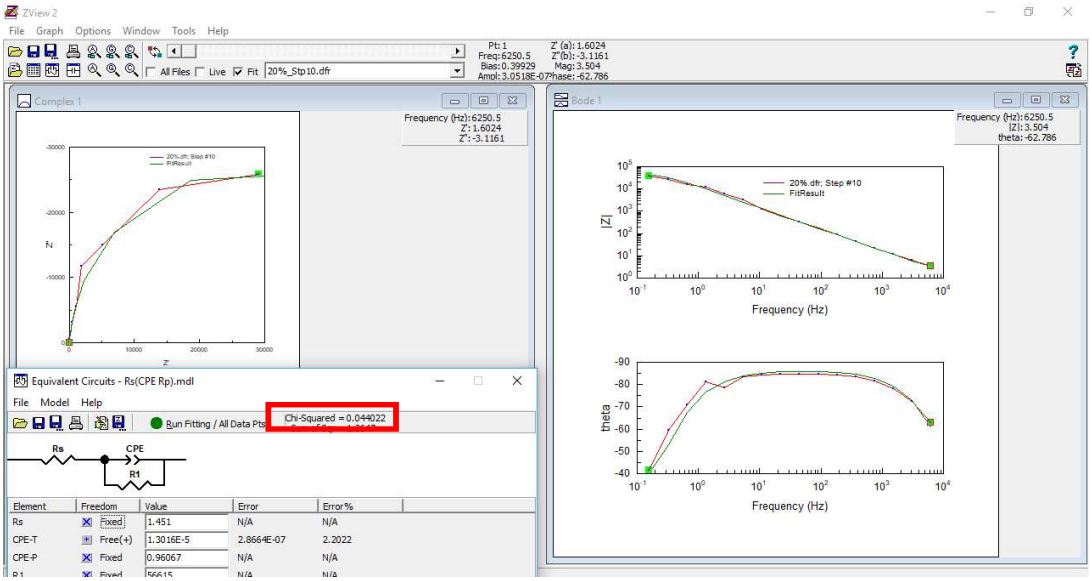

Figure 8-4 – Screenshot of Zview2 EIS analysis of 316L in 20% wt. nitric acid at 0.4V vs. SCE. Chi-Squared value highlighted in red.

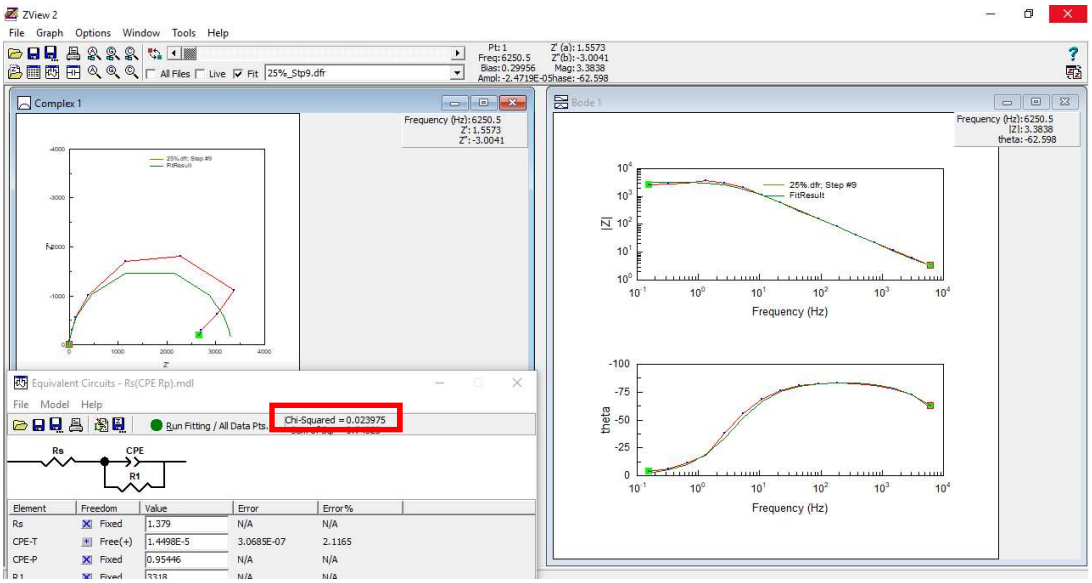

Figure 8-5 – Screenshot of Zview2 EIS analysis of 316L in 25% wt. nitric acid at 0.3V vs. SCE. Chi-Squared value highlighted in red.

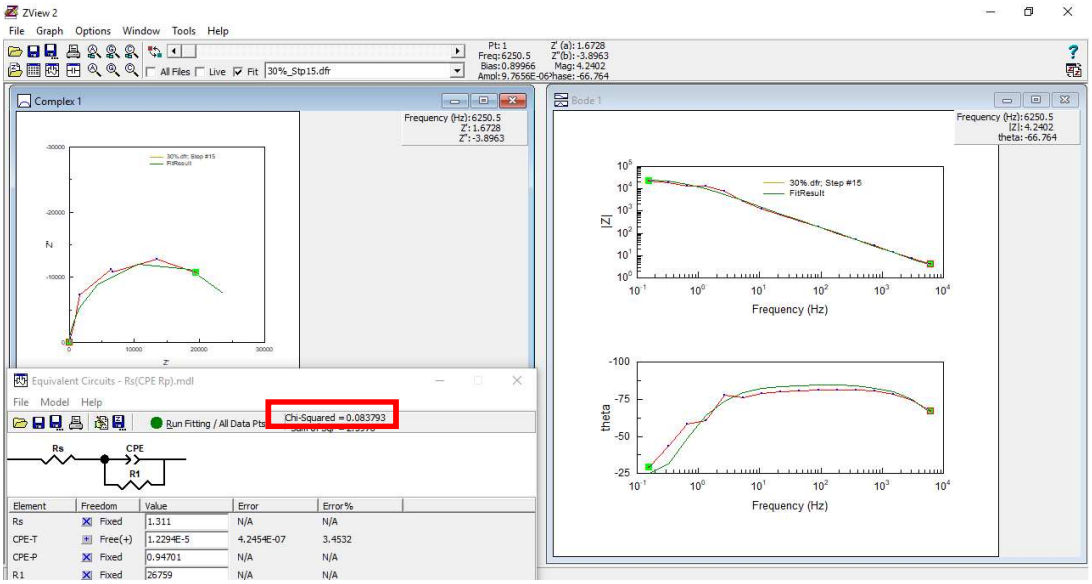

Figure 8-6 – Screenshot of Zview2 EIS analysis of 316L in 30% wt. nitric acid at 0.9V vs. SCE. Chi-Squared value highlighted in red.

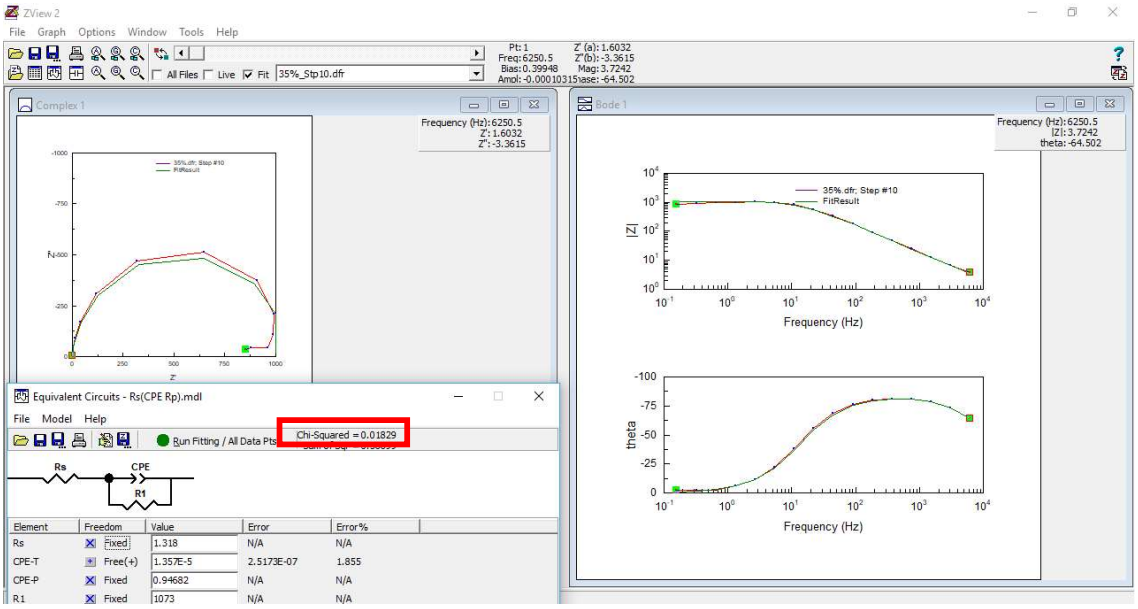

Figure 8-7 – Screenshot of Zview2 EIS analysis of 316L in 35% wt. nitric acid at 0.4V vs. SCE. Chi-Squared value highlighted in red.

Appendix 3

Published work:

"Fixed Contamination on Steel Surfaces - First Use of QCM to Measure Oxide Growth on Process Steels Under Conditions Typical of Nuclear Reprocessing" [205]

Mater. Res. Soc. Symp. Proc. Vol. 1383 © 2012 Materials Research Society
DOI: 10.1557/opl.2012.211

Fixed Contamination on Steel Surfaces: First Use of Quartz Crystal Microgravimetry to Measure Oxide Growth on Process Steels Under Conditions Typical of Nuclear Reprocessing.

Rebecca C. Woodhouse, Richard J. Wilbraham and Colin Boxall*
Engineering Department, Lancaster University, Lancaster LA1 4YW
*Email: c.boxall@lancaster.ac.uk

ABSTRACT

During the lifetime of a nuclear facility, radioactive material may become deposited onto process and structural material surfaces. Due to their high corrosion resistance, steels comprise the largest class of metal-based materials encountered on nuclear sites. A greater understanding of the mechanisms of how contaminant radionuclides interact with and attach to process steels in nuclear plant environments is required in order to enable informed decisions to be made about the design and effective application of decontamination techniques, reducing secondary wastes.

There is limited literature relating to radionuclide sorption mechanisms on steels. Key studies have found that sorbed contamination is almost entirely located in the outermost oxide layers formed at steel surfaces. Thus, a molecular level investigation of contaminant uptake during induced oxide formation would be beneficial in developing steel decontamination strategies.

Stainless steel 316L is commonly employed in the nuclear industry in process streams and pipework. Thus, we describe work carried out on electrochemically accelerated oxide growth on 316L and SS2343 (a 316L analog) in nitric acid media and its characterisation using combined voltammetric and microgravimetric measurements. These allow identification of active, passive, high voltage passive, transpassive and secondary passivation regimes in the associated current voltage curves. EQCM on SS2343 coated quartz crystal piezoelectrodes, combined with potentiodynamic polarisation data have allowed us to determine that fastest net growth of surface oxide occurs in the low voltage passive regime. Further, we have directly measured the growth of that layer by using in situ microgravimetry for the first time. We will be shortly using the methods described above and radionuclide surrogates for the study of contaminant uptake during oxide formation and uptake onto preformed oxide layers. XPS will be used to determine layer composition and mode of contaminant uptake.

INTRODUCTION

Decontamination of nuclear facilities for decommissioning allows for the reduction of waste classification levels with concomitant decreases in waste consignment costs, remote handling, hazard and personnel risk. Development of cost effective decontamination strategies, including selection of a suitable technique, identification of their R&D needs, confidence in efficacy and minimising of secondary wastes, requires a fundamental understanding of the interfacial science of radionuclide contaminants and the way in which they are associated with surfaces to be decontaminated. Due to their high corrosion resistance, steels are ubiquitous on nuclear sites as process plant and construction materials. Current understanding of the mechanisms of adherence and penetration of contamination into steels is inadequate to support informed choice of decontamination methods.

Surface contamination, generally derived from the "plating out" of solids, colloids or metal ions from a liquid/solution phase, is broadly classified as being of two main types: non-fixed and fixed contamination. Whilst Rouppert *et al* [1] have suggested that fixed contamination is chemisorbed and non-fixed is physisorbed, the distinction between the two types is in reality more subtle. Studies indicate that inter-conversion between fixed and a non-fixed state is possible, depending upon the environmental conditions.

This aside, it is clear that contamination adheres via a range of surface sorption mechanisms which, in approximate order of increasing strength, may be listed as being through: Van de Waals forces; hydrogen bonding; electrostatic attraction; outer sphere complexation; inner sphere complexation; surface precipitation of polynuclear / colloidal material; and incorporation, either through co-precipitation, compound formation or interstitial insinuation.

Large quantities of "plated out" contamination is loosely bound to the surface through weak electrostatic interactions and is easily removed by most clean up techniques, including swabbing, and shall not be considered here. Electrostatically held and some complexed metal ions may be removed by relatively benign methods e.g. wiping the surface with a surfactant solution (SGDS, N10) containing a chelating agent that exhibits a high affinity for the metal ion in question e.g. citrate, EDTA. Again, this type of contamination shall not be considered here.

Difficulties start to arise after the removal of weakly bound material. The surface may then be only slightly contaminated but the associated contaminant may be fixed in some way e.g. for metals, held within difficult to remove oxide layers, molecularly bound to the solid surface or sequestered in surface cracks/crevices. For these fixed contaminants on metals, the most common methods of (electro) chemical decontamination are the use of simple mineral acids or the more sophisticated MEDOC process (MEtal Decontamination by Oxidation with Cerium), Recently developed extreme methods involve flushing with reactive microemulsions of organic acids in supercritical CO_2 [2] and the use of foams as carriers for decontaminants. However, these all result in dissolution of a layer of substrate surface increasing secondary waste and burdens on downstream effluent treatment plants.

There is limited literature relating to radionuclide sorption mechanisms on engineering metals such as steels and, in order to decontaminate such surfaces more efficiently (high decontamination factor, fewer secondary wastes etc.), there is a need to understand the chemistry of the contamination process i.e. how contaminant radionuclides interact with and attach to process engineering materials in plant environments.

Key studies [1,3] have found that sorbed contamination is almost entirely located in the outer-most oxides on coated metal surfaces. The passivating oxide coating formed on steel is influenced by the type of steel as well as by environmental factors, including oxygen, moisture, the presence of other ions, and the electrostatic potential of the surface and pH of the local environment [2]. The aim of the work presented here is to determine the conditions required for oxide formation on SS316L in nitric acid (HNO_3). The next stage in this work will then deliberately grow oxide layers in the presence of surrogates for radionuclide contaminants and to determine their extent and mode of incorporation in the oxide layer.

EXPERIMENT

All chemicals were purchased from Sigma-Aldrich Ltd. (Gillingham, UK), the nitric acid being ACS reagent 70% wt. All solutions were prepared using doubly deionised water. The 316L steel bars for the working electrode were purchased from Advent Research Materials. The bars

were mounted on a brass head, sealed in epoxy resin and moulded into a cylindrical shape. The working electrode pre-treatment consisted of polishing on emery paper up to 1200 grade and polishing using 6 and 1 micron diamond paste, degreased in acetone and rinsed with purified water. The electrochemical quartz crystal microbalance (EQCM) piezoelectrode crystals were quartz, AT cut, with a resonant frequency of 5 MHz and a 25°C temperature profile, purchased from Q-Sense (Biolin Scientific, UK). All experiments were carried out at room temperature (20 ±2°C). Voltammetry was carried out at a scan rate of 10 mV s^{-1}. A three electrode cell was employed featuring a platinum mesh counter with a saturated calomel electrode (SCE) reference electrode for the polarisation experiments and a silver chloride electrode (Ag/AgCl) for EQCM experiments. All potentials are referred to vs. SCE (-0.241 V vs. SHE). EQCM experiments were carried out using a quartz crystal microbalance from Maxtek (5980 Lakeshore Drive, Cypress, CA, USA) and a Q-Sense open module (Gothenburg, Sweden) with a combined Autolab PGSTAT20 potentiostat from Windsor Scientific Ltd. (Slough, UK).

DISCUSSION

Polarisation Studies

Figure 1(a) shows potentiodynamic polarisation curves for 316L stainless steel in a range of HNO_3 concentrations, 5-35% over the potential range -0.5V to 1.5V. This range of concentrations was chosen because [HNO_3] ≤15% are representative of concentration regimes encountered in reprocessing streams whilst 35% is representative of conditions encountered in highly active liquid evaporators.

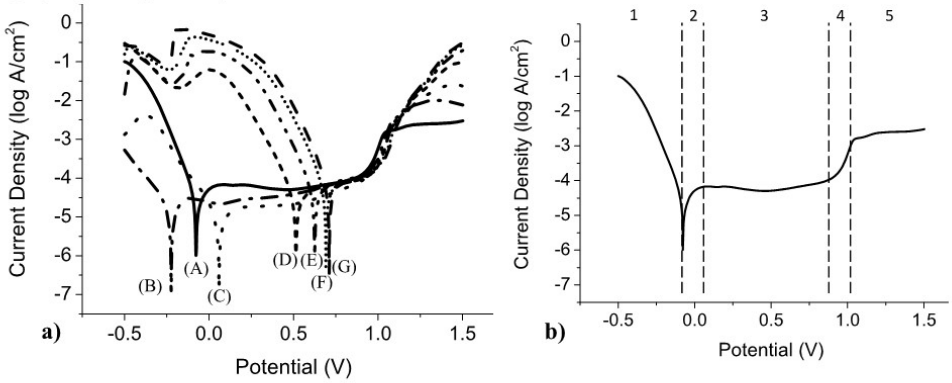

Figure 1. a) Potentiodynamic polarisation plots of type 316L SS in 5%-35% (A-G) HNO_3 at room temperature (20 ±2°C). Plots were measured in the potential range -0.5V to 1.5V (sweep rate, 10mVs^{-1}), (a) Shows the polarisation curves for 5%-35% HNO3. b) Potentiodynamic polarisation plot for 5% HNO_3.

Five distinct regions may be identified on all polarisation curves of figure 1(a) which, for the sake of illustrative clarity are indicated on the curve recorded at 5% nitric acid, figure 1(b), are as follows: region 1; active dissolution, region 2; passivation, region 3; passivity, region 4;

transpassive dissolution and region 5; secondary passivation/oxygen evolution [4]. The results of figure 1 clearly show that there is a shift in the corrosion potential between 15 and 20% HNO_3 concentrations. In 5 to 15% the steel begins to passivate in the region of -0.2 to -0.1V, whereas at higher nitric acid concentrations (20-35%) passivation does not occur until a potential of 0.5V (0.5-0.75V) is reached. This shift results in a much narrower passive region, this is due to the increase in [HNO_3] which increases the corrosion potential.

The shift in the corrosion potential can be explained by the electrochemical nature of stainless steels and nitric acid. The good corrosion resistance of stainless steels arises from a Cr enriched, Cr-Fe oxide film that forms on the surface. These oxides are extremely thin <5nm. However, they are strongly adherent and chemically stable [5]. At lower potentials, Cr exists in its trivalent state, Cr_2O_3. When the potential increases to ~0.355-0.555V, the oxidation state increases to its hexavalent state. The oxides formed in this environment are generally more soluble in HNO_3, leading to Cr dissolution from the oxide layer, causing the passive film to disintegrate [6,7]. This transpassive dissolution of Cr leads to an increase in the fraction of Fe(III) in the remaining oxide. According to modelled work, when the surface fraction of Fe(III) in the outermost later exceeds that of Cr then secondary passivation can occur [8,9].

HNO_3 complicates the electrochemical behaviour of stainless steels. The reduction of HNO_3 is autocatalytic in nature, with the generation of aqueous nitrous acid (HNO_2). With increasing HNO_3 concentration the reduction rate of HNO_3, and thus the oxidising power due to the formation of HNO_2, also increases. This autocatalytic behaviour accelerates the corrosion rate due to the oxidation of alloying elements, such as Fe and Cr. Consequently Cr, which is important to passive film stability, depletes from the surface. Thus, increasing the HNO_3 concentration leads to an increase in the corrosion potential and corrosion current density [10,11].

316L enters the transpassive region at around 1V in all concentrations of nitric acid. Secondary passivation (a supplementary Fe rich oxide layer formation, characterised by a levelling off of the current after onset of transpassive dissolution) is observed at the lower concentrations of nitric acid. This feature occurs more distinctly in 5% and 10% nitric, with almost a complete levelling off of current, compared to 15% where the current is seen to increase beyond the transpassive region before starting to level off. This secondary passivation feature does not occur in higher nitric concentrations. This may be due to the increasing oxidative power of the nitric acid, preventing the formation of the Fe enriched secondary layer. These results indicate that to artificially 'grow' oxide layers on steel surfaces the applied potential needs to be <1V for samples in all nitric acid concentrations, to avoid transpassive dissolution, and above -0.2V to allow active passivation to occur. Although, due to the narrowing of the passivation region with increased nitric concentration, this does not apply to all the tested nitric concentrations. Having determined the regions of corrosion, passivation and transpassivation of 316L steel in nitric acid, we now describe EQCM studies of the passive region between -0.2V to 1V.

Electrochemical Microgravimetry Studies using the EQCM

Using EQCM, chronoamperometric-microgravimetric measurements were made by means of a potential 'staircase' experiment in which the potential was stepped by 0.15V from an initial value of -0.2V to 1.15V. At each step on the 'staircase' the potential was held for 1 hour and the resultant current transient and change in electrode mass was recorded.

Figure 2a shows the time dependence of the changes in electrode mass (as determined by the use of the Sauerbray equation [12]) that occur in response to the potential 'staircase' as a function of HNO_3 concentration, from [HNO_3] of 5% (figure 2a) to 35% (figure 2g). For lower concentrations of nitric (≤15%), mass gain occurs rapidly at potentials -0.2V due to formation of the passive film. This mass gain slows between 0.25V and 0.4V, corresponding to the region where it has been suggested that Cr oxidation from Cr(III) to Cr(VI) occurs [6]. Cr(VI) is more soluble and is therefore slowly released from the electrode surface, leading to a lower rate of mass increase. At higher potentials, ~0.7V to 0.85V, a mass decrease is observed, most likely due to increase rapid dissolution of the high valency Cr(VI) that precedes the onset of transpassive dissolution [7]. At 1V transpassive dissolution leads to a renewed strong decrease in mass.

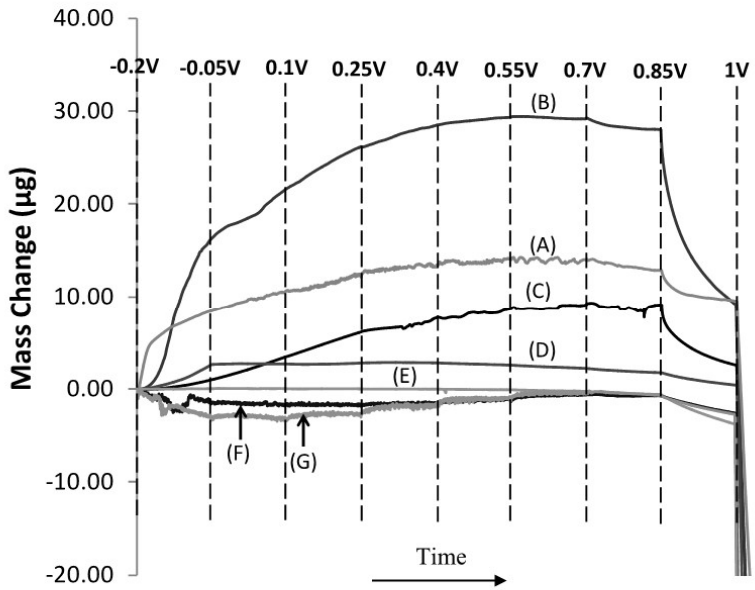

Figure 2. Mass Change of SS2343 as a function of time during potential step experiments in 5-35% (A-G respectively) nitric acid. Polarisation conditions: Start potential = -0.2V, end potential = 1V, potential step = 0.15V, time in between steps = 60mins.

At [HNO_3] ≥20% the pattern of mass change alters. This agrees with our polarisation experiment results, figure 1, wherein changes in electrode behaviour were observed between 15% and 20%. Due to the autocatalytic nature of HNO_3 driven oxidation processes on steel at higher [HNO_3], the active-passive transition shifts to a higher potential, >0.5V, at [HNO_3] of ≥20%. This narrowing of the passive region leads to a mass decrease at lower potentials for these higher nitric concentrations, probably due to the oxidation of Fe and Cr by HNO_2, thereby increasing corrosion. There are small increases in mass at the higher potentials where the oxide usually forms. The smaller size of this change compared to that obtained at lower nitric

concentrations indicates that a much thinner film is formed in higher concentrations of HNO_3, if it is formed at all. One consistent pattern of behaviour is the rapid decrease in mass at 1V, corresponding to the passive-transpassive transition; this does not appear to be affected by the increase in HNO_3 concentration.

CONCLUSIONS

In the first study of its type, we have used EQCM to study the induced formation of the passive oxide layer at a 316L analog as a function of HNO_3 concentration (5% to 35%). At $[HNO_3] \leq 15\%$, the maximum extent of oxide growth is observed at E=~0.55V. Beyond this point, the transpassive processes leads to a mass loss from the electrode surface, the first time such a feature has been observed on passivated stainless steel. Oxide growth is not seen at $[HNO_3] \geq 20\%$, with all samples presenting substantial mass loss at E=0.7V, a transpassive process also seen in the case of samples studied at ≤15%. This has repercussions for the use of stainless steels in highly oxidising environments, such as those that may occur in the concentrated HNO_3 highly active raffinate liquor solutions that are found in evaporators.

These studies have provided us with information that will allow us to artificially 'grow' oxide layers in any concentration of HNO_3. The addition of radioactive simulants alongside further EQCM studies and X-ray photoelectron spectroscopy (XPS) will allow us to determine the chemical composition, thickness of the oxide layers formed and provide details of how radioactive materials have become incorporated into these layers.

REFERENCES

1. F. Rouppert, A. Ivoallan and C.Argeron, presented at the WM'02 Conference, Tuscon, AZ, 2002.
2. R. Shimizu, K. Sawada, Y. Enokida and I. Yamamato, J. Nucl. Sci. Technol. **43** (6), 694-698 (2006).
3. A. J. Francis, C. J. Dodge, J. B. Gillow, G. P. Halada and C. R. Clayton, Report No.64946, 2001.
4. M. Bojinov, I. Betova, and R. Raicheff, *J. Electroanal. Chem.* **430** (1-2), 169-178 (1997).
5. T. L. S. L. Wijesinghe and D. J. Blackwood, App. Sci. **253** (2), 1006-1009 (2006).
6. C. –O. A. Olsson and D. Landolt, *Electrochim. Acta.* **48** (9), 1093-1104 (2003).
7. N. Padhy, R. Raul, U. Kamachi Mudali and B. Raj, *App. Surf. Sci.* **257** (11), 5088-5097 (2011).
8. I. Betova, M. Bojinov, T. Laitinen, K. Makela, P. Pohjanne and T. Saari, *Corr. Sci.* **44** (12), 2675-2697 (2002).
9. M. Bojinov, I. Betova, G. Fabricius, T. Laitinen, R. Raicheff, and T. Saario, *Corr. Sci.* **41** (8), 1557-1584 (1999).
10. N. Padhy, S. Ningshen, U. Kamachi Mudali, and B. Raj, *Scripta Materialia.* **62**(1), 45-48 (2010).
11. P. Fauvet, F. Balbaud, R. Robin, Q. T. Tran, A. Mugnier, and D. Espinoux, *J. Nucl. Mat* 375, 52-64 (2008).
12. Inc, Maxtek, *RQCM: Research Quartz Crystal Microbalance; operation and service manual*, (2002).

Appendix 4

Published work:

"Nitric Acid Reduction on 316L Stainless Steel Under Conditions Representative of Reprocessing" [183]

ECS Transactions, 53 (21) 33-44 (2013)
10.1149/05321.0033ecst ©The Electrochemical Society

Nitric Acid Reduction On 316L Stainless Steel Under Conditions Representative Of Reprocessing

R. C. Woodhouse, C. Boxall, R. J. Wilbraham

Department of Engineering, Lancaster University, Lancaster, LA1 4YR

Steels comprise the largest class of metal-based materials encountered on nuclear sites. An understanding of how process steels interact with HNO_3 in spent fuel treatment plant environments is required to enable informed decisions to be made about the design and effective application of different steel types within nuclear environments. Stainless steels readily passivate in nitric acid. However, increasing the oxidising power of the media can lead to passive film dissolution, resulting in rapid transpassive corrosion. The corrosion of steels in nitric acid is further complicated by the autocatalytic reduction of HNO_3 to aqueous HNO_2 which attacks the steel surface. This paper describes the effect of this behaviour on process steels in stagnant and/or flowing conditions using electrochemical and microgravimetric based methods. We describe linear sweep voltammetry studies performed on 316L stainless steel rotating disk electrodes in varying concentrations of nitric acid and rotation speeds and provide a qualitative interpretation of the results and what these imply about the mechanism of HNO_3 reduction. These findings will be used in follow on studies to determine the kinetic parameters of the nitric acid reduction reaction at the surface of 316L stainless steel.

Introduction

Reprocessing of spent nuclear fuel is an important step in closed nuclear fuel cycles. Reprocessed uranium and plutonium may be used in uranium oxide, mixed oxide (MOX) or breeder reactors, recycling the bulk of the spent fuel material and reducing waste output significantly (1). In the UK, spent nuclear fuel is reprocessed at the THORP facility at Sellafield, Cumbria, using the Plutonium URanium EXtraction process (PUREX). The initial step in this process is the dissolution of spent fuel rods in high concentration nitric acid, ~30% wt. (2, 3). The dissolved U and Pu are subsequently controllably separated into either an aqueous HNO_3 stream or a non-aqueous tri-n-butyl phosphate (TBP) and odourless kerosene (OK) stream. As a result of dilution, and also dissolved fission product/minor actinide induced radiolysis of HNO_3, the concentration of HNO_3 in the aqueous stream may vary through the PUREX flowsheet, to a minimum of ~4% wt. (2-4).

Structurally, austenitic stainless steels are used in reprocessing pipework and tanks due to their ability to form thin, nm scale, iron/chromium protective oxide films in

response to highly oxidising conditions, leading to passivation of the steel surface and consequent high corrosion resistance.

The steel may also autocatalytically interact with the HNO_3 resulting in a variety of nitrogen-oxygen based reduction products. This HNO_3 reduction process has been previously studied on platinum and on 304L stainless steels in nitric acid condensates (5). For concentrations of 1 to 10 mol dm^{-3} HNO_3 two different mechanisms of nitric acid reduction have been proposed by Vetter and Schmid (6-8; 9-13). Vetter (6-8) describes the autocatalytic reduction of HNO_3 as a heterogeneous process, where the chemical regeneration of NO_2 (electroactive species) occurs at the electrode surface. In this case stirring would be expected to have no influence on the current density due to the adsorbed nature of the electroactive species. Schmid (9-13) describes the reduction of HNO_3 as an autocatalytic process moderated by the chemical regeneration of NO^+ (electroactive species).

There is currently broad consensus in the literature that the Schmid mechanism obtains and may be simply expressed as:

$$HNO_2 + H^+ + e^- \rightarrow NO_{ads} + H_2O \quad [1]$$

$$2NO + HNO_3 + H_2O \rightarrow 3HNO_2 \quad [2]$$

Reaction [2] has been shown to be slow at $[HNO_3]$ <6 mol dm^{-3} (14), with only reaction [1] occurring with appreciable rate over that concentration range. At $[HNO_3] > 6$ mol dm^{-3}, as a result of increased $[HNO_2]$ and increased thermodynamic stability of the intermediates (specifically NO_2 (14), see below), reaction [2] proceeds fast enough to produce, in concert with reaction [1], an autocatalytic cycle for HNO_2 reduction and regeneration, leading ultimately to enhanced rates of HNO_3 reduction on the electrode surface.

As mentioned above, this high level reaction is broadly accepted in the literature. However, there are two distinct schools of thought as to the mechanism of reaction [2]. One view, extensively studied by Balbaud (15) and Fauvet (14) is based on the reaction of a series of surface bound intermediates.

$$HNO_3 + NO_{ads} \rightarrow HNO_2 + NO_{2ads} \quad [3]$$

$$2NO_{2ads} + H_2O \rightarrow HNO_3 + HNO_2 \quad [4]$$

The other, most recently described by Lange (16) and essentially revisiting some early studies by Carta and Pigford (17) and Abel and Schmid (18-20), suggests the following solution phase mechanism:

$$HNO_3 + HNO_2 \rightarrow 2NO_2 + H_2O \quad [5]$$

$$NO_2 + NO + H_2O \rightarrow 2HNO_2 \quad [6]$$

This latter mechanism may be facilitated by NO desorption, as a result of high NO generation fluxes that might obtain from reaction [1] under autocatalytic acceleration by reaction [2].

The mechanism of reactions [3] and [4] is surface based, whilst that of reactions [5] and [6] is solution based. One objective of the current study is to resolve which is occurring at high nitric acid concentrations on 316L stainless steel (SS). Whilst the electrochemical reduction of HNO_3 is otherwise well understood, the effect of nitric acid concentrations > 5% wt., typical of those found in aqueous reprocessing streams, on nuclear process steel, such as 316L SS, has hitherto not been extensively explored and this comprises the second objective of this study.

Thus, here we investigate the electrochemical behaviour of 316L SS stainless steel as a function of nitric acid concentration. In order to determine the region of electrochemical passivity of 316L SS, we first describe baseline polarisation studies on 316L SS as a function of nitric acid concentration in the range 5-35% wt. This is followed by an electrochemical quartz crystal microbalance (EQCM) study of the *in situ* growth of SS 2343 (a 316L SS analogue) passive oxide layers, again as a function of nitric acid concentration. It is possible that the growth of a passive oxide on the 316L SS will inhibit the nitric acid reduction reaction, due to the oxide restricting access to sites on the steel surface that would allow the reduction of reaction to occur. Finally, in order to obtain insight into whether the reduction of HNO_3 at 316L SS is a heterogeneous surface or homogenous solution process, we also describe rotating disk electrode studies on 316L SS as a function of $[HNO_3]$.

Experimental

Materials

All chemicals were of AnalaR grade or better and supplied by Sigma-Aldrich Ltd. (Gillingham, Dorset, UK), the nitric acid being ACS reagent 70% wt. The 10 mm diameter stainless steel 316L bars, from which working electrodes were fabricated, were purchased from Advent Research Materials (Eynsham, Oxford, UK). EQCM piezoelectodes comprised of polished stainless steel 2343 (similar composition to 316L SS as shown in Table I) were purchased from Q-sense (Biolin Scientific, Coventry, UK). The piezoelectrode crystals were quartz, AT cut, with a resonant frequency of 5 MHz and a temperature of optimum stability of 25°C.

TABLE I. Composition of 316L SS and SS2343 (wt. %).

Stainless Steel Type	Cr	Ni	C	Mn	Si	P	S	Mo	Nb
316L	17	12	0.03	2	1.0	0.045	0.03	2.5	0.004
2343	16.6	11	0.026	1.51	0.36	0.033	0.025	2.53	0.005

All nitric acid solutions were prepared using doubly deionised water. Double deionised water was prepared using a Direct-Q 3 UV Millipore water purification system (Millipore, Watford, UK) to a resistivity of 18.2 MΩ.cm. Unless otherwise noted, electrolyte solutions were de-aerated by bubbling high purity nitrogen (BOC, UK) before all electrochemical measurements.

316L SS Electrode Preparation

The 10mm diameter stainless steel 316L bars were sliced and mounted on a brass head using silver loaded epoxy. This assembly was then placed in a cylindrical shape mould and sealed in epoxy resin in order to produce a suitable working electrode. Pre-treatment of the resultant working electrode consisted of polishing on 1200 grade emery paper, 6 and 1 micron diamond paste, before degreasing in acetone and rinsing with deionised water.

Linear Sweep Voltammetry of 316L SS in Nitric Acid

Linear sweep voltammetric (LSV) studies on the stainless steel (316L) electrodes immersed in nitric acid were measured using an Autolab potentiostat PGSTAT100. A three electrode cell was employed using a platinum mesh counter with a double junction saturated calomel electrode (SCE) as the reference electrode. LSV measurements on 316L SS in the presence of increasing concentrations of nitric acid were performed in 100 mL solutions of 5% wt. – 35% wt. nitric acid. Before the LSV studies, the 316L SS electrodes were left to settle for one hour, to attain a steady open circuit potential (E_{oc}). After 1h at E_{oc}, measurements of polarisation curves were made. During the LSV studies the potential was run from -0.5 to 1.5 V, at a scan rate of 0.1 V/min.

Microgravimetric Potential Step and Polarisation Studies of SS2343 in Nitric Acid

The EQCM is a well-established method for the measurement of small changes in mass due to reactions at the electrode-solution interface. Importantly, the EQCM has also been used to investigate passive film growth on metallic surfaces (21-26). It provides *in situ* information of mass change at the electrode surface and a time resolution sufficient to provide real time growth curves of the passive film, as established by Olsson *et al* (27). This makes microgravimetry useful in the study of the dynamic responses of passive metals and alloys to redox changes in the aqueous environment and particularly, applied potential.

A detailed description of QCM theory may be found in various texts (28-31). Assuming mass is rigidly bound, the measured shift in the resonant frequency is converted to a mass change via the Sauerbrey equation, Equation [7]

$$\Delta f = -C_f \Delta m \qquad [7]$$

where Δf is the change in resonant frequency (Hz), Δm is the mass change (g) and C_f is the sensitivity constant. The value of C_f can be determined from electrochemical deposition and dissolution of copper via cyclic voltammetry (32, 33); we have found it to be 0.059 Hz (ng cm^{-2}), which is in excellent agreement with a theoretical value of 0.056 Hz (ng cm^{-2}) quoted by the manufacturer (Q-sense, Biolin Scientific, Manchester, UK).

EQCM experiments were carried out using a quartz crystal microbalance from Maxtek (5980 Lakeshore Drive, Cypress, CA, USA) and a Q-Sense open module (Gothenburg, Sweden) with a combined Autolab PGSTAT20 potentiostat from Windsor Scientific Ltd. (Slough, UK). Stainless steel QCM crystals (Q-Sense, Biolin Scientific, Manchester, UK)

were SS 2343, a 316L analogue. Current and mass-response profiles were always recorded simultaneously. Polarisation and potential step measurements were performed in 1.5 mL (1.5 cm^3) solutions of 5 – 35% wt. HNO_3.

Rotating Disk Electrode (RDE) Studies

RDE studies on 316L SS electrodes were set up akin to the polarisation studies. First, in order to condition the electrode, a reverse polarization scan was performed from 0.75 V down to a potential of 0.25 V. Then the potential was then held whilst the rotation of the electrode was varied from 100-3000 rpm and the current measured. At each rotation speed the current was allowed to stabilize for 5 minutes before a reading was taken.

Results and Discussion

Polarisation Studies

Figure 1(a) shows potentiodynamic polarisation curves for 316L SS electrodes recorded in HNO_3 concentrations from 5-35% (1.13 – 7.89 mol dm^{-3}) over the potential range -0.5 to 1.5 V. This range of concentrations was chosen because [HNO_3] ≤15% (≤3.38 mol dm^{-3}) is representative of concentration regimes encountered in typical nuclear plant reprocessing streams, whilst 35% (7.89 mol dm^{-3}) [HNO_3] is representative of conditions encountered in highly active liquid evaporators.

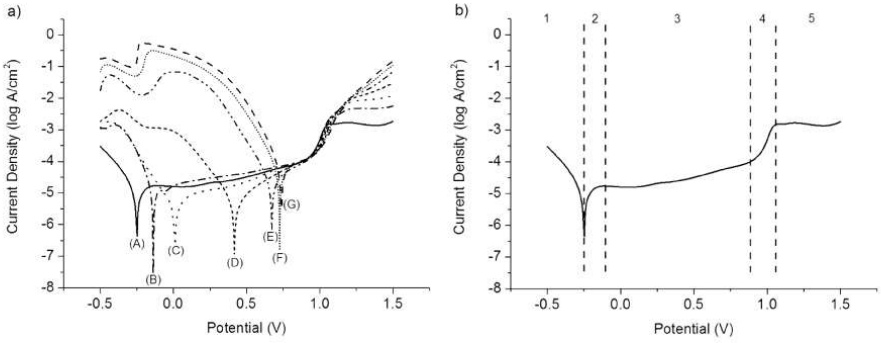

Figure 1. Potentiodynamic polarisation plots of SS316L in 5-35% (A-G) HNO_3 at room temperature (20 ±2°C). Plots were measured in the potential range -0.5 to 1.5 V (sweep rate, 10 mVs^{-1}). (a) Shows the polarisation curves for 5-35% HNO_3 b) polarisation curve for 5% HNO_3, zones 1-5 are described in the text.

From Figure 1(a) it can be observed that at all HNO_3 concentrations studied, five distinct regions may be identified which, for the sake of illustrative clarity, are indicated on the annotated curve recorded at 5% (1.13 mol dm^{-3}) nitric acid, Figure 1(b). These regions correspond to (1) active dissolution, (2) onset of passivation, (3) passivity, (4) transpassive dissolution and (5) secondary passivation/oxygen evolution (34). Returning to Figure 1a, it can be seen that there is a shift in the corrosion potential (E_{corr}) between

15 and 20% (3.38 and 4.51 mol dm^{-3}) HNO_3. This is consistant with previous results reported by Otero (35), on 316L SS, and Whillock (36), on 304L SS, and may be explained as follows. The corrosion potential of the 316L steel surface in the presence of HNO_3 is controlled by the concentration of HNO_2 available to interact with the steel surface, as shown by reaction [1] (14). At low concentrations of HNO_3 (≤15%) the autocatalytic regeneration of HNO_2 is slow (as described above). However, at high HNO_3 concentrations (>15%) the regeneration of HNO_2 is fast due to both the increased availability of HNO_3 in reaction [2] and the increased stability of NO_2 at higher acidities. Thus, charge transfer at the steel surface through reaction [1] is not limited by the concentration of HNO_2, resulting in an increase in the observed corrosion potential.

E_{corr} and i_{corr} Analysis. Corrosion potential (E_{corr}) and corrosion current density (i_{corr}) were calculated using Tafel extrapolation of the linear segments of the measured potential-current density curves of Figure 1a, in the vicinity of E_{corr}. As nitric acid is an oxidising agent, E_{corr} and i_{corr} are dependent on the autocatalytic reduction of nitric acid and both are known to increase with higher autocatalytic contribution via reactions [1] and [2] to the global reduction of nitric acid (36). Figure 2a shows calculated E_{corr} values obtained at 5-35% [HNO_3]. From Figure 2a it can be seen that E_{corr} varies sigmoidally with HNO_3 concentration, with E_{corr} increasing in the range 10-25% (2.26-5.53 mol dm^{-3}) [HNO_3], before plateauing at [HNO_3] ≥25%.

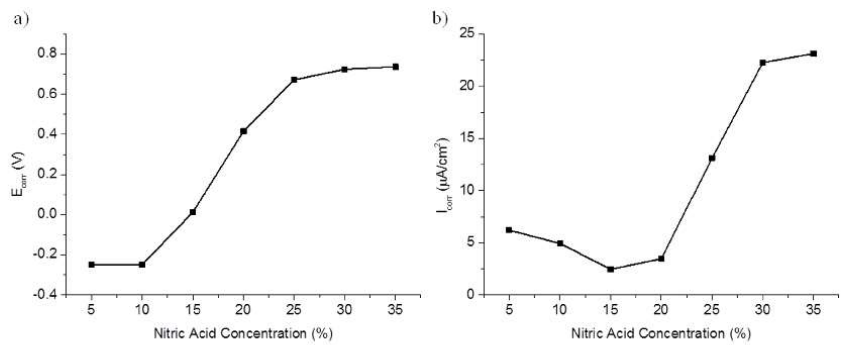

Figure 2. a) Corrosion potential, E_{corr}, values vs [HNO_3] b) Corrosion current density, [HNO_3] vs. i_{corr}, values calculated from Figure 1a for 316L SS in 5-35% nitric acid.

Figure 2b shows the i_{corr} values for 5-35% [HNO_3]. i_{corr} values decrease when [HNO_3] is increased at [HNO_3] ≤20%. This suggests an increase in the thickness of the passivating oxide film, consistent with the observed increase in E_{corr} in this [HNO_3] range. This, is turn, suggests that system behaviour is governed by the coupling of the steel surface oxidation and nitric acid reduction half reactions. The coupling of the nitric acid reduction with any nitrogen-oxygen species seems to play a minor role at best. This is only to be expected given the low concentration, in added nitric, of nitrous acid and thus low availability for participation in oxidation reactions. At [HNO_3] ≥20% (4.51 mol dm^{-3}) i_{corr} increases indicating that the passive oxide film on the surface of the steel is degrading resulting in an increase in the corrosion rate.

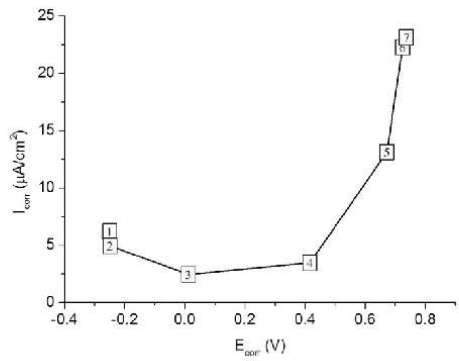

Figure 3. i_{corr} vs. E_{corr} calculated from Figure 1a for 316L SS in 5-35% (1-7 respectively) nitric acid.

Figure 3 shows i_{corr} vs. E_{corr} calculated from LSV results in Figure 1a. At ≥20% (4.51 mol dm^{-3}) where E_{corr} equals 0.4 V, i_{corr} increases with increasing concentration of nitric acid. This indicates that at ~20% HNO_3 E_{corr} begins to move into the transpassive region for 316L SS; dissolution of the passive film is occurring and the corrosion rate is increasing. This point will be discussed further in relation to the EQCM results.

Potential Step Studies

Using the EQCM, chronoamperometric-microgravimetric measurements were made by means of a potential 'staircase' experiment in which the potential was stepped at 0.15 V intervals from an initial value of -0.2 to 1.15 V. At each step on the 'staircase' the potential was held for 1 hour and the resultant current transient and change in electrode mass was recorded.

Figure 4 shows the time dependence of the changes in electrode mass (as determined by the use of the Sauerbrey equation (38)) that occur in response to the potential 'staircase' as a function of HNO_3 concentration, from [HNO_3] of 5 (Figure 4A) to 35% (Figure 4G). At lower concentrations of HNO_3 (≤15%), net mass gains are observed in the potential range -0.2 to 0.25 V due to the formation of the Cr/Fe oxide passive film. The mass gain then slows between 0.4 and 0.7 V. This corresponds to the region where it has been suggested that slow Cr(III) to Cr(VI) begins to occur at high potentials in the passive region immediately prior to transpassivity (39, 40)). At higher potentials, ~0.85 to 1 V, a mass decrease is observed, indicating the onset of transpassivity, most likely due to faster formation of Cr(VI) ions and rapid dissolution (41, 42).

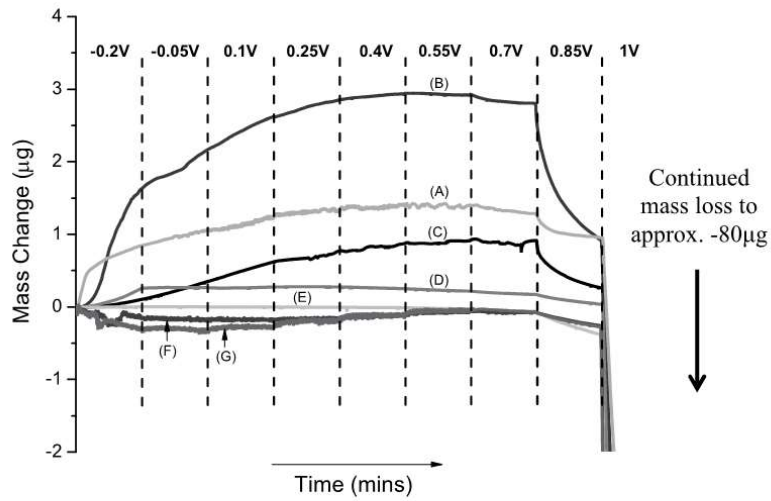

Figure 4. Mass change of SS 2343 as a function of time during potential step experiments in 5-35% (A-G respectively) HNO_3. Polarisation conditions: Start potential = -0.2 V, end potential = 1 V, potential step = 0.15 V, time between steps = 45 mins.

At $[HNO_3]$ ≥20% the pattern of mass change alters. This is in agreement with the polarisation experiment results of Figure 1a, the i_{corr} results of Figure 2b and also the i_{corr} vs. E_{corr} plot in Figure 3, wherein changes in electrode behaviour are observed between 15% and 20% $[HNO_3]$ as described previously. At $[HNO_3]$ ≥20%, larger current densities are observed in the low potential passive region of -0.25 to 0.25 V than at $[HNO_3]$ <20% (Figure 1a). From Figure 4, it can be seen that this larger current density occurs in the same region as a net mass decrease in the low potential region for $[HNO_3]$ ≥20%, suggesting that passive film formation is being, at least in part, inhibited. This further facilitates the reactions involved in the reduction of nitric acid at the steel surface, increasing the current density further.

It can also be seen from Figure 4 that moving to higher potentials (≥0.25 V) leads to small net increases in mass. Mass increase is concurrent with the decrease in the current density in Figure 1a, again indicative of passive film formation. The smaller size of this mass change compared to that obtained at lower nitric concentrations indicates either that: 1) a much thinner film is formed or 2) the film is still not fully formed and is only partially passive in character. One consistent pattern of behaviour is the rapid decrease in mass at 1 V, corresponding to the passive-transpassive transition. This does not appear to be affected by the increase in HNO_3 concentration and is associated with the onset of transpassive dissolution of the passive film.

Rotating Disk Electrode Studies

In order to investigate the effect of solution flow on the HNO_3 reduction process, RDE studies were performed using 316L SS disk electrodes. Importantly, oxide formation is likely to inhibit the nitric acid reduction on the steel surfaces. In order to remove this

inhibition as a factor in our rotation studies, the polarisation curves were first run in reverse, scanning cathodically from the transpassive region. Figure 5 shows a linear potential scan of 316L SS in a 5% HNO_3 solution. A current peak is observed in the 0.1 to 0.4 V region. This has been attributed to the surface electrode reaction from reaction [1] where HNO_2 is reduced at the electrode surface to, in the first instance, NO (16). Maximum current density is observed at 0.25 V. Consequently this was selected as the applied potential for all subsequent rotation speed studies. The decrease in reduction current at E <0.25V has been attributed to the further reduction of NO/HNO_2 to N_2O with a consequent impact on the autocatalysis facilitated by reaction 2 (16).

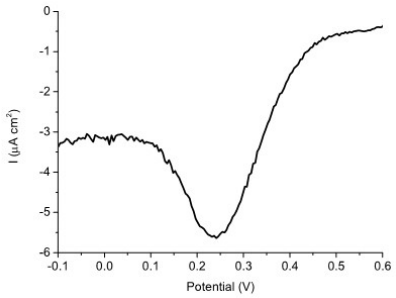

Figure 5. Polarisation curve showing a cathodic scan of 316L SS in 5% nitric acid at a rate of 10 mVs^{-1}.

Figure 6 shows a plot of current density vs. √angular velocity at 0.25 V in 5, 20 and 35% nitric acid. The results show that at the lower nitric acid concentrations of 5 and 20%, current density is independent of rotation speed. This indicates that the net HNO_3 reduction reaction of reactions [1] and [2] is mediated by electroactive species that are entirely adsorbed at the electrode surface. At 35% [HNO_3] the reduction current is substantially greater than that recorded at 5 and 20% [HNO_3] and decreases with increasing rotation speed. This indicates that at least a proportion of the net HNO_3 reduction is now being mediated by an autocatalytic mechanism making electroactive species (or precursor to some) in the bulk solution phase.

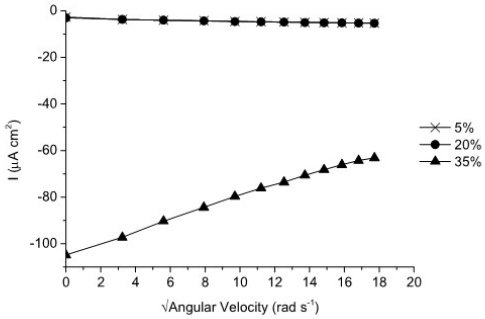

Figure 6. Current density vs. square root of angular velocity at 0.25 V/SCE as a function of HNO_3 concentration.

According to Abel & Schmid (10-13) and supported by, *inter alia*, Balbaud (15), Fauvet (14) and Lange (16) the electroactive species in this reaction is believed to be HNO_2 as per reaction [2]. At 5 and 20% (1.13 and 4.51 mol dm^{-3}) HNO_3, the observed reduction current shows a slight current increase with increasing rotation speed. This is most likely due to the increased flux of nitric acid to the surface of the steel, allowing it to react with the surface adsorbed NO via reaction [3]. Compared to results recorded at 35% HNO_3, electrode rotation at 5 and 20% [HNO_3] has little influence because the reaction is following the Balbaud (15) and Fauvet (14) reaction mechanism of reactions [3] and [4], where the electroactive reaction intermediates, or their immediate precursors, are adsorbed at the electrode surface.

At 35% (7.89 mol dm^{-3}) the rotation of the electrode leads to a decrease in the autocatalytically enhanced reduction current density. This inverse dependence of the current density on rotation speed is consistent with the loss, due to the stirring, of a solution phase electrogenerated electroactive entity or electrogenerated solution phase precursor of an electroactive entity. This is most likely to be NO in accordance with Lange's (16) solution phase mechanism of reaction [5] and [6]. Here, at high concentrations of HNO_3, NO is rapidly produced at the electrode surface, the resultant excess of NO leads to its subsequent desorption. This desorption allows NO_2, formed in solution via reaction [5], to react and regenerate electroactive species HNO_2. This is supported by the solution based reaction mechanism supported by Lange (16) and consistent with chemistry originally suggested by Carta and Pigford (17). The stirring of the solution would lead to the dispersal of NO into the bulk solution, preventing the regeneration of HNO_2, thus, retarding the autocatalytic cycle and leading to a decrease in the current density. The mechanism proposed by Balbaud (15) and Fauvet (14) may still occur in parallel at the electrode surface but more rapidly than at lower concentrations of nitric acid, due to the increased thermodynamic stability of NO_2 at the lower pH. Verification of this suggested explanation of the results shown in Figure 6 is currently being explored in our laboratory.

Conclusions

We have described the LSV and EQCM studies performed on 316L SS RDEs at varying concentrations of nitric acid and rotation speeds. The study led to the following conclusions.

The polarisation and EQCM results indicate a shift in electrochemical behaviour with increasing nitric acid concentration. RDE studies indicate two forms of Schmid's mechanism obtain on steels: 1) [HNO_3] $\leq$20%, the reaction of surface adsorbed intermediates such as NO and NO_2 dominates (as proposed by Balbaud (14) and Fauvet (15)) and the associated reduction current then shows no dependence on electrode rotation speed. 2) At [HNO_3] $\geq$20%, the reaction of NO and NO_2 intermediates in the bulk solution phase dominates (proposed by Lange (16) and Carta and Pigford (17)) and the associated reduction current then decreases with increasing rotation speed.

The latter behaviour is important when considering stainless steel pipework within nuclear environments that contain high concentrations of HNO_3. At higher concentrations

any stagnation or reduction in the flow rate may lead to an increase in the autocatalytic reduction process of nitric acid which, in turn, will lead to an increase in the corrosion potential, moving towards transpassive behaviour. This will over time lead to rapid corrosion and subsequent pipework failure. This knowledge will aid in determining conditions which may move stainless steels away from their passive domain, enabling decisions to be made to ensure the durability of the UK's spent fuel treatment plants.

Further work will involve numerical treatment of the RDE results obtained in this study, including Koutecky-Levich analysis (28). RDE studies for potentials either side of the 0.25 V peak shown in Figure 6 will also be required to further investigate influence of potential on the the kinetics of this nitric acid reduction mechanism at the stainless steel surface under concentrations representative of nuclear reprocessing.

Acknowledgments

We thank the Nuclear Decommissioning Authority (NDA) and Lloyd's Register Foundation (LRF). LRF, a UK registered charity and sole shareholder of Lloyd's Register Group Ltd, invests in science, engineering and technology for public benefit, worldwide.

References

1. P.D. Wilson, *The Nuclear Fuel Cycle: From Ore to Waste*, OUP Oxford (1996).
2. J.L. Robertson, *Chapter 9 - Nuclear Fuel Reprocessing*, in, NTEC (2011).
3. K.V. Hecke, P. Goethals, *Research on Advanced Aqueous Reprocessing of Spent Nuclear Fuel : Literature Study*, SCK●CEN (2006).
4. J.M. McKibben, *Radiochim. Acta*, **36**, 3-15 (1984).
5. F. Balbaud, G. Sanchez, G. Santarini and G. Picard, *Eur. J. Inorg. Chem.* **2000**(4) 665-674 (2000).
6. K. Vetter, *Z. Phys. Chem.* **194**, 199-206 (1950).
7. K. Vetter, *Z. Phys. Chem.* **194**, 284-296 (1950).
8. K. Vetter, *Z. Elektrochem., Ber Bunsenges. physik. Chem.* **63**, 1189-1191 (1959).
9. G. Schmid, *Z. Elektrochem., Ber. Bunsenges. physik. Chem.* **63**, 1192-1188 (1959).
10. G. Schmid, J. Delfs, *Z. Elektrochem., Ber. Bunsenges. physik. Chem.* **63**, 1192-1197 (1959).
11. G. Schmid, *Z. Elektrochem., Ber. Bunsenges. physik. Chem.* **65**, 531-534 (1961).
12. G. Schmid, G. Krichel, *Z. Elektrochem., Ber. Bunsenges. physik. Chem.* **68**, 677-688 (1964).
13. G. Schmid, M. A. Lobeck, *Z. Elektrochem., Ber. Bunsenges. Chem.* **73**, 89-199 (1969).
14. P. Fauvet, F. Balbaud, R. Robin, Q.T. Tran, A. Mugnier, D. Espinoux, *Journal of Nuclear Materials*, **375**, 52-64 (2008).
15. F. Balbaud, G. Sanchez, P. Fauvet *et al*. *Corros. Sci.*, **42** (10), 1685-1707 (2000).
16. R. Lange, E. Maisonhaute, R. Robin, V. Vivier, *Electrochem. Comm.*, **29**, 25-28 (2013).
17. G. Carta, R. Pigford, *Ind. Eng. Chem. Fundam*., **329**(6), 329-335 (1983).
18. E. Abel, H. Schmid, *Z. Phys. Chem.* **132**, 56, 64 (1928a).

19. E. Abel, H. Schmid, *Z. Phys. Chem*, **134**, 279 (1928b).
20. E. Abel, H. Schmid, *Z. Phys. Chem*, **136**, 153, 419 (1928c).
21. P. Schmutz, D. Landolt, *Electrochim. Acta*, **45**, 899-911 (1999).
22. P. Schmutz, D. Landolt, *Corros. Sci.*, **41**, 2143-2163 (1999).
23. D. Hamm, C.O.A. Olsson, D. Landolt, *Corros. Sci.*, **44**, 1009-1025 (2002).
24. C.O.A. Olsson, D. Hamm, D. Landolt, *J. Electrochem. Soc.*, **147**, 2563-2571 (2000).
25. M. Itagaki, H. Nakazawa, K. Watanabe, K. Noda, *Corros. Sci.*, **39**, 901-911 (1997).
26. C.O.A. Olsson, D. Landolt, *J. Electrochem. Soc.*, **148**, B438-B449 (2001).
27. C.O.A. Olsson, D. Hamm, D. Landolt, *J. Electrochem. Soc.*, **147**, 4093-4102 (2000).
28. A. Bard, L. Faulkner, *Electrochemical Methods: Fundementals and Applications*, John Wiley & Sons, New York (2001).
29. D.A. Buttry, *Electroanal. Chem.*, pp. 1-85 (1991).
30. D.A. Buttry, in *Electrochemical Interfaces: Modern Techniques for In-Situ Interface Characterisation*, H.D. Abruna, Editor, VHC Publishers Inc., pp. 529-566, (1991)
31. M.R. Deakin, D.A. Buttry, *Anal. Chem.*, **61**, 1147A-1154A, (2008).
32. C. Gabrielli, M. Keddam, R. Torresi, *J. Electrochem. Soc.* **138**(9), 2657-2660 (1991).
33. G.L. Borges, K. K. Kanazawa, J. G. Gordan II, *J, Electroanal. Chem.* **364**(1-2) 281-284 (1994).
34. M. Bojinov, I. Betova, R. Raicheff, *J. Electroanal. Chem.*, **430**, 169-178 (1997).
35. F. Otero, A. Pardo, F. Sáenz, M. V. Utrilla, P. Hierro, *Corr. Sci.*, **38**(9), 1485-1493 (1996(.
36. G.O.H. Whillock, T.J. Binks, C.J. Donahoe, *Corrosion,* **68**(11), 967-981 (2012).
37. N. Padhy *Role of Passivity and Surface Modification on the Corrosion Behaviour of AISI 304L Stainless Steel in Nitric Acid Medium*, Homi Bhabha National Institute (HBNI) (2010).
38. M. Inc., *RQCM: Research Quartz Crystal Microbalance; operation and service manual* (2002).
39. C.O.A. Olsson, D. Landolt, *Electrochim. Acta*, **48**, 1093-1104 (2003).
40. A. Fattah-alhosseini, A. Saatchi, M.A. Golozar, K. Raeissi, *Electrochim. Acta.*, **54**, 3645-3650 (2009).
41. N. Padhy, R. Paul, U. Kamachi Mudali, B. Raj, *App. Surf. Sci.*, **257** 5088-5097 (2011).
42. I. Betova, M. Bojinov, T. Laitinen, K. Mäkelä, P. Pohjanne, T. Saario, *Corr. Sci*. **44**, 2675-2697 (2002).